SCUOLA DI DOTTORATO
UNIVERSITÀ DEGLI STUDI DI MILANO-BICOCCA

MISSIONE 4
ISTRUZIONE
RICERCA

Department of **Environmental and Earth Sciences**

PhD program in **Chemical, Geological and Environmental Sciences**

Cycle **XXXVIII III**

Curriculum in **Geological Sciences**

TREE STABILITY IN URBAN FORESTRY TO SUPPORT BIODIVERSITY SYSTEMS

Matteo Andreozzi

mat.763651

Supervisor: *Riccardo Pietro Castellanza*

Co-Supervisor: *Matteo Oryem Ciantia*

Tutor: *Federico Agliardi*

Coordinator: *Marco Giovanni Malusà*

Academic year 2025/2026

Finanziato dall'Unione europea NextGenerationEU
Ministero dell'Università e della Ricerca
Italiadomani PIANO NAZIONALE DI RIPRESA E RESILIENZA

Acknowledgement

Sometimes
I slowly drift away
From all the dull routine
That's with me every day
A fantasy
Will come to me
(From now on - Supertramp)

To my Family,
To my Dad,

A long journey full of experiences,
A life story,
A professional path,

Special thanks go to my two supervisors, Riccardo Castellanza and Matteo Ciantia, who gave me this opportunity.

Thanks also to Davide, Giacomo, Andrea, David, Brian, Massimiliano, and Jonathan.

Thanks to the University of Milano-Bicocca, which was my second home. Thanks to Scotland, England and Switzerland, which welcomed me.

And finally, thanks to me too.

from now on

Abstract

Urban trees provide essential ecosystem services, but their failure under wind action is an increasingly critical issue for public safety and green space management where aerodynamic exposure is strongly influenced by urban morphology and where extreme events can combine strong gusts with adverse soil and hydrological conditions. Despite the widespread use of Visual Tree Assessment and non-destructive on-site testing, significant uncertainties remain in translating experimental results—such as soil-root system rotations—into robust estimates of anchoring capacity, especially when soil-root interaction is non-linear, anisotropic, and subject to cyclic and dynamic stresses.

The doctoral thesis focuses on the quantitative assessment of uprooting stability through activities that combine controlled experimentation, full-scale field tests, long-term monitoring, computational wind modelling and operational tools to support the mitigation of failure risk. The work began with an experimental campaign at the University of Dundee Botanic Garden, during which both non-destructive and destructive tensile tests were conducted on multiple trees and different pull configurations, interpreting the results considering a site-specific geotechnical characterization of the soil. In parallel, a method was developed to estimate the aerodynamic resistance coefficient from coupled wind-tilt time series. Based on data from uprooting tests, non-destructive tests and dynamic wind-tilt monitoring, safety factors were then evaluated. Finally, a new approach for generalizing the Wessolly curve was proposed through the application of Bayesian theory. In a further phase, a 1-g physical model was created, aimed at reproducing the main load mechanisms under controlled boundary conditions and directly measuring both the reactions at the base (forces and moments) and the kinematic response (tilt and accelerations) induced by the wind load.

A long-term monitoring campaign was conducted at the Vivaio Bicocca (Milan) during which wind intensity and direction measurements were measured, together with recordings of the inclination at the base of the trunk on different tree species exposed to the same local conditions; the aim of the activity was both to assess the variability in response of the different species planted in rows and to validate the monitoring data as support for re-inspection planning. In parallel, CFD simulations were performed, from the district scale to that of the individual tree, to visualize how urban morphology affects wind speed and pressure fields and, consequently, the aerodynamic loads acting on them. Finally, the use of LiDAR technology was validated, with its geometric surveys providing direct support for the design and verification of consolidation measures.

Overall, the thesis proposes an organic approach to exploring, testing and implementing methods for the quantitative assessment of tree stability. The aim is to improve the interpretation of experimental data, correlate anchoring capacity with soil conditions and wind exposure, and thus provide solid technical support for green space management and the mitigation of tree fall risk in urban areas.

Publications

Andreozzi, M., Marrazzo, G., Marsiglia, A., Boldrin, D., Castellanza, R. P., Knappett, J., & Ciantia, M. O. (2025). On the Uprooting Stability of Trees: Combined Loading Effect on Tree Stability Assessment. *Forests*, *16*(12), 1780.

Andreozzi, M., Castellanza, R., Ciantia, M., & Canepa, D. (2025). La sicurezza del verde urbano nell'era tecnodigitale. Metodologie innovative per la gestione e mitigazione del rischio di caduta alberi. In *Libro Bianco del Verde. Focus 24/25. Il verde nella città che cambia*. KEPOS-LIBRO BIANCO DEL VERDE APS.

Marrazzo, G., **Andreozzi, M.**, Boldrin, D., Galli, A., & Ciantia, M. O. (2026). Real-scale tests on the cyclic response of trees under toppling loads: experimental investigation and geotechnical interpretative framework. *Canadian Geotechnical Journal*, (ja).

Summary

Introduction

Background

The frequency and intensity of extreme weather events, such as storms and cloudbursts, have increased markedly in recent decades, with impacts that extend from human populations and man-made structures to animals and vegetation. Climate change is expected to significantly affect basic transport infrastructures and the built environment worldwide, as weather patterns become more arid, erratic and storm-prone (Satterthwaite et al., 2007). Because vegetation itself acts as a carbon sink, it is increasingly urgent not only to expand green infrastructure but also to protect and properly manage the existing green heritage, while developing low-carbon stabilization measures.

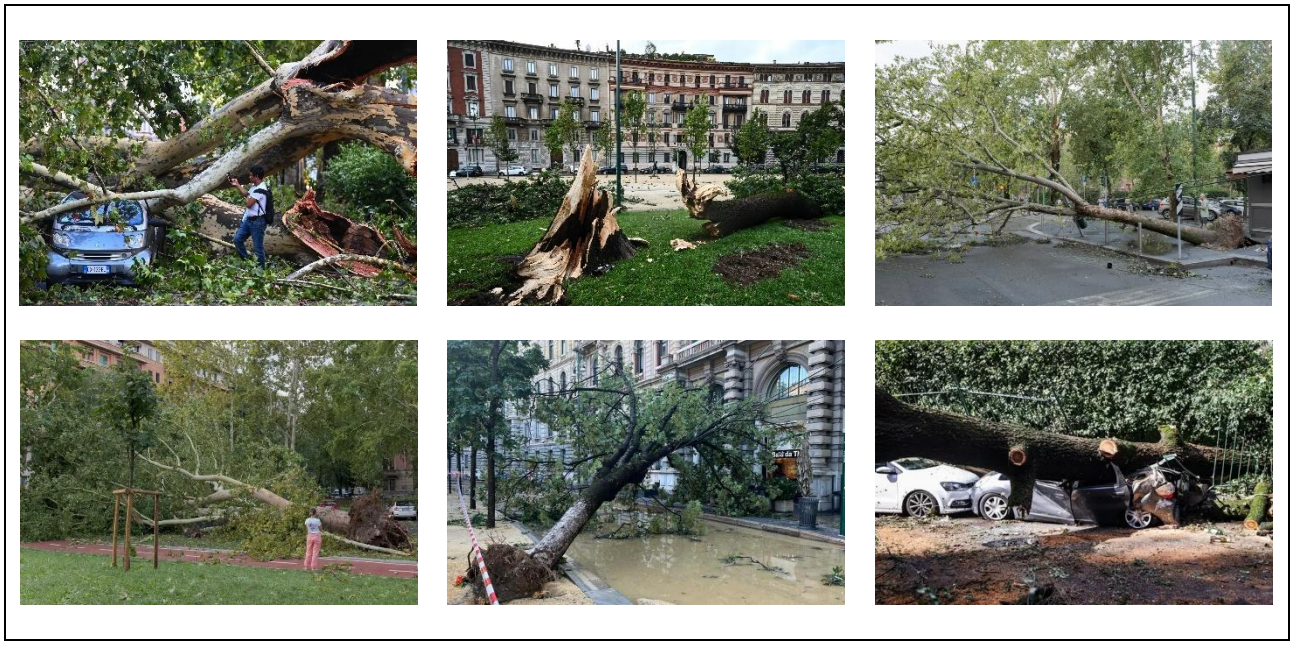

Figure 1: The result of the storm that struck northern Italy on July 24-25, 2023. The images refer to the city of Milan, where more than 6,000 trees fell. Source: PIERO CRUCIATTI/Getty Images.

Within this broader climate-resilience framework, urban trees play a distinctly dual role. On the one hand, they provide very high value in terms of ecosystem services, including mitigation of the urban heat island effect through shading and evapotranspiration, stormwater management, air-quality improvement, carbon sequestration and noise attenuation (Carinanos & Calaza, 2018; Speak & Salbitano, 2021; Cavender-Bares et al., 2022; Hand et al., 2019; D. Liang & Huang, 2023; Salmond et al., 2016). On the other hand, the same trees can become sources of hazard when subjected to strong wind gusts that exceed the loading conditions to which they are typically adapted. In such

circumstances, storms and severe winds may lead to stem breakage or uprooting, causing damage to buildings and infrastructure, disruption to transport networks and other services, injuries and, in the worst cases, loss of human life. The exposure of tall trees in urban areas—namely their spatial position relative to nearby structures, pedestrian and traffic flows, and local wind-amplification effects—plays a key role in determining the associated risk of failure (Giachetti et al., 2021; Ciftci et al., 2014).

This risk is further amplified in many cities by ageing tree populations, often established under past design criteria that did not anticipate current or future wind regimes, and by the lack of systematic monitoring and maintenance interventions. The combination of mature or over-mature stands with more intense wind gusts induced by climate change contributes to the urgent need to assess tree safety against breakage and uprooting. Similar concerns arise in forestry and agricultural contexts, where wind damage has long been recognized as a major issue, with the potential to compromise entire stands or commercial crops. Several authors have highlighted the need to quantify both the likelihood and the extent of wind damage, and to integrate this knowledge into standard management and forest planning tools in order to mitigate wind-related risks (Dupont & Brunet, 2008; Gardiner & Quine, 2000; Mickovski et al., 2005; Moore et al., 2008). In urban areas, where exposure and vulnerability are inherently high, the risk associated with tree failure has become an integral component of broader risk-management frameworks and is increasingly recognized in technical standards and best-practice guidelines.

Tree risk assessment has therefore become an integral component of broader risk-management analyses (BS 3998, 2010) and, as such, calls for dedicated mitigation strategies. Over the past two decades, the methods most commonly employed to evaluate tree condition have evolved from traditional Visual Tree Assessment (VTA; Mattheck & Breloer, 1994) towards the use of quantitative, geometry-based indicators, such as the slenderness ratio. In standard agronomic practice, the safety of trees against uprooting is typically evaluated through in situ, non-destructive static pulling tests. The corresponding predictions are derived from a phenomenological interpretation of the measured response, following the procedure originally proposed by Wessolly & Erb, 1998.

The possibility of measuring trees under actual wind-loading conditions has attracted growing interest. Field campaigns combining wind measurements with tree inclination or acceleration data have been conducted by various researchers (James et al., 2006; Moore & Maguire, 2008). The relationship between wind velocity and basal inclination is, however, inherently more complex than in static pulling tests, as it is influenced by turbulence, crown aerodynamics, dynamic amplification and soil–

root non-linearities. Despite this complexity, statistical approaches such as those described by Bejo L. et al. 2022 offer a way to evaluate tree stability directly under operational wind conditions.

Within a bio-engineering context, the stability assessment of trees is therefore a key element in the management of urban areas, where robust analysis techniques can substantially contribute to protecting both natural heritage and human activities. Since the approach proposed by Wessolly & Erb, 1998 was introduced, substantial effort has been devoted to improving the geotechnical and structural understanding of tree–soil interaction during uprooting. Field experimental research has investigated root architecture, soil conditions and failure mechanisms in a range of species and sites (Coutts, 1983a; Coutts, 1986; Crook & Ennos, 1998; Nicoll et al., 2006; Nicoll et al., 2008; Défossez et al., 2021; Galli et al., 2024). In parallel, laboratory physical modelling (Marsiglia et al., 2022; Zhang et al., 2020; Zhang et al., 2023), wind tunnel experiments (Cao et al., 2012; Gromke & Ruck, 2008) and numerical studies (Dupuy et al., 2005; Yang et al., 2014; Dattola et al., 2020) have been used to explore non-standard loading paths, investigate parametric dependencies and refine conceptual models of root-plate behaviour. Numerical and small-scale physical modelling are particularly well suited to controlling test repeatability and performing detailed parametric analyses (Zhang et al., 2023). By contrast, full-scale field testing is logistically complex, complete load–displacement curves are seldom reported, tests are usually performed in a single pulling direction, and the unloading phase is almost never documented, limiting the potential to fully characterize hysteresis and stiffness degradation.

Taken together, static field tests, laboratory experiments, numerical modelling and dynamic monitoring under real wind loads offer a complementary, yet still incomplete, view of tree stability. This highlights the need for a comprehensive framework that can integrate these different sources of information to support the risk management of urban trees.

Aims and outlooks

This PhD thesis aims to advance the quantitative assessment of tree stability in urban environments in relation to wind, with the broader goal of supporting risk management strategies that preserve the ecological and social value of urban forests, and therefore biodiversity. To this end, the thesis combines field testing, laboratory experimentation, monitoring, numerical modelling and applied engineering solutions in order to address the recurring practical issue that tree failure risk is often

inferred from incomplete information (typically short, low-amplitude static tests), whereas the mechanisms governing real wind loading depend on the interaction between aerodynamic forces and the nonlinear response of the soil–root system.

More specifically, the thesis pursues five complementary objectives. First, it aims to characterize the mechanical context in which anchorage develops, by linking tree stability to soil conditions through targeted geotechnical investigation and parameterization suitable for interpretation of uprooting resistance. Second, it evaluates the reliability and potential sources of bias in on-site non-destructive pulling tests, including the influence of loading direction and pull geometry, and it benchmarks extrapolation procedures against destructive uprooting tests to clarify when current practice is conservative or potentially misleading. Third, it seeks to bridge static and dynamic assessment by deriving wind-induced loading from in situ wind–inclination measurements, with particular focus on estimating an effective drag formulation that can be used consistently within safety-factor calculations and compared with standard tabulated assumptions. Fourth, it develops a controlled, laboratory-scale, physical model designed to measure the force transmitted into the root-plate system. This enables repeatable experiments where the forcing and boundary conditions are known, the possibility for validating the measurement chain and signal-processing and testing a real-time monitoring system. Finally, it extends the scope from the mechanics of individual trees to operational tools for managing tree risk. This involves combining medium- and long-term monitoring with CFD-based wind modelling across scales to describe exposure, as well as high-resolution 3D surveying workflows that directly support the planning, design and verification of stabilization or consolidation measures.

Looking to the future, this work naturally leads to several possibilities. The first priority is scaling up: expanding the size of the datasets across species, architecture, soil types and urban morphologies while explicitly accounting for the seasonal effects (e.g. soil moisture, canopy state and growth) that can alter both wind loading and anchorage response. A second area of focus is integration, involving the coupling of response indicators derived from monitoring with CFD exposure maps and mechanically consistent models, creating a unified, uncertainty-aware workflow that can be implemented as a 'digital twin' for high-value sites. From an applied perspective, further work should focus on translating these approaches into practical guidance for municipalities and professionals, defining minimum monitoring requirements and validation protocols against post-event performance and low-impact mitigation strategies, so that tree safety and biodiversity objectives can be pursued together rather than being treated as separate priorities.

Structure of thesis

The thesis is divided into two main parts:

- Part I focuses on single-tree investigation, combining controlled experimentation and full-scale field testing.
- Part II extends the analysis towards tools and applications that support risk management in real settings.

Part I is composed of two chapters:

- Chapter I reports on the field-testing campaign carried out at the University of Dundee Botanic Garden, detailing the non-destructive and uprooting tests used to compare the resulting moment–rotation responses. Particular attention is given to practical sources of variability, including the influence of pulling direction and pull angle, and to the suitability of extrapolation procedures commonly used in operational practice. A first step toward the creation of a predictive model based on a Bayesian approach will also be introduced.
- Chapter II presents the development of a 1-g physical model conceived to reproduce key features of root–soil interaction under controlled boundary conditions. The chapter describes the structural design, the force- and kinematic-measurement architectures (including calibration), the actuation and data acquisition chains, and the main outcomes that support interpretation of combined and cyclic loading effects.

Part II is composed of three chapters:

- Chapter III describes a long-term monitoring campaign at Vivaio Bicocca (Milan), where wind forcing and tree inclination were recorded under natural loading conditions to characterise species-specific responses within the same exposure.
- Chapter IV introduces a computational fluid dynamics approach to wind modelling at different scales, illustrating how urban morphology and local flow patterns can affect tree exposure and the resulting aerodynamic demand.
- Chapter V closes the technical body of the thesis with three applied case studies in tree consolidation, showing how advanced survey techniques and engineering calculations can be combined to design and verify stabilisation measures in different operational scenarios.

Literature review

Introduction

Climate change is expected to alter hazard regimes affecting transport infrastructure and the built environment, with many regions experiencing more frequent extremes and greater weather variability, including drier coma conditions punctuated by intense storm events (Satterthwaite et al., 2007). Across Europe, tree failure under wind loading occurs predominantly through overturning rather than stem breakage (B. Gardiner, 2021). Urban trees play a distinctly dual role: they provide very high value in terms of ecosystem services, including mitigation of the urban heat island effect (Carinanos & Calaza, 2018; Speak & Salbitano, 2021; Cavender-Bares et al., 2022; Hand et al., 2019; D. Liang & Huang, 2023; Salmond et al., 2016) but the same trees can represent a hazard when exposed to strong wind gusts that exceed the conditions to which they are typically adapted. Storms and severe winds can lead to stem breakage or uprooting in such circumstances, causing damage to buildings and infrastructure, disruption to transport networks and other services, and injuries. In the worst cases, loss of human life can occur.

Figure 2: afterwards of the storm that hit Northern Italy in July 2023 (specifically on the 24th-25th of July), 5400 trees had fallen in the metropolitan area of Milan.

The spatial positioning of tall trees in urban areas relative to nearby structures, pedestrian and traffic flows, and local wind amplification effects plays a key role in determining the associated risk of

failure (Giachetti et al., 2021; Ciftci et al., 2014). A striking example is the storm that hit northern Italy in July 2023 (24 and 25 July), when 5400 trees fell in the Milan metropolitan area (Figure 2). Of these trees, 4160 were in parks and green spaces, while 1266 were on streets and the species most affected were *Quercus robur, Acer campestre, Fraxinus excelsior, Populus nigra, Cedrus deodara, Cupressus, Carpinus betulus, Pinus nigra*, *Acer platanoides, Tilia, Robinia pseudoacacia, Aesculus hippocastanum*. The damages amounted to over €41.4 million, of which €24.7 million was in the public sector and €16.7 million in the private sector.

These observations have sustained strong interest in tree biomechanics under lateral loading, particularly the coupled behaviour of the stem–root–soil system, as it underlines assessments of windthrow resistance and supports the design of forest management strategies aimed at mitigating wind risk (Mickovski & Ennos, 2003; Nicoll et al., 2008; Stokes, 1999; Dupont & Brunet, 2008; Gardiner & Quine, 2000; Moore et al., 2008). Beyond forestry, the mechanics of root–soil interaction are also relevant to civil engineering and public safety, because windthrow can endanger people and damage nearby assets (Schmidlin, 2009), and—on slopes—may contribute to instability and initiate or exacerbate landsliding processes (Jakob & Lambert, 2009; Nelson et al., 2015). Finally, improving the understanding and prediction of uprooting is important for the conservation of old and culturally valuable trees.

Because below-ground architecture is highly heterogeneous and the mechanics of root–soil coupling are difficult to characterise directly, earlier studies have often described tree stability in a pragmatic, empirical way by linking resistance under quasi-static lateral loading to above-ground attributes that are readily observable—such as crown characteristics, stem geometry, and site exposure to wind (Guitard & Castera, 1995; Ruel, 2000; Sellier & Fourcaud, 2009). Methodologically, this body of work has been driven primarily by in situ winching/pulling experiments (Coutts, 1983a; Crook & Ennos, 1996; Nicoll et al., 2006), complemented by measurements of strain and deformation in the basal stem region, detailed surveys of root system architecture (Danjon et al., 2005, 2008), and targeted mechanical testing of individual roots to constrain strength and stiffness properties (Schwarz et al., 2011). To investigate controlling factors under repeatable conditions, and to capture how water content and soil state may vary with depth within the rooting zone, several authors have adopted reduced-scale 1g laboratory physical modelling as a controlled experimental framework for studying root–soil interaction (Mickovski et al., 2010; Harnas et al., 2016; Zhang et al., 2018). Such setups allow key parameters to be systematically varied and enable the instrumented monitoring of hydro-

mechanical conditions along the model profile. This supports the interpretation of how changes in soil moisture and stratigraphy influence anchorage behaviour in a mechanistic way.

Analytical and numerical approaches have similarly been widely adopted to explore the mechanics of root–soil interaction and to predict anchorage capacity. On the analytical side, several families of models have been proposed—among the most cited are the *Blackwell–Rennolls–Coutts* model (Blackwell et al., 1990), the *Fibre Bundle Model* (Pollen & Simon, 2005), and the *Root Bundle Model* (Schwarz et al., 2010). While these frameworks have proved useful for interpretation and parametric studies, they typically represent root architecture and root material behaviour in a strongly idealised manner, relying on simplified geometries and effective biomechanical properties to estimate anchorage strength. In parallel, numerical simulations based on the Finite Element Method have been used to resolve the coupled response of soil and roots under lateral loading, providing a more detailed representation of stress transfer and deformation within the composite system (Dupuy et al., 2005; Yang et al., 2014, 2017, 2018, 2020). More recently, macroelement formulations—where the root system is idealised as an embedded shallow foundation—have been introduced as an efficient compromise between mechanistic fidelity and computational cost for modelling tree pull-over response (Dattola et al., 2020a).

Regarding the study of tree response under dynamic conditions, several investigations have focused on estimating the aerodynamic drag coefficient C_d using three main approaches: wind-tunnel testing, field inference from structural response, and hybrid in situ methods combining sensors and imaging. Early wind-tunnel work on conifers provided some of the first systematic C_d estimates (Mayhead, 1973), while later studies quantified wind-speed-dependent reconfiguration and frontal-area changes through photographic measurements (Vollsinger et al., 2005; Rudnicki et al., 2011). In the field, C_d has been derived by coupling wind records with stem deflection and independently measured stiffness, enabling reconstruction of aerodynamic loads and C_d (Koizumi et al., 2010). For urban trees, the definition of the reference area has been shown to be a critical source of uncertainty in both crown area and C_d estimates (Kane & Smiley, 2011). Additional evidence from windbreak-oriented studies highlights canopy porosity as a key control on drag, limiting the transferability of coefficients among species and architectures (Grant & Nickling, 1998). The same issue underpins comparisons between model trees and real specimens, where aerodynamic similarity requires consistent geometry, porosity, and reconfiguration capability (Manickathan et al., 2018). Most recently, hybrid in situ measurements on mature solitary trees indicate that uncertainty in frontal area $A$is a dominant driver of the spread in reported values C_d (Bekkers et al., 2022).

Biomechanical Response of Trees to Lateral Forcing

Much of the early, foundational work aimed at clarifying uprooting mechanisms—and, in particular, the role played by soil conditions and root architecture—was carried out in the UK (Fraser & Gardiner, 1967; Coutts, 1983b, 1986). Those campaigns established the typical field configuration for controlled overturning tests and provided some of the first moment–rotation curves describing anchorage behaviour under lateral loading (Figure 2). Building on these observations, (Crook & Ennos, 1996) described tree anchorage as primarily governed by a set of thick, near-surface lateral roots from which vertical "sinker" roots branch, often complemented by one or more tap roots (Figure 4a). Under overturning, the mechanical roles of these components become strongly asymmetric: lateral roots on the leeward side mainly oppose rotation through bending resistance, whereas windward sinkers and tap roots primarily contribute by resisting uplift and soil extraction (Figure 4b).

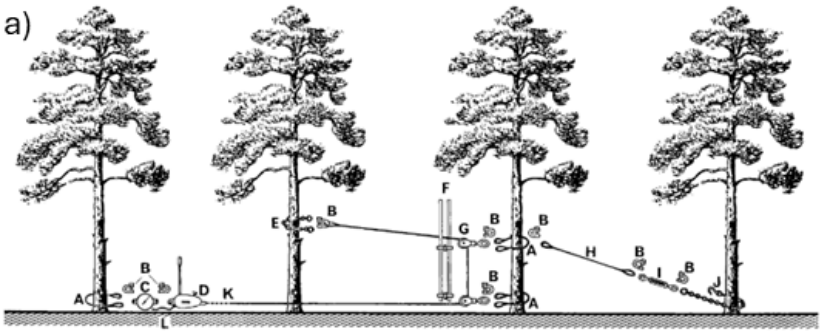

Figure 1. Tree Pulling Technique: Layout of Equipment.

A —Wire rope slings
B —Screw D shackles
C —Dynamometer
D —Tirfor hand winch
E —Chain sling with reevable egg links
F —Adjustable pulley block spacer, fabricated from alloy scaffold poles and coupler clips
G —Single sheave swivel snatch-blocks
H —Backstay wire rope
I —Rigging screw
J —Chain sling with shortener hook
K —White paint marks on rope
L —Free end of wire rope

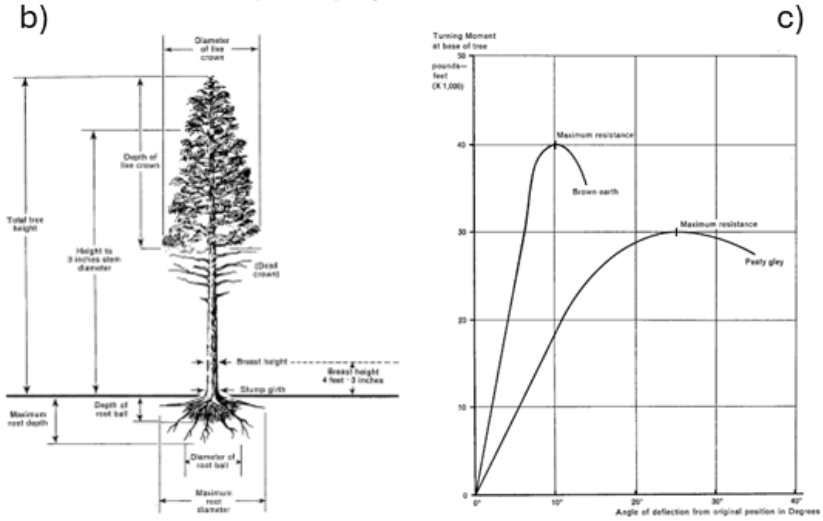

Figure 3: tree pulling technique and moment-rotation curves as first reported by (Fraser & Gardiner, 1967).

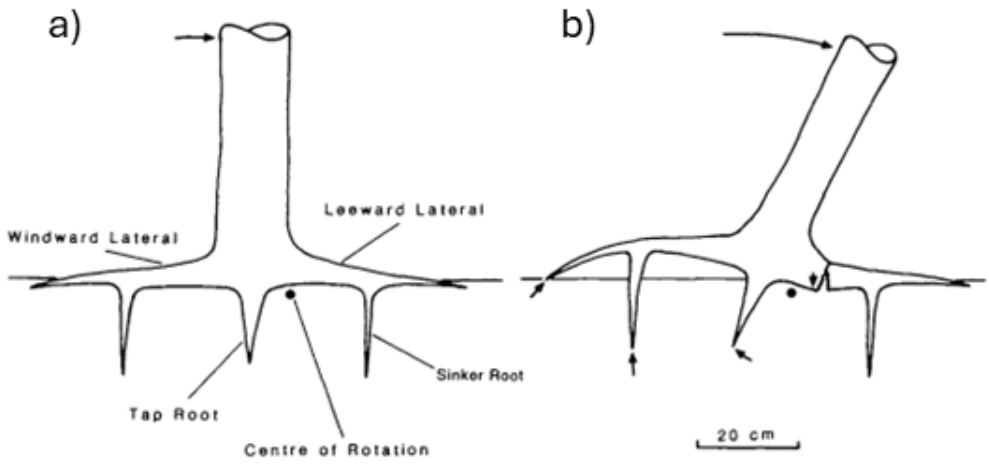

Figure 4: Trunk and root movements (a) before and (b) under lateral loads (Crook & Ennos, 1996).

Anchorage failure is commonly associated with breakage of the leeward laterals close to the stem, accompanied by progressive uprooting of windward sinkers; concurrently, the tap root—being less laterally confined during rotation—tends to rotate through the soil together with the stem–root plate. To investigate these coupled mechanisms in situ, winch (pulling) tests have been widely adopted, in which a controlled horizontal force generates an overturning moment and the resulting stem rotation is recorded to characterise moment–rotation response.

Winch test setup and results

A direct assessment of a tree's resistance to lateral loading is most reliably obtained from full-scale field experiments in which the overturning moment and the associated rotation of the root–soil plate are measured up to incipient uprooting. These investigations—commonly referred to as winching or pulling tests— lateral forces are applied to the stem with a winch to pull the tree over (Figure 5). With advances in field instrumentation, winching has become a standard approach for deriving moment–rotation relationships and quantifying anchorage capacity across species and site conditions (Coutts, 1983a, 1986; Crook & Ennos, 1998; Nicoll et al., 2008). From an operational standpoint, the pulling line is typically attached to a polyester sling around the stem at a height chosen to promote root-plate mobilisation while minimising the risk of premature stem breakage. In contemporary protocols, the load is applied at a relatively low inclination to the horizontal and commonly between one-third and one-half of total tree height; consequently, local damage to the lower stem is often unavoidable (Marchi et al., 2018). The test is conducted under quasi-static conditions, with a datalogger recording force through a load cell and rotation/tilt through clinometers or inclinometers (Nicoll et al., 2006).

Figure 5: an example of an overturned Sitka spruce tree showing a shallow root – soil plate with many small roots extending from the edge. The stem belonging to the plate is on the top right corner of the figure (Achim & Nicoll, 2009).

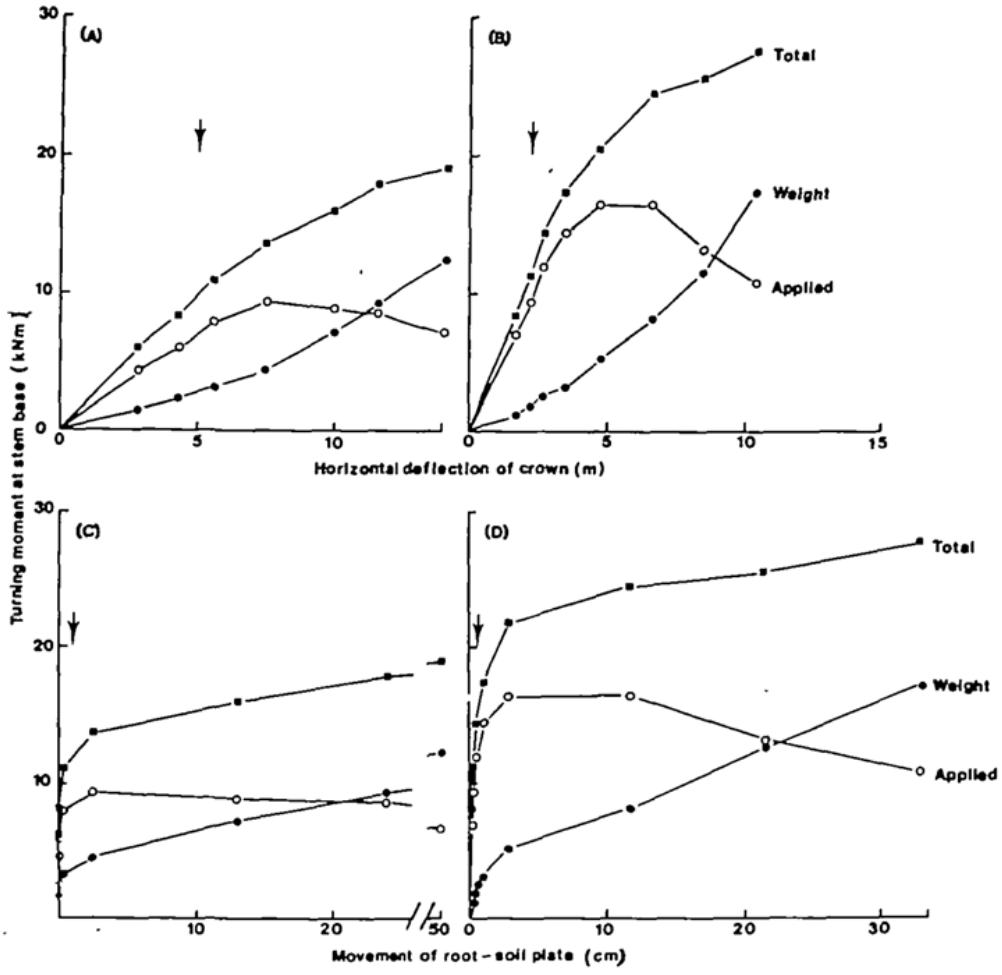

Figure 6: first moment rotation curves reported in the literature (Coutts, 1986).

The resulting moment–rotation curves generally exhibit an initial quasi-elastic segment followed by a peak (interpreted as a critical or maximum resisting moment) and a post-peak softening trend leading to failure (Figure 6). Importantly, accurate estimation of the overturning moment at the base requires accounting for self-weight effects, which become increasingly influential as deflection grows and the gravitational component contributes to the overall overturning demand. Consistent with this, Nicoll et al. (2006) reported an approximately linear relationship between critical turning moment and stem mass across different soil types (Figure 7), and similar evidence was observed for trees established on sloping terrain (Achim et al., 2003). Collectively, these findings indicate that tree mass is not a secondary detail but a governing factor in $M_{\mathrm{crit}}$and should be explicitly incorporated in anchorage analyses.

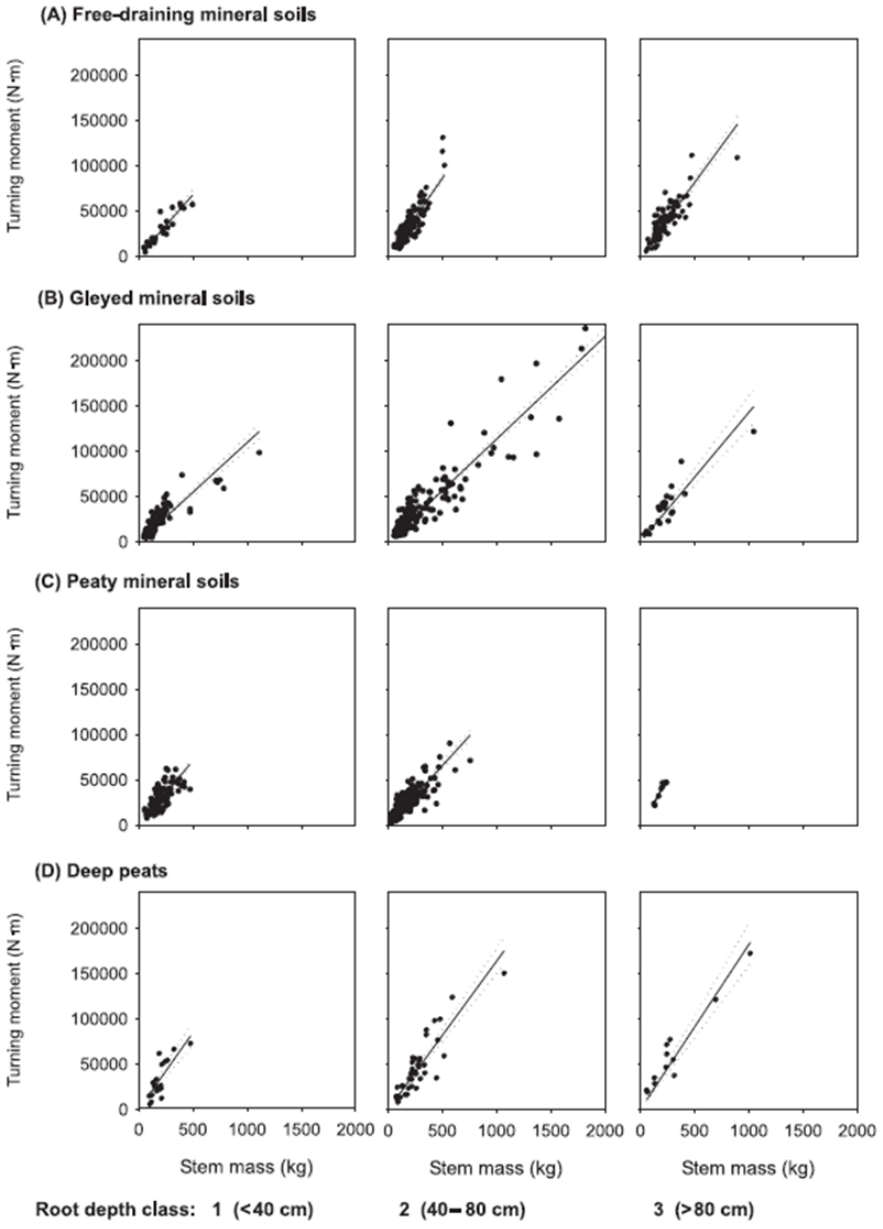

Figure 7: relationship between critical turning moment and stem mass for each Sitka spruce soil and root depth grouping (Nicoll et al., 2006).

Complete moment–rotation curves extending to root-plate failure are only sporadically available in the published literature. In many cases, datasets derived from winching tests are disseminated primarily through summary metrics or fitted relationships, with the underlying raw curves either omitted or reported only partially (Figure 8). For this reason, as part of the present literature review, a targeted screening of sources was conducted to identify studies that explicitly publish full moment–rotation responses up to failure. The associated field-test metadata were compiled in a summary table (Table 1) to enable consistent comparison across sites, species, and testing protocols. Figure 9 reproduces the original moment–rotation plots for all winch tests to failure retrieved in this review, whereas Figure 10 presents the digitized versions of a subset of these curves, which are subsequently adopted as a reference dataset for comparative analyses in this research.

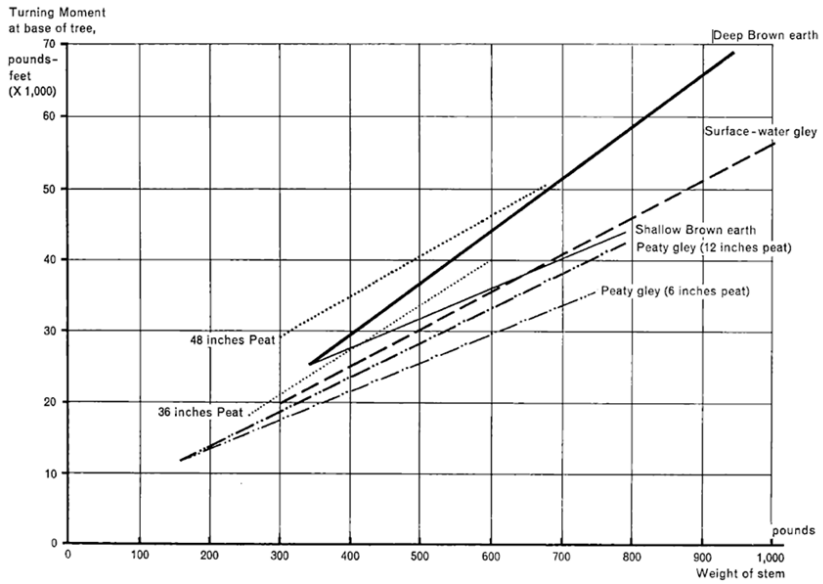

Figure 8: mean regression of turning moment on stem weight for several trees pulled over on different soils types (Fraser & Gardiner, 1967).

Table 1: results of winch tests field data inclusive of the full M-φ curve

Reference	Type of soil	Type of trees	N° of tests	Range of DBH	Range of tree heights (h)	Range of M_L (kNm)	Range of φ (deg)
Fraser & Gardiner, 1967	brown earth, peaty podzol	*Picea sitchensis*	368	15 - 23	11 - 14	16-53	ott-25
Coutts, 1986	peaty gley	*Picea sitchensis*	10	15 – 27	18 - 20	6 – 20	/
Crook & Ennos, 1996	sandy clay loam	*Larix europea x japonica*	22	12 - 20	10 - 13	giu-24	16-28
L. X. Dupuy et al., 2007	clayey sand	*Populus trichocarpa, Populus deltoides*	6	24 - 28	/	16	/
Ghani et al., 2009	sandy clay	*Eugenia grandis*	28	21	13,8	20	/

Dèfossez et al., 2021	medium sand	*Pinus pinaster*	12	16 – 19	9 – 12	ago-16	giu-20
			10	14.3±3	12.4±1.8	3–24	
Urata et al., 2012	brown forest soil	*Picea glehnii*	10	12.3±3.1	9.6±2.1	3.8–13	14-22
			9	17.7±2.9	10.3±1.7	7–29	

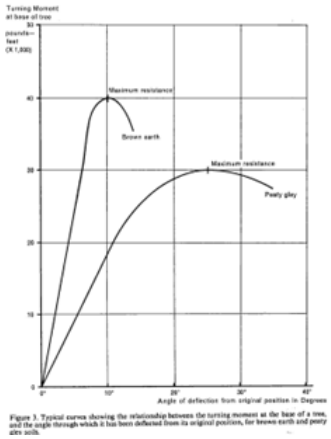

(Fraser & Gardiner, 1967)

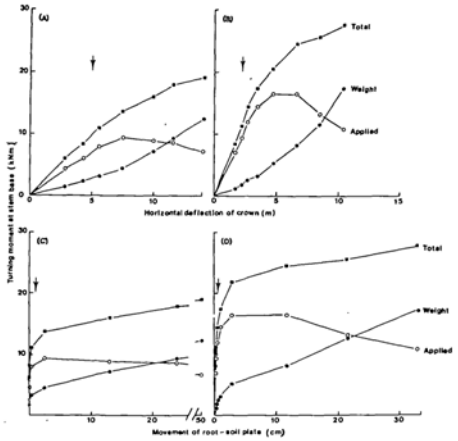

(Coutts, 1986)

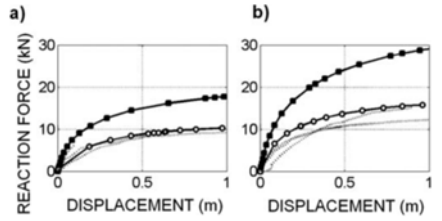

Fig. 7. Simulated curves of force vs. displacement (with a mesh size of 1372) for (a) the Beaupré and (b) the Raspalje cultivars. Experimental

(L. X. Dupuy et al., 2007)

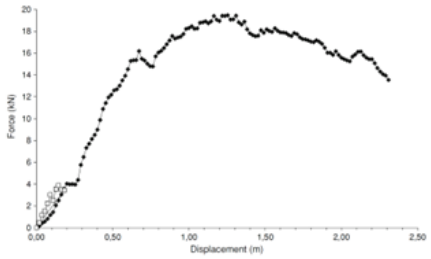

(Ghani et al., 2009)

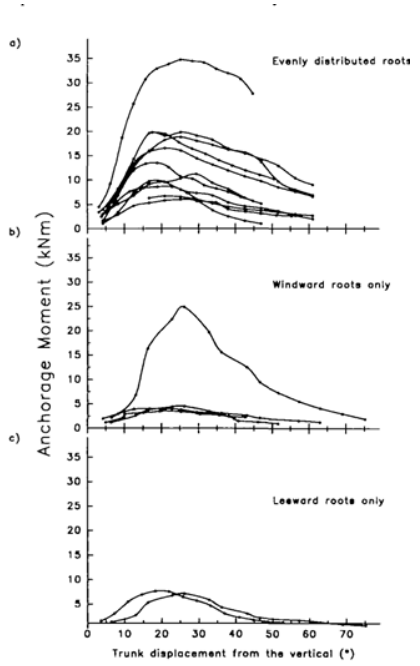

(Crook & Ennos, 1996)

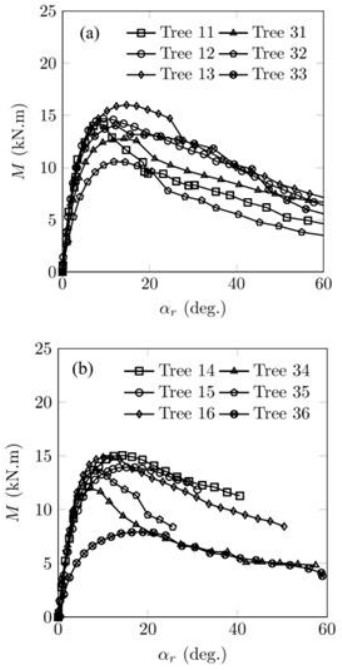

(Défossez et al., 2021)

Figure 9: Moment rotation curves of winching test to failure found in literature.

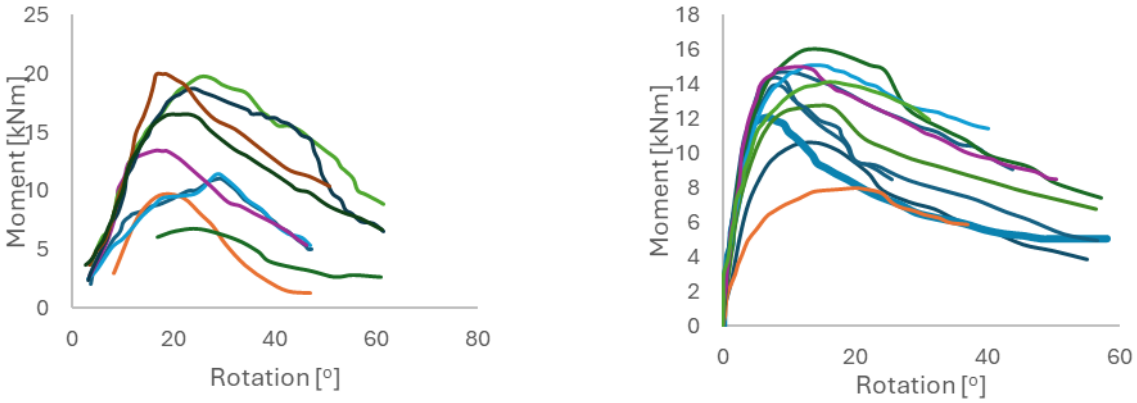

Larch (Crook & Ennos, 1996) Pinus Pinaster *(Défossez et al., 2021)*

Figure 10: Digitalised moment rotation curves.

The moment–rotation responses (Figure 11) reported by Urata et al. 2012 provide clear evidence that test configuration—specifically whether the crown is retained or removed—can markedly influence the measured overturning behaviour. When the crown is present, both aerodynamic area and mass distribution are altered, and the gravitational contribution associated with a leaning stem becomes non-negligible. As rotation increases, the tree's self-weight generates an additional overturning component, such that the effective bending moment at ground level is higher than would be inferred from the applied lateral load alone. Consequently, accounting for self-weight effects is essential for the correct interpretation of winching tests, especially when comparing results obtained under different crown conditions.

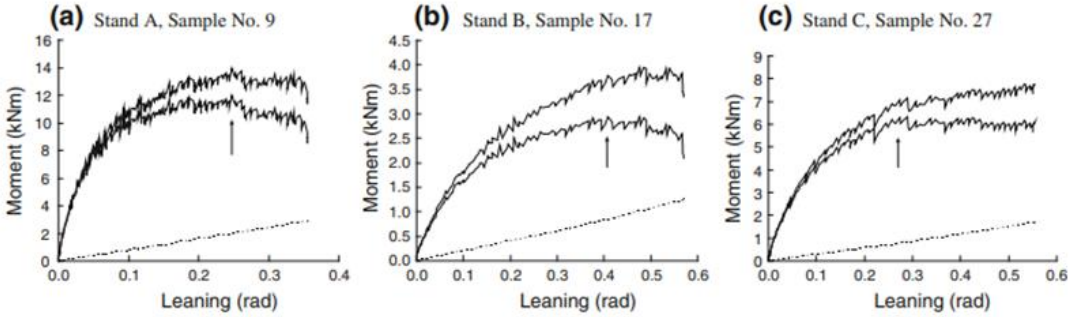

Figure 11: Moment of a tree with a leaning stem. Thick line total moment, thin line pulling load moment, dotted line self-loading moment. Arrows indicate the maximum pulling load moment. Stem displacement was measured using a displacement sensor attached 1 m high on the opposite side of the stem from the source of the pulling.

Although full moment–rotation traces are often not provided, several studies report key scalar outcomes from winching tests—most commonly the limit moment M_L, the corresponding rotation φ_L,

and basic biometric descriptors such as DBH. For clarity, these outputs are synthesized in Table 2 to enable cross-study comparison even when raw curves are unavailable. Using a large dataset, Detter et al. 2023 further explored statistical relationships linking anchorage capacity to tree size and mechanical response parameters. As an example, Figure 12 illustrates how anchoring strength scales with tree dimensions across multiple species and highlights associations between maximum capacity and rotational stiffness derived from the early part of the response. Such correlations are particularly valuable from an operational perspective because they suggest a pathway to estimate ultimate anchorage resistance by exploiting the initial, quasi-elastic segment of the moment–rotation behaviour, thereby reducing the need for destructive loading to failure.

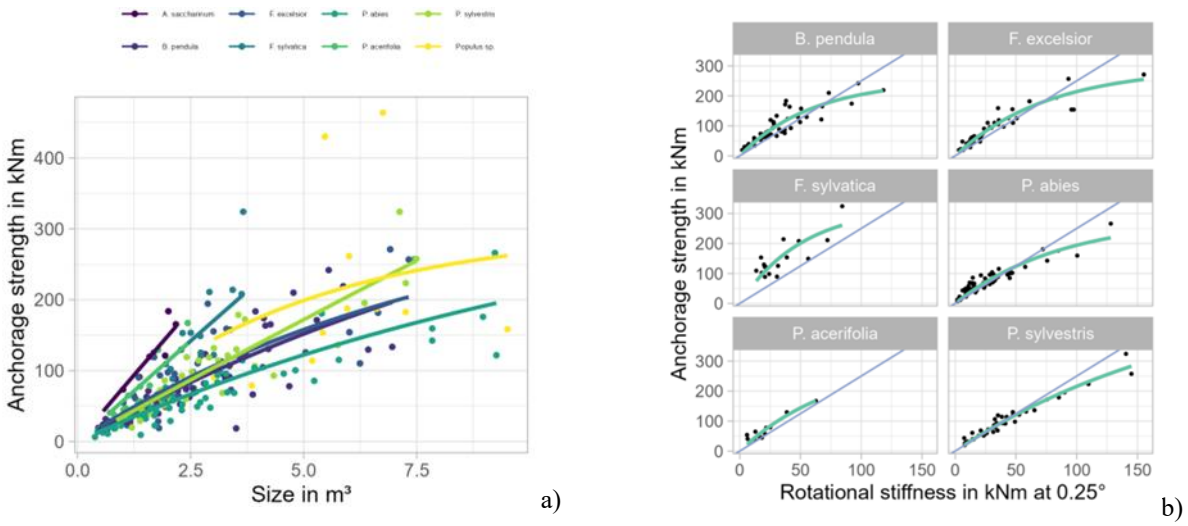

Figure 12: a) species effect on anchoring strength and b) the relationship between rotational stiffness and anchorage strength varied from linear to curved depending on species.

Table 2: Results of winch tests field data not inclusive of the full M-φ curve

Reference	type of soil	type of trees	number of tests	range of DBH (cm)	range of tree heights (m)	range of ML (kNm)	range of φ_L (deg)
(Peltola et al., 2000)	Fine sand / coarse silt	Pinus sylvestris	51				18.4
		Picea abies	33	14 - 23	13 - 20	5.9 – 19.2	19.7
		Betula spp	11				20.1
		Betula pendula	78	33	24	25-250	-
		Picea abies	65	32	25	12-260	-
		Fraxinus excelsior	48	34	25	20-260	-

(Detter et al.. 2023)	Different ones – urban and forest soil types of Europe and North America	*Pinus sylvestris*	48	31	25	12-320	-
		Fagus sylvatica	21	33	26	90-320	-
		Populus sp.	18	44	30	80-450	-
		Platanus acerifolia	12	28	18	40-160	-
		Acer saccharinum	7	28	17	75-190	-
		Acer pseudoplatanus	5	22	23	-	-
		Prunus sp.	3	33	13	-	-
		Quercus robur	3	54	19	-	-
		Tilia sp.	3	32	14	-	-
		Robinia pseudoaccacia	2	48	19	-	-
		Alnus glutinosa	1	72	21	-	-
		Acer platanoides	1	34	10	-	-
		Pseudotsuga menziesii	1	31	22	-	-
(Kamimura et al., 2012)	brown forest soil	*Chamaecyparis obtusa*	23	12.7 - 19.5	6.7 – 16.4	9.2 – 72.2	-
(Kane & Clouston, 2008)		*Acer spp.*	24	45 - 71	16.8 – 18.5	110 - 278	-
Ow et al., 2010	(1) soil with 80% granite chips and 20% sandy loam soil. (2) soil with 50% granite chips and 50% sandy loam soil	*Samanea saman*	20	50 - 55	/	9 - 16	-

Analytical and numerical models

Modelling tree anchorage capacity remains challenging because it depends on tightly coupled processes involving root-system architecture, soil type and stratigraphy, depth-dependent changes in soil state, and the strong modulation introduced by soil moisture. Therefore, uprooting resistance is frequently characterized empirically through pulling experiments and then expressed through relationships with readily measurable above-ground attributes—most commonly stem diameter and, in some cases, tree height—following approaches widely adopted in practice (Wessolly & Erb, 1998). The following sections therefore review a range of modelling strategies, spanning simplified

empirical formulations to more mechanistic frameworks, that have been proposed to represent tree response under lateral loading.

Blackwell, Rennolls and Coutts (RBC) root plate model

The *Blackwell, Rennolls and Coutts (BRC)* model, is a mechanistic model, which considers the weight of a root-soil plate, soil strength, pull-out and bending capacity of roots was described in (Blackwell et al., 1990). In the BRC model the root-soil plate of a tree is considered as a rigid body which rotates around a 'hinge' located on the leeward side of the tree (Figure 13a). By means of rotational equilibrium equation it is used to estimate the critical limit moment (M_L).

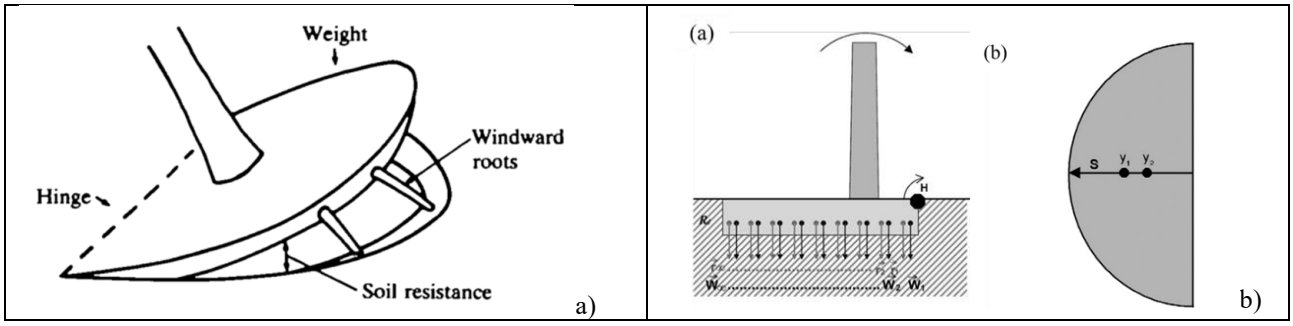

Figure 13: a) description of RBC model (Coutts, 1986); b) representation of the resistance model. (a) Side view showing the hinge point H as a tree is overturned. (b) Top view: s is the radius of the plate, y1 is the centre of gravity of the arc and y2 is the centre of gravity of the semicircle (Achim & Nicoll, 2009).

Achim & Nicoll 2009 improved the BRC model by comparing the limit (critical) resisting moment of the model M_L to the experimental limit moment determined in field tests calculated in tree-pulling tests but also ignored the contribution of roots which are in compression on leeward sides (Figure 13b) as they found that the weight of the root-soil plate and windward roots provide almost 85 percent of total anchorage strength (Coutts, 1986). The modelled root–soil system resisting moment equals to the sum of the resistance force of each root multiplied by the perpendicular distance to the hinge point:

$$M_{root} = K_1 \pi s y_1 \qquad \text{Eq. [1]}$$

where K_1 (unit: Nm-1) is a constant, s (unit: m) is the radius of the semicircle and y_1 (unit: m) is the distance between the hinge and the centre of gravity of the arc (see Figure 13). For an arc of 180°, y_1 could be calculated as:

$$y_1 = 2s/\pi \quad \text{Eq. [2]}$$

Therefore

$$Mroot = K_1 \pi s 2s\pi = 2K_1 s_2 \quad \text{Eq. [3]}$$

Assuming that the shape of the root-soil plate, with depth equal to Rd, is a half cylinder, the moment of self-weight resistance (Mweight) can be simply calculated as:

$$M_{weight} = \frac{\pi s^2}{2} R_d \rho g y_2 \quad \text{Eq. [4]}$$

where y2 is the centre of gravity of the root-soil plate, which is calculated as:

$$y_2 = 4s/3\pi \quad \text{Eq. [5]}$$

Therefore

$$M_{weight} = \frac{\pi s^2}{2} R_d \rho g \frac{4s}{3\pi} = \frac{2}{3} s^3 R_d \rho g \quad \text{Eq. [6]}$$

In this case, ML, which is the sum of Mroot and Mweight reads:

$$M_L = M_{root} + M_{weight} = 2K_1 s^2 + \frac{2}{3} s^3 R_d \rho g \quad \text{Eq. [7]}$$

Root bundle model

The *Root Bundle Model (RBM)*, proposed by Schwarz et al. 2010 explicitly considers geometry (branching characteristics, tortuosity, and diameter-length proportion), root-size spatial distribution (dimension and number of roots), mechanical characteristics (Young's modulus and tensile strength) and different soil conditions (soil type, soil moisture, and confining pressure). The RBM model is a compromise between complexity due to root-soil interactions and oversimplifications of parameters

used to describe key features of the geometry and mechanics of pulled roots. The model follows an algorithm shown in Figure 14.

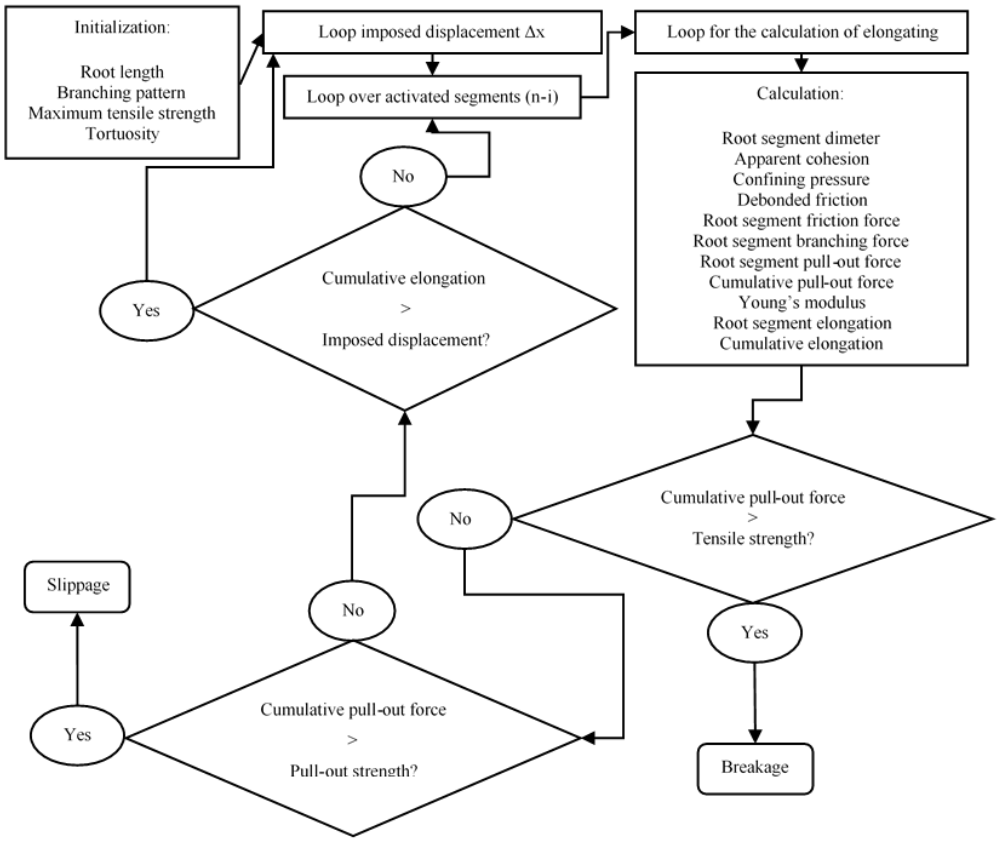

Figure 14: The algorithm of RBM.

It should be noted that this is a strain step loading model and there is no interaction between neighbouring roots and overlapping may result in a more complex mechanism of force redistribution. Moreover, despite the ability to identify root pull–out and breakage failure modes by introducing root breakage strength and root-soil interfacial friction, the RBM ignores the root flexural properties, which are known to substantially affect the root anchorage and pull–out resistances.

Winkler foundation (BNWF) approach

In geotechnical engineering, a widely adopted analytical framework for representing pile behaviour under combined lateral and axial loading is the beam-on-a-nonlinear *Winkler foundation (BNWF)* formulation (Allotey & Foschi, 2005). Within this approach, the pile is idealised as an elasto-plastic, displacement-based beam whose interaction with the surrounding ground is captured through discrete nonlinear springs. Different spring families are introduced to represent distinct mechanisms: shaft shear transfer is described through *t-z* springs (with t denoting mobilised interface shear and z the

relative axial displacement), tip resistance in compression is represented by *q-z* springs, and lateral soil reaction is modelled via *p-y* springs linking horizontal resistance p to pile deflection y. The remote ends of these springs are assigned appropriate constitutive properties so that their deformation represents free-field soil movement, thereby providing an efficient, modular description of soil–structure interaction (Duckett, 2014). Liang et al. 2015 extended the BNWF modelling approach to describe the individual root-soil interaction both pre- and post-failure (Figure 15). Existing p–y formulations from piling engineering were validated against large direct shear tests. This approach is versatile, computationally efficient and can be used to deal with the case involving different soil types, nonlinear soil behaviour, different root properties and layered soil. Meijer et al. 2019 extended the approach by using both p–y and t–z curves to describe the flexural and axial responses of the root system, respectively.

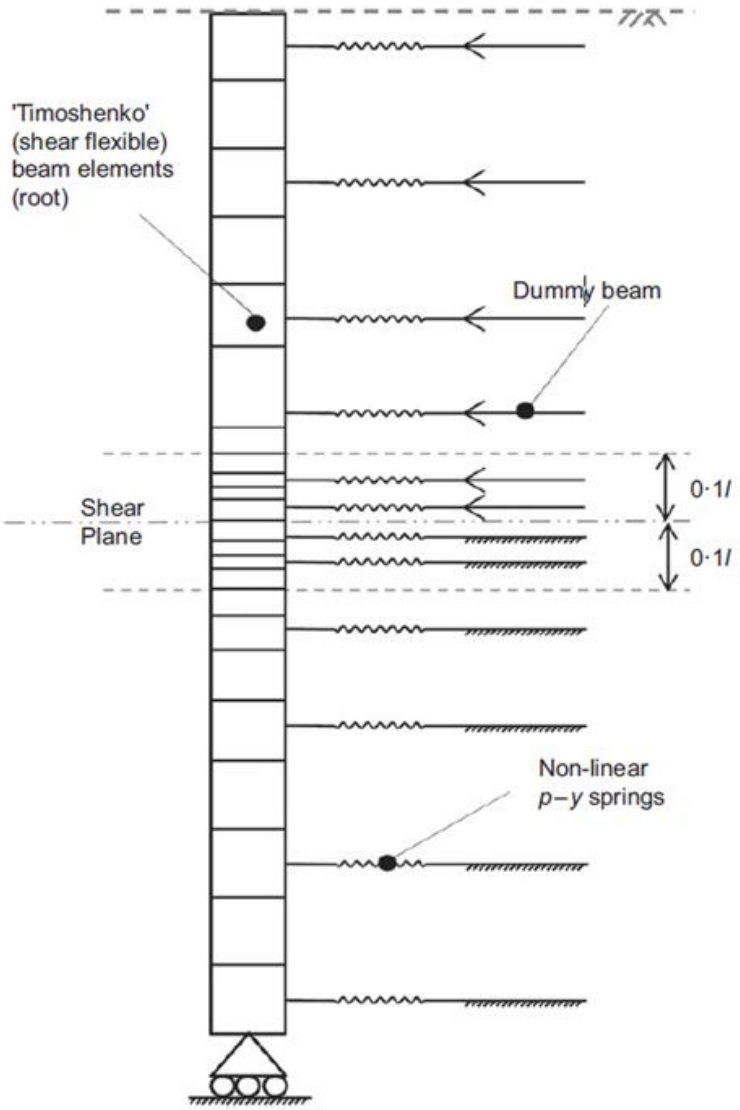

Figure 15: schematic diagram of root–soil system undergoing shear loading (Liang et al., 2015).

Macroelement approach

From a geotechnical point of view, pulling tests consist in imposing a combined set of horizontal (H), vertical (V) and toppling (M) loads on the root system, characterized by a positive (i.e. downward oriented) vertical load component. Such type of loading is typical of many geotechnical structures which were shown to be successfully modelled using the Macroelement approach (Nova & Montrasio, 1991) (Figure 16).

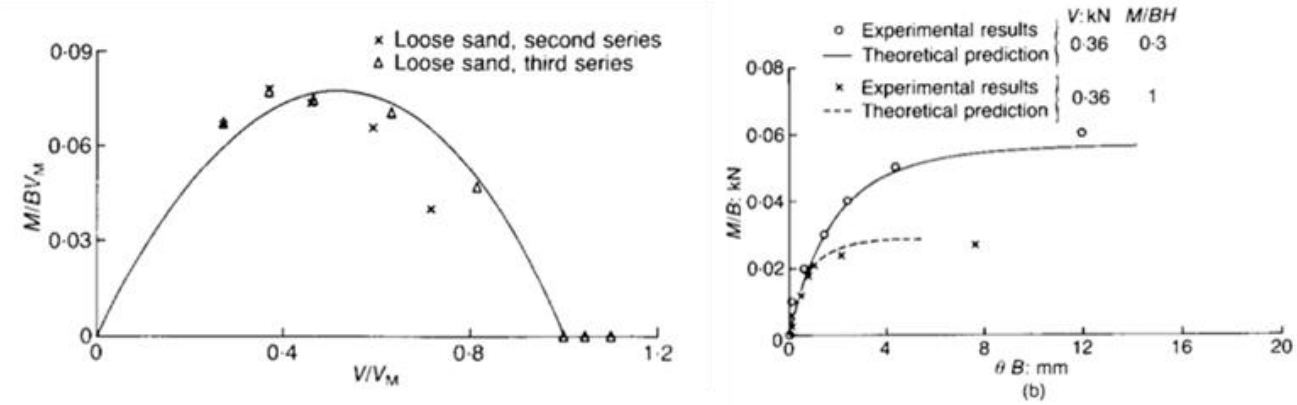

Figure 16: Performance of macro element modelling of shallow foundations under combined (V, H, M) loading (Nova & Montrasio, 1991).

Dattola et al. 2020 showed that a tree under wind loads can hence be interpreted within the macroelement framework by assimilating the model tree to a tall vertical structure, founded on an equivalent circular rigid foundation of diameter D and subject a complex loading path in the V,H,M space. They show how the theory can capture and how the vertical load (V) influences the limit moment M_L (Fig. 2 17). In the perspective of the stability assessment of tree against wind loading, the calibrated shape of the limit surface shows that static pull tests (characterized by compressive V forces) would overestimate limit moment as wind loading has no compressive loading V which, on the other hand, can sometimes be negative because of wind pulling effects.

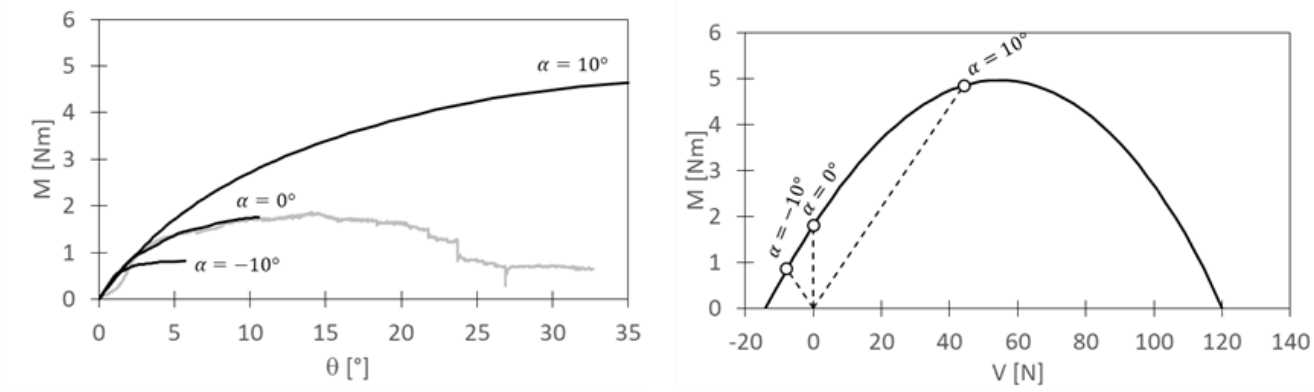

Figure 17: left) influence of the vertical load component on M-θ curves; (right) loading paths in M-V plane for three different inclinations of the applied load (Dattola et al., 2020b)

FEM modelling

The Finite Element Method (FEM) provides a flexible numerical framework for solving equilibrium in complex engineering systems and has increasingly been applied to reproduce tree pulling tests and to represent the coupled soil–root response under lateral loading. As with any FEM analysis, predicted behaviour is strongly controlled by the constitutive descriptions assigned to the interacting media; for tree anchorage problems, this requires soil models capable of capturing nonlinearity and failure, as well as a representation of root damage and breakage mechanisms. Within FEM-based studies of root biomechanics, two main discretisation strategies have been employed: continuum (solid) elements and reduced-order beam elements. Early contributions by Dupuy et al. 2005 and Fourcaud et al. 2008 modelled roots using 2D solid elements to describe combined axial and flexural behaviour, differing primarily in the treatment of the root–soil interface—Coulomb frictional contact in Dupuy et al. 2005 versus a rigidly bonded interface in Fourcaud et al. 2008.

To reduce computational cost while retaining the essential mechanics, several later studies represented roots through beam formulations, typically based on Timoshenko beam theory. In this context, Yang et al. 2014 introduced damage-based constitutive laws within a root embedded beam element (EBE) to reproduce diameter-dependent root behaviour and to allow failure in tension, compression and/or bending. The same modelling framework was subsequently adopted and extended to investigate overturning resistance and the contribution of root breakage to anchorage capacity under lateral loading (Yang et al., 2017; 2018).

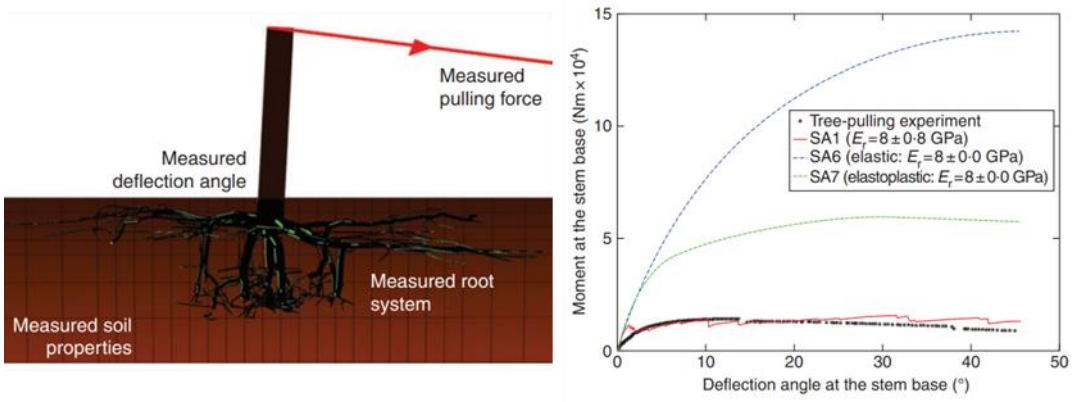

Figure 18: FEM modelling of pull tests showing importance of using advanced elastoplastic models inclusive of root damage (Yang et al., 2014).

In this respect Yang et al. 2014 Figure 18 show how an advanced soil model and a sophisticated root model are required properly reproduce tree pull test data. More recently Zhu et al. 2014 extended Yang et al. 2014 EBE modifying the constitutive stress–strain relationship to calculate uprooting

resistance by considering the root–soil interfacial shearing and the strength decline as root pulls out. The power of FEM is that in principle any mechanism, static and dynamic can be solved. For example, Yang et al. 2020 recently modelled the dynamic interaction of a tree subject to wind loading. Figure 18 shows some images of the FEM results depicting the power of such numerical tool. Nonetheless FEM results still rely on the constitutive model adopted and maybe time consuming and often require costly software not always accessible to everyone.

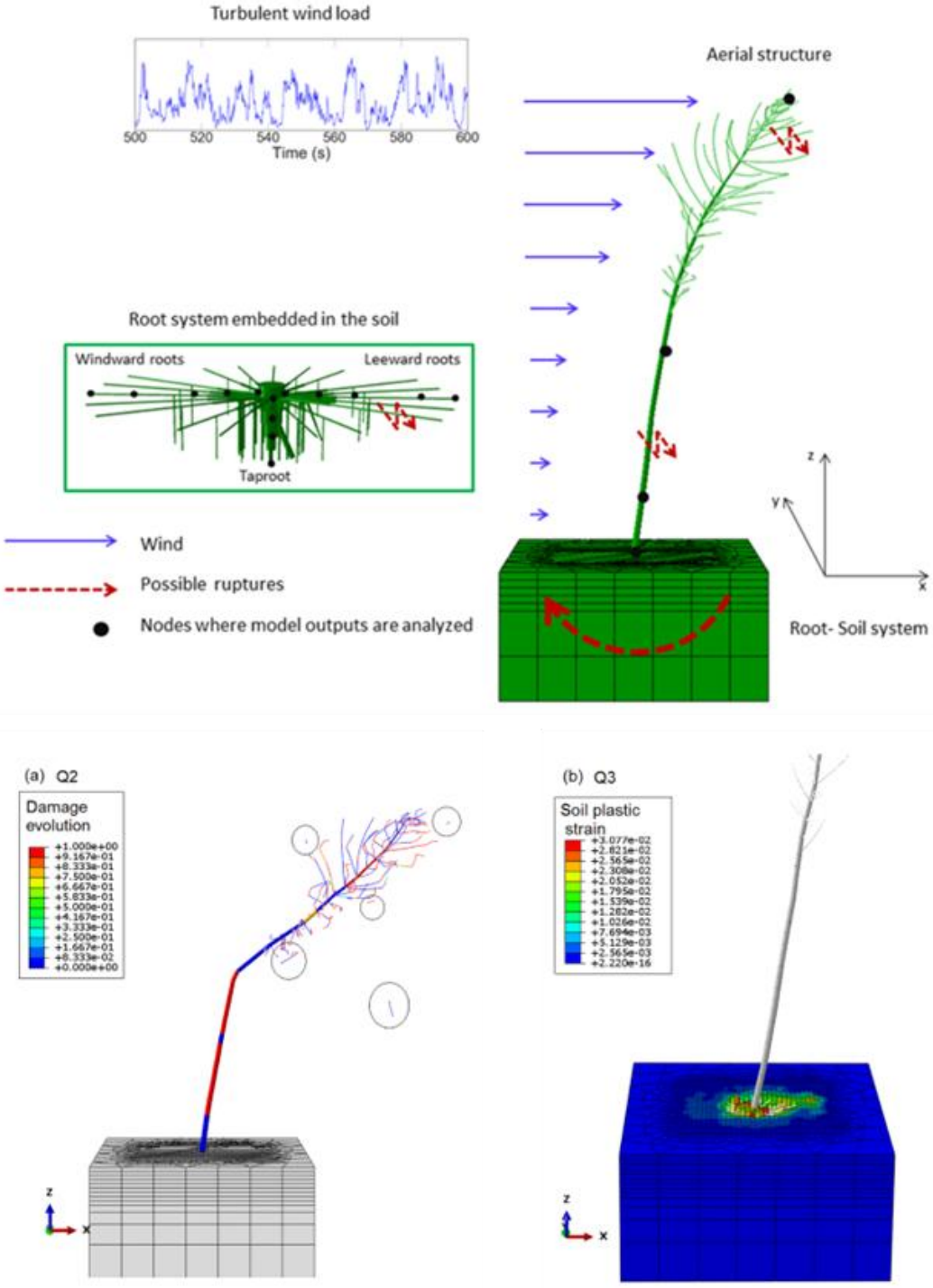

Figure 19: dynamic FEM modelling of wind tree interaction on elastoplastic soil bed (Yang et al., 2020).

Tree safety assessment in practice

Visual Tree Assessment (VTA)

The Visual Tree Assessment (VTA) procedure introduced by Mattheck & Breloer 1994 is the most widespread approach adopted for tree inspection and symptoms recognition. It requires high arboriculture expertise and although some quantitative geometry-based indexes, like the ratio of the thickness t of the wood wall to the radius R of the trunk (t/R) ratio or the slenderness coefficient (ratio of the height of the tree to the diameter of the trunk), are employed, the method remains quite subjective. The basis behind VTA is the identification of symptoms, which the tree produces in reaction to a weak spot, or area of mechanical stress. It is essential that any arborist using VTA has a broad range of experience of different tree species, as individuals and in groups, to enable them to make informed and reasoned decisions about 'tree safety. The VTA method is an internationally spread and acknowledged method for trees inspection.

The VTA is built upon the axiom of uniform stress. A tree is a self-optimizing mechanical structure (Mattheck & Breloer, 1994) which reacts to mechanical and physiological stresses by growing more vigorously to reinforce weak areas, while depriving less stressed parts. It is by understanding such principle that according to the authors an Arborist can make informed judgements about the condition of a tree. In practical terms the VTA is implemented by implementing the four steps:

1. **Inspection for detect symptoms**: it is the first look to the tree, where the first investigation of potential defects is performed by a general visual inspection;
2. **Confirmation of defects and measurement**: It is a deeper investigation and consists in the use of specific instrumentation to determine the drilling resistance, sound speed in the trunk (it sets if the trunk is hollow or not), wood strength measurements and the estimation of the age of the tree.
3. **Assessment of the defects**: it is the establishment of the criteria for determining the safety of different typologies of trees: hollow trees, trees with root damages and health but high trees Figure 20
4. **Determination of further actions**: determinations of the potential intervention required based on the results of the first three.

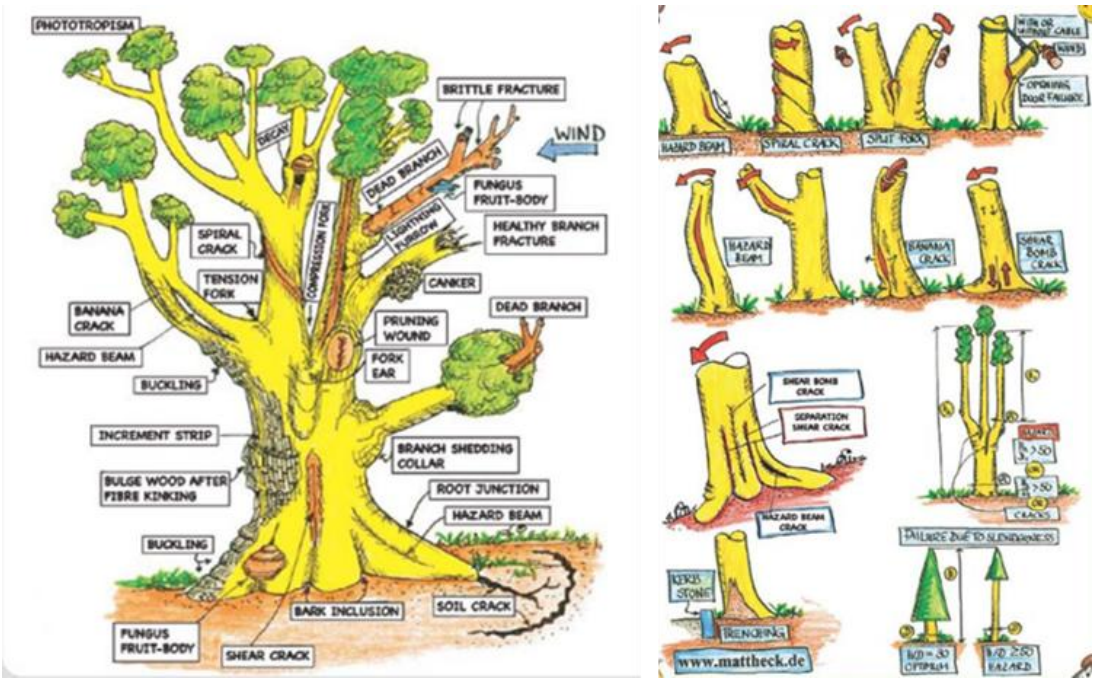

Figure 20: Schematic drawings describing VTA analysis and tree symptoms (Mattheck et al., 2015)

To standardize and facilitate the implementation of the VTA Lonsdale 2007 introduced a basic procedure for tree hazard assessment in a situation where people or property are potentially at risk Figure 21

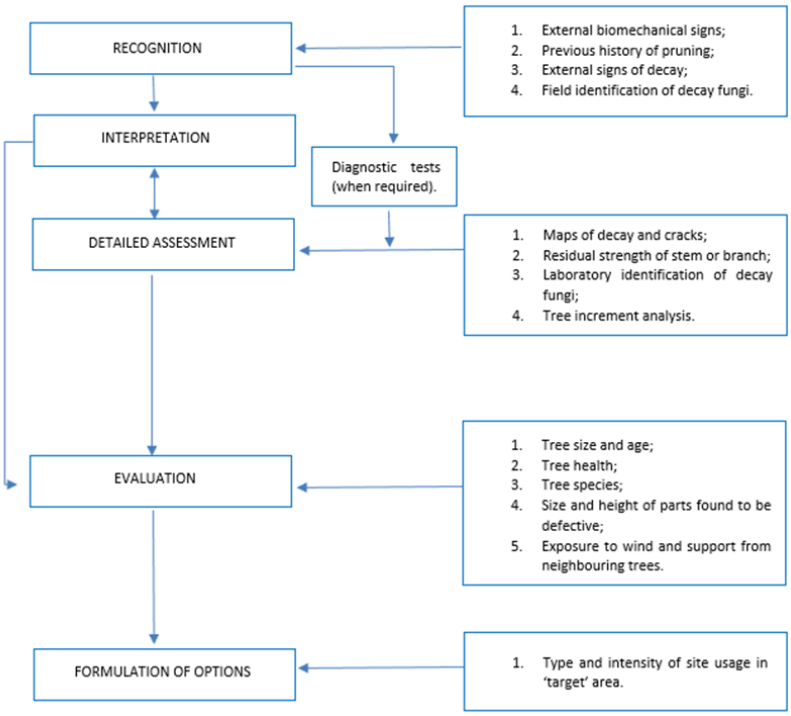

Figure 21: VTA implementation flowchart edited after Lonsdale 2007.

Non-destructive operative method: static pulling test

In routine tree risk assessment, the non-destructive static pull test is widely regarded as one of the most dependable procedures for evaluating stability, and its outcomes are commonly recognized in professional practice, including by insurance stakeholders. Conceptually, the test follows the same loading scheme as destructive winching campaigns but is conducted within a controlled range intended to avoid permanent damage. As outlined by Kim et al. (2020), a force F is applied to the stem at a known height H, with a defined inclination α relative to the horizontal ground surface, and the resulting rotation φ of the root plate is measured (Fig. 2-22). The recorded force–rotation response is then used to characterise the mechanical behaviour of the anchorage system under lateral loading.

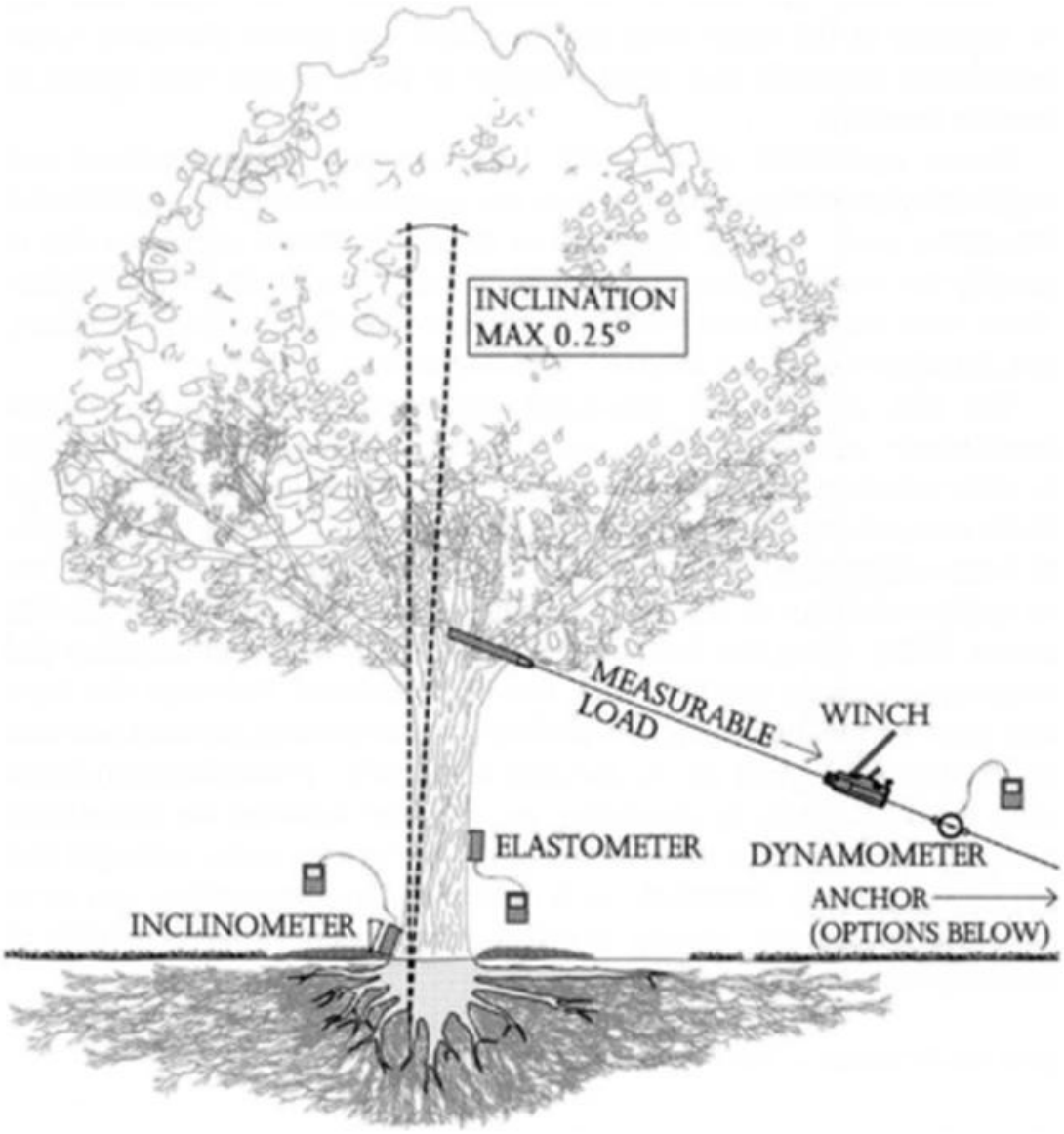

Figure 22: schematic diagram of a static pull test setup (van Wassenaer & Richardson, 2009).

To minimise the risk of inducing root damage, the applied load is typically restricted so that the measured root-plate rotation remains small, commonly not exceeding about 0.25°. The resulting force–rotation response is then interpreted by fitting the experimental data with the tipping relationship introduced by Wessolly & Erb (1998), which provides a practical basis for extrapolating anchorage behaviour beyond the non-destructive loading range.

$$\varphi[^\circ] = \frac{1}{3}\tan\left(\frac{100}{73.85}\frac{F}{F_L}\right) + \frac{1}{2}\left(\frac{F}{F_L}\right)^2 - \frac{1}{10}\frac{F}{F_L} \qquad \text{Eq. [8]}$$

where the fitting parameter F_L represents the reference limit value of the force F, implicitly fixed at a rotation φ_L=1.914°. The safety factor is then determined as

$$F_s^S = \frac{M_L}{M_{wind}^{max}} \qquad \text{Eq. [9]}$$

where M_L is the limiting overturing moment determined using F_L and M_{wind}^{max} is calculated from the geometric parameters of the tree, the characteristic aerodynamic drag factor of the given species and the expected maximum wind velocity value in the area:

$$M_{wind}^{max} = A_{cr} p_w^{max} C_d h_{cr} = A_{cr}\left(\frac{1}{2}\mu v_{max}^2\right) C_w h_{cr} \qquad \text{Eq. [10]}$$

In this formulation, A_{cr} denotes the projected crown area, $p_w^{max}$is the peak wind pressure associated with the design wind speed (i.e., it depends on air density $\rho$and v_{max}through the dynamic pressure term, typically $p \approx \frac{1}{2}\rho v^2$; for $\rho \approx 1.225\ \mathrm{kg\ m^{-3}}$and $v_{max} = 33\ \mathrm{m\ s^{-1}}$, $p_w^{max}$is about 667 Pa), C_d is the aerodynamic drag factor, and $h_{cr}$is the height of the crown's centroid. In practical applications, A_{cr} is often obtained via image-based tools that estimate crown area from photographs (see Figure 124), while the aerodynamic factors C_d are commonly adopted from tabulated values reported by Wessolly & Erb (1998).

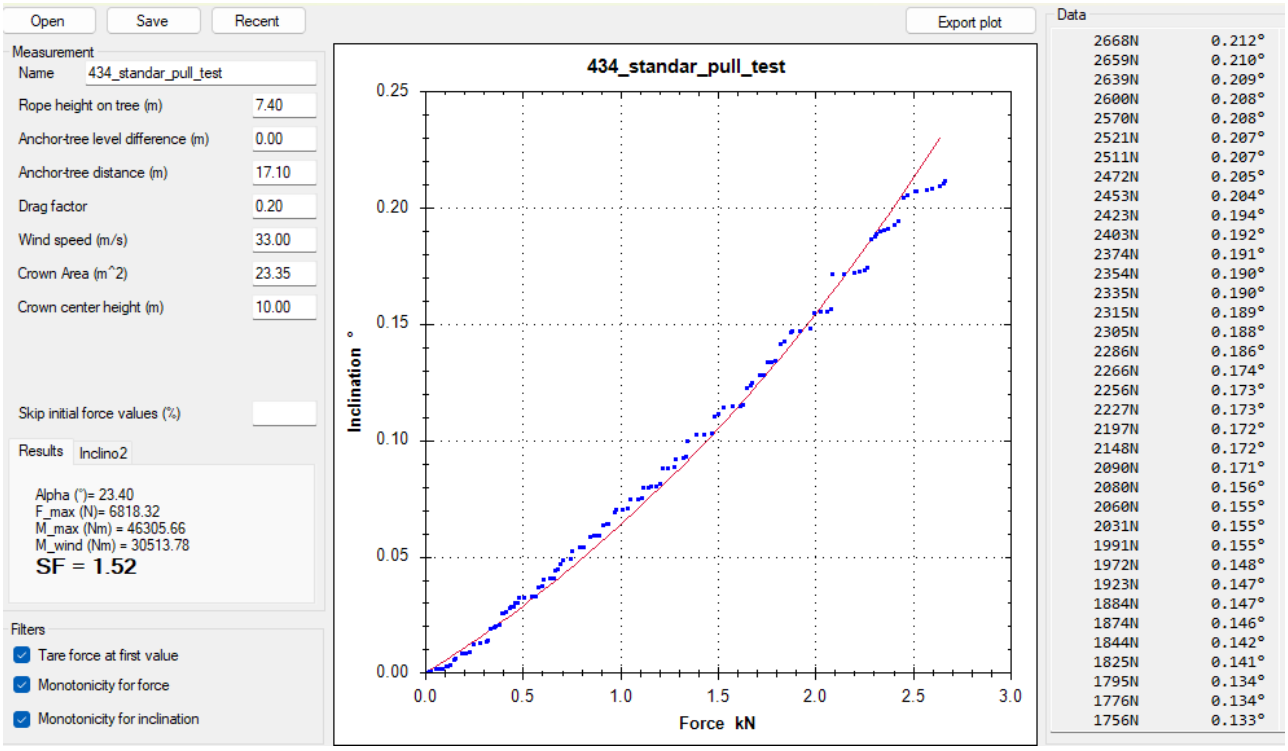

Figure 23: typical non-destructive pull-test results and Fs estimation..

Principles of dynamic tree response

In dynamic wind loading, tree overturning risk is primarily governed by three interacting components: (i) the tree's geometric and mass characteristics, (ii) the intensity and direction of the aerodynamic forcing, and (iii) the anchorage capacity of the coupled soil–root system. Under moderate wind conditions, trees typically exhibit complex sway responses driven by fluctuating wind pressure rather than monotonic loading. The incoming wind energy is partitioned between dissipation mechanisms within the tree—through damping associated with the stem, crown and branch motion—and energy transmitted to the soil–root plate via the base of the stem. When anchorage and surrounding soil can accommodate this transferred energy without progressive damage or loss of resistance, uprooting is avoided and the tree remains stable. Dynamic resistance is therefore not determined solely by peak load, but also by how effectively the tree–soil system attenuates and redistributes wind-induced energy over time. Accordingly, the assessment of tree stability under dynamic conditions should account for the following three aspects:

1. amount of the energy transferred to the tree from the wind;
2. amount of the transferred energy is dissipated by the tree components above ground;
3. how efficiently the root plate and soil dissipate the remaining wind energy.

The amount of energy imparted to a tree by the wind field can be inferred from the characteristics of the incoming flow together with canopy architecture and the effective frontal area exposed to the wind. Early work suggested that the maximum energy transfer is closely linked to the first natural frequency of the tree, as resonance-like conditions can enhance motion when dominant forcing scales align with the fundamental mode (Holbo et al., 1980; Peltola, 1996). In practice, because structural dynamics can be investigated through either free or forced vibrations, the fundamental frequency is commonly identified from free-decay tests: the stem is displaced from equilibrium, released, and the dominant oscillation frequency of the ensuing response is taken as the natural frequency. Observations indicate that free oscillations are largely governed by the most massive component of the system, i.e. the trunk (Sellier & Fourcaud, 2005). Consistent with this, increases in natural frequency have been reported following complete de-branching, reflecting the effect of crown mass and distribution on dynamic behaviour (Moore & Maguire, 2005), whereas the influence of root architecture on the first mode appears limited (Jonsson et al., 2007). Under forced vibrations (i.e., during wind excitation), the response depends on both the spectral content of the aerodynamic forcing and the dynamic properties of the tree itself. A key quantity in this context is the energy dissipated within the tree before being transmitted to the root plate—often described as damping-related dissipation—which varies with structural characteristics and with the type and intensity of the wind event. Numerous studies have therefore focused on estimating dynamic parameters, particularly damping, to improve predictions of wind-induced motion. Recent evidence further supports the notion that the fundamental frequency is a stable and informative descriptor for comparing tree motions and that it scales strongly with overall tree size (Jackson et al., 2021) (Figure 24).

By examining the power spectrum, which can be interpreted as a proxy for how wind energy is transferred into tree motion—previous work has shown that, at sufficiently high wind speeds, the link between wind loading and stem deflection tends to become primarily governed by wind speed itself. In contrast to static pulling tests, where the moment–rotation relationship can be defined in a controlled and relatively deterministic manner, the association between wind velocity and root-plate rotation in natural conditions is more complex because it is mediated by unsteady forcing and dynamic system properties. Nevertheless, the statistical frameworks proposed by Bejo L. et al. (2022) provide a practical route to stability assessment that circumvents explicit estimation of wind-load time histories, fundamental frequency and damping ratio. The underlying concept, introduced by, is to directly correlate concurrent, in situ measurements of wind speed and root-plate rotation, thereby inferring stability-relevant behaviour from observed co-variation rather than from a fully parameterized Bejo et al. (2017) dynamic model.

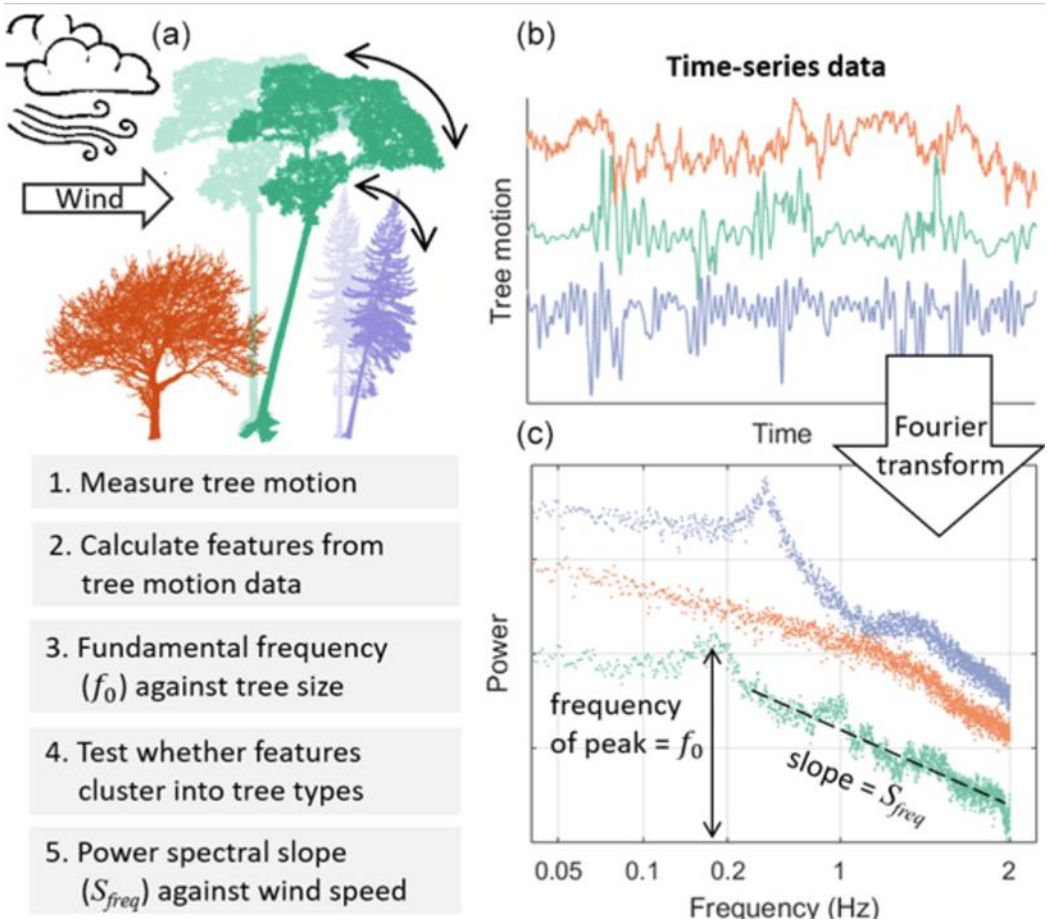

Figure 24: a) conceptual diagram of data collection showing three "types" of trees swaying in the wind. b) A 5 min sample of tree motion data for three trees. (c) Fourier transformed data used to calculate the fundamental frequency, slope of the power spectrum, and related features (Jackson et al., 2021).

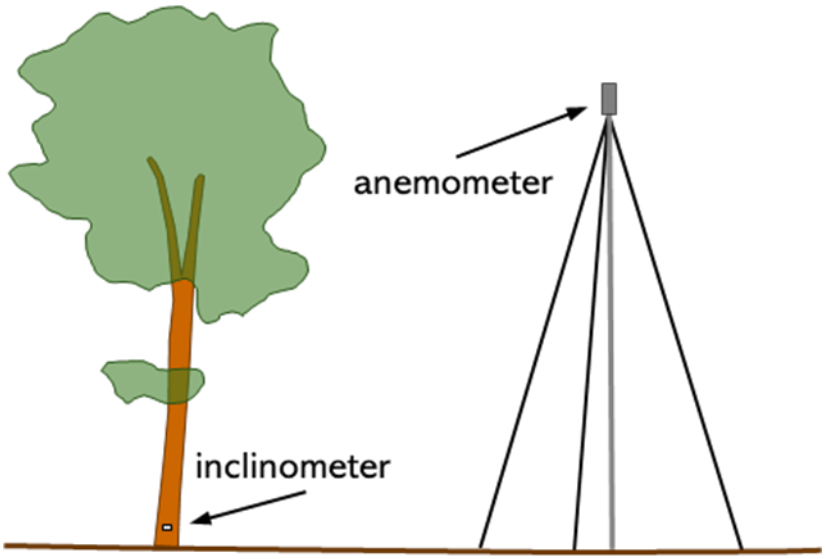

Figure 25: schematic diagram of a dynamic tree stability assessment.

As outlined schematically in Figure 25, the method was conceived as a dynamic analogue of the safety-assessment framework adopted for static pulling tests (see previous section). Rather than applying a controlled load, it relies on a statistical coupling between wind intensity and measured inclination, computed over moving time windows of several minutes. Following the procedure described by Bejo et al. (2017), this relationship can be used to extrapolate a limiting wind-pressure threshold for the tree, which is then directly comparable to the maximum wind pressure expected under severe wind conditions. In practical terms, this formulation recasts Eq. [9] into a simple ratio between the inferred limit pressure and the design maximum pressure, thereby bypassing the explicit use of geometric descriptors and the adoption of empirical aerodynamic drag factors.

$$F_s^d = \frac{p_w^L}{p_w^{max}} \qquad \text{Eq. [11]}$$

If the Wessolly & Erb (1998) equation is used to fit the pressure deflection results, since h_{cr} and A_{cr} are independent of wind pressure then (Eq. [8]) can be written as

$$\varphi = \frac{1}{3}\tan\left(\frac{100}{73{,}85}\frac{p}{p_w^L}\right) + \frac{1}{3}\left(\frac{p}{p_w^L}\right)^2 - \frac{1}{10}\frac{p}{p_w^L} \qquad \text{Eq. [12]}$$

and used to estimate p_w^L and hence F_s^d.

Drag coefficient estimation

Wind-induced aerodynamic loading is a key component of tree stability assessments in forest and urban environments. The total drag force exerted by the wind on the tree's canopy is described using the drag equation.

$$F_D = 0.5\,\rho\,C_d\,A\,v^2 \qquad \text{Eq. [13]}$$

where ρ is air density, v is wind speed, $A$is a reference area (typically the projected frontal area of the crown), and C_d is the aerodynamic drag coefficient. Equivalently, introducing the dynamic pressure $q = 0.5\,\rho\,v^2$, the drag force can be expressed as $F_D = C_d\,A\,q$. When the objective is to quantify overturning effects, the force can be converted into a bending/overturning moment of the root collar

or another reference section by multiplying by an effective lever arm (e.g., the height of the centre of pressure).

However, estimating Cd for a real tree is non-trivial. Trees behave like porous, deformable bodies that undergo aerodynamic reconfiguration (streamlining) when wind speed increases. Consequently, the frontal area A and the drag coefficient C_d cannot be assumed to be strictly constant. In many cases, the apparent reduction in aerodynamic loading with increasing wind speed is attributed to the combined effects of (i) a decrease in projected area, and (ii) changes in drag associated with wind-driven modifications to the shape and porosity of the crown. This physical framework has been addressed in several experimental studies and authoritative reviews on wind–plant interactions.

The literature on drag coefficient estimation can be broadly grouped into three main methodological families: (1) wind-tunnel experiments on real trees or physical models; (2) field measurements that combine wind observations with mechanical response (deflection/inclination) to infer aerodynamic forcing; and (3) hybrid in situ approaches that estimate drag and frontal area simultaneously using sensors and imaging, which are also valuable for calibrating parameterizations in numerical models. Some of the earliest systematic estimates of drag coefficients were provided by wind-tunnel investigations on real trees and crowns, including the pioneering work of (Mayhead, 1973), who derived drag coefficients for commercial conifers under controlled flow conditions (Figure 26). Subsequent studies have explicitly highlighted the importance of aerodynamic reconfiguration (streamlining) and the velocity-dependent evolution of frontal area. These studies have often incorporated photographic methods to quantify the reference area under different wind regimes (Vollsinger et al., 2005) (Figure 27).

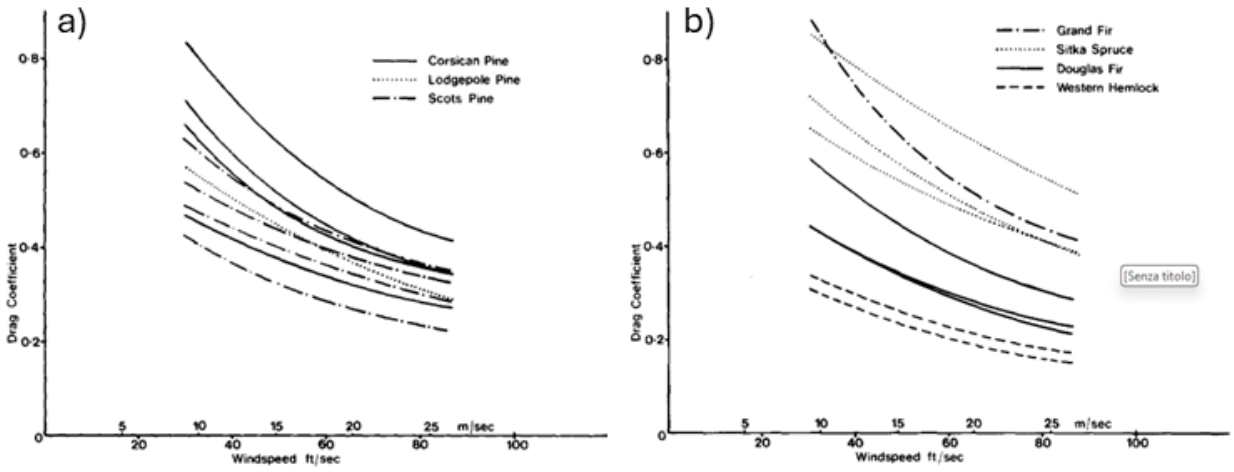

Figure 26: a) drag coefficient of pines in relation to windspeed; b) drag coefficient in relation to windspeed. (Mayhead, 1973)

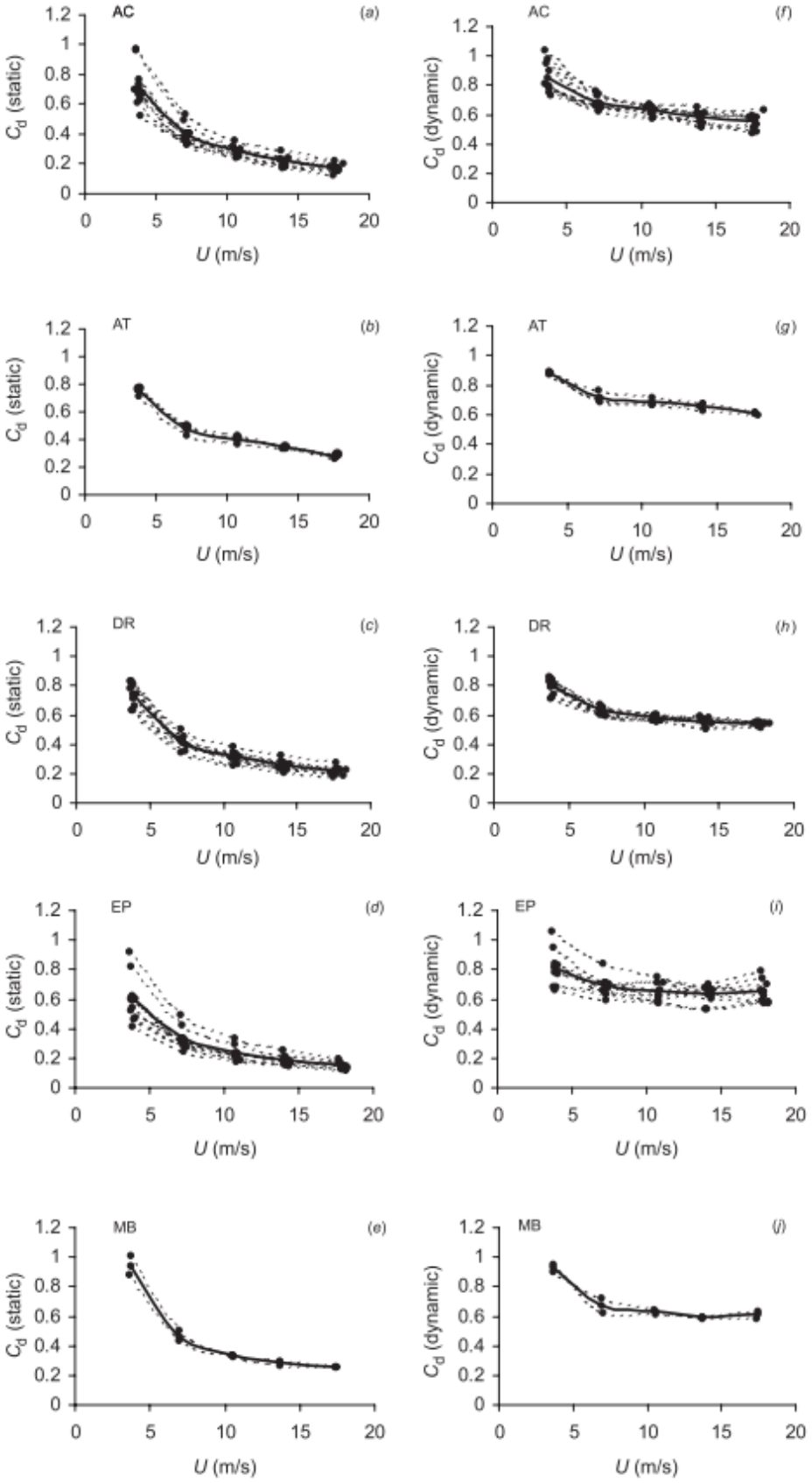

Figure 27: drag coefficients calculated using still-air frontal area (Cd static) for wind speeds from 4 to 20 m/s for (a) black cottonwood (AC), (b) trembling aspen (AT), (c) red alder (DR), (d) paper birch (EP), and (e) bigleaf maple (MB), and drag coefficients calculated using wind-speed-specific frontal area (Cd dynamic) for (f) black cottonwood, (g) trembling aspen, (h) red alder, (i) paper birch, and (j) bigleaf maple. Dotted lines are individual trees, while heavy solid lines are means. (Vollsinger et al., 2005).

Complementary evidence has been obtained through full-scale field approaches that infer aerodynamic forcing from the structural response of trees. (Koizumi et al., 2010) proposed a method in which wind speed and stem deflection are measured simultaneously and the aerodynamic force is reconstructed from the measured deflection and stem stiffness, as determined by bending tests.

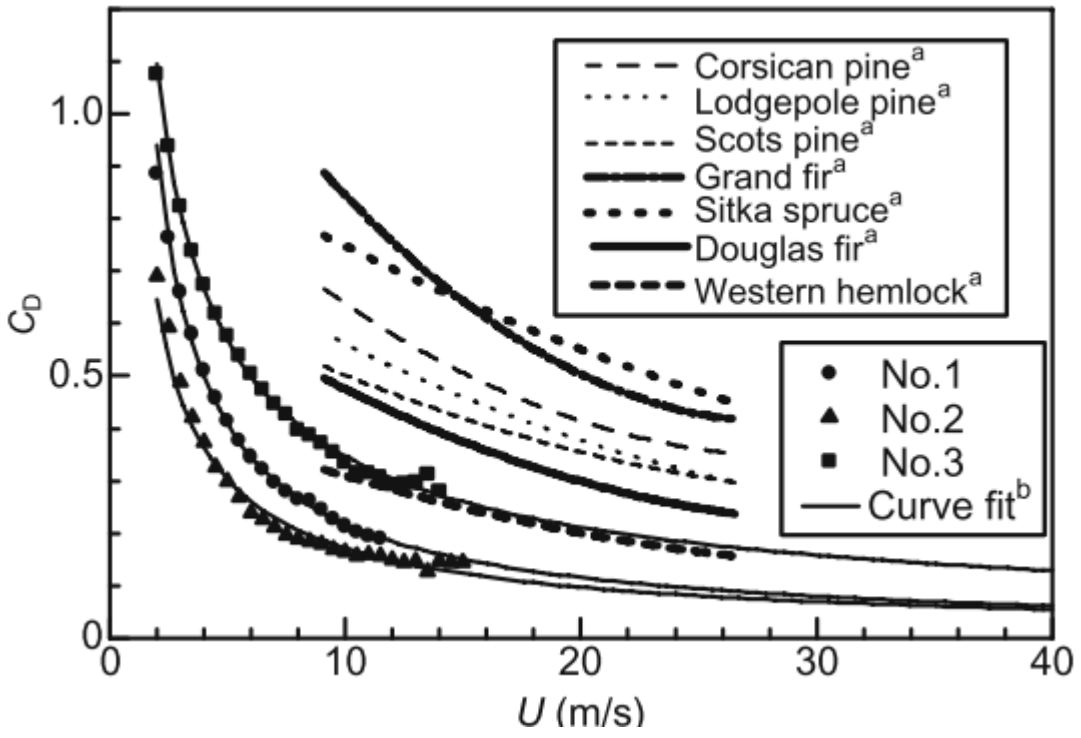

Figure 28: comparison between CD values of poplars and conifers obtained from a wind tunnel study. a) Reported by Mayhead.3 b) Tree no. 1, Y =1.77 X−0.911; tree no. 2, Y = 1.14 X−0.824; tree no. 3, Y = 1.79 X−0.714. (Koizumi et al., 2010)

This enables the estimation of Cd and its dependence on wind speed. Similarly, (Kane & Smiley, 2011) discussed the estimation of Cd and crown area for urban trees, emphasizing that the resulting drag estimates are highly sensitive to the definition of the reference area. Beyond these approaches, direct field measurements of vegetation, often motivated by windbreak applications, have shown that porosity exerts a significant influence on drag. This provides guidance on the limitations of transferring drag coefficients across species and canopy architectures (Grant & Nickling, 1998) (Figure 29). (Manickathan et al., 2018) demonstrated in wind-tunnel experiments that achieving aerodynamic similarity requires comparable geometric form, porosity and reconfiguration capability (Figure 30). More recently, hybrid in situ methods combining anemometric measurements with image-based estimates of frontal area have been proposed for mature solitary trees in natural wind conditions. These studies show that uncertainty in determining A is one of the main reasons for the variation in Cd values reported in the literature (Bekkers et al., 2022) (Figure 31).

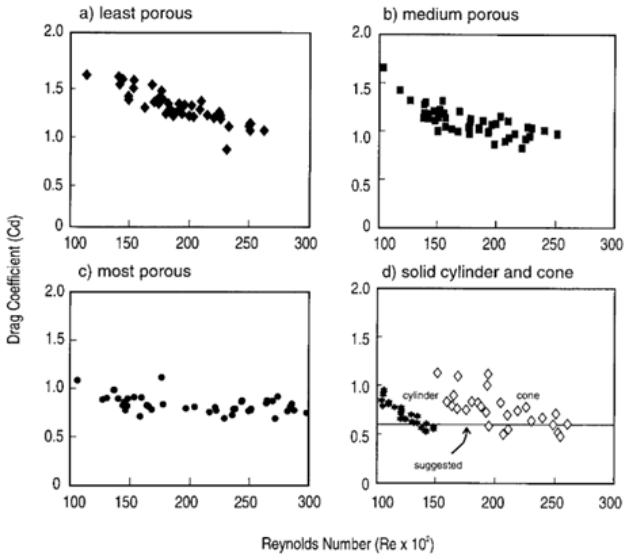

Figure 29: Drag curves for a) the least, b) medium and c) most porous shrub and for d) the cone and cylinder. (Grant & Nickling, 1998)

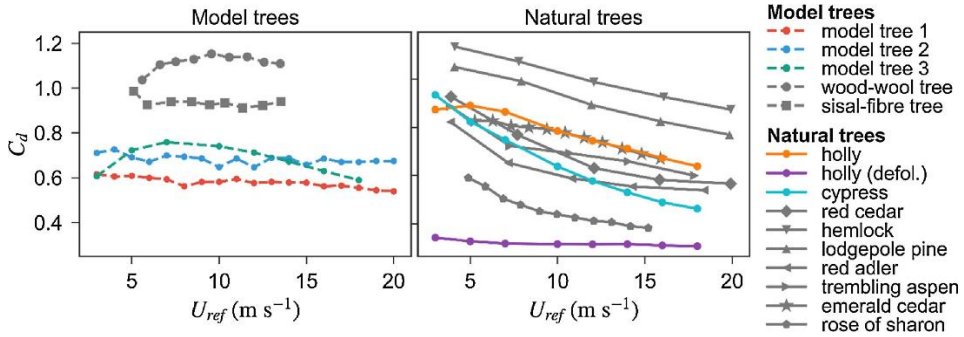

Figure 30: Drag coefficient vs. wind speed for various model trees (dashed lines) and natural trees (solid lines). (Manickathan et al., 2018)

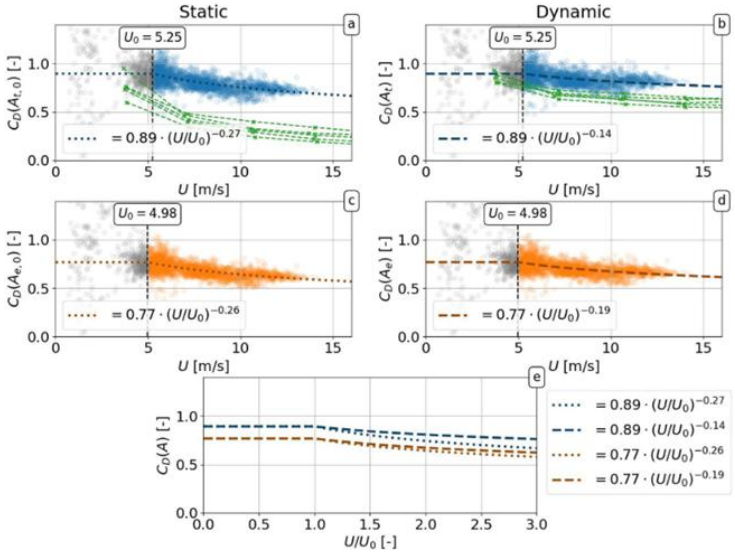

Figure 31: Estimates of the drag coefficient as a function of wind speed for different definitions of the frontal area: Panels a and c use the frontal areas determined for $U \leq U0$ (static Cd), panels b and d use the wind-speed dependent frontal areas (dynamic Cd). The green dashed lines denote the results from small deciduous trees in the wind tunnel study by Vollsinger et al. (2005). A Levenberg–Marquardt algorithm is used to produce a fit in the form of $m \cdot (U/U0)a$ and is indicated by dotted and dashed lines for $U \geq U0$. A summary of all fitted functions is given in the bottom panel e.(Bekkers et al., 2022)

Part I

Single tree analysis and investigation

Chapter I

On the uprooting stability of trees

(field testing campaign at Botanic Garden of Dundee)

Overview

The University of Dundee Botanic Garden, founded in October 1971, provides an excellent setting in which nature-based and community-oriented approaches can be explored in relation to climate adaptation and mitigation (Frediani K., 2021). The site covers approximately 9.5 hectares on elevated ground overlooking the River Tay and contains a wide-ranging plant collection, including both native British species and notable specimens introduced from other regions. The site boundaries are shown in Figure 32 (white outline). Several sectors of the garden are formally designated as outdoor research laboratories and are routinely used for experimental activities, including tree stability testing. The trees selected for this study were healthy, well-established individuals dating back to the early plantings of the garden, but were scheduled for removal within a wider renovation programme aimed at enhancing biodiversity.

Figure 32: u*niversity of Dundee Botanic Gardens—study area, western Dundee (UK, Scotland), and 365 m from the River Tay; 9.5 ha with about 5000 trees. In white circles the zone containing tested trees.*

Geological settings

The Dundee Formation, as defined by (Armstrong & Paterson, 1970), consists predominantly of cross-bedded sandstones with interbedded siltstone and mudstone, interpreted as lacustrine–deltaic to delta-front deposits. Within the Dundee Botanic Garden area, superficial materials comprise (i) late-glacial raised marine deposits, including littoral sand, deltaic sand, silt, and subtidal clay, and (ii) glaciofluvial meltwater deposits of sand and gravel. The gardens occupy a sloping terrace near the crest of an ice-age cliff. Bedrock exposure varies across the site, with sandstone occurring at lower elevations and volcanic felsite at higher elevations (although the mapped boundary is not shown).

Overall, the presence of marine- and glacial-derived sands, gravels, and clays suggests that the site may have experienced substantial landscaping, potentially involving soil reworking and/or importation. Figure 33 presents post-test photographs from selected uprooting events described later in the chapter. These observations indicate likely vertical variability in soil moisture conditions. Additional visual evidence includes cobbles and sandstone slabs of variable thickness (approximately 2–5 cm).

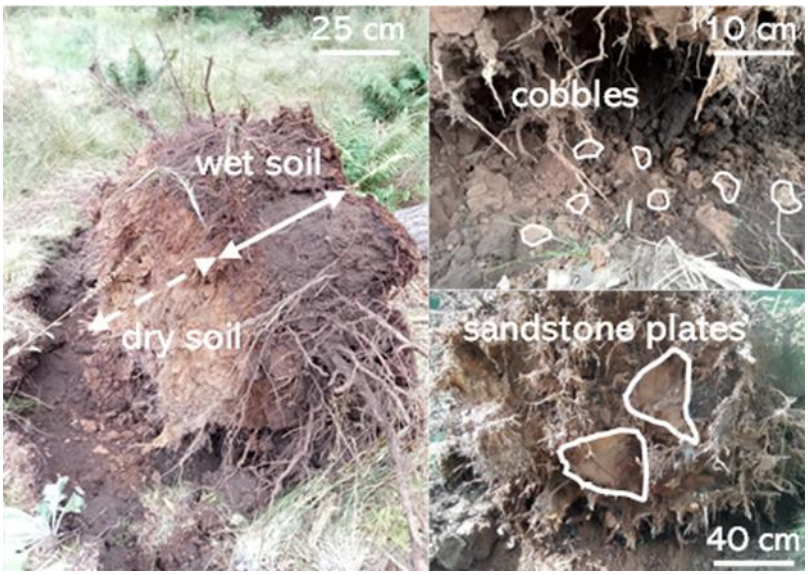

Figure 33: visual evidence of ground conditions following uprooting tests.

Topsoil characterization

A suite of field and laboratory investigations was carried out to characterize the near-surface soil horizons hosting the tree root systems. The testing programme included the following:

- **Corkscrew (CS)** testing, following the procedure reported in (G. J. Meijer et al., 2018; G. Meijer et al., 2019). The device was screwed into the soil and then pulled out vertically at a constant rate of 100 mm/min using a lever mechanism instrumented with a load cell (Figure 34), which recorded the extraction force G. Meijer et al., 2019. The mobilized shear stress was derived from the measured pull-out force and the lateral surface area of the soil cylinder engaged by the corkscrew. Tests were carried out at four locations around each tree, typically at a radial distance of about 1 m along the cardinal directions, and—where feasible—were repeated at increasing depths in sequence until refusal.

Figure 34: application of corkscrew in the Botanic Garden.

- **Vane shear testing (VST)**, commonly employed for in situ assessment of undrained shear strength in cohesive soils (Chandler, 1988). Measurements, using the instrument shown in Figure 35 were taken at four locations around each tree along the cardinal directions (N–E–S–W); where required, additional test points were included, mirroring the spatial layout adopted for the corkscrew tests.

Figure 35: vane test apparatus used in the field test campaign.

- Water content measurements were performed using an **ML2 Theta Probe** (Delta-T Devices, Cambridge, UK) shown in Figure 36, a capacitive sensor that estimates volumetric water content from the soil dielectric permittivity. Readings were collected at four locations around each tree along the cardinal directions (N–E–S–W), consistent with the sampling scheme adopted for the corkscrew and vane shear tests.

Figure 36: use of the ThetaProbe for in situ measurement of soil moisture content.

- **Particle size distribution (PSD)**. Disturbed samples were collected in the vicinity of the tested *Pinus nigra* (258, 260, 268, 270), *Acer platanoides* (433, 434, 604), and *Nothofagus* (568, 606) individuals and used to derive PSD curves through a combination of vibratory sieving and sedimentation. For reporting purposes, the Botanic Garden was subdivided into zones, within which trees were grouped (Figure 32). Given the high organic matter content, samples were pre-wetted prior to sieving of the finest fraction (silt–clay); sedimentation was quantified using an automated Pario analyzer (Meter Group, Washington, DC, USA): the suspension was agitated in distilled water for 60 s, left to settle for 2.5 h, and then processed to obtain the grain-size percentages. All the procedure is shown in next Figure 37.

Figure 37: PSD experimental setup: Sieving and densimeter..

The combined approach yielded continuous PSD curves that were consistent between the two replicate samples collected at each location (Figure 38a). According to the resulting texture classification, all soils fell within the sandy loam domain (Figure 38b).

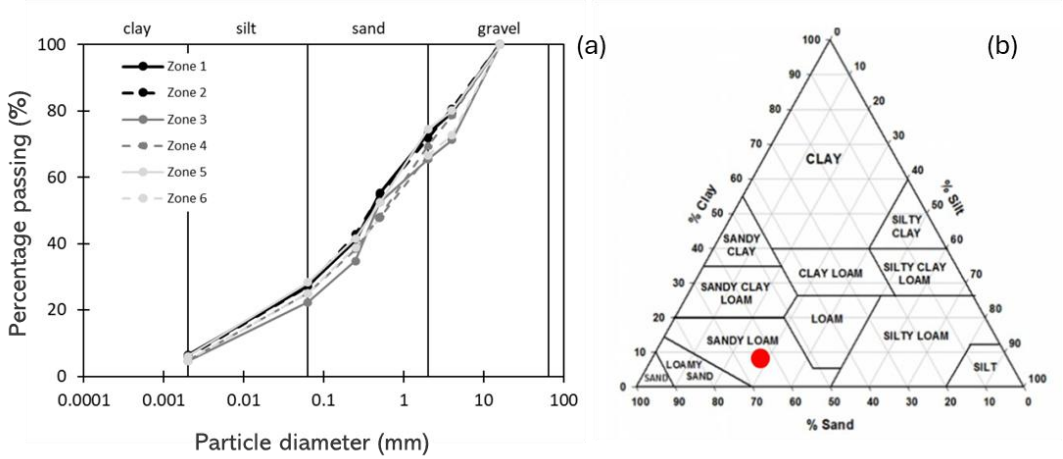

*Figure 38: (**a**) Particle size distribution curves and (**b**) soil texture (the red dot) of the Botanic Garden topsoil.*

- **Soil water retention curve (SWRC)**. Undisturbed cores (50 mm diameter, 40 mm height) were collected for SWRC determination. After saturation for 24 h in degassed water, specimens were placed on a ceramic plate with an air-entry value (AEV) of 100 kPa (Soilmoisture Equipment Corp., Goleta, CA, USA) to ensure hydraulic contact and to equilibrate matric suction at 1, 5, 20, and 50 kPa. Suctions in the higher range (50–1500 kPa) were then applied using a pressure-plate apparatus (Soilmoisture Equipment Corp., Goleta, CA, USA). The measured water retention data were fitted using the van Genuchten model (van Genuchten, 1980). Figure 39 presents a representative SWRC for the vegetated topsoil in zone 3, while the corresponding curves for the remaining zones are reported in Appendix A.

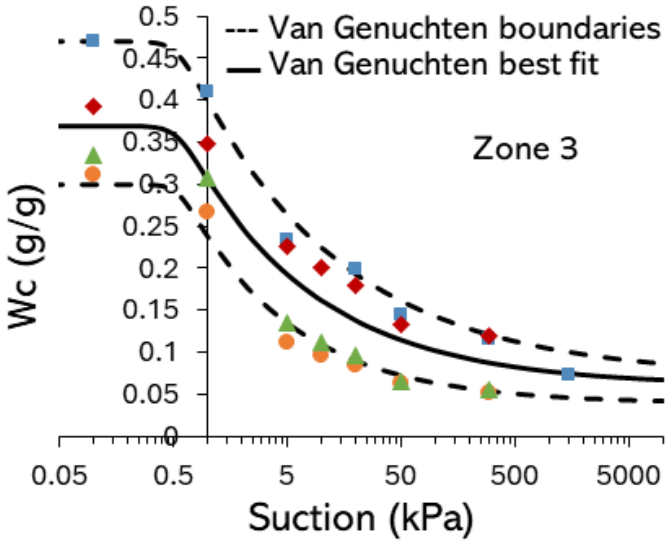

Figure 39: Example soil water retention curve for Botanic Garden topsoil (rich vegetated soil, zone 3, Figure 32). Dashed lines indicate upper and lower limits. Each colour series, along with its distinct symbol, represents a different soil-sample dataset.

- **Direct shear tests on large samples**. Three cylindrical specimens (150 mm diameter, 300 mm height) were collected from zones 2, 3, and 5 (Figure 32). Sampling was performed using a purpose-built metal tube with the same internal dimensions, which was driven into the ground until flush with the surface, with a rubber separator used for protection during driving. The cores were then extracted using a lever system (as for the corkscrew tests) and transferred into pre-prepared plastic cylinders with a press to minimize disturbance; specimens were sealed to limit changes in moisture content (Figure 40).

Figure 40: tube sampling procedure for direct shear tests.

The plastic cylinders were assembled in two sections (100 mm and 200 mm high), separated by inserts to define the intended shear plane, and fitted with a drainage mesh at the base. Direct shear testing was carried out using a dedicated apparatus (T. Liang et al., 2015) at a shear displacement rate of 50 mm/min (Figure 41).

Figure 41: direct shear testing setup.

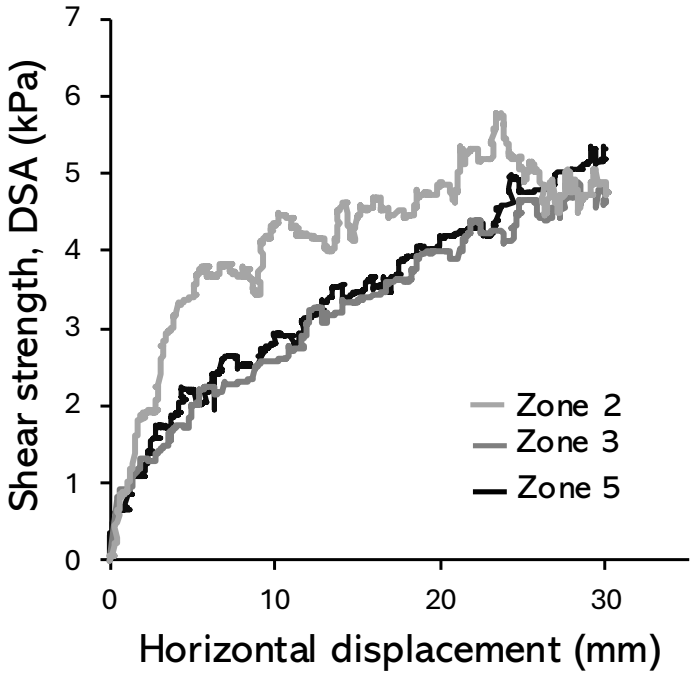

Figure 42: Large-sample direct shear apparatus (DSA) test curves.

Prior to testing, samples were saturated for 24 h and then manually drained by applying pressure with a metal spatula before shearing. The resulting shear stress–displacement curves (Figure 42) did not exhibit pronounced peak strengths, plausibly because visible roots contributed to reinforcement and promoted a more ductile response (G. Meijer et al., 2019).

Figure 43 provides a consolidated view of shear strength and water content data collected at a representative site (*Pinus nigra* 268, zone 3). Figure 43c also maps the distribution of roots within the subsoil; across all destructive tests, roots were not observed to extend into the underlying bedrock. Equivalent summaries for the remaining zones are reported in Appendix A. The combined dataset shows a general reduction in soil shear strength with increasing depth. This trend cannot be attributed to increasing saturation, since water content also decreases with depth, consistent with drainage into the underlying sandstone. A more plausible interpretation is that the root-influenced horizon—primarily within the upper ~0.4 m—exhibits enhanced shear strength as a result of root reinforcement. This is further supported by the pronounced spatial variability in strength measured around the tree within this upper layer, which likely reflects differences in the amount of root material intercepted at each test point. The direct shear apparatus (DSA) results obtained from soil with negligible root content provide a lower-bound estimate relative to the strength values measured within the root bulb using the in-situ methods. In Figure 43, corkscrew (CS) and vane shear test (VST) results are also compared and grouped by depth interval. VST measurements are systematically higher than those derived from CS testing, in line with the upper range reported by (G. Meijer et al., 2019) for measurements around *Picea sitchensis* grown in sandy silt (Figure 44).

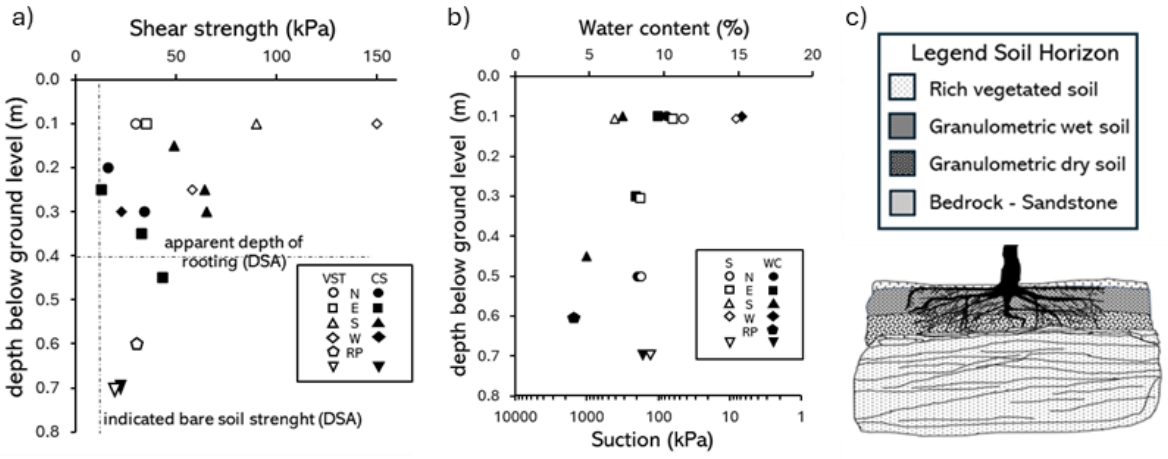

*Figure 43: Comparative summary of soil state and strength data (Zone 3): (**a**) shear strength from corkscrew (CS), vane shear tests (VST), and DSA; (**b**) depth distribution of soil water content and suction inferred from zone 3 SWRC; (**c**) soil profile indicating soil horizons. Test data from different locations related to the trunk, where N, E, S, and W are cardinal directions, RP = root-plate, and H = soil under root-plate.*

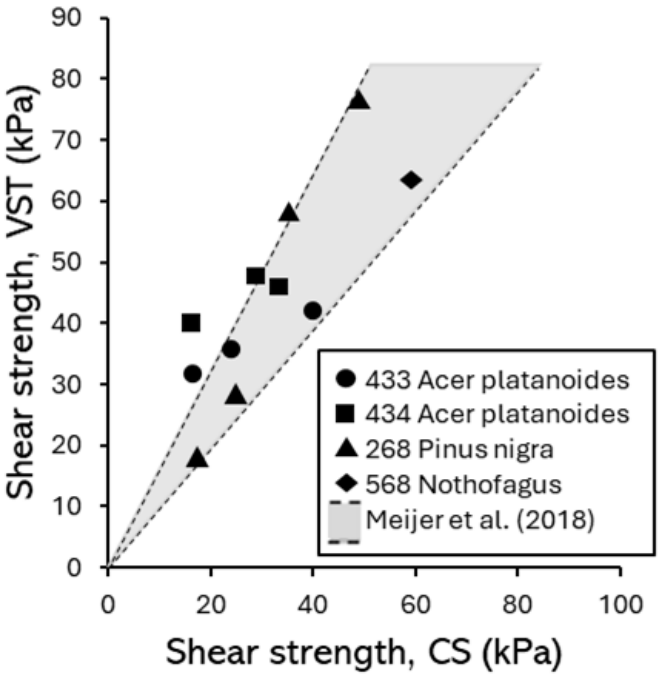

Figure 44: Correlation between corkscrew (CS) and vane shear test (VST) data and comparison to measurements in a similar soil type at an alternative site (G. Meijer et al., 2019).

Appendix A

The following figures present the soil water retention curves for the remaining zones (1, 2, 4, 5, and 6), together with the plots summarizing the geomechanical characterization of the topsoil obtained from the Corkscrew (CS) and vane shear test (VST) measurements:

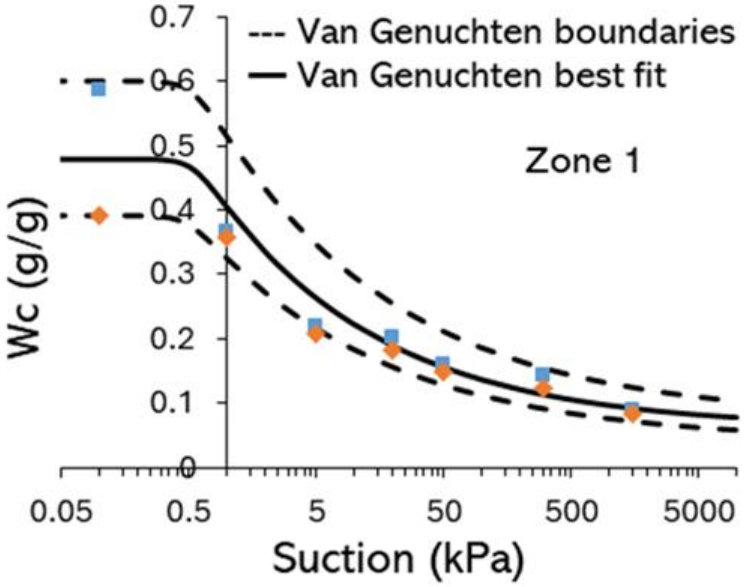

Figure A1: Example soil water retention curve for Botanic Garden topsoil (rich vegetated soil, zone 1, Figure 32). Dashed lines indicate upper and lower limits. Each colour series, along with its distinct symbol, represents a different soil-sample dataset.

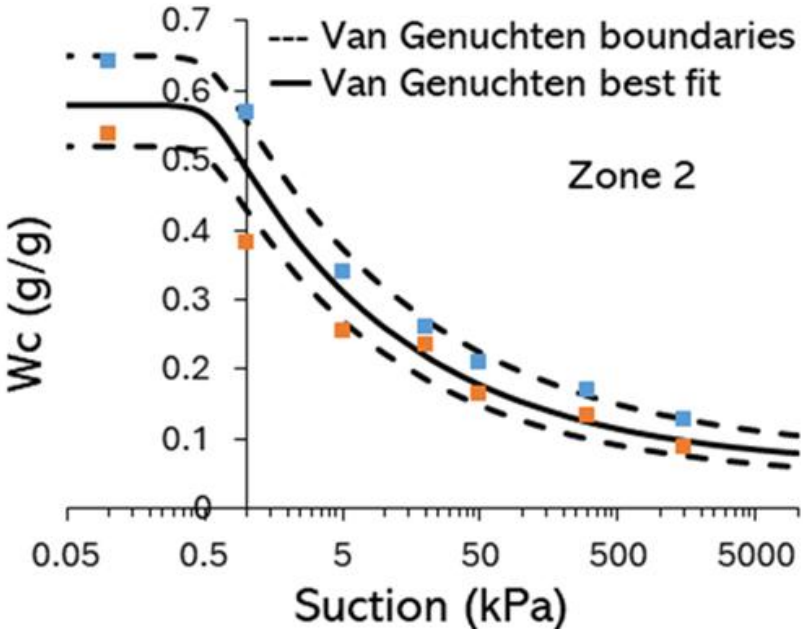

Figure A2: Example soil water retention curve for Botanic Garden topsoil (rich vegetated soil, zone 2, Figure 32). Dashed lines indicate upper and lower limits. Each colour series, along with its distinct symbol, represents a different soil-sample dataset.

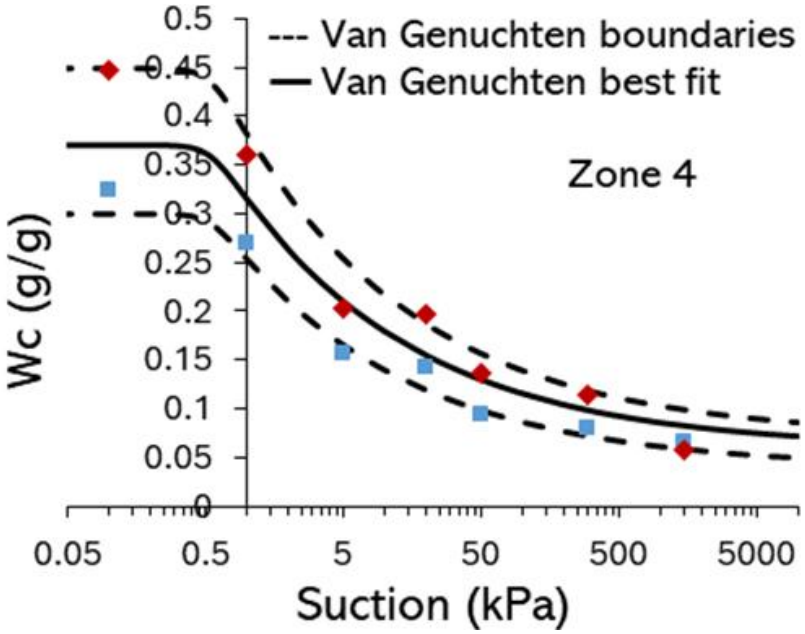

Figure A3: Example soil water retention curve for Botanic Garden topsoil (rich vegetated soil, zone 4, Figure 32). Dashed lines indicate upper and lower limits. Each colour series, along with its distinct symbol, represents a different soil-sample dataset.

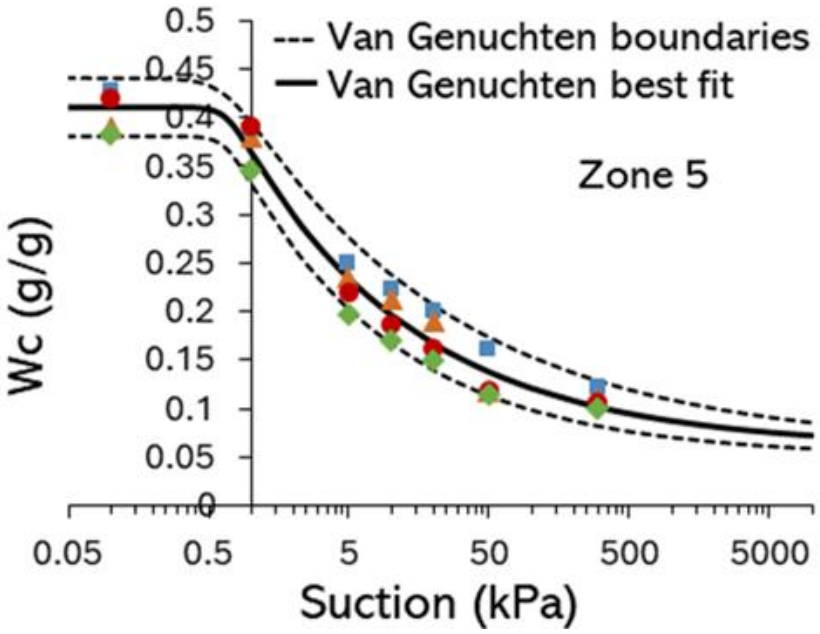

Figure A 4: Example soil water retention curve for Botanic Garden topsoil (rich vegetated soil, zone 5, Figure 32). Dashed lines indicate upper and lower limits. Each colour series, along with its distinct symbol, represents a different soil-sample dataset.

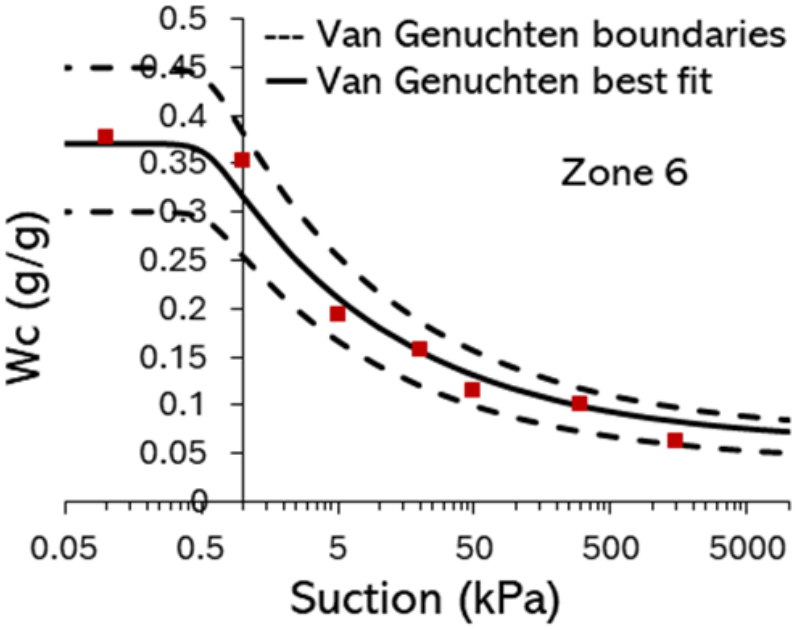

Figure A5: Example soil water retention curve for Botanic Garden topsoil (rich vegetated soil, zone 6, Figure 32). Dashed lines indicate upper and lower limits. The red square markers indicate the soil-sample dataset.

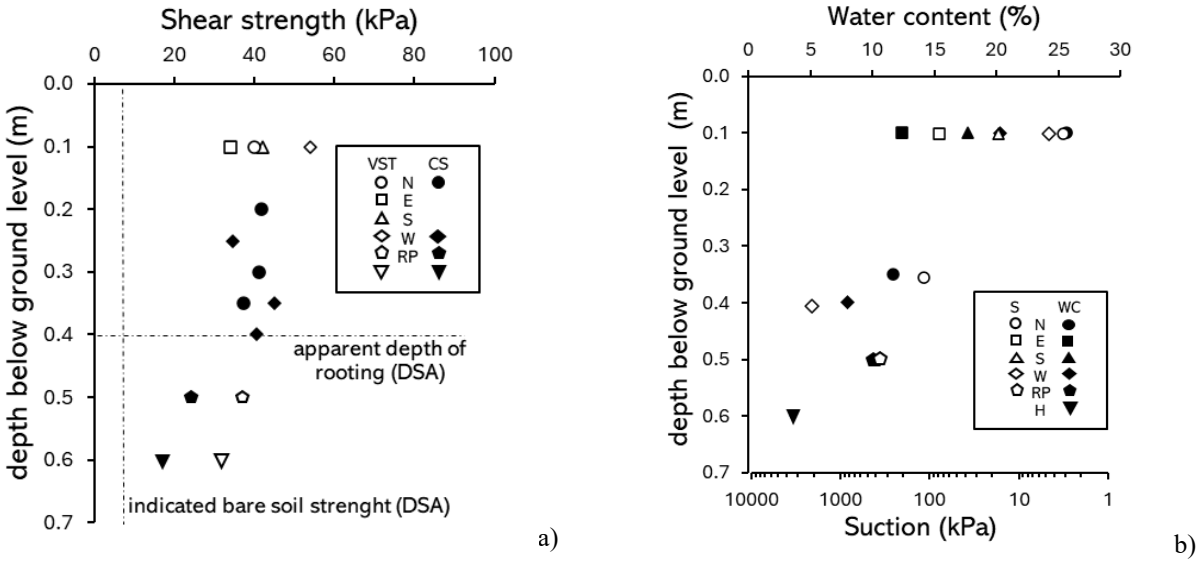

Figure A6: Comparative summary of soil state and strength data (433—Acer platanoides): (a) shear strength from corkscrew (CS), vane shear tests (VST), and DSA; (b) depth distribution of soil water content and suction inferred from zone 3 SWRC. Test data from different locations related to the trunk, where N, E, S, and W are cardinal directions, RP = root-plate, and H = soil under root-plate.

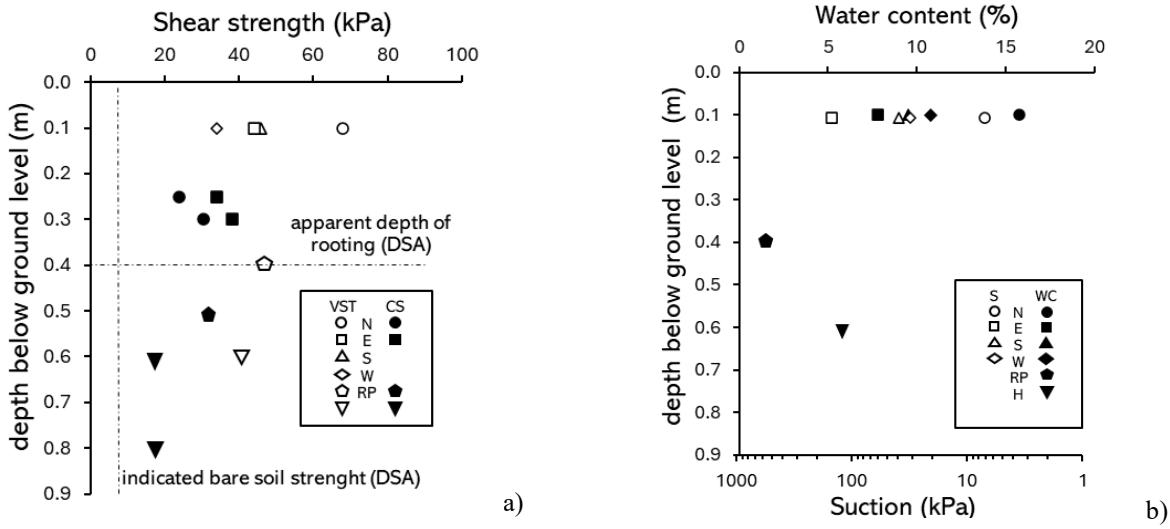

Figure A7: Comparative summary of soil state and strength data (434—Acer platanoides): (a) shear strength from corkscrew (CS), vane shear tests (VST), and DSA; (b) depth distribution of soil water content and suction inferred from zone 3 SWRC. Test data from different locations related to the trunk, where N, E, S, and W are cardinal directions, RP = root-plate, and H = soil under root-plate.

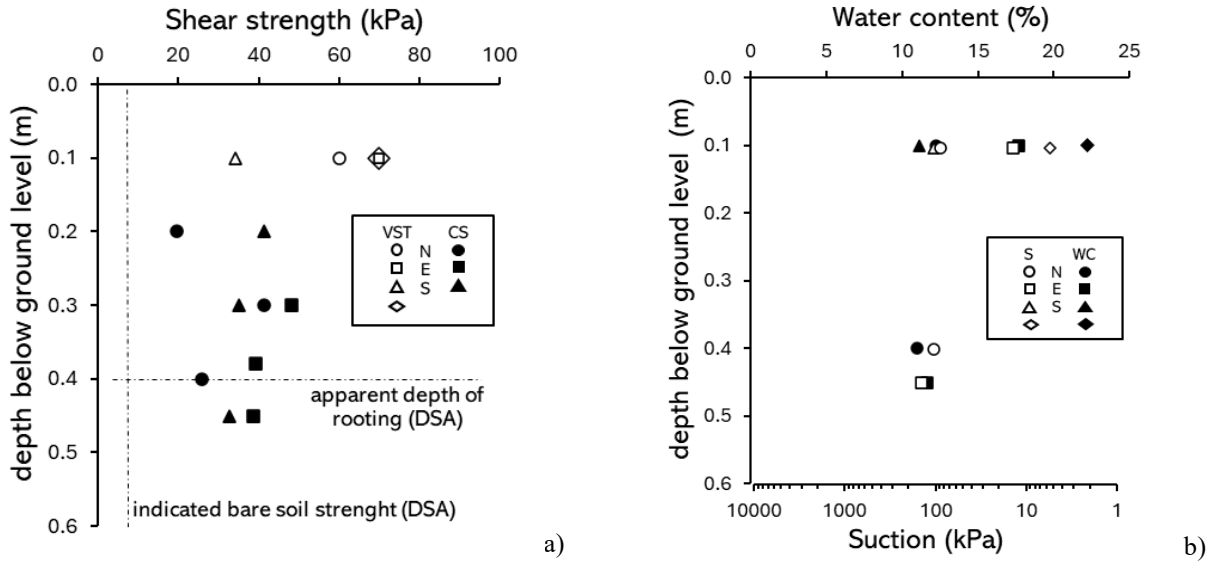

Figure A8: Comparative summary of soil state and strength data (568—Nothofagus): (a) shear strength from corkscrew (CS), vane shear tests (VST), and DSA; (b) depth distribution of soil water content and suction inferred from Zone 3 SWRC. Test data from different locations related to the trunk, where N, E, S, and W are cardinal directions, RP =root-plate, and H = soil under root-plate.

Tree stability assessment through non-destructive and destructive test

In this context, the present study examines tree uprooting stability through an extensive experimental campaign carried out at the University of Dundee Botanic Gardens (Scotland, UK). The primary objectives were to quantify the influence of pulling direction and pulling height on overturning resistance and to interpret uprooting behaviour in light of a detailed geotechnical characterization of the near-surface soils. In total, twenty-one mature trees were investigated across both coniferous and broadleaved species (*Pinus nigra*, *Picea abies*, *Tsuga*, *Betula*, *Quercus*, *Acer platanoides*, *Nothofagus*, and *Eucalyptus*) under a range of loading configurations—an approach that, to the best of the authors' knowledge, has not been systematically addressed previously. Each tree underwent multiple static pulling tests in which both the azimuth of loading and the pulling angle were varied to reproduce different wind-loading scenarios (Figure 45). In addition, a subset of trees was tested destructively to uprooting in order to obtain complete failure curves. The measured responses were subsequently compared with predictions derived from Wessolly's extrapolation method (and alternative approaches), with the specific aim of assessing their robustness under changes in loading direction and inclination.

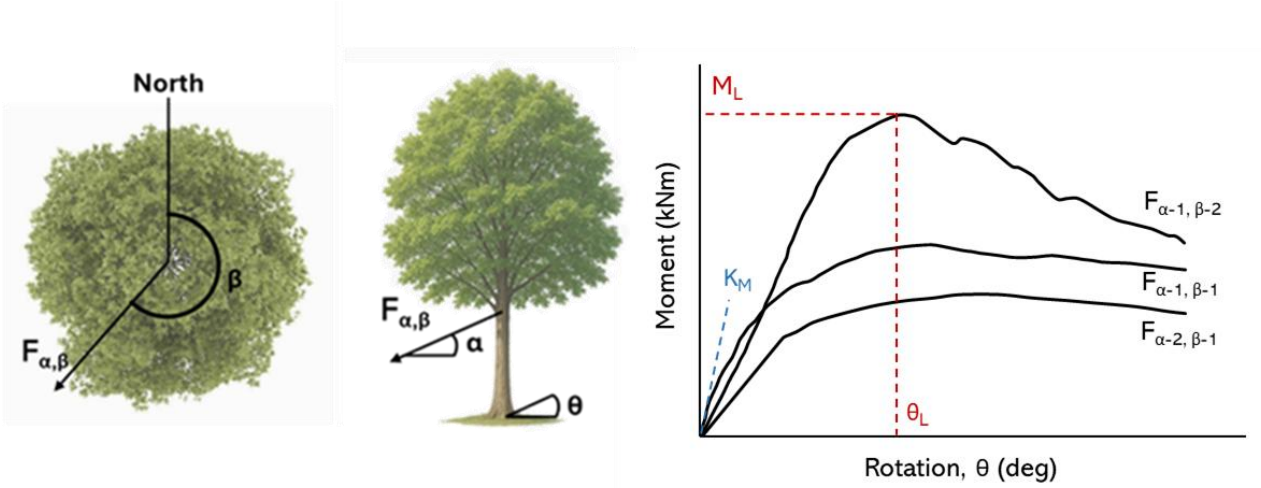

Figure 45: (a) Plan and elevation views of a tree showing pulling direction (β), inclination angle (α), rotation at the root-plate (θ), and pulling force ($F_{\alpha,\beta}$); (b) schematic uprooting curves from different pulling directions and heights, showing definitions of limit moment and limit rotation angle (M_L, θ_L) and stiffness K_M.

Winching test setup

Winching tests were performed either up to a serviceability threshold—defined here as 0.25° rotation at the stem base in the pulling direction and referred to as non-destructive—or continued to uprooting, representing the ultimate limit state. As illustrated in Figure 46, a rope was fixed to the test tree at a prescribed height and connected via a winch to a nearby anchor tree, with the rope secured at the base of the anchor. Tensile force was measured using an in-line load cell (Kaliber 5 t force meter, Budapest, Hungary; working load limit 50 kN; 10 N resolution; 1 Hz sampling). Tree-base rotation was monitored using two orthogonally oriented inclinometers (±30° range; 0.001° resolution; 10 Hz sampling), aligned parallel and perpendicular to the pulling direction and mounted horizontally at the stem base (dual-axis inclinometer from the DynaTree Root and Trunk Testing System, BtFakopp Enterprise Bt, Sopron, Hungary). Prior to each test, canopies were pruned as needed to prevent rope snagging, and the geometry of the setup was documented, including inter-tree distance, attachment heights on both trees, and the initial dimensional characteristics of the test tree. Each tree was typically tested along two approximately orthogonal azimuths (predominantly N–S and E–W), with N–S corresponding to the dominant regional wind direction at the site. In addition, selected tests were repeated at different attachment heights to modify the relative contributions of vertical force, horizontal force, and overturning moment transmitted to the root–soil system. During the larger-deformation uprooting tests, the inclinometers required intermittent re-leveling to maintain measurement capability as rotation increased. After reaching peak resistance, the post-peak (residual)

response was also recorded. Complete loss of resistance was not captured, as the inclinometers were removed once large rotations became visually evident.

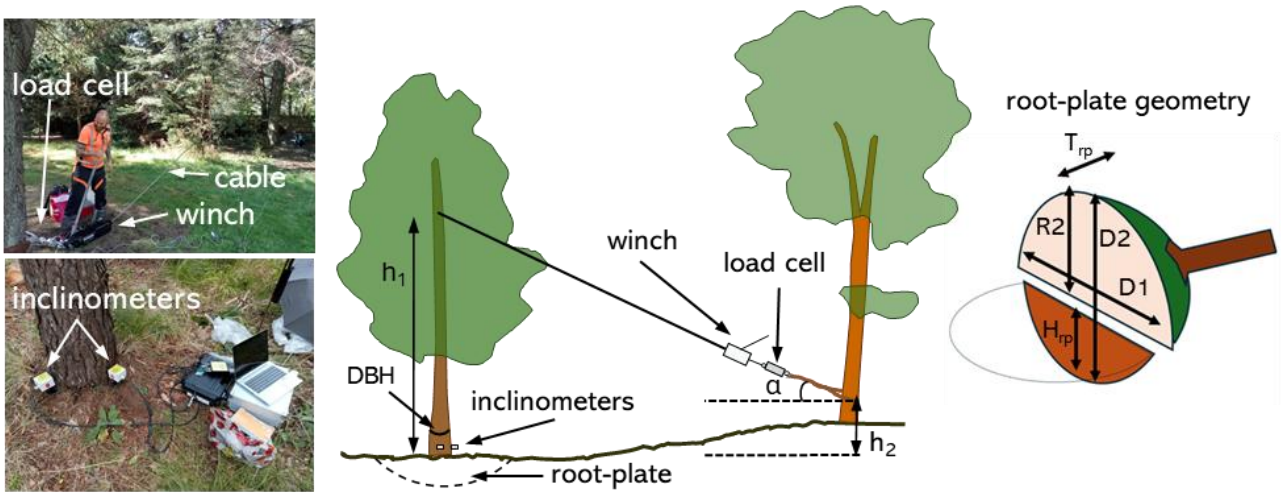

Figure 46: Setup of non-destructive and uprooting tests.

Figure 47 shows the test location and directions of pulling for the winching tests re-ported in this study. A total of 21 trees were tested, divided into conifers and deciduous species. The conifers included *Pinus nigra*, *Picea abies*, and *Tsuga*, while the deciduous species consisted of Acer platanoides, Nothofagus, Betula, Eucalyptus, and Quercus. Each tree was assigned a unique identification code (ID), codes used by curator of the Botanic Garden. Table 3 summarizes the individual tree characteristics (height, H, and diameter at breast height, DBH) and test types conducted at each location.

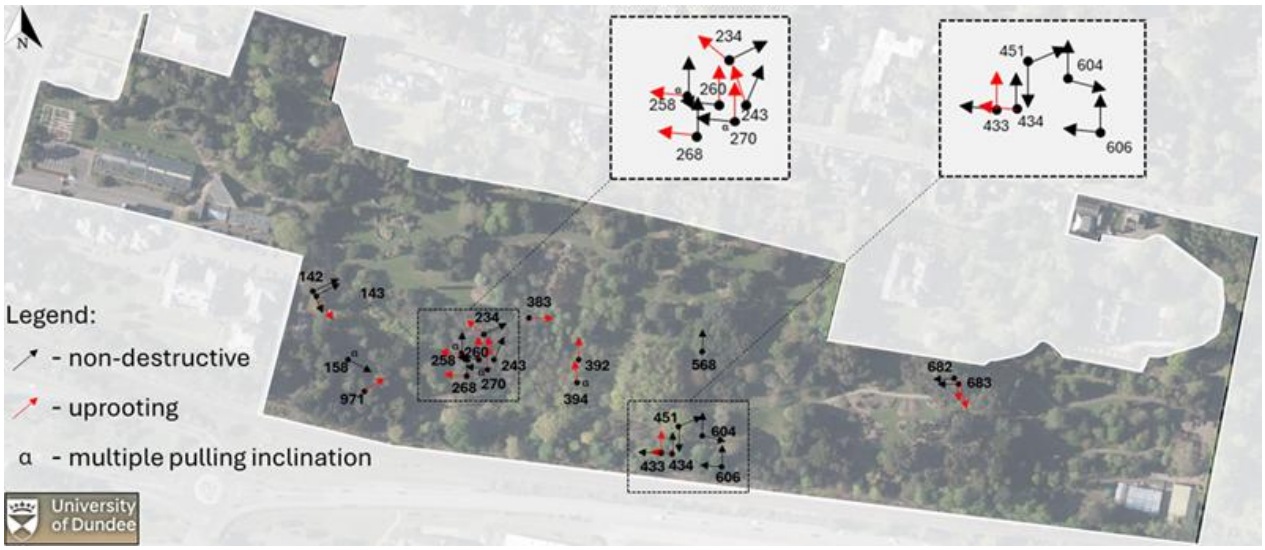

Figure 47: Summary of different pulling tests, indicating pulling directions.

Table 3: Summary of the individual tree characteristics and test types conducted at each location.

Tree ID	Zone	Ground Characterization					Test Type			Species	DBH (cm)	H (m)
		Corkscrew	Vane Test	Water Content	SWRC	PSD	Non-Destructive	Uproot	Multiple α			
433	5	x	x	x	x	x	x	x		*Acer platanoides*	23.2	13.5
434	5	x	x	x	x	x	x	x		*Acer platanoides*	27.1	13.2
260	3	x	x	x	x	x	x	x		*Pinus nigra*	37.6	16.2
268	3	x	x	x	x	x	x	x		*Pinus nigra*	44.6	16.5
568	5	x	x	x	x	x	x			*Nothofagus*	50.9	15.6
258	3					x	x	x	x	*Pinus nigra*	35.6	17.0
270	3					x	x	x	x	*Pinus nigra*	28.6	17.6
158	2						x		x	*Picea abies*	54.1	20.0
604	5						x			*Acer platanoides*	41.4	9.3
451	5	x					x			*Acer platanoides*	120.0	27.0
606	5						x			*Nothofagus*	85.0	25.0
142	1						x			*Pinus*	53.0	18.0
383	3				x		x	x		*Betula*	52.0	13.0
682	6						x	x		*Eucalyptus*	72.0	16.0
683	6		x	x	x	x	x	x		*Eucalyptus*	69.0	15.0
143	1	x	x	x	x	x	x	x		*Pinus*	51.0	17.7
234	3		x	x	x	x	x	x		*Pinus*	48.0	12.7
243	3	x	x	x	x		x	x		*Pinus*	53.0	12.3
392	4		x	x	x		x	x	x	*Quercus*	22.6	13.0
394	4	x	x	x	x		x	x	x	*Quercus*	37.0	17.0
971	2	x	x	x	x	x	x	x		*Tsuga*	78.0	12.7

Trees were initially assessed under non-destructive loading so that multiple repeat tests (typically 2–4 per tree, with only two exceptions) could be carried out on the same individual while groundwater conditions remained effectively unchanged. For a subset of trees, the in-plan pulling direction was modified while keeping the pulling angle to the horizontal (α) as close to constant as practicable, given the need to identify suitable nearby anchor trees. These repetitions were used to examine whether rotational stiffness and inferred capacity differed between the dominant wind direction and the orthogonal direction. For other trees, the plan direction was kept fixed and α was intentionally varied, either by changing the rope attachment height on the test tree (i.e., h1 in Figure 10) or by selecting an alternative anchor tree, thereby altering the horizontal span between the pulling and anchorage points.

Non-destructive winching tests are commonly employed to estimate a tree's ultimate uprooting resistance by extrapolating the measured moment–rotation response within the elastic range (up to 0.25°) using the Wessolly and Erb relationship between overturning moment (M) and stem-base rotation (θ) (Wessolly & Erb, 1998):

$$\theta = \frac{1}{3}\tan\left(1.35\frac{M}{M_L}\right) + \frac{1}{2}\left(\frac{M}{M_L}\right)^2 - \frac{1}{10}\frac{M}{M_L} \qquad \text{Eq. [14]}$$

ML is the estimated moment (overturning) capacity that was obtained by fitting Eq. [14] using a least-squares fitting procedure. Finally, fifteen of the twenty-one trees were subjected to uprooting tests after the programme of non-destructive tests was complete. The system configuration used for these tests was similar to that employed for the standard pulling test, but winching was continued until failure by uprooting. For safety reasons, the canopy was completely removed prior to the uprooting tests.

Non-destructive test results

Figure 48 shows pull test results for tree 260. The extrapolated ML and rotational stiffness KM are summarized in Table 4. In the table, the loading direction (using cardinal direction symbols) and the angle of pull to the horizontal (α) are also reported. Pull test curves of the other trees are reported in Appendix B.

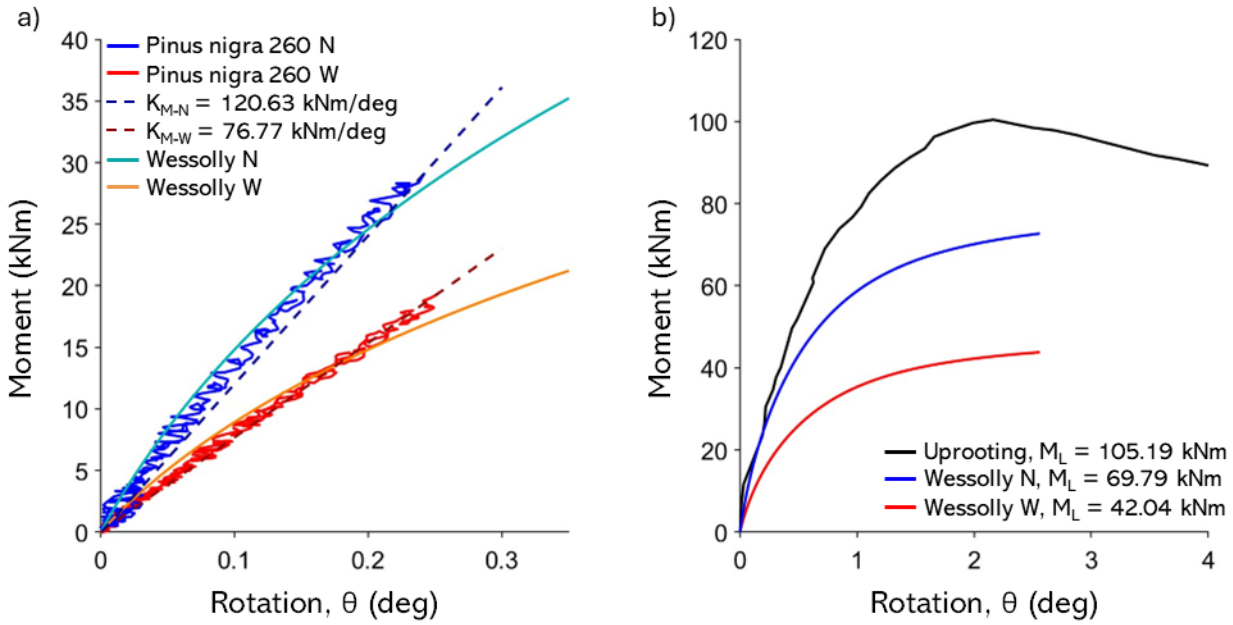

*Figure 48: **(a)** non-destructive test curves with Wessolly interpolation and stiffness (N pulling angle α = 16.6°, W pulling angle α = 17.8°); **(b)** comparison of extrapolated Wessolly curves with uprooting test (uprooting direction N pulling angle α = 16.6°).*

Table 4: Non-destructive pulling tests results. h1 and h2 are the heights, as indicated in Figure 10. KM is the stiffness, and ML is the maximum moment predicted by Equation (1). N, E, S, and W represent the cardinal directions north, east, south, and west.

Tree-ID	h_1 (m)	h_2 (m)	α (deg)	Pull Direction	K_M (kNm/deg)	M_L (Wessolly) (kNm)
433	5.9	0.0	17.6	N	53.4	31.3
	5.9	0.0	21.9	W	49.8	29.5
434	7.4	0.0	23.4	N	73.0	42.5
	7.4	0.0	21.3	W	71.7	43.4
260	6.0	0.0	16.6	N	120.6	69.8

	6.0	0.0	17.8	W	76.8	42.0
268	6.0	0.0	11.8	N	220.4	127.9
	6.0	0.0	16.3	W	212.3	125.4
568	6.5	−1.5	20.9	N	682.3	402.7
	6.5	−1.5	20.2	W	668.9	405.1
258	3.0	0.0	5.7	N	171.2	98.2
	6.0	0.0	11.3	N	150.0	89.4
	9.0	0.0	16.7	N	134.0	80.7
	6.0	0.0	16.6	W	114.6	64.6
270	6.0	0.0	12.9	N	29.7	17.6
	3.0	0.0	6.4	W	38.0	20.9
	6.0	0.0	12.6	W	30.2	18.0
	9.0	0.0	18.5	W	35.0	21.2
158	6.0	0.0	25.8	W	470.3	289.8
	9.0	0.0	36.0	W	466.22	281.3
	12.0	0.0	44.1	W	488.0	322.7
604	3.0	0.0	17.7	N	133.6	83.9
	3.0	0.0	15.2	W	104.4	61.8
451	7.9	−1.0	16.0	E	3566.5	1444.9
	7.9	0.0	26.3	S	6924.8	2864.8
606	12.0	−0.45	24.8	N	2453.8	1182.1
	12.0	0.0	25.2	W	1667.0	718.6
142	9.6	0.3	25.7	SE	298.5	185.7
	9.6	−0.4	20.2	NE	366.1	215.0
383	6.2	0.45	20.8	E	142.5	81.2
682	5.5	0.0	14.0	SE	342.9	187.1
	5.5	0.0	9.9	W	203.5	122.4
683	5.0	0.0	14.0	SE	213.5	118.6
	5.0	0.0	11.8	W	169.4	102.2
143	11.7	0.5	35.7	SE	526.0	311.3
	11.7	−0.5	24.1	NE	458.4	243.2
234	11.0	0.0	19.5	NW	135.0	75.1
	11.0	0.0	33.2	NE	152.4	82.8
243	10.0	0.0	25.5	NE	77.4	46.0
	10.0	0.5	33.2	NW	99.1	58.8
392	8.0	0.0	20.0	N	78.7	42.5
	8.0	0.0	34.8	N	89.0	46.7
	8.0	0.0	69.4	N	76.2	39.3
	4.6	0.0	11.8	N	57.8	33.7
394	4.6	0.0	10.9	N	147.1	86.8
	8.0	0.0	18.4	N	150.9	92.1
	8.0	0.0	28.1	N	149.2	97.2
	8.0	0.0	53.1	N	165.8	90.8
971	8.0	−0.85	11.6	NE	385.5	234.7

Uprooting test results

The complete set of moment–rotation responses measured during the uprooting trials is presented in Figure 49. For illustration, Figure 48b compares the experimentally observed response of tree 260 with the Wessolly curves extrapolated from non-destructive tests conducted in two different pulling directions. Key parameters from all uprooting tests are compiled in Table 3: the geometric descriptors h_1, h_2, α, and pulling direction follow the definitions introduced earlier (Figure 46), whereas M_L and θ_L (the limit rotation angle) were determined directly from the destructive test records. Post-test

measurements of the uprooted root plates are also reported. The results highlight that peak rotations range between 1.59 and 2.93 degrees.

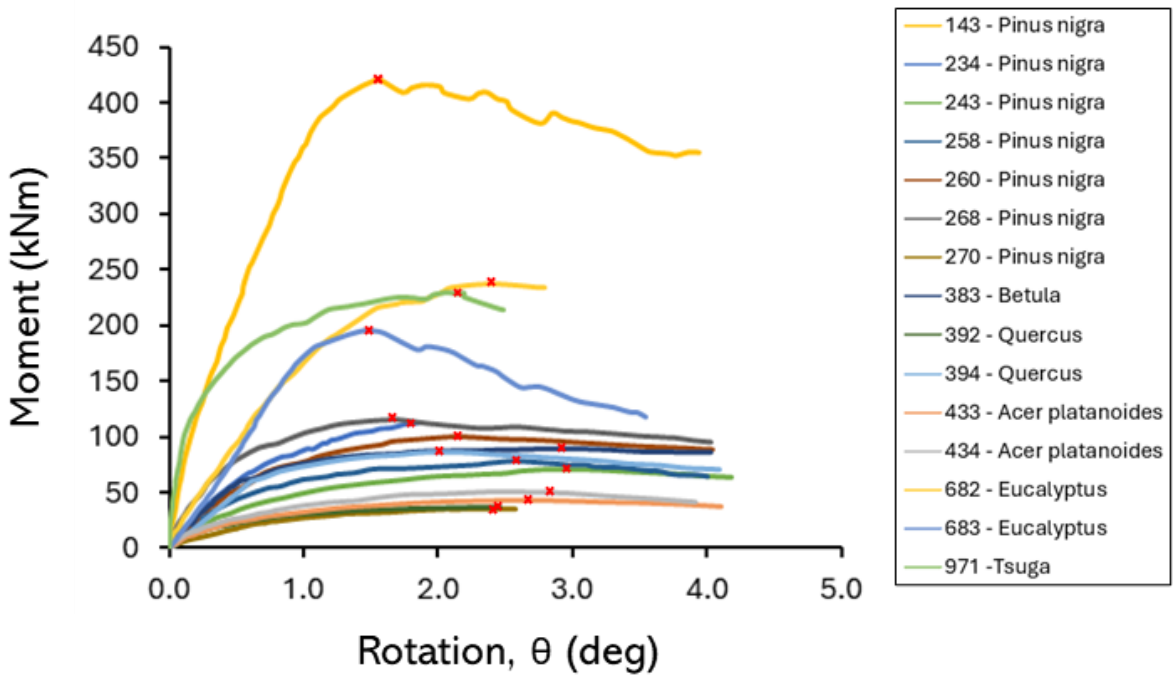

Figure 49: Summary of moment–rotation curves from uprooting tests. The red crosses indicate the peak values of the moment for each curve.

Table 5: Key data from the uprooting tests.

Tree-ID	h_1 (m)	h_2 (m)	α (deg)	Uproot Direction	K_M (kNm/deg)	M_L (kNm)	θ_L (deg)	Root-Plate Geometry				
								D_1 (m)	D_2 (m)	R_2 (m)	Hrp (m)	Trp (m)
433	5.9	0.0	17.6	N	62.4	45.5	2.61	2.4	2.6	-	0.5	-
434	7.4	0.0	22.3	W	72.6	53.5	2.93	3.0	2.7	-	0.5	-
260	6.0	0.0	16.6	N	130.0	105.2	2.15	1.3	2.0	-	0.7	-
268	6.0	0.0	16.3	W	206.6	120.0	1.59	2.6	3.0	-	0.6	-
258	6.0	0.0	16.6	W	107.2	77.3	2.61	2.2	1.4	-	0.9	-
270	6.0	0.0	12.9	N	43.7	36.5	2.40	2.0	1.5	-	0.8	-
383	6.2	0.45	20.8	E	130.8	89.0	2.90	3.0	2.3	1.5	0.7	-
682	5.5	0.0	14.0	SE	219.5	182.8	2.30	-		-	-	-
683	6.0	0.0	17.5	SE	153.1	196.0	1.80	1.6	1.1	-	1.2	1.0
143	11.7	0.5	35.7	SE	578.0	420.0	1.60	2.7	1.5	0.51	0.8	0.4
234	11.0	0.0	12.0	NW	131.5	114.0	1.85	-	-	-	-	-
243	10.0	0.0	11.0	NW	86.0	71.0	2.96	1.7	1.53	1.03	0.63	1.15
392	4.6	0.0	11.8	N	89.6	36.4	2.46	2.5	1.55	0.93	1.65	0.61
394	4.6	0.0	10.9	N	92.3	86.9	1.95	3.0	1.7	0.89	0.5	0.64
971	8.0	0.85	13.0	NE	542.5	229.0	2.20	4.54	4.57	-	0.52	0.45

Other evidences of the field test carried out at the Botanic Garde are shown in Figure 50:

Figure 50: pull test setup and evidences after uprooting tests.

Discussion about non-destructive and uprooting tests

Effect of direction of pull (in plan)

Regarding potential bias in overturning resistance along the prevailing wind axis, Table 6 summarizes results for the ten trees tested in the west and north pulling directions. Figure 51 includes a dashed parity line corresponding to a ratio of 1 between the extrapolated moments in the two directions, while the solid line marks the threshold where the north-to-west ratio reaches 2. Only three trees showed higher inferred mechanical strength when pulled towards the west. By contrast, the remaining individuals exhibited greater resistance in the north direction, with differences of up to 66%. Considering the entire dataset, anchorage capacity was, on average, 23% higher in the north direction, based on the Wessolly-derived extrapolated limit moment (M_L). This consistent directional imbalance in inferred capacity is compatible with a wind-acclimation effect, whereby the root–soil system develops relatively greater resistance along the dominant wind axis.

Table 6: Comparison between extrapolated limit moment in west (MLW) and north (MLN) directions.

Tree-ID	M_{LW} (kNm)	M_{LN} (kNm)	N/W
433	29.54	31.28	1.06
434	43.44	42.5	0.98
260	42.04	69.79	1.66
260	125.38	127.85	1.02
568	405.14	402.72	0.99
258	64.62	89.35	1.38
270	18.01	17.64	0.98
604	61.81	83.91	1.36
606	718.61	1182.13	1.65
			average = 1.23

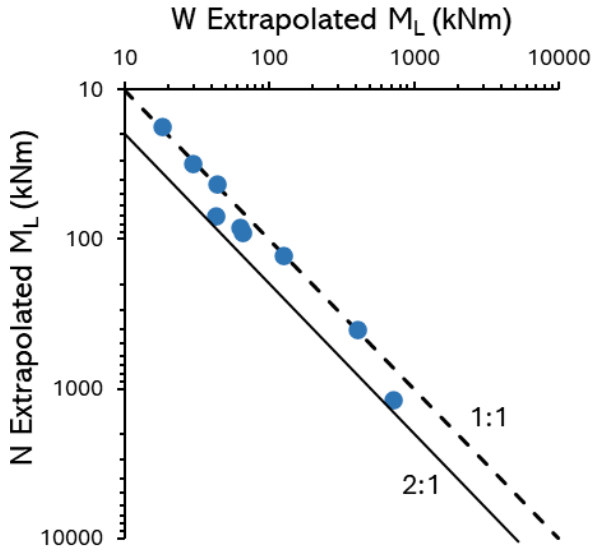

Figure 51: Effect of loading direction on extrapolated limit moment. The blue symbols represent different individual trees.

Effect of the height of pull (angle of pull in elevation)

Table 7 summarizes the results from the non-destructive tests, first conducted at different pulling heights and then after uprooting (Deq is the average of dimensions D1 and D2 of the root-plate geometry; Figure 46). Moment capacity based on extrapolated values appears to be insensitive to even very large changes in the pulling angle, as shown in Figure 52. Using a VHM yield surface approach gives the following (Dattola et al., 2020):

$$\frac{M_L}{D_{eq}V_c} = \eta\sqrt{\xi^2(1-\xi)^{2\beta} - \left(\frac{H}{\mu V_c}\right)^2} \quad \text{Eq. [15]}$$

where the normalized vertical load (ξ) is given by:

$$\xi = \frac{\frac{V}{V_c} - \left(\frac{V_t}{V_c}\right)}{1 - \left(\frac{V_t}{V_c}\right)} \quad \text{Eq. [16]}$$

and η = 3, β = 0.95, μ = 150, and Vt/Vc = −0.12. Substituting the VHM stress path for a winching test (Zhang et al., 2023), which is defined by:

$$\frac{H}{\mu V_c} = \frac{1}{\mu\, tan\theta_F}\left(\frac{V}{V_c}\right) \quad \text{Eq. [17]}$$

$$\frac{M}{D_{eq}V_c} = \frac{L\, cos\theta_F}{D_{eq}}\left(\frac{V}{V_c}\right) \quad \text{Eq. [18]}$$

it can be shown that the moment capacity (M_L) is insensitive to alpha. For trees 258 and 270, the maximum difference between the extrapolated M_L values and the mean value are 10% and 5%, respectively, despite the maximum tested angle being approximately three times the minimum. For tree 392, the maximum difference between the extrapolated M values and the mean value is 17%, with the maximum tested angle being approximately five times the minimum. For tree 394, the maximum difference between the extrapolated M values and the mean value is 5%, with the maximum tested angle being approximately five times the minimum. The small differences in the extrapolated moment are consistent with the analytical insensitivity to alpha. Additional data from a

large database of uprooting tests from (Nicoll et al., 2006), which is also shown in Figure 52, also shows no clear trend between α and measured M_L.

Table 7: Comparison of extrapolated limit moments for different pull angles with measured limit moments from uprooting tests.

	Non-Destructive		Uprooting	
Tree-ID	***α* (deg)**	***M_L* (kNm)**	***M_L* (kNm)**	***D*eq (m)**
258	5.7	98.24	-	-
	11.3	89.35	-	-
	16.6	80.73	77.26	1.8
270	6.4	20.87	-	-
	12.9	18.01	36.50	1.75
	18.5	21.15	-	-
392	19.9	42.47	-	-
	34.8	46.76	-	-
	69.4	39.28	-	-
	11.8	33.65	36.40	2.01
394	10.9	86.82	86.90	2.36
	18.4	92.11	-	-
	28.1	97.19	-	-
	53.1	90.77	-	-

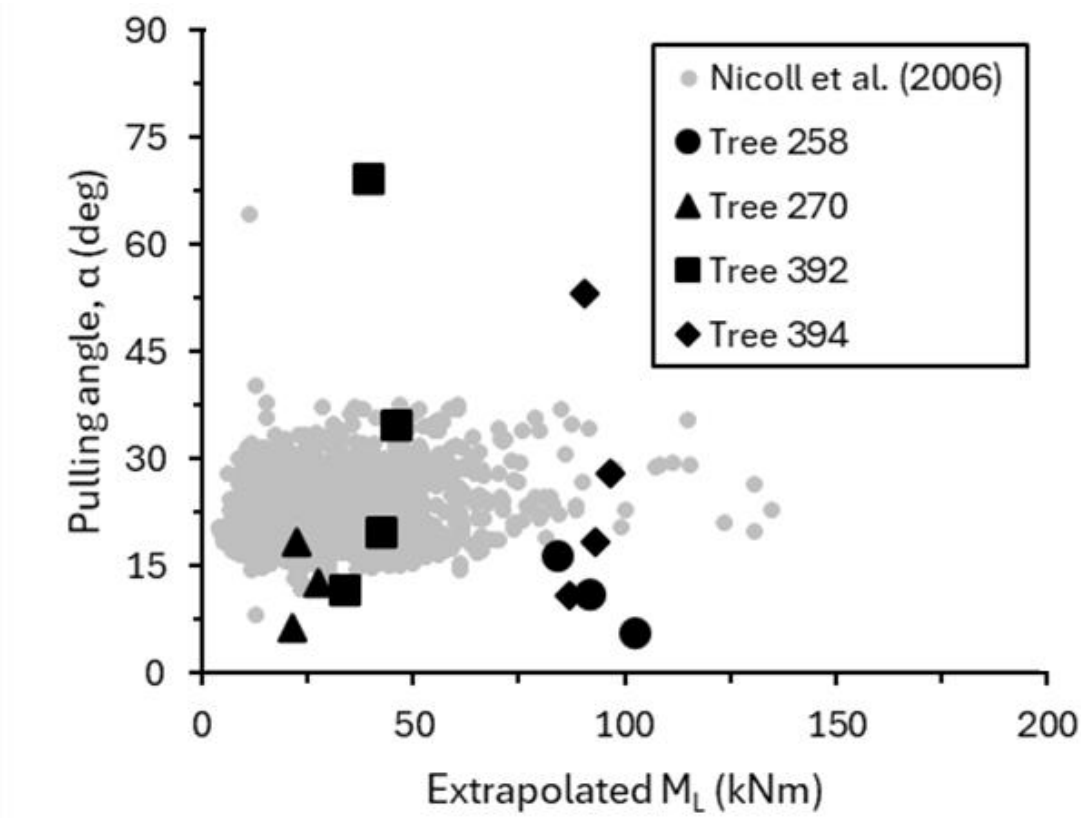

Figure 52: Insensitivity of extrapolated limit moment to pulling angle (α). Data from a large UK uprooting test database [29] shown for context

Suitability of extrapolation method for non-destructive test

In the destructive tests, peak bending moments were observed between 1.6 and 2.9° of rotation, which aligns reasonably well with the predictions of the Wessolly and Erb model (Eq. [14]). For 9 out of 15 trees, the percentage difference between the observed and estimated moment is within 20% (6 below 10% and 3 between 10%–20%). For the remaining six trees, the percentage difference ranges from 35% up to a maximum of 107% (in the case of Pinus nigra 270). Only for 4 out of 15 trees was the predicted overturning moment capacity overestimated compared to the measured value with a maximum percentage difference of 4%. An alternative stiffness-based approach to determining capacity from non-destructive test data is based on the fact that for rotations from 0 to 0.25 degrees, the response falls within the elastic range, and therefore the moment–rotation curve can be approximated by a straight line. According to the Wessolly and Erb model, a rotation of 0.25° corresponds to 40% of the maximum moment, and thus the law is as follows:

$$M_L = \frac{M(0.25°)}{0.4} = 2.5 \times M(0.25°) \qquad \text{Eq. [19]}$$

It is noteworthy that for 11 out of 15 trees, the maximum overturning moment underestimated by either Eq. [14] or Eq. [19] represents an inherent safety factor. This finding supports the general applicability of both the moment-based and stiffness-based approaches for estimating tree anchorage capacity (Figure 53a), at least for the soil and groundwater conditions considered herein. The variability in the value of rotation when peak moment is reached can, in part, be explained by local soil conditions; for instance, (Zhang et al., 2023) demonstrated that soil saturation levels significantly influence rotational behaviour during winching tests, a parameter that is typically not recorded during field assessments. Water content and suction data for the different zones considered at the Botanic Gardens that is shown in the Appendix A demonstrates local variation in groundwater conditions between zones. Alternative prediction approaches which do not utilize non-destructive test data, such as the root-plate model proposed by (Achim & Nicoll, 2009), capture the general trend observed in the (Nicoll et al., 2006) dataset, albeit with considerable scatter (Figure 53b). However, when applied to the Botanical Garden dataset, the fit appears less satisfactory, especially when using the formulation where resistance is proportional to the square of the equivalent root-plate diameter (D_eq^2). This discrepancy suggests that factors beyond root-plate weight may influence anchorage capacity. In particular, it is plausible that structural roots extending beyond the conventional root-plate contribute additional resistance, which is not adequately accounted for in simplified geometric

models. It also demonstrates that there is additional value in conducting non-destructive tests to obtain improved predictions of capacity and therefore better estimates of risk.

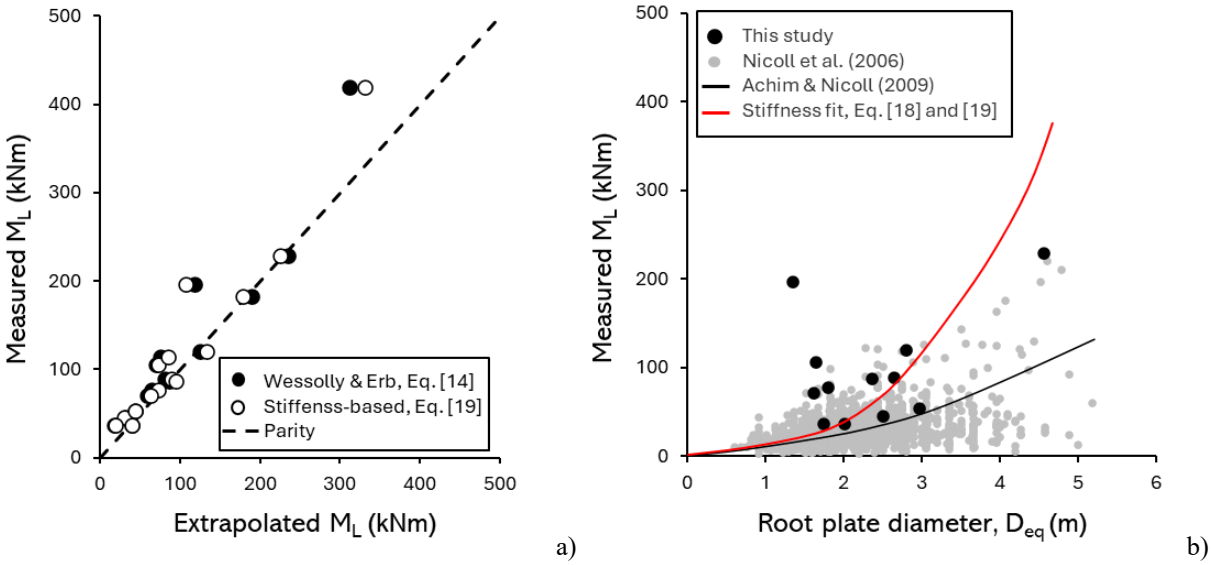

Figure 53: (a) Comparison between measured limit moment and extrapolated values using the Wessolly and Erb method and a stiffness-based approach; (b) effect of measured root-plate diameter on measured limit moment. Data (grey dots) from a large UK uprooting test database (Nicoll et al., 2006) shown for con-text and model fitting by (Achim & Nicoll, 2009).

Applying the circular footing model to the Botanic Garden dataset (Figure 54), the interpolation appears less satisfactory. This suggests that the stiffness of the model may be proportional to the cube of the root-plate diameter and possibly less than the square, as assumed in the model by (Achim & Nicoll, 2009).

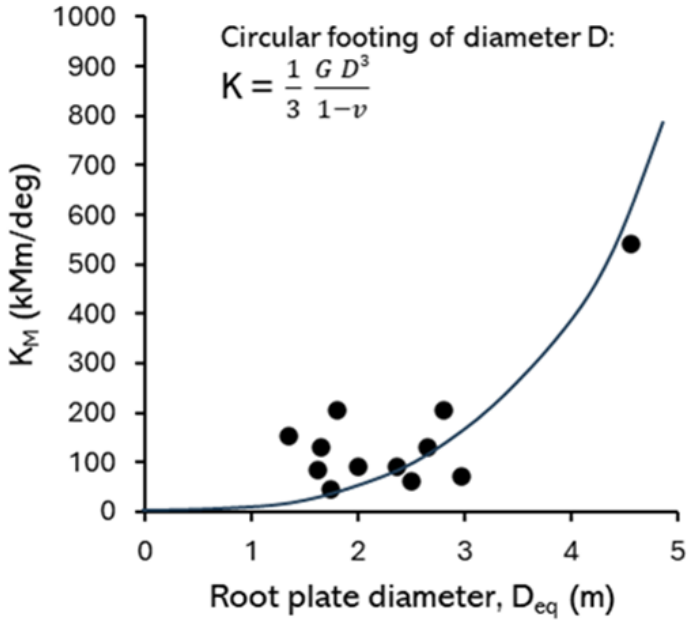

Figure 54: Effect of measured root-plate diameter on measured stiffness from uprooting tests and comparison to an equivalent circular footing of diameter Deq (v is Poisson's number).

Conclusion

In this work, static pulling tests were conducted to study the stability of mature trees. Specifically, non-destructive tests were performed, varying both the pulling directions and angles, as well as uprooting tests. Soil characteristics, such as shear strength, moisture content, suction, and particle size distribution, were analyzed to evaluate their influence on root anchorage. The tests were conducted on twenty-one trees from the Botanic Garden of Dundee University, belonging to eight different species (*Pinus nigra*, *Picea abies*, *Tsuga*, *Betula*, *Quercus*, *Acer platanoides*, *Nothofagus*, *Eucalyptus*). Fifteen out of twenty-one trees were uprooted to determine the maximum overturning moment and compare it with the values estimated using the cited methods. The data collected and analyzed indicate the following:

- As depth increases, the shear strength of the soil decreases. This is not due to an increased level of saturation, as the water content also decreases in depth (the soil is under-drained by the sandstone). The most plausible explanation is that the soil layer contains the root system.
- Peak moments in destructive tests were observed between 1.59° to 2.93°. This confirms the need for destructive testing so that the ultimate limit state is verified.
- Regarding bias in overturning resistance in the predominant wind direction, among the 10 trees tested along the north (main wind direction) and west directions, for 7 of them, the predicted overturning moment was higher in the north direction compared to the west.
- Regarding the insensitivity of moment capacity to pull angle, the moment capacity appears unaffected by substantial changes in the pulling angle.
- Regarding the evaluation of existing methods for predicting overturning moment, only 4 out of 15 trees had their predicted overturning moment overestimated compared to the experimental values. For the remaining 11 trees, the maximum overturning moment underestimated by both models provides a safety margin. These results appear to support the general applicability of both the moment-based and stiffness-based approaches for estimating tree anchorage capacity.
- Attempting to fit the data using the root-plate model, which assumes that the ultimate overturning resistance is proportional to the square of the root-plate diameter, did not yield satisfactory results. In contrast, a reasonable fit was obtained using the circular foundation root-plate model, where the stiffness is assumed to be proportional to the cube of the root-plate diameter.
- In conclusion, there is no correlation between the maximum overturning moment for uprooting and trees of the same species with similar biometric parameters. This suggests that

overturning stability depends much more on the site-specific conditions of each individual tree.

Appendix B

Below are the figures summarizing the results of the non-destructive and uprooting tests, as done for *Pinus nigra* 260 in Figure 48.

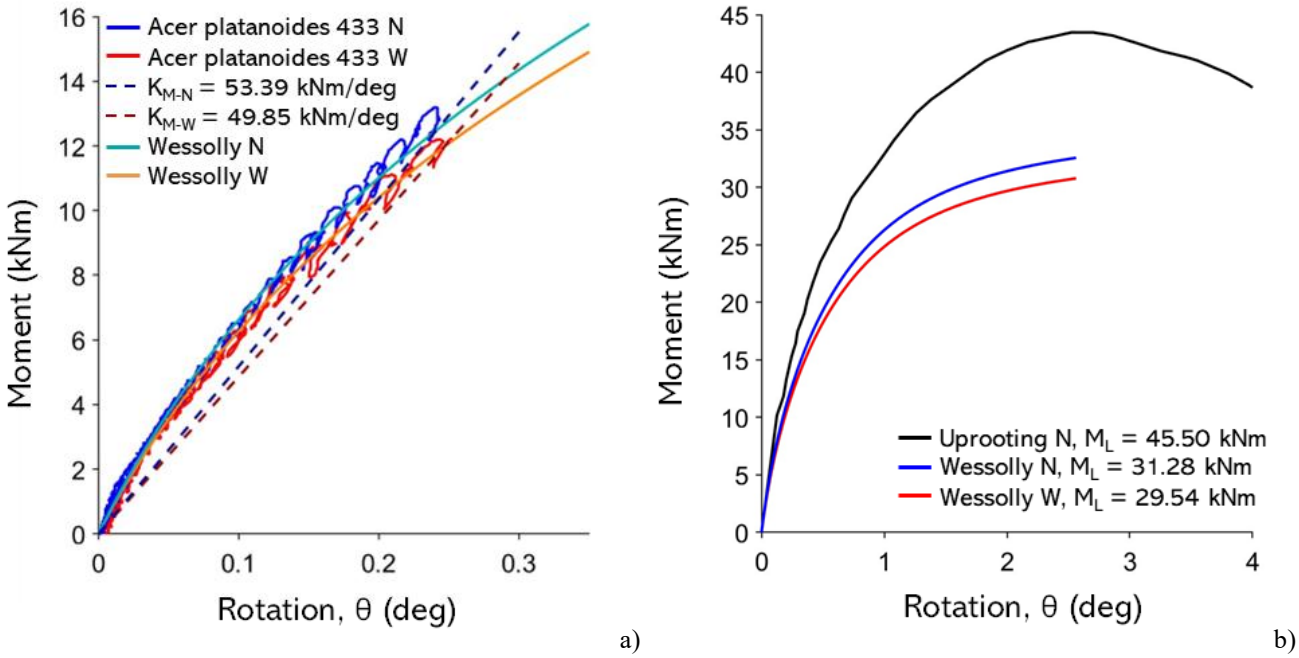

Figure A9: (a) non-destructive test curves with Wessolly interpolation and stiffness (N pulling angle α = 17.6°, W pulling angle α = 21.9°); (b) comparison of extrapolated Wessolly curves with uprooting test (uprooting direction N pulling angle α = 17.6°).

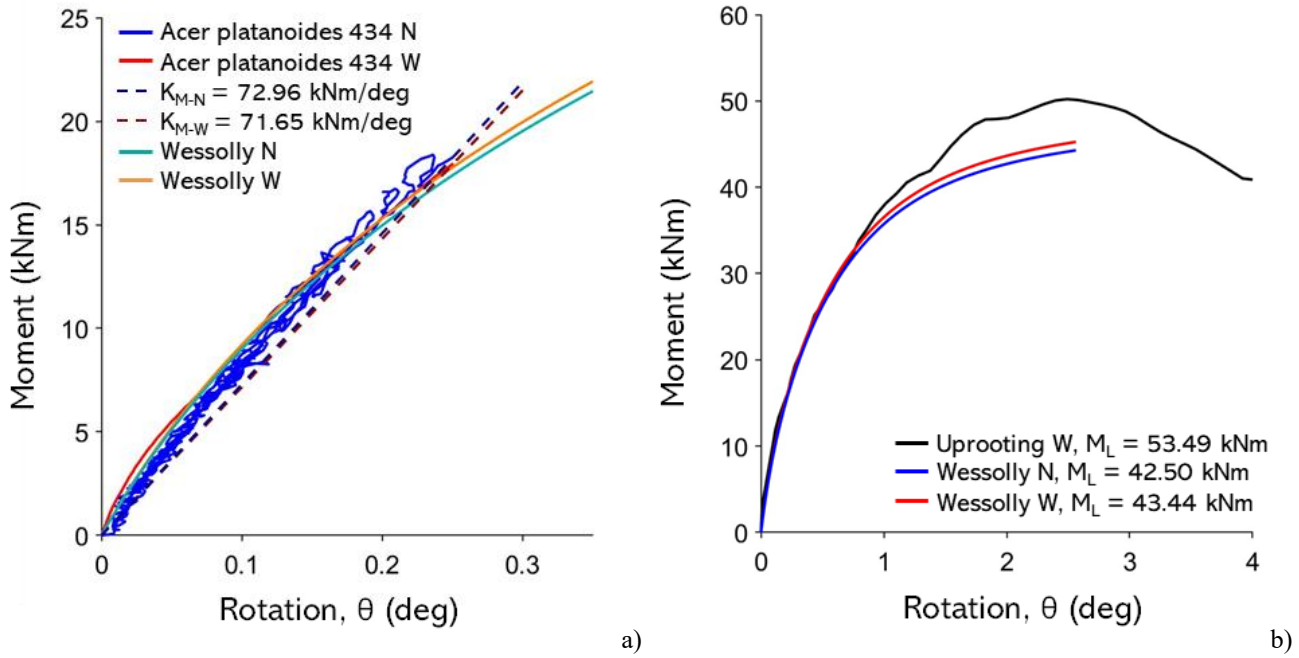

Figure A10: (a) Non-destructive test curves with Wessolly interpolation and stiffness (N pulling angle α = 23.4°, W pulling angle α = 21.3°); (b) comparison of extrapolated Wessolly curves with uprooting test (uprooting direction W pulling angle α = 21.3°).

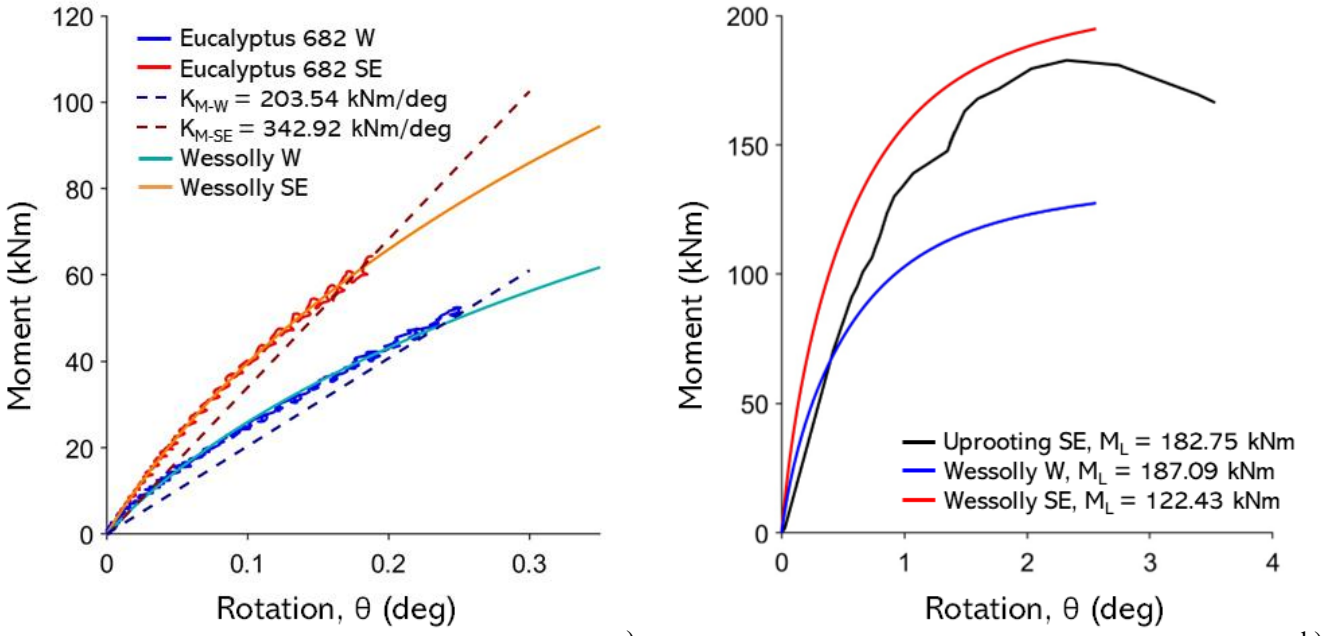

a) b)

Figure A11: (a) Non-destructive test curves with Wessolly interpolation and stiffness (SE pulling angle α = 14.0°, W pulling angle α = 9.9°); (b) comparison of extrapolated Wessolly curves with uprooting test (uprooting direction SE pulling angle α = 14.0°).

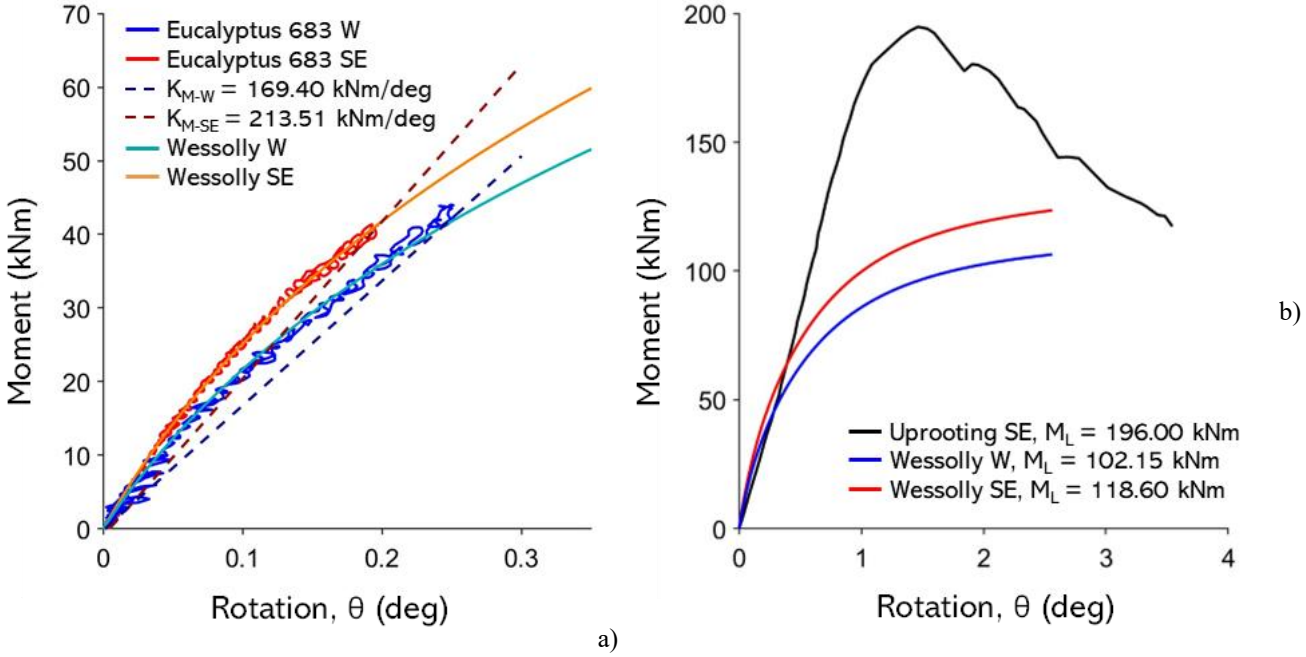

a) b)

Figure A12: (a) Non-destructive test curves with Wessolly interpolation and stiffness (SE pulling angle α = 14.0°, W pulling angle α = 11.8°); (b) comparison of extrapolated Wessolly curves with uprooting test (uprooting direction SE pulling angle α = 14.0°).

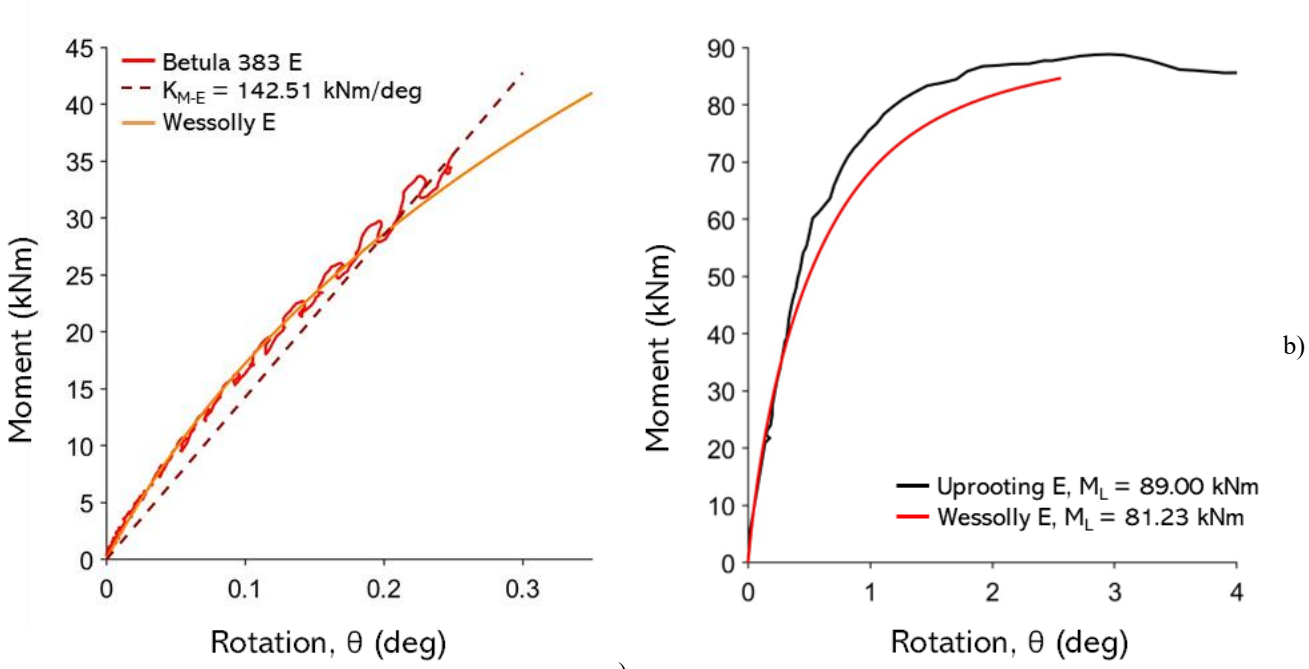

a) b)

Figure A13: (a) Non-destructive test curves with Wessolly interpolation and stiffness (E pulling angle α = 20.8°; (b) comparison of extrapolated Wessolly curves with uprooting test (uprooting direction E pulling angle α = 20.8°).

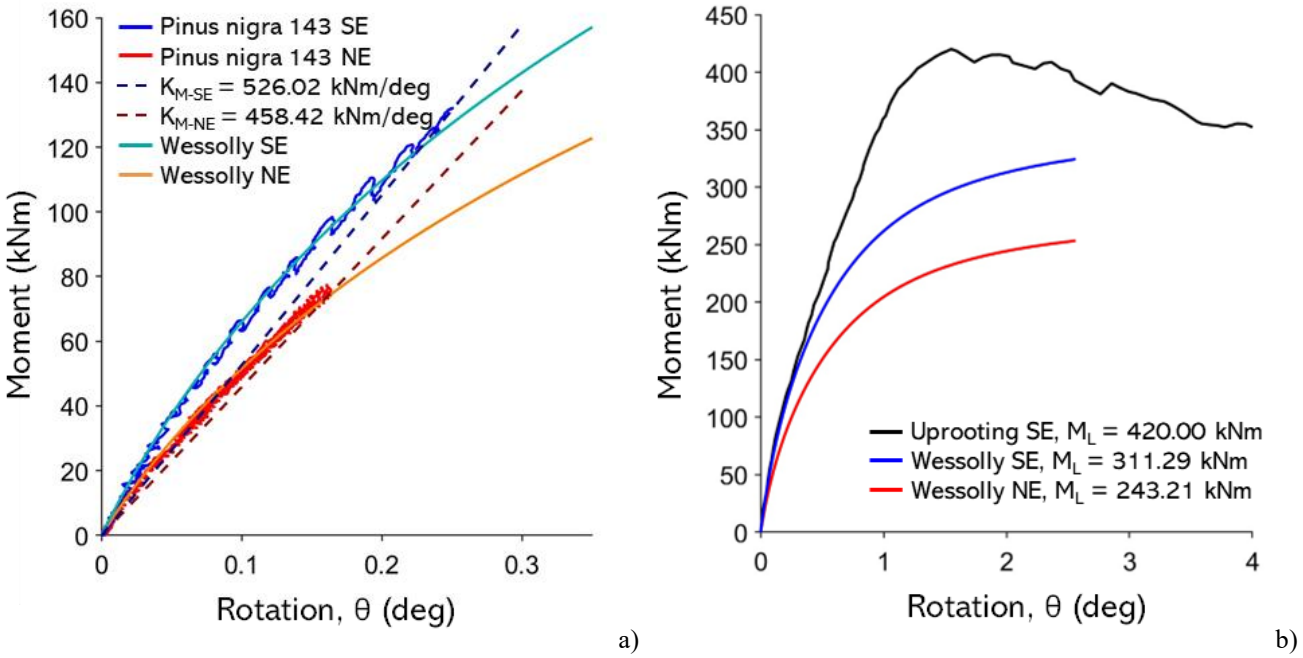

a) b)

Figure A 14: (a) Non-destructive test curves with Wessolly interpolation and stiffness (SE pulling angle α = 35.7°, NE pulling angle α = 24.1°); (b) comparison of extrapolated Wessolly curves with uprooting test (uprooting direction SE pulling angle α = 35.7°).

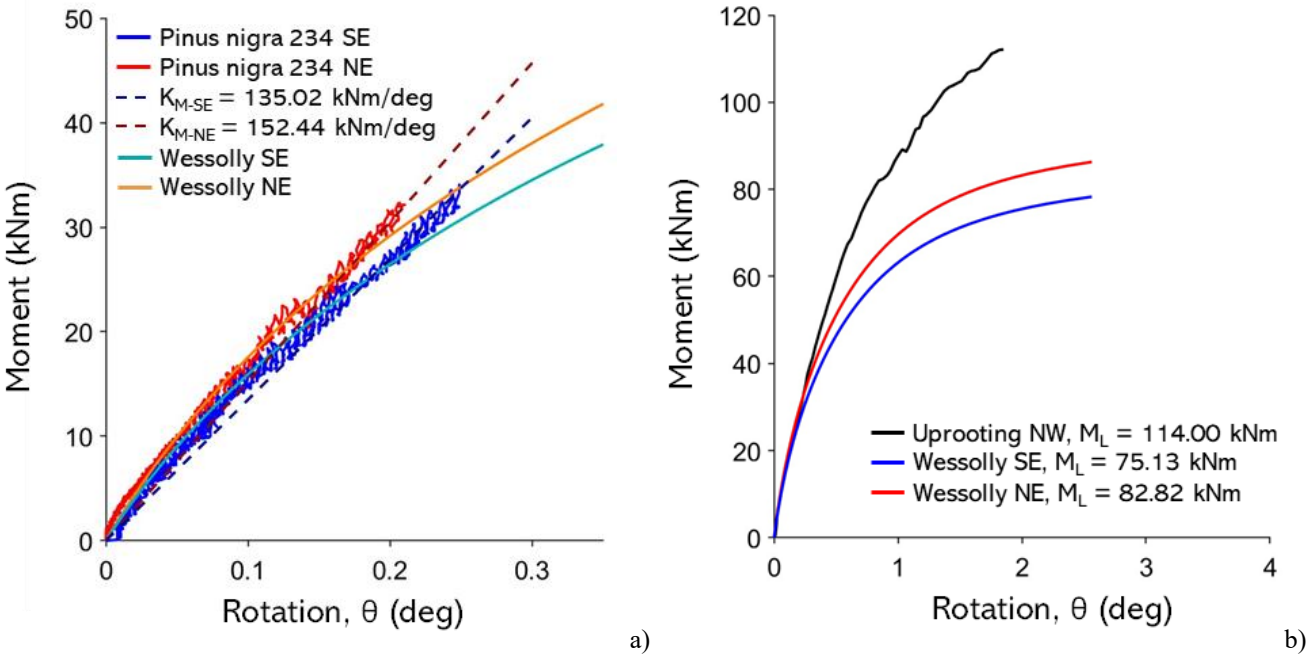

Figure A15: (a) Non-destructive test curves with Wessolly interpolation and stiffness (NW pulling angle α = 19.5°, SE pulling angle α = 33.2°); (b) comparison of extrapolated Wessolly curves with uprooting test (uprooting direction NW pulling angle α = 33.2°).

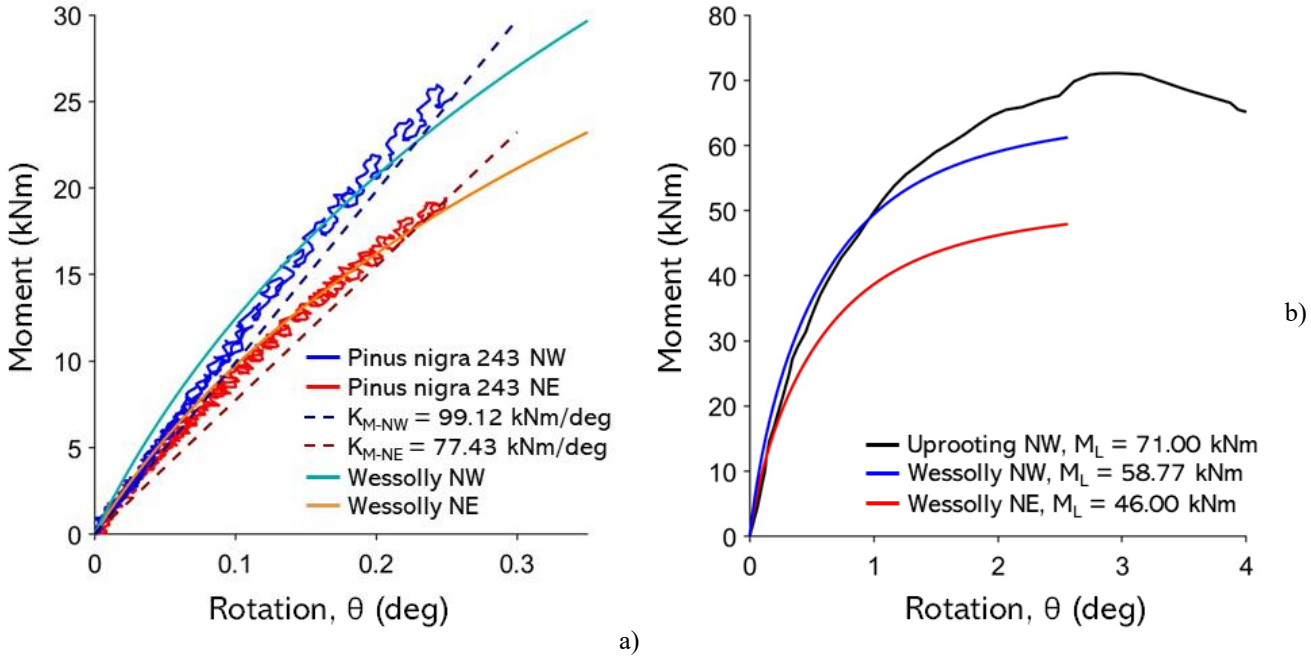

Figure A16: (a) Non-destructive test curves with Wessolly interpolation and stiffness (NW pulling angle α = 33.2°, NE pulling angle α = 25.5°); (b) comparison of extrapolated Wessolly curves with uprooting test (uprooting direction NW pulling angle α = 33.2°).

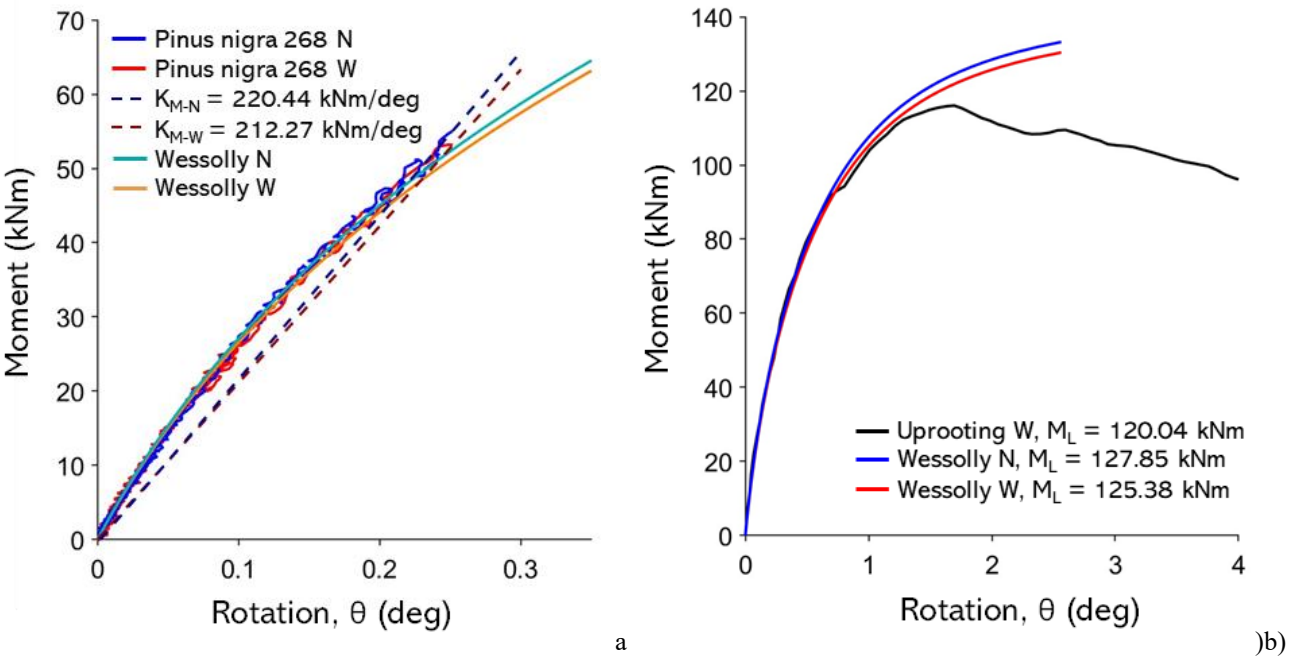

a)b)

Figure A17: (a) Non-destructive test curves with Wessolly interpolation and stiffness (N pulling angle α = 11.8°, W pulling angle α = 16.3°); (b) comparison of extrapolated Wessolly curves with uprooting test (uprooting direction W pulling angle α = 16.3°).

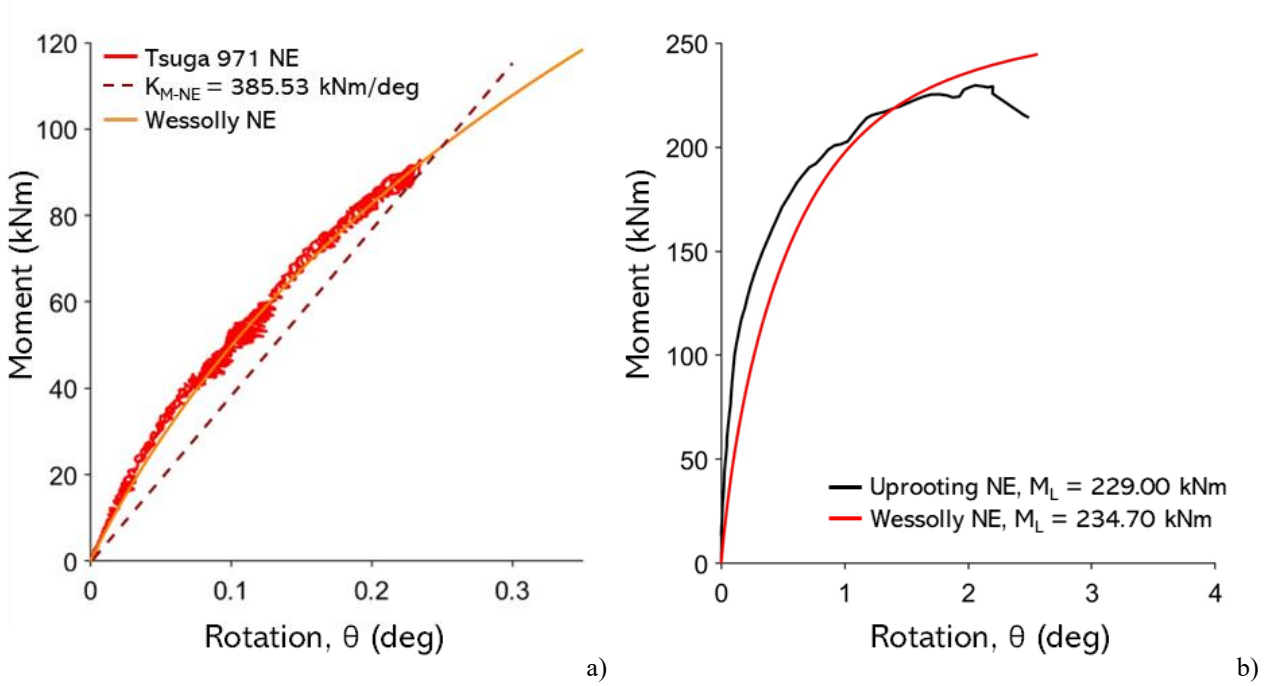

a) b)

Figure A18: (a) Non-destructive test curves with Wessolly interpolation and stiffness (NE pulling angle α = 11.6°; (b) comparison of extrapolated Wessolly curves with uprooting test (uprooting direction NE pulling angle α = 11.6°).

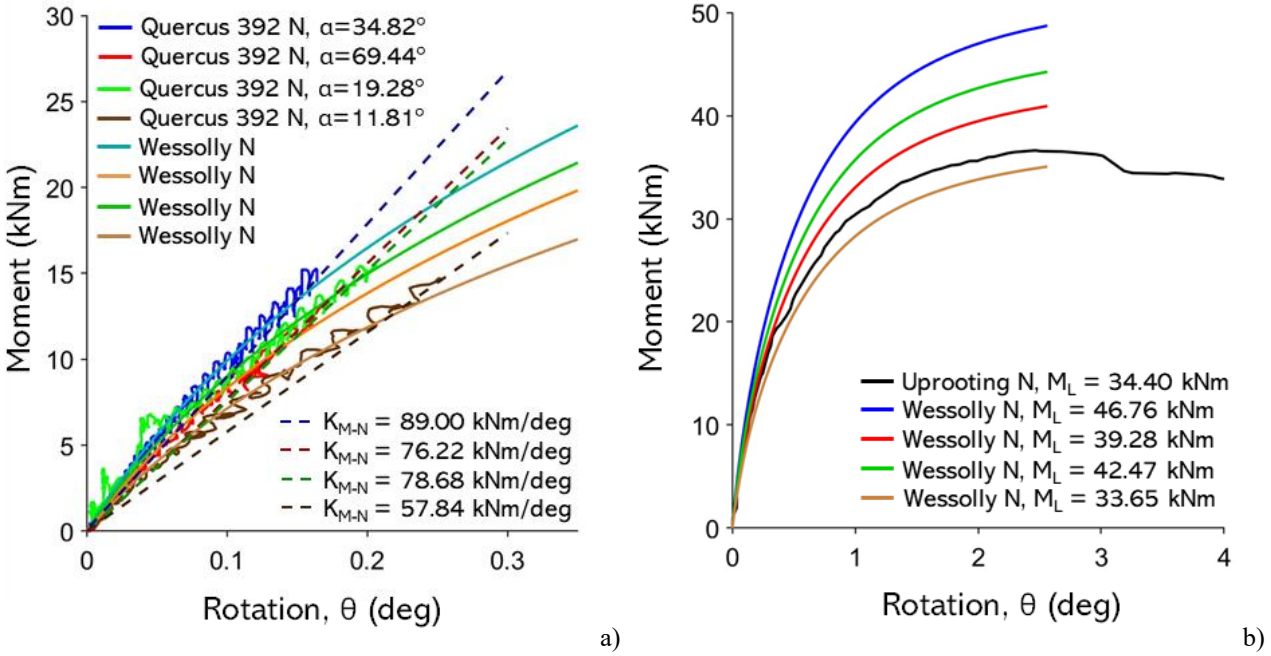

Figure A19: (a) Non-destructive test curves with Wessolly interpolation and stiffness; (b) comparison of extrapolated Wessolly curves with uprooting test, uprooting direction N pulling angle 69.4°.

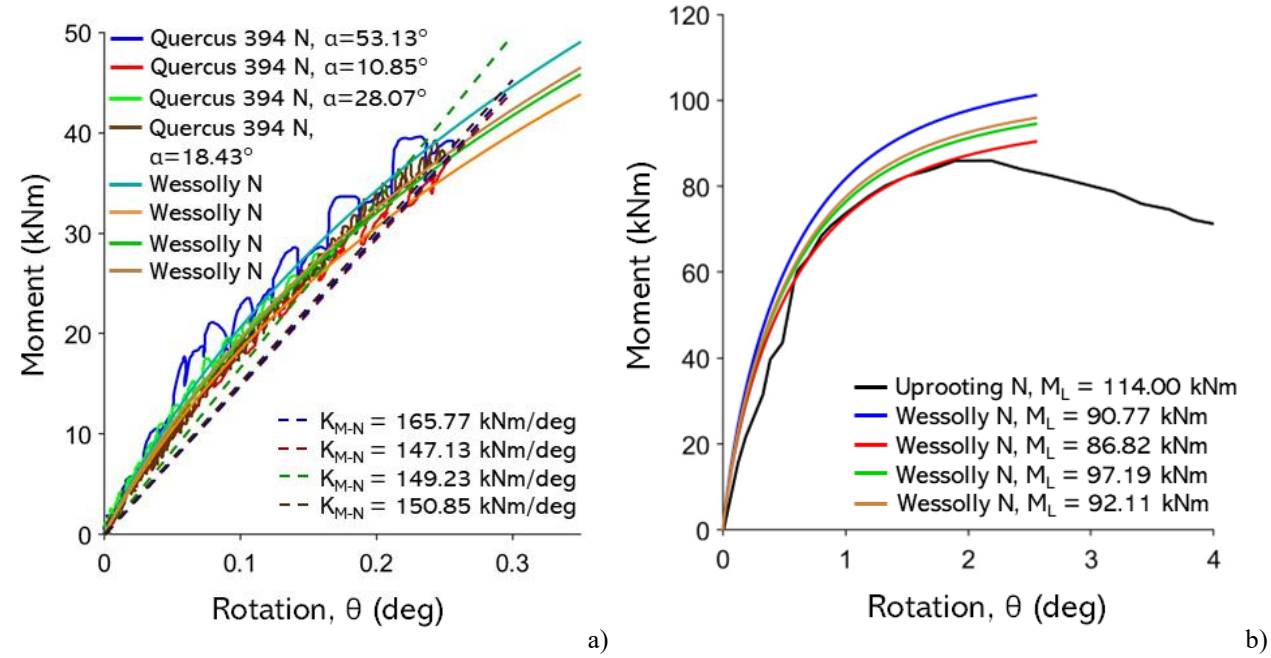

Figure A20: (a) Non-destructive test curves with Wessolly interpolation and stiffness; (b) comparison of extrapolated Wessolly curves with uprooting test, uprooting direction N pulling angle 10.9°.

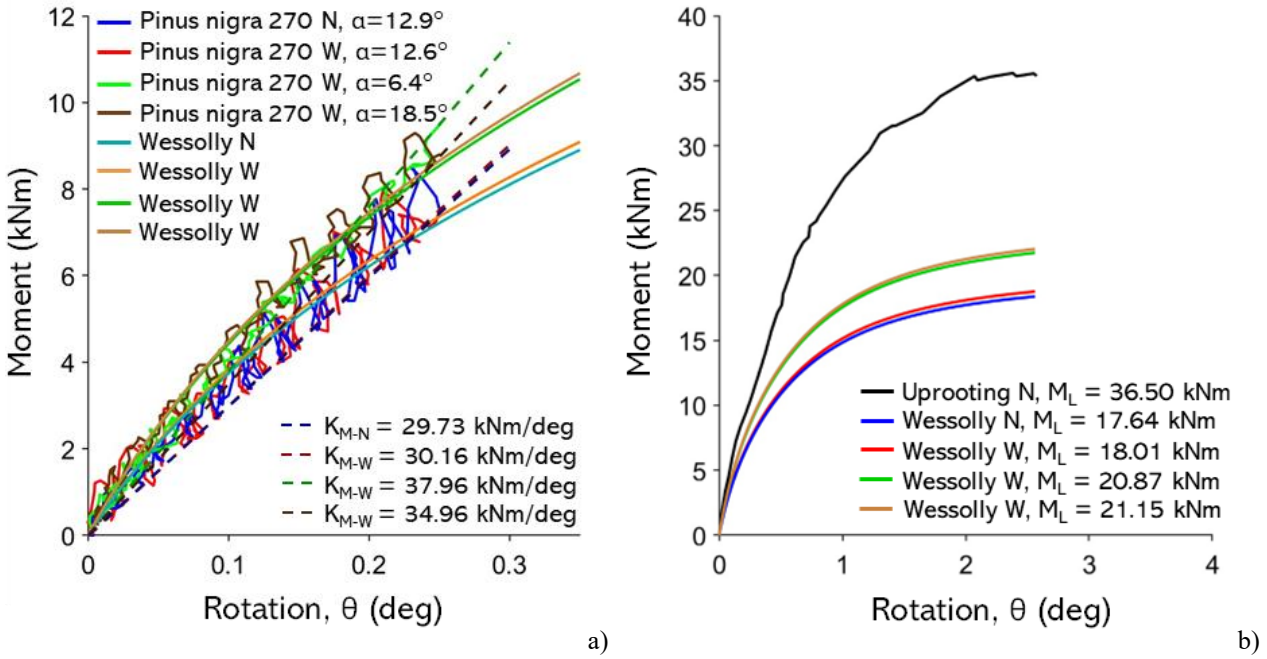

Figure A21: (a) Non-destructive test curves with Wessolly interpolation and stiffness; (b) comparison of extrapolated Wessolly curves with uprooting test, uprooting direction N pulling angle 12.9°.

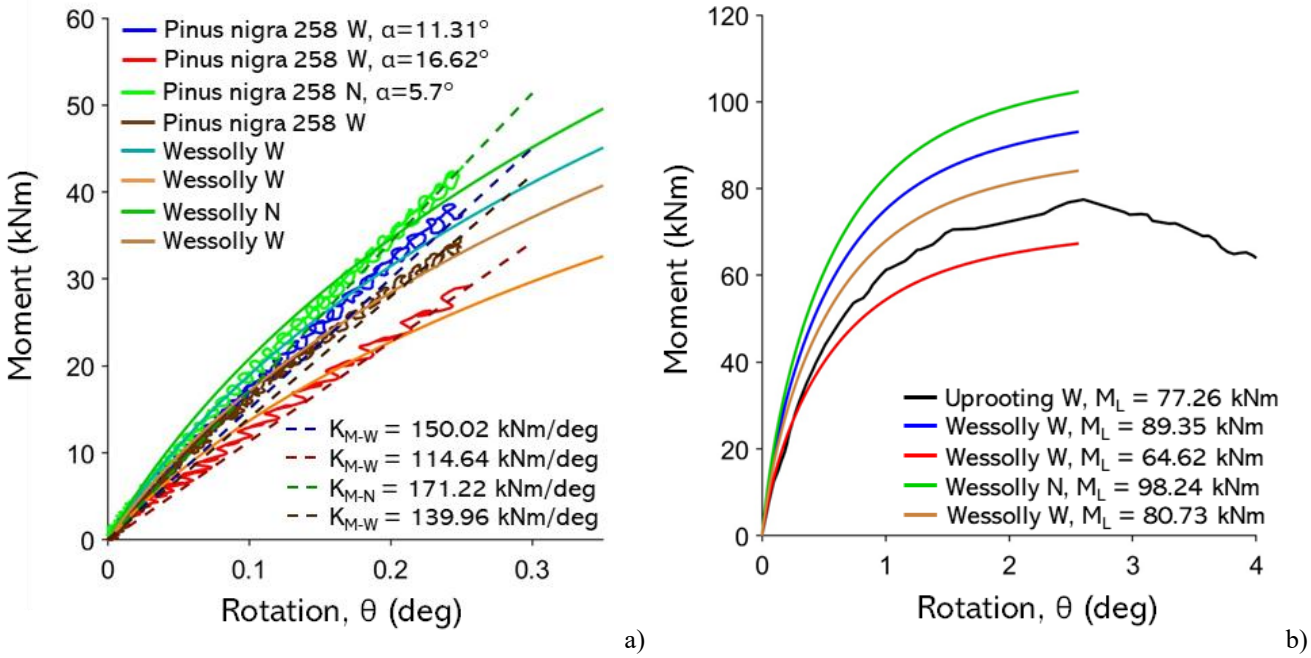

Figure A22: (a) Non-destructive test curves with Wessolly interpolation and stiffness; (b) comparison of extrapolated Wessolly curves with uprooting test, uprooting direction N pulling angle 16.6°.

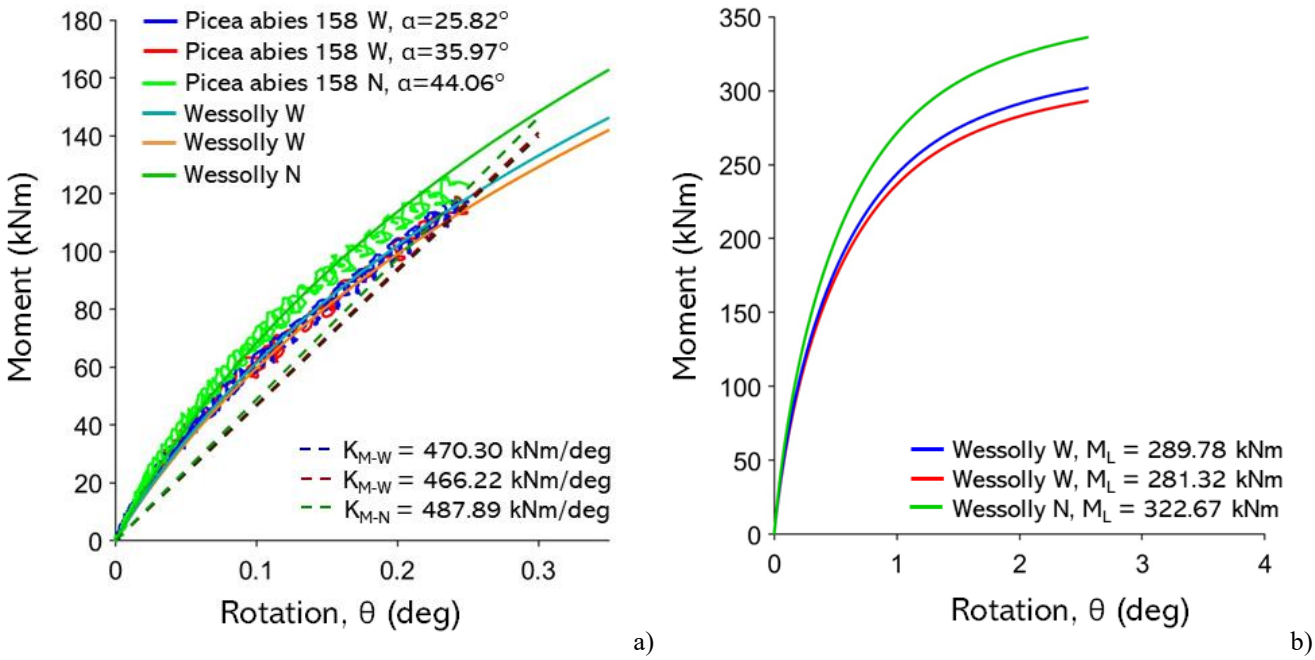

Figure A23: (a) Non-destructive test curves with Wessolly interpolation and stiffness; (b) comparison of extrapolated Wessolly curves with uprooting test.

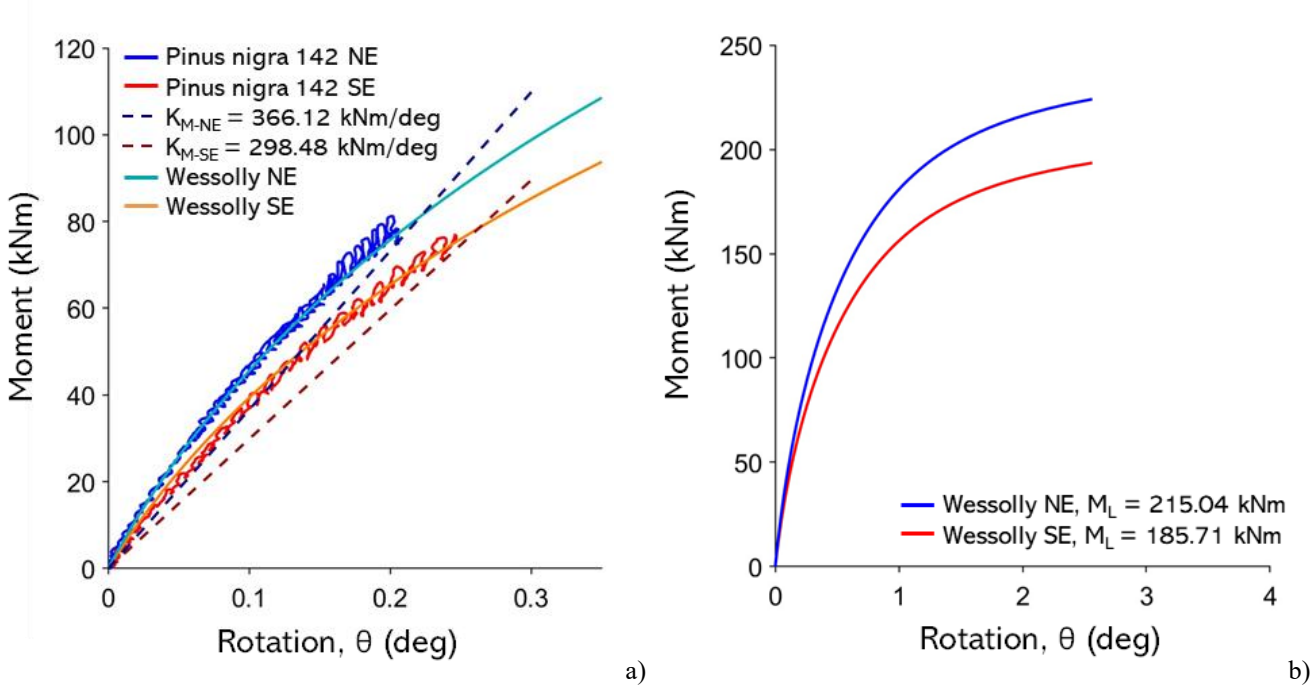

Figure A24: (a) Non-destructive test curves with Wessolly interpolation and stiffness (NE pulling angle α = 20.2°, SE pulling angle α = 25.7°); (b) comparison of extrapolated Wessolly curves with uprooting test.

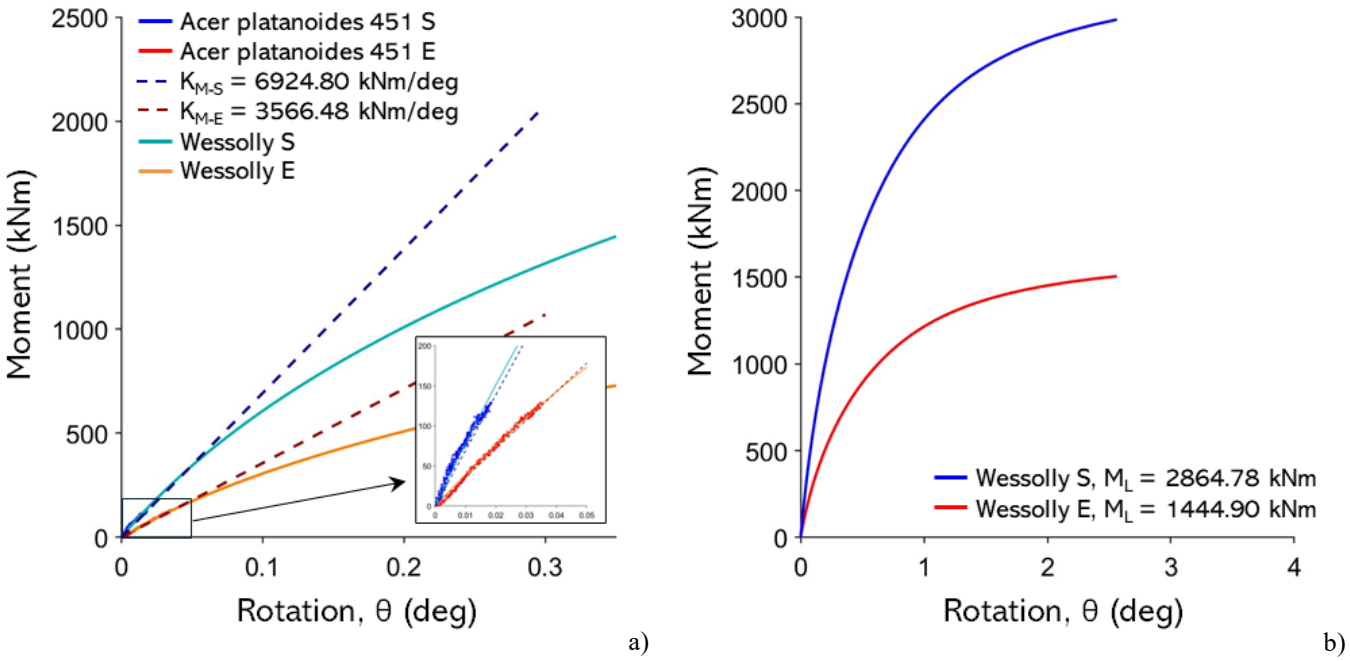

Figure A25: (a) Non-destructive test curves with Wessolly interpolation and stiffness (E pulling angle α = 16.0°, S pulling angle α = 26.3°); (b) comparison of extrapolated Wessolly curves with uprooting test.

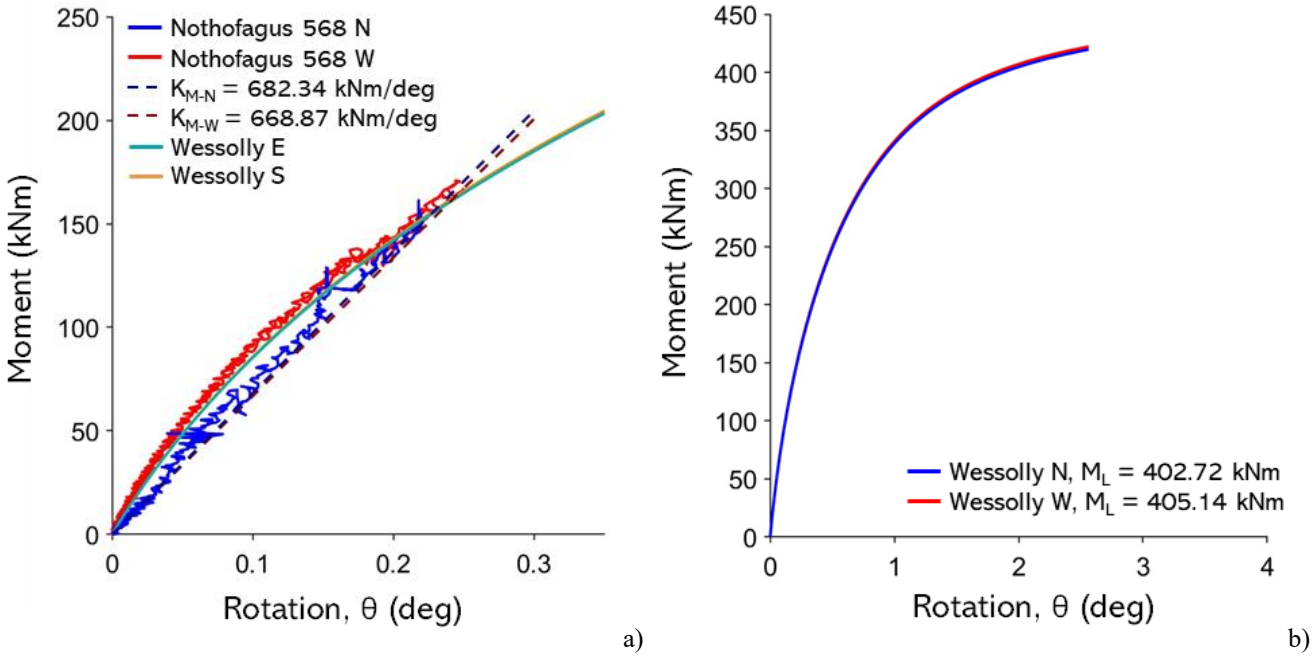

Figure A26: (a) Non-destructive test curves with Wessolly interpolation and stiffness (N pulling angle α = 20.9°, W pulling angle α = 20.2°); (b) comparison of extrapolated Wessolly curves with uprooting test.

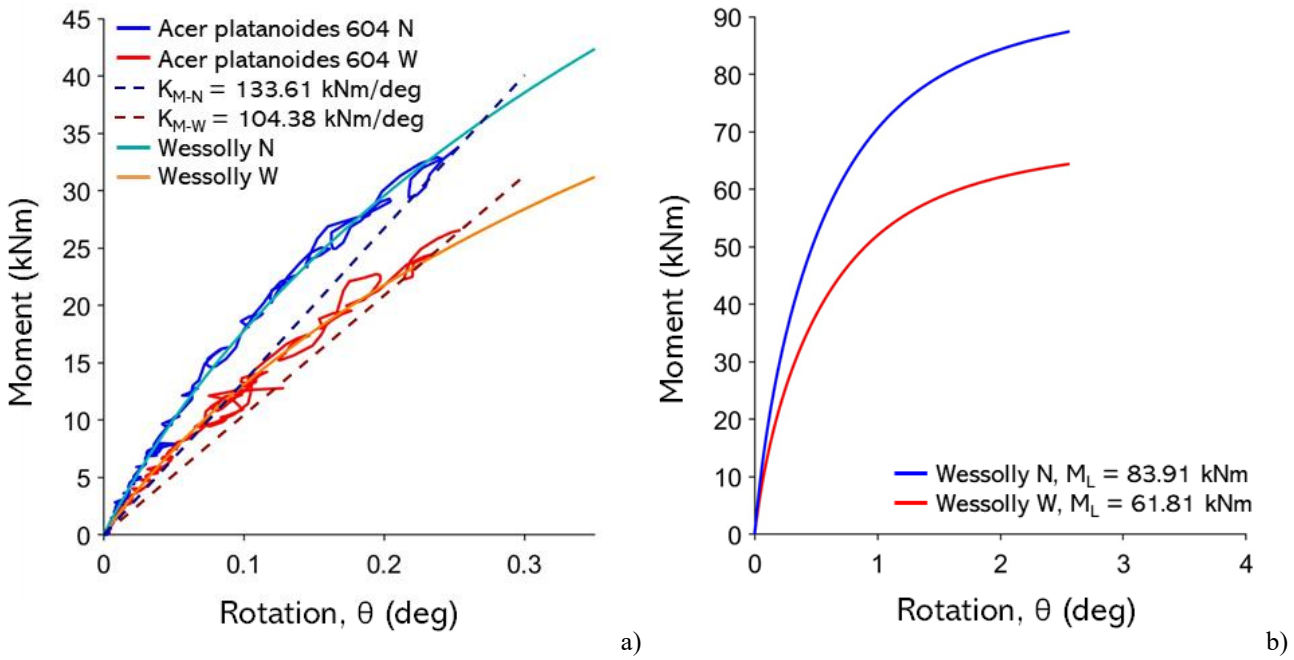

a) b)

Figure A27: (a) Non-destructive test curves with Wessolly interpolation and stiffness (N pulling angle α = 17.7°, W pulling angle α = 15.2°); (b) comparison of extrapolated Wessolly curves with uprooting test.

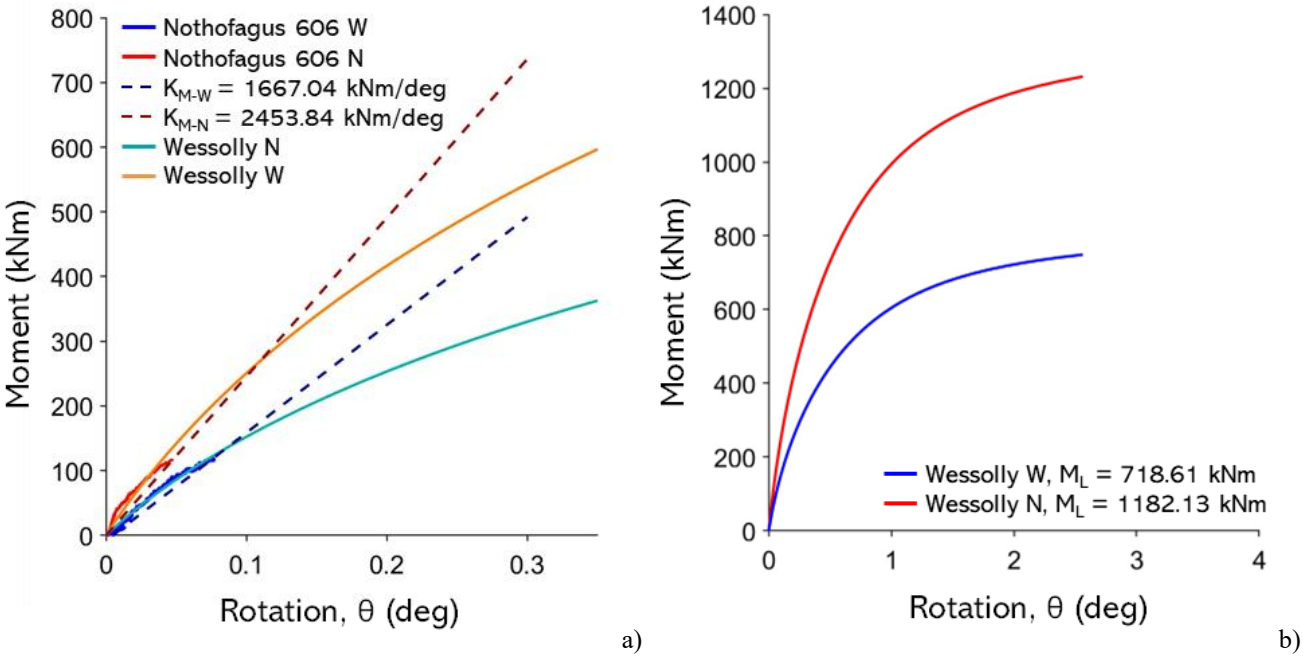

a) b)

Figure A28: (a) Non-destructive test curves with Wessolly interpolation and stiffness (N pulling angle α = 24.8°, W pulling angle α = 25.2°); (b) comparison of extrapolated Wessolly curves with uprooting test.

Dynamic dataset and methods

During the data-acquisition campaign carried out at the Botanic Garden of Dundee (Scotland, UK), inclinometer records were collected for 16 out of 21 trees, alongside wind data (speed and direction). The trees monitored are both evergreen and deciduous, and are as follows: five *Pinus nigra* (Tree ID: 142, 143, 234, 260, 268), two *Quercus* (Tree ID: 392, 394), four *Acer platanoides* (Tree ID: 433, 434, 451, 604), two *Nothofagus* (Tree ID: 568, 606), two *Eucalyptus* (Tree ID: 682, 683) and one *Tsuga* (Tree ID: 971). The monitored trees and the anemometric station are highlighted in Figure 55 and their biometric data used in the following paragraphs are collected in Table 8.

Both the inclinometer and wind measurements were recorded using Fakopp instrumentation (Figure 56). The Fakopp system includes an anemometer and a dual-axis inclinometer, both designed for continuous field campaign. The anemometer wind speed sampling frequency is 1 Hz over a measurement range of 0–150 km/h, with stated accuracy of 0.2 km/h. The device integrates a GPS for georeferencing and synchronizing the measurements over time and stores the recorded data locally on a 16 GB SD card. To ensure accurate wind measurements, the anemometer should be installed in an open, unobstructed area, ideally 10 metres above ground level, to minimize interference from buildings, trees or other large structures. The unit is fully weatherproof, enabling reliable operation in adverse environmental conditions. The dual-axis inclinometer operates over a ±5° range with 0.001° resolution and is temperature-compensated to limit drift during changing environmental conditions. Data are recorded at 10 Hz, with integrated GPS and 16 GB SD-card storage. The sensor is mounted via a single screw, powered at 12 V (≈30 mA), and is weather-proof. Both instruments were powered by portable batteries that ensured continuous acquisition for approximately 4 days.

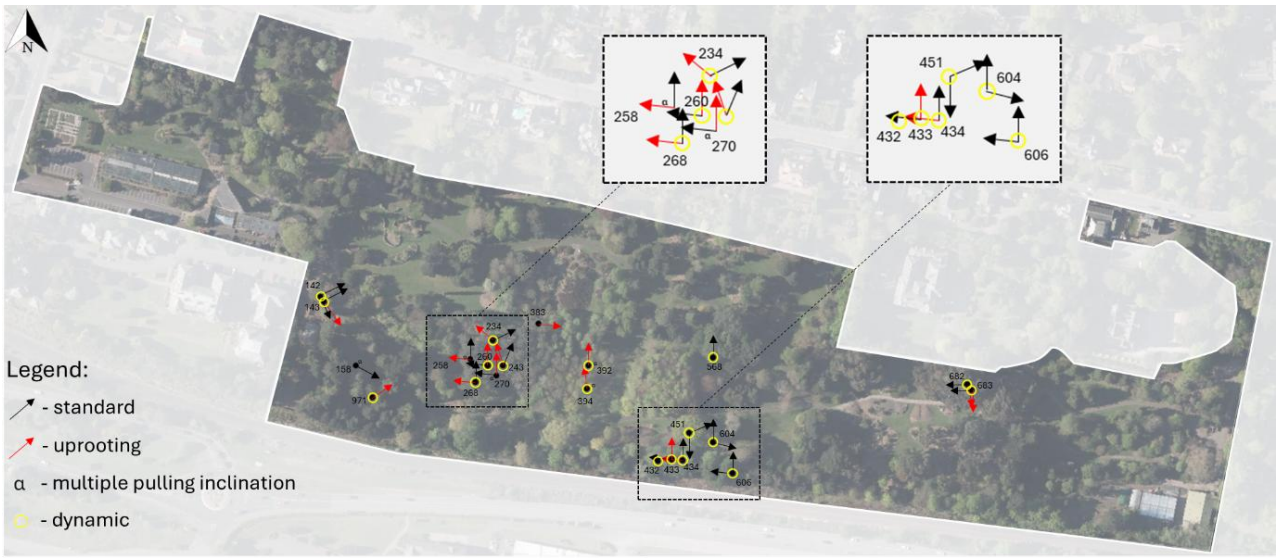

Figure 55: identification (yellow circles) of the trees monitored in dynamic conditions.

Table 8: biometric data of the monitored trees useful for the dynamic analysis.

Tree-ID	A_{cr} (m^2)	h_{cr}
433	15.00	8.50
434	23.00	10.00
260	20.00	16.00
268	13.80	12.80
568	50.00	13.50
604	35.00	9.70
451	107.00	15.00
606	112.00	18.00
142	31.00	12.00
682	85.00	10.50
683	38.60	10.70
143	30.00	16.00
234	20.00	9.00
392	10.80	12.00
394	30.00	10.00
971	47.20	6.78

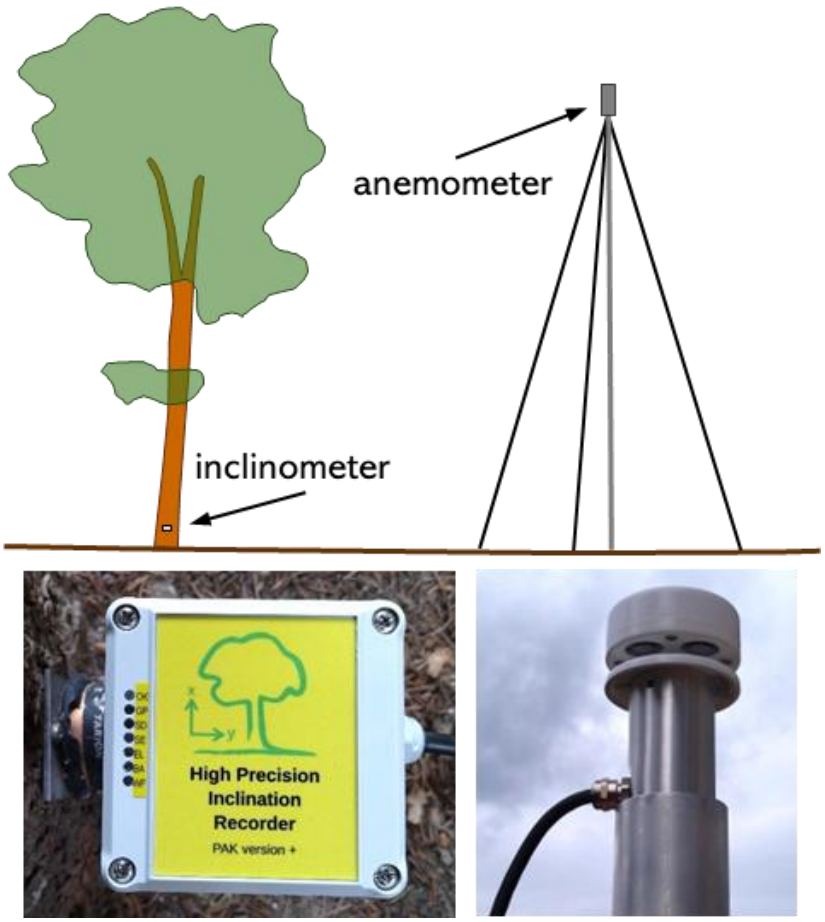

Figure 56: dynamic acquisition setup.

For each tree, multiple acquisitions were performed over the monitoring campaign. This approach was adopted firstly to increase the amount of data available for subsequent analyses, and secondly to capture tree responses under different meteorological conditions.

The aims of the data acquisition campaign are as follows:

- acquire rootplate inclination data in dynamic conditions, i.e., in real conditions under the action of wind;
- for estimating the aerodynamic drag coefficient of the tree;
- for estimating the overturning limit moment based on dynamic data and comparison with the methods described in the previous chapter.

Dynamic data processing

The procedure begins with the definition of the physical and numerical parameters that govern the entire workflow. Wind speed is converted into dynamic pressure using air density (ρ) (kg/m³). An optional smoothing step (moving average) can be applied to wind speed and inclination. The smoothing horizon is defined in seconds and converted to several samples using the estimated sampling frequency. Within each time window, the representative wind-pressure value can be selected as either the maximum ('peak' mode) or a percentile value (e.g. 'p95', 'p90', etc.). Construction of (P, α) pairs enforces a causality constraint: inclination (α) is only searched for after the time at which the representative pressure value has been identified, within a prescribed maximum delay (α_lag_sec). This establishes a link between each pair and a subsequent tree response.

The code takes a file containing at least three columns as input: time, wind speed and inclination. If the file path is not provided, the user can select the dataset interactively via a dialogue window. The data import function is designed to be robust with respect to common formats (CSV, TXT and XLSX). For text files, multiple delimiters are tested (e.g. ';', tab and ','), and the comma is supported as a decimal separator. This approach reduces dependence on instrument-specific export formats and enables the workflow to be replicated across heterogeneous datasets.

After importation, the script attempts to automatically identify the time, wind, and inclination columns by analysing header names (e.g., keywords such as time/timestamp, wind/speed, alpha/inclination). If any of the three columns cannot be identified, execution is stopped to prevent unreliable analyses.

The time vector is converted to seconds. If the data are in milliseconds, the conversion t[s] = t[ms]/1000 is applied. Otherwise, if the unit is not explicit, normalisation based on the order of magnitude of the values is performed. The sampling frequency (fs) is estimated by computing the

median of successive time differences (dt) and setting fs = 1/dt. If the estimate is unreliable (if dt is not finite or positive), a fallback value of 10 Hz is used instead.

To ensure physical consistency in pressure computation, the code constructs two representations of wind speed: v_(km/h) for initial visualisation and v_(ms) for processing. If the wind column is recognised as being expressed in km/h v_(ms) is obtained by dividing v_(km/h) by 3.6. Otherwise, the data are treated as being in m/s already, and v_(km/h) is computed for plotting consistency ($v_{(km/h)} = 3.6 \cdot v_{(m/s)}$). Now an optional signal smoothing is feasible, if enabled, smoothing is performed using a moving average with window length w = round(smooth_sec · fs) samples (with w >= 1). The moving average is applied to v_m/s, v_km/h, and α (in degrees). This filtering reduces high-frequency noise and yields a more stable peak selection within the analysis windows. Then, the procedure allows to select a time window of interest: before extracting (P, α) pairs, the user selects the time interval to analyze by clicking twice on a plot showing wind speed (km/h) and inclination (α, in degrees) on two separate y-axes over the same x-axis. This selection isolates a coherent event or interval (e.g. a significant gust) and excludes irrelevant portions of the signal. The data are then masked and cropped to include only samples between t_0 and t_1. Over the selected window, wind speed expressed in m/s is converted into dynamic pressure (Pa) according to: $P(t) = q(t) = 0.5 \cdot \rho \cdot v(t)^2$. This transformation enables the use of a physically meaningful measure of aerodynamic forcing, consistent with subsequent analyses linking wind input and structural response of the tree. Now there's the core of the procedure that is the automatic optimization of segmentation parameters. The code implements a grid search (autotune) to identify the temporal segmentation parameters that maximize the quality of the relationship between wind pressure and inclination. The explored parameters are: (i) analysis window duration W (minutes) and (ii) overlap O (minutes), with the constraint O < W. For each (W, O) combination, the data are segmented into windows of W samples, advancing by a step equal to (W - O). From each window, (P, α) pairs are extracted (as explained below). The quality of a given combination is assessed via an origin-constrained regression of the form $\alpha = k \cdot P$ and by computing the coefficient of determination R^2 in a no-intercept manner (consistent with the origin constraint). A combination is only considered valid if it produces a minimum number of pairs and a finite R^2. Among valid combinations, the one with the highest R^2 is selected (and, if R^2 is equal for multiple combinations, the one producing the largest number of pairs is selected). If no valid combination is found, predefined fallback values are used for the window and overlap.

The filtered dataset is constructed by sliding overlapping windows over the signal. Within each window, only finite (non-NaN) samples are considered, and the window is discarded if it does not reach a minimum number of valid samples. A time instant t_P is identified within the window that

corresponds to a representative pressure value, either the maximum ("peak") or a percentile ("pXX"), by selecting the sample closest to the percentile threshold. Once t_P has been set, the inclination is only searched for within the subsequent interval [t_P, t_P + α_(lag,sec)], on the assumption that the tree response follows the wind forcing within a prescribed maximum delay. The maximum inclination α and the corresponding time t_α within this interval are then selected. For each valid window, one row is stored containing the following information: wind pressure (Pa), inclination (in degrees), t_P and t_α. The lag is calculated as lag = t_α - t_P and truncated to a non-negative value. The row also contains the window index. Storing times and a window identifier enables each extracted pair to be traced and verified a posteriori.

Once the optimal parameters have been selected by autotuning, the code performs the final extraction of pairs and re-computes the origin-constrained regression, $\alpha = k \cdot P$. The slope, k, is estimated using the least squares method, $k = \Sigma(P \cdot \alpha) / \Sigma(P^2)$. The results are visualized in the form of a scatter plot of (P, α), with the regression line superimposed, and only the R^2 value is reported. This plot allows you to immediately check the consistency of the extracted points and the quality of the coupling between the forcing and the response.

Finally, the mean lag time (in seconds) of the extracted pairs is calculated and displayed. This value is a synthetic indicator representing the average response time to changes in wind pressure within the analyzed window.

Estimation of the aerodynamic drag coefficient (Cd) from dynamic data

The aim of the following procedure is to estimate the aerodynamic drag coefficient (Cd) associated with a given tree using pre-processed wind–rotation dynamic data (i.e. the filtered file mentioned in the previous paragraph). The Cd value is determined by ensuring consistency with an independent static reference test (non-destructive dataset): the maximum overturning moment obtained from the dynamic data (after converting P → M and applying a Wessolly fit) must equal the maximum moment of the static dataset (also evaluated via Wessolly fitting). Mathematically, the objective is to find the Cd value for which $M_{max, dynamic}(Cd) - M_{max, non-destructive} = 0$.

The procedure uses two data sources: (i) a static SIM file, which contains information on rotation and moment; and (ii) a dynamic filtered file, which is produced by the dynamic-data filtering procedure. Two external functions are required: Wessolly fit equation for non-destructive dataset and Wessolly fit equation for dynamic dataset. These functions must return the estimated maximum moment (ML_non-destructive), and optionally the Wessolly curve (rotation and moment) for visualisation. The code reads the static non-destructive file and two vectors are extracted: rotation and moment.

The non-destructive data are then fitted to the Wessolly-based reference curve using the Wessolly fit equation. The limit moment ML_(non-destructive) is then estimated from the fitted curve.

The estimation of the drag coefficient C_d follows a stiffness-based method. In practice, C_d is treated as an unknown scaling parameter and is determined by identifying the value that makes the overturning moment capacity M_L inferred from the dynamic dataset coincide with the capacity obtained from the non-destructive dataset. Operationally, this condition is reached when the Wessolly curve fitted to the dynamic dataset overlaps the curve fitted to the non-destructive dataset, i.e., when the two fits provide the same estimate of M_L.

The procedure continues with the selection of the dynamic filtered file, and the extraction of the vectors pressure and rotation. Two geometric/operational quantities are used to convert wind pressure into an equivalent bending moment: the reference area (m^2), which is representative of the effective aerodynamic area and the centre-of-pressure height (H_c, in meter), which is representative of the lever arm of the aerodynamic resultant with respect to the chosen rotation point. For a given Cd, the instantaneous dynamic moment is computed as M = P · A · Cd · H_c, where M(t) has units of N·m. In the code, the moment is expressed in kN·m by dividing by 1000: M = P · A · Cd · H_c / 1000.

Cd estimation is formulated as a minimization problem. It has been used with a function that:

1) for an assigned Cd, the moment vector M_test is computed from P as M_test = P · A · Cd · Hc/1000;
2) a Wessolly fit is performed on the dynamic data (M_test, rot) using fit_Wessolli_M, yielding the estimated maximum moment Mmax_test;
3) the difference d(Cd) = Mmax_test − M_SIM_max is returned.

The Cd search is restricted to the plausible interval [Cd_(low), Cd_(high)], which is initially set to [0.01, 5.00]. The code evaluates d(Cd_(low)) and d(Cd_(high)). If both values are finite and opposite sign, the equation d(Cd) = 0 is bracketed within the interval, and *fzero()* is used to find the root. If there is no sign change (i.e. a root is not guaranteed within the interval), the code uses *fminbnd* to minimize |d(Cd)| over the interval and selects the Cd value that minimizes the difference between the maximum moments. An additional robust fallback is implemented: if the numerical routines fail, a Cd grid (e.g. 0.1:0.01:3) is explored, and the value that minimizes |d(Cd)| is selected. Once the optimal value *best_Cd* is obtained, the dynamic moment time series associated with the filtered dataset is computed as: M_DYN = (P · A · *best_Cd* · Hc)/1000. This residual provides a quantitative indicator of the alignment between static reference and dynamic reconstruction. Two main figures are produced: Figure 57 that shows M–rotation plot of dynamic filtered data and non-destructive data, and Figure 58 that includes the results of the iteration loop showing the overlayed Wessolly-fitted curves for both datasets.

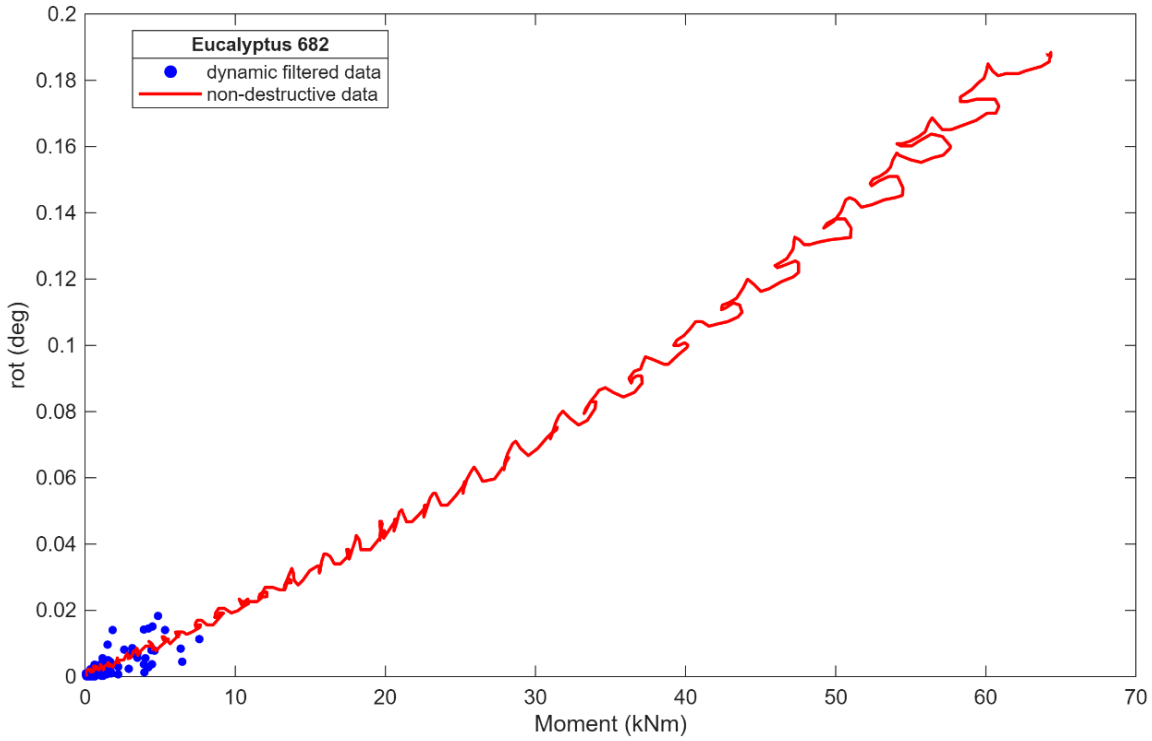

Figure 57: M–rotation plot of dynamic filtered data and non-destructive data.

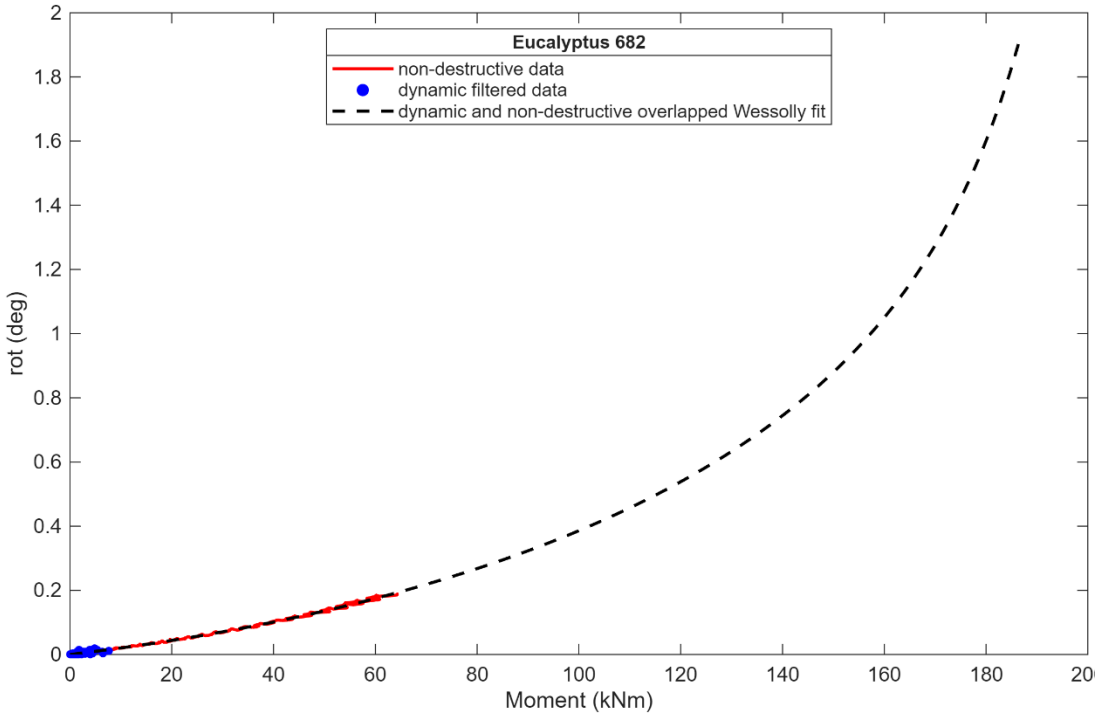

Figure 58: results of the iteration loop showing the overlayed Wessolly-fitted curves for both datasets.

Resuming:

1. a non-destructive data with rotation and moment;
2. a filtered dynamic data with rotation and pressure;
3. geometrical parameters A and Hc set consistently with the tree;

4. fit Wessolly function, returning consistent Mmax values (and, if needed, curves for plotting);
5. verification that the [Cd_low, Cd_high] interval is appropriate; for specific species or contexts it may need to be narrowed or widened.

The procedure described above has been replicated many times on the multiple dynamic data acquired on the field, at the Botanic Garden of Dundee, on the sixteen trees.

The purpose of the final part of the procedure is to assess the effect of different values of the aerodynamic drag coefficient (Cd) on the reconstruction of the moment from dynamic data, and consequently on the moment–rotation curve obtained through Wessolly fitting and so the ML estimation. The workflow relies on:

- non-destructive dataset, containing rotation and bending moment;
- all available dynamic filtered dataset of the same tree, produced by the dynamic data filtering procedure, containing at least: wind pressure P and rotation;
- fit Wessolly function, returning consistent Mmax values.

Firstly, the code reads the non-destructive data that includes moment and rotation values. A Wessolly fit is then performed on the non-destructive dataset. This returns an interpolated reference curve, which is then used to compare the reconstructed dynamic curves. At this point, the Cd values obtained differ from one another. To clearly compare the data trends based on the different Cd values, each of them was used to recalculate the new time series (moment, rotation) using all datasets. Therefore, the *all-filtered* dataset is the union of all the previously filtered datasets. This was done because the set of various data chosen on time windows taken on different days and therefore also in different environmental conditions provides a more complete picture of the dynamics of the tree under the action of the wind.

Therefore, for each Cd scenario (i.e., each dataset contains M values calculated with the Cd got on its own dataset, obtained from the previous procedure), the script applies the Wessolly fit to the converted dynamic data using Wessolly's interpolating equation; therefore, n-curves are obtained for n values of Cd. Two other interpolations by Wessolly were performed. The first was done using the Cd_{tab} (tab=tabulated) value found in literature and usually used in agronomy. The second, is an interpolation made on *all-filtered* dataset, using the Cd_{af} (af = all-filtered) estimated on the just mentioned dataset through the previous procedure. Table 9 includes, for Tree-ID, the species, the lag time (s) calculated, the R^2 and the values of Cd_{af}.

Table 9: resuming data calculated Cd_{af} values, lag time and R^2 for the monitored trees.

Species	Tree-ID	Cd_{af}	Lag time (s)	R^2
Acer platanoides	433	0.16	2.4	0.78
Acer platanoides	434	0.14	2.4	0.81
Acer platanoides	604	0.13	2.1	0.82
Acer platanoides	451	0.15	2.51	0.78
Pinus nigra	142	0.36	2.28	0.77
Pinus nigra	143	0.57	2.34	0.70
Pinus nigra	234	0.17	2.18	0.70
Pinus nigra	260	0.24	1.38	0.83
Pinus nigra	268	0.22	2.29	0.72
Quercus	392	0.22	2.5	0.70
Quercus	394	0.14	2.19	0.65
Nothofagus	568	0.15	2.3	0.60
Nothofagus	606	0.27	2.53	0.77
Eucalyptus	682	0.18	2.12	0.60
Eucalyptus	683	0.15	2.44	0.73
Tsuga	971	0.18	2.35	0.70

Thus, there are *n* curves equal to the number of Cd values calculated on the individual filtered datasets, one on the union of the filtered datasets, and one calculated on the Cd values tabulated in the literature. The Figure 59 shows all the curves obtained from Wessolly's interpolation equation of the non-destructive data and the dynamic filtered data.

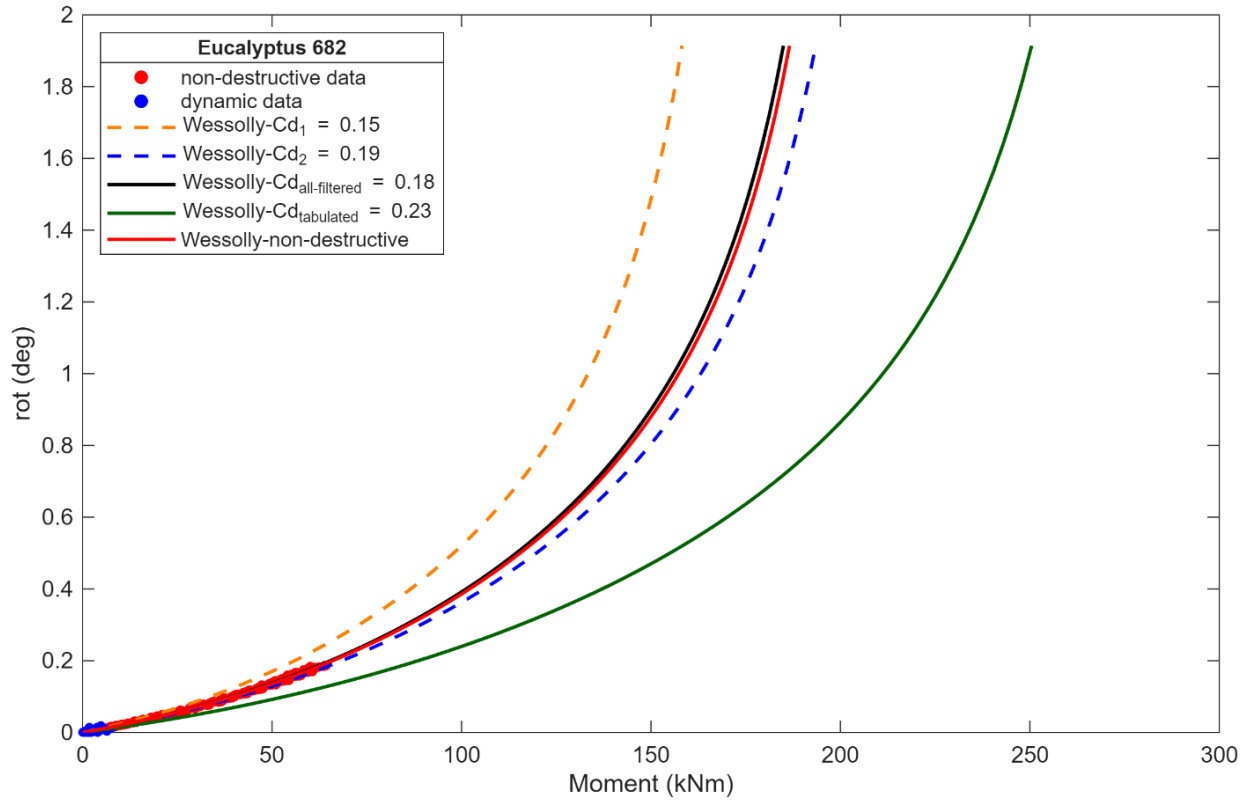

Figure 59: Wessolly's interpolation of the dynamic datasets (M-rot) obtained for each Cd values.

The curve closest to that obtained from non-destructive data are that got by the *all-filtered* dataset. This highlights the need to acquire more data at different times and under different environmental conditions in order to get a set of values that cover the entire "spectrum" of tree behavior under dynamic conditions.

Discussion

The final part of the chapter focuses on comparing the M_L values obtained with the different approaches: the M_L measured in the field during uprooting tests, the M_L estimated by applying the Wessolly method to the non-destructive data, and the two M_L estimates derived from the dynamic data using the two alternative C_d values ("af" and "tab"). Table 10 includes data of the eleven monitored, showing the Tree-ID, the measured limit moment (from uprooting test), the extrapolated moment from non-destructive test and the two extrapolated ones from dynamic datasets using Cd types, *tabulated* and *all-filtered*.

Table 10: measured and extrapolated M_L values for the eleven trees considered for discussion.

Tree-ID	M_L Measured (kNm)	M_L non-destructive (kNm)	M_L Cd_{af} (kNm)	M_L Cd_{tab} (kNm)
433	45.5	31.28	29.76	47.92
434	53.49	43.44	43.32	73.14
260	105.19	69.79	70.44	60.15
268	120.04	125.38	123.33	111.95
682	182.75	189.07	184.94	250.47
683	196	118.60	117.81	178.26
143	420	311.29	309.65	99.26
234	114	75.13	75.79	78.93
392	36.4	39.28	38.60	43.81
394	86.9	86.82	84.64	149.79
971	229	234.70	231.53	250.92

When the M_L values estimated with Wessolly from the non-destructive data are compared against those estimated (Figure 60) from the dynamic data, a clear pattern emerges. Using the ratio between the non-destructive M_L and the M_L obtained with Cd_{af} the maximum percentage deviation is 5% and occurs only for tree 433. For 9 out of the 11 trees the difference remains within 2%, while tree 394 shows a deviation of 3%. Overall, this indicates that the procedure adopted to estimate Cd (= Cd_{af}) is reasonably robust, yielding dynamic-based M_L estimates that closely match the non-destructive Wessolly-based values. In contrast, performing the same comparison using the M_L estimated with Cd_{tab} leads to substantially larger discrepancies: only 4 trees out of 11 falls within a 12% difference,

and none are below 5%. For tree 260 the deviation is 16%, whereas for the remaining six trees it exceeds 16%, reaching differences on the order of 40%; in the most extreme case (tree 143), the discrepancy increases to 214%. These results suggest that adopting Cd_{tab} instead of Cd_{af} can produce a marked over- or under-estimation of the resulting M_L values.

From the ratio between the M_L values measured in the field during uprooting tests and those estimated with the Wessolly approach from dynamic data using $C_{d,\mathrm{af}}$, five out of the eleven trees show a percentage difference within 6% (trees 268, 260, 392, 394, and 971). All the remaining cases exceed 20%, with the estimates consistently lower than the measured M_L (i.e., on the conservative side in terms of safety factor). When the same comparison is carried out using $C_{d,\mathrm{tab}}$, none of the deviations falls below 5%, and only four trees (433, 268, 683, and 971) lie in the 5–10% range. The other seven cases exhibit discrepancies greater than 16%, among these, four trees (434, 682, 392, and 394) overestimate M_L relative to the uprooting measurements. Therefore, also in this case, comparing the measured values with the estimates obtained using the two drag coefficients (Cd_{af} and Cd_{tab}) indicates that M_L computed with Cd af is generally more accurate than M_L computed with Cd_{tab}. This conclusion remains valid even when considering that none of the M_L values derived with Cd_{af} overestimates the measured M_L, meaning that the method stays on the conservative side in terms of safety factor.

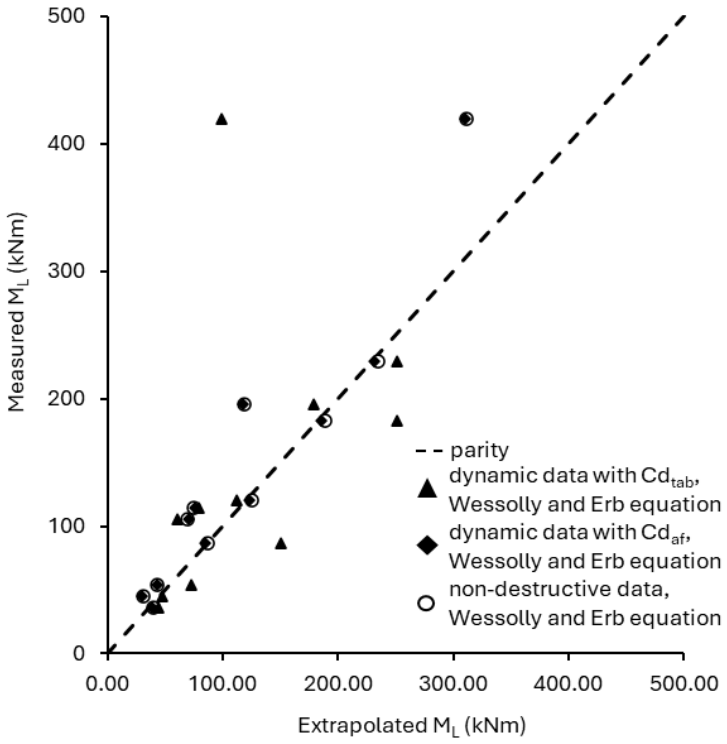

Figure 60: Comparison between measured limit moment and extrapolated values using the Wessolly and Erb method.

Below, the appendix figures for this chapter are provided for each monitored tree.

Appendix C

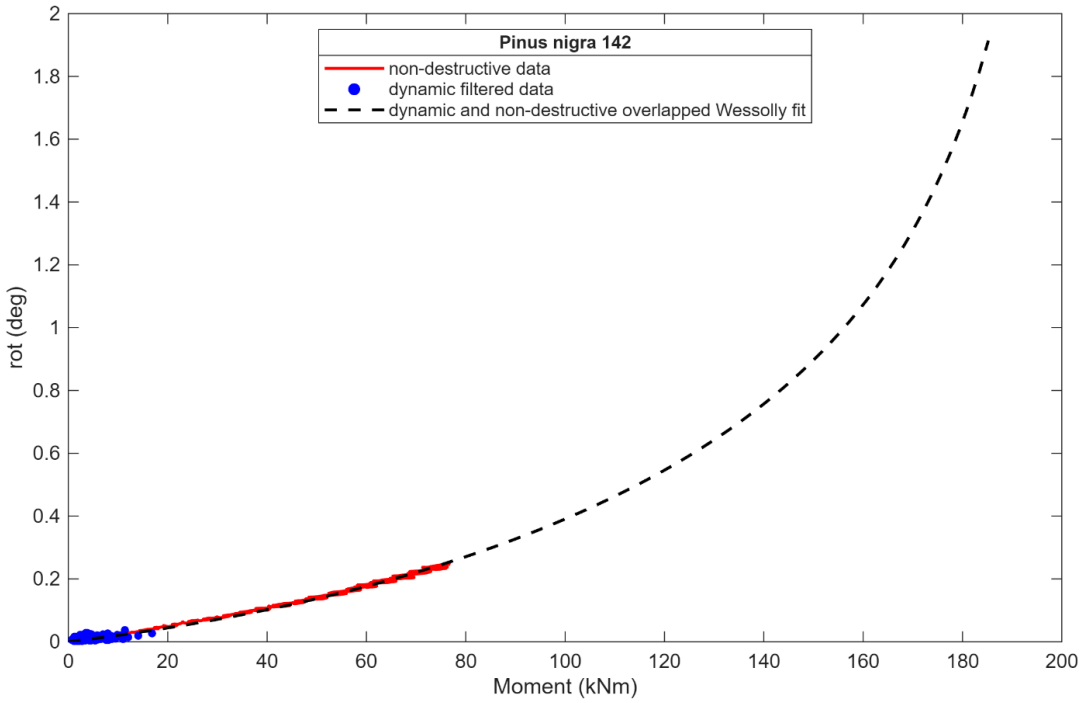

Figure A29: results of the iteration loop showing the overlayed Wessolly-fitted curves for both datasets.

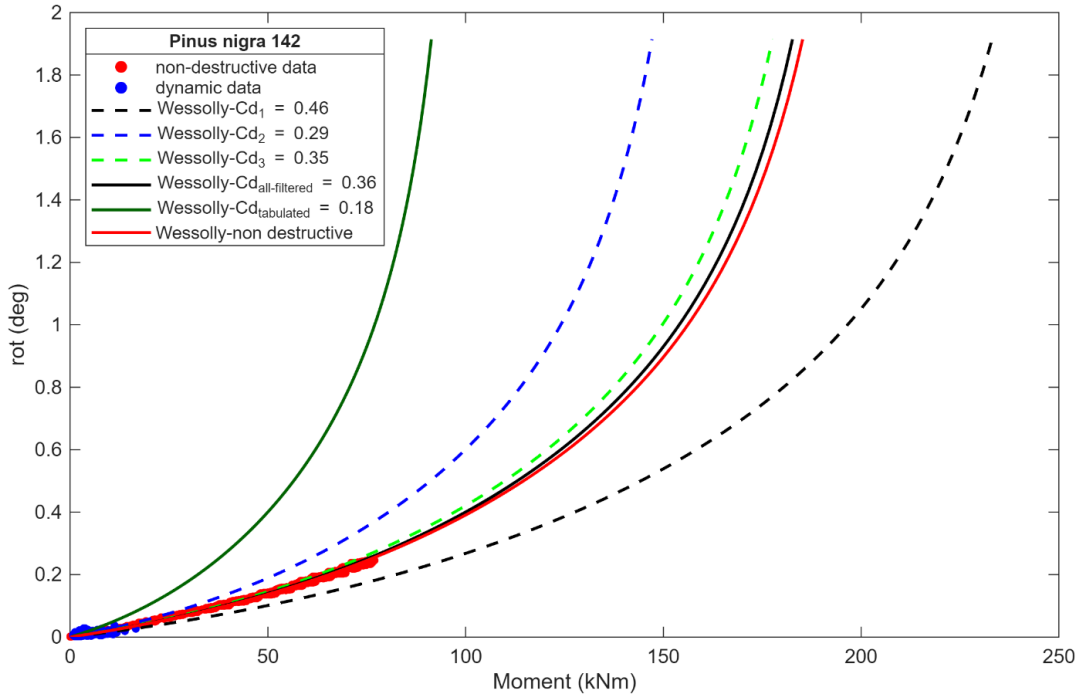

Figure A30: Wessolly's interpolation of the dynamic datasets (M-rot) obtained for each Cd values and comparison with non-destructive dataset.

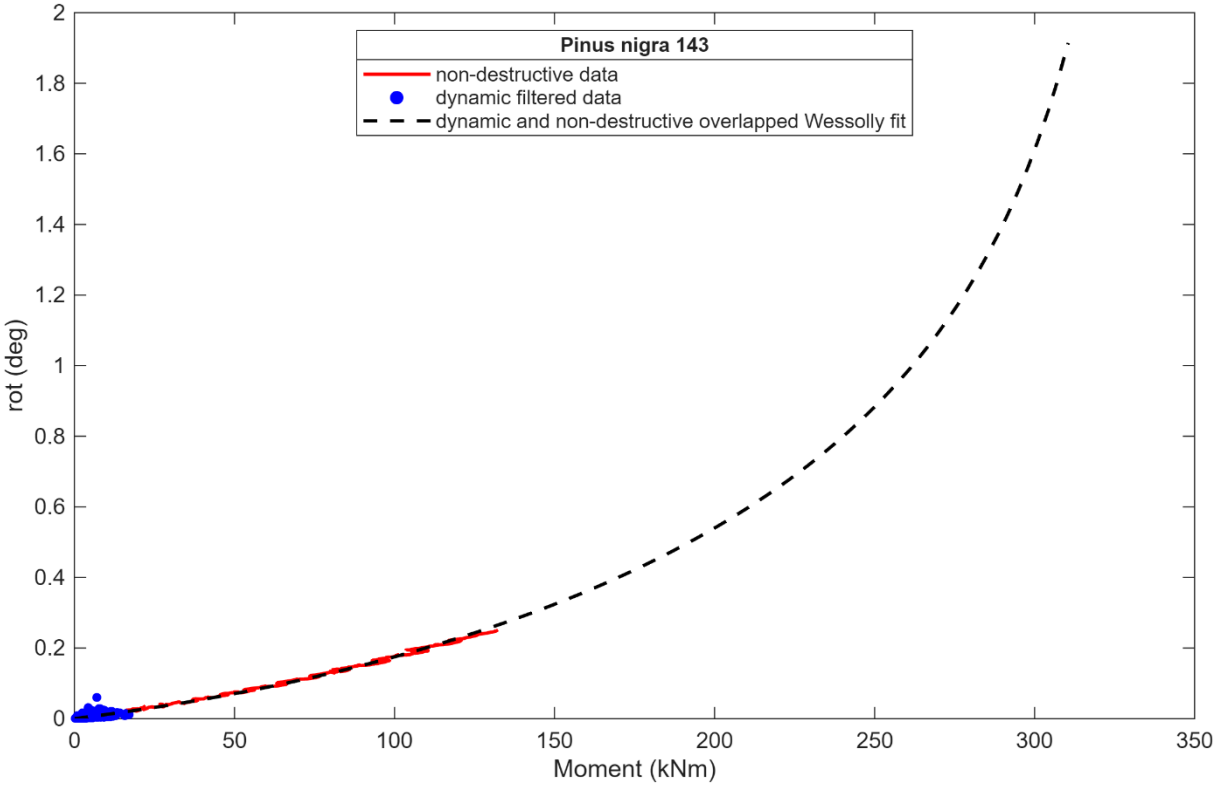

Figure A31: results of the iteration loop showing the overlayed Wessolly-fitted curves for both datasets.

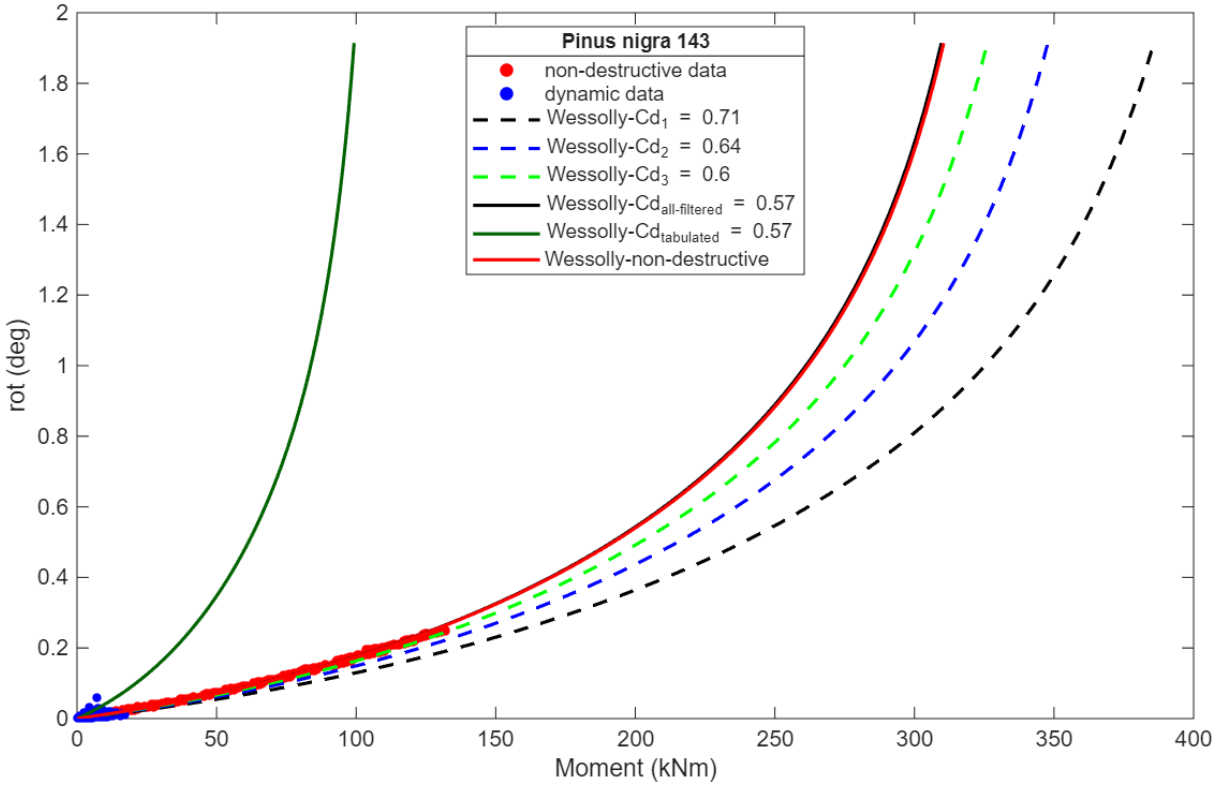

Figure A32: Wessolly's interpolation of the dynamic datasets (M-rot) obtained for each Cd values and comparison with non-destructive dataset.

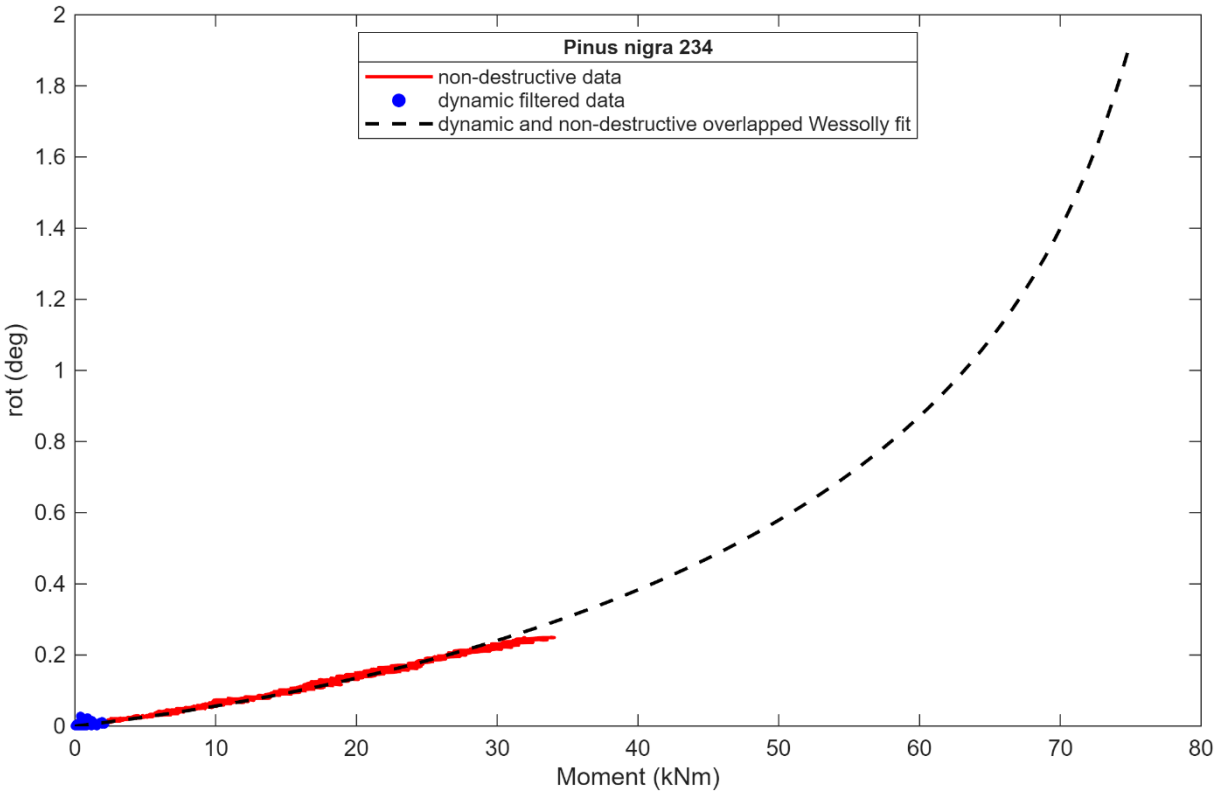

Figure A33: results of the iteration loop showing the overlayed Wessolly-fitted curves for both datasets.

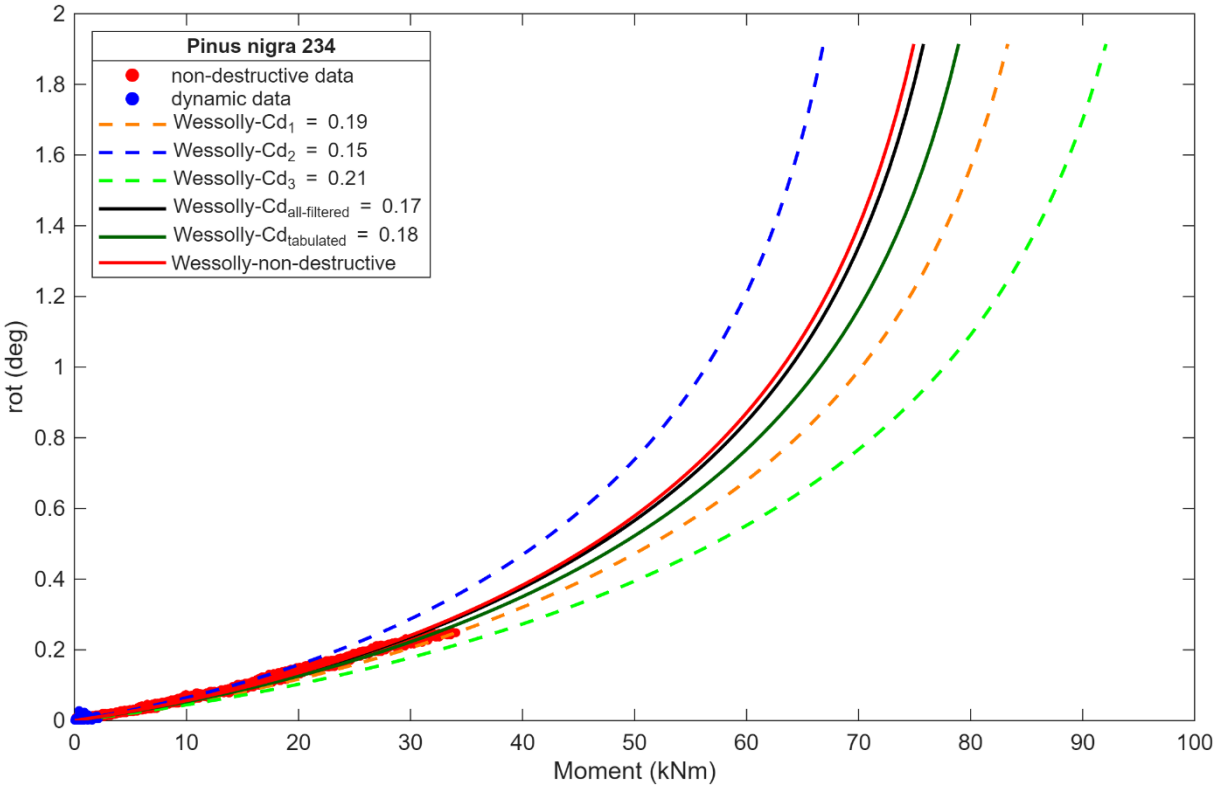

Figure A34: Wessolly's interpolation of the dynamic datasets (M-rot) obtained for each Cd values and comparison with non-destructive dataset.

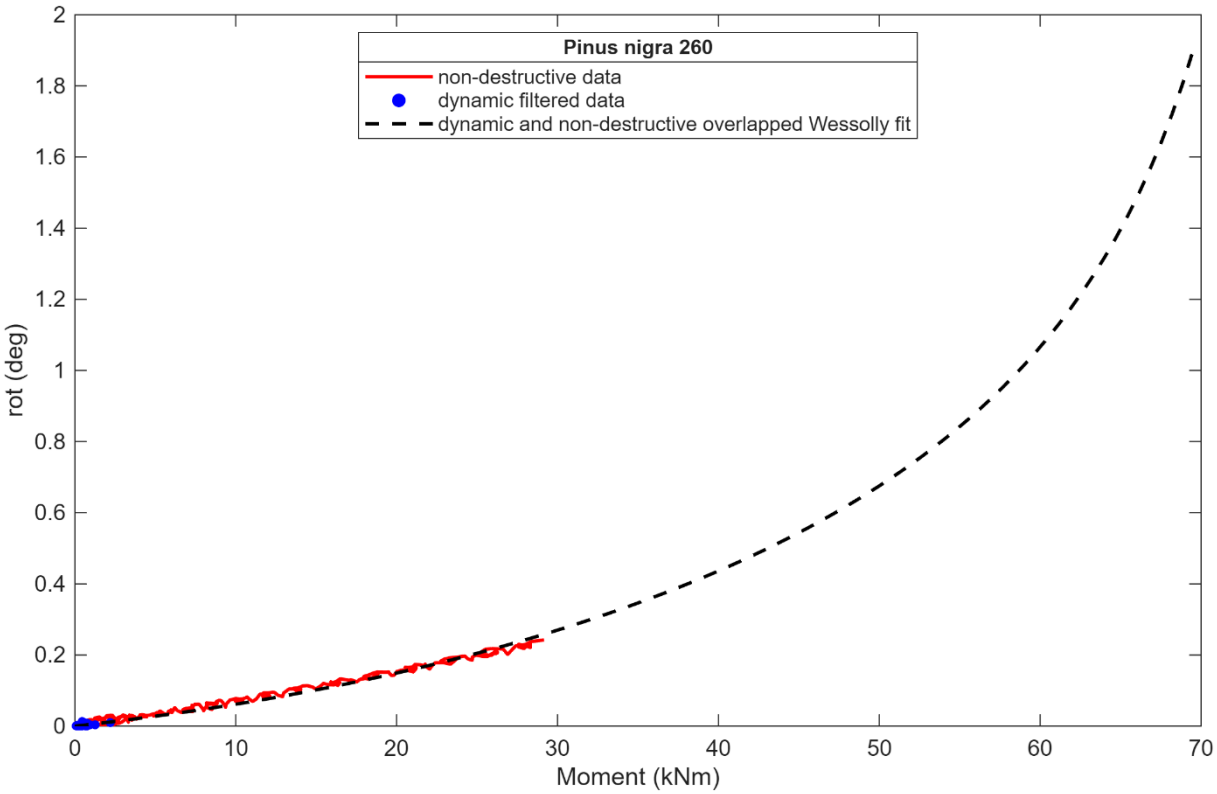

Figure A35: results of the iteration loop showing the overlayed Wessolly-fitted curves for both datasets.

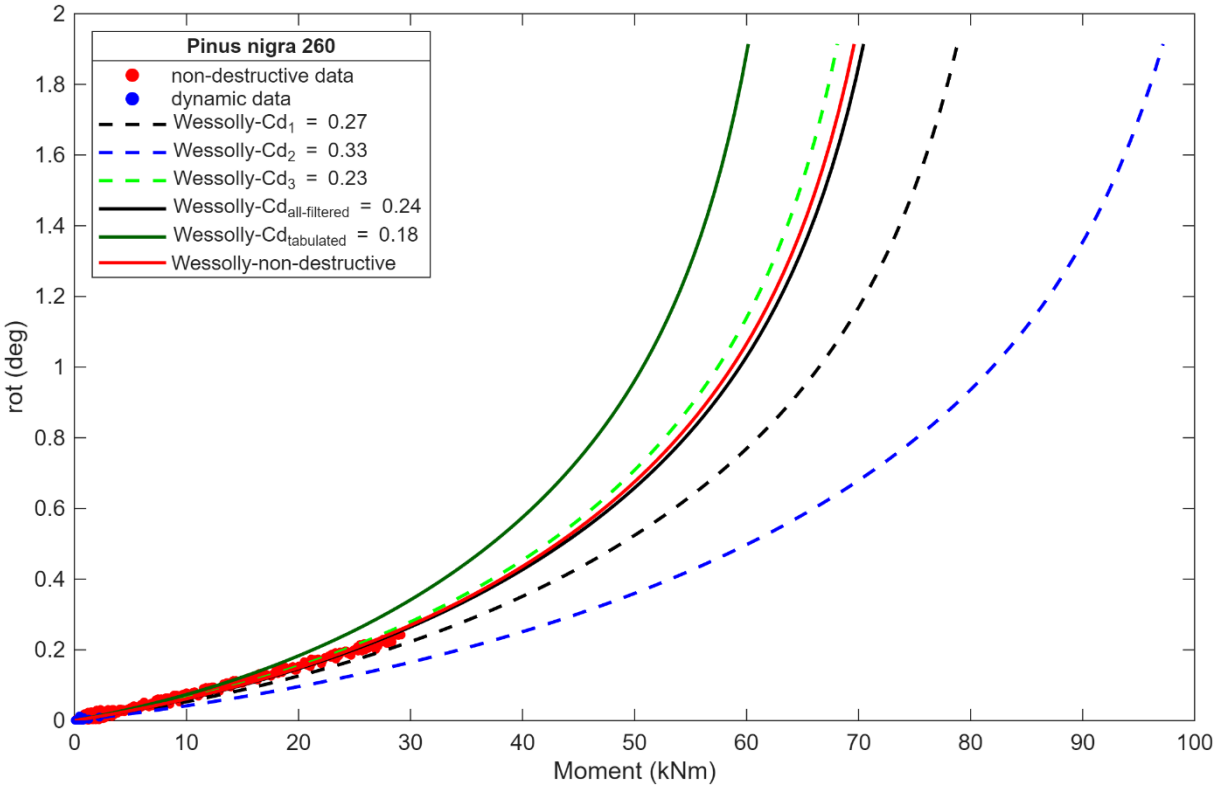

Figure A36: Wessolly's interpolation of the dynamic datasets (M-rot) obtained for each Cd values and comparison with non-destructive dataset.

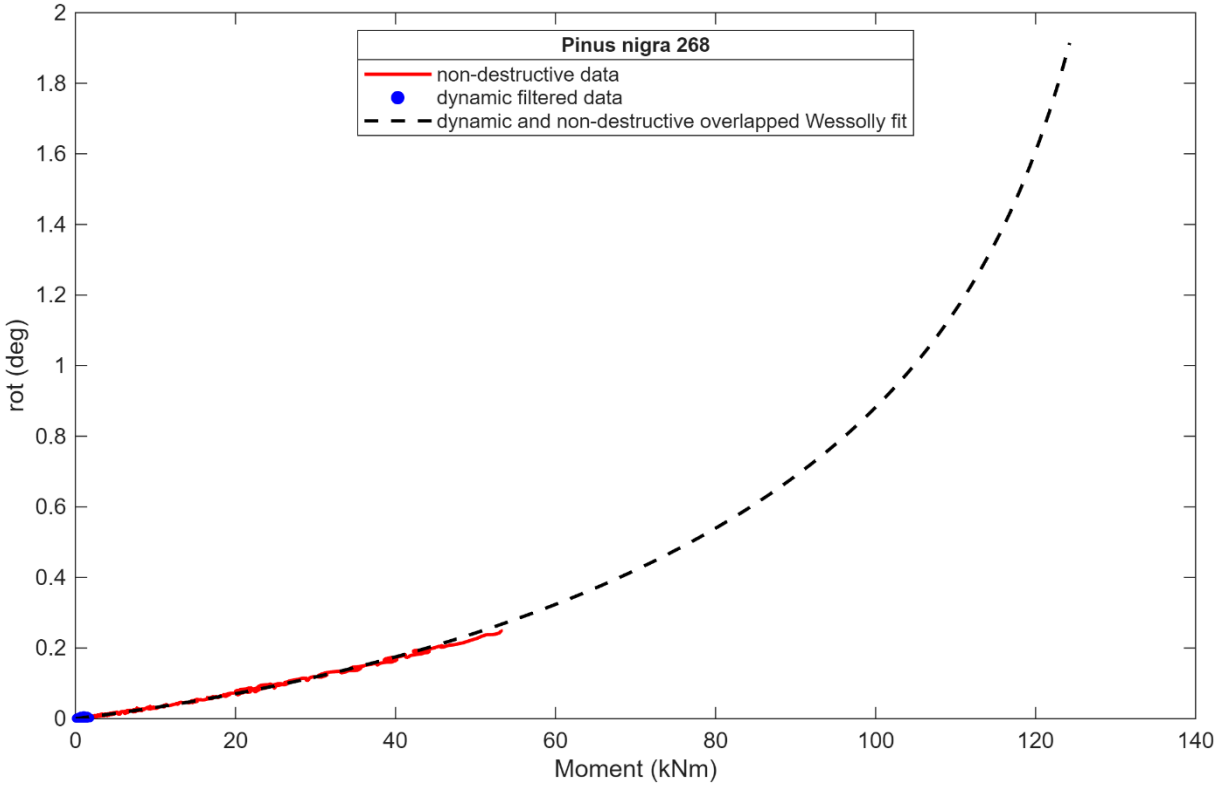

Figure A37: results of the iteration loop showing the overlayed Wessolly-fitted curves for both datasets.

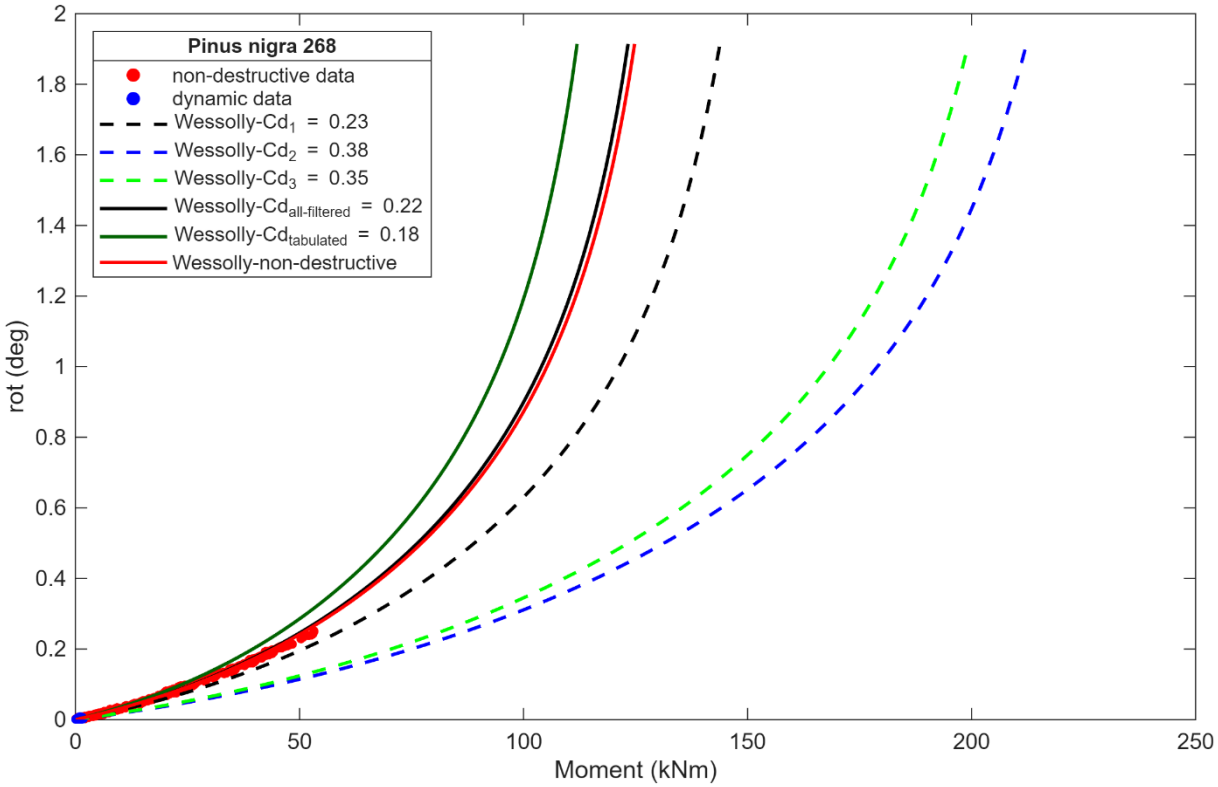

Figure A38: Wessolly's interpolation of the dynamic datasets (M-rot) obtained for each Cd values and comparison with non-destructive dataset.

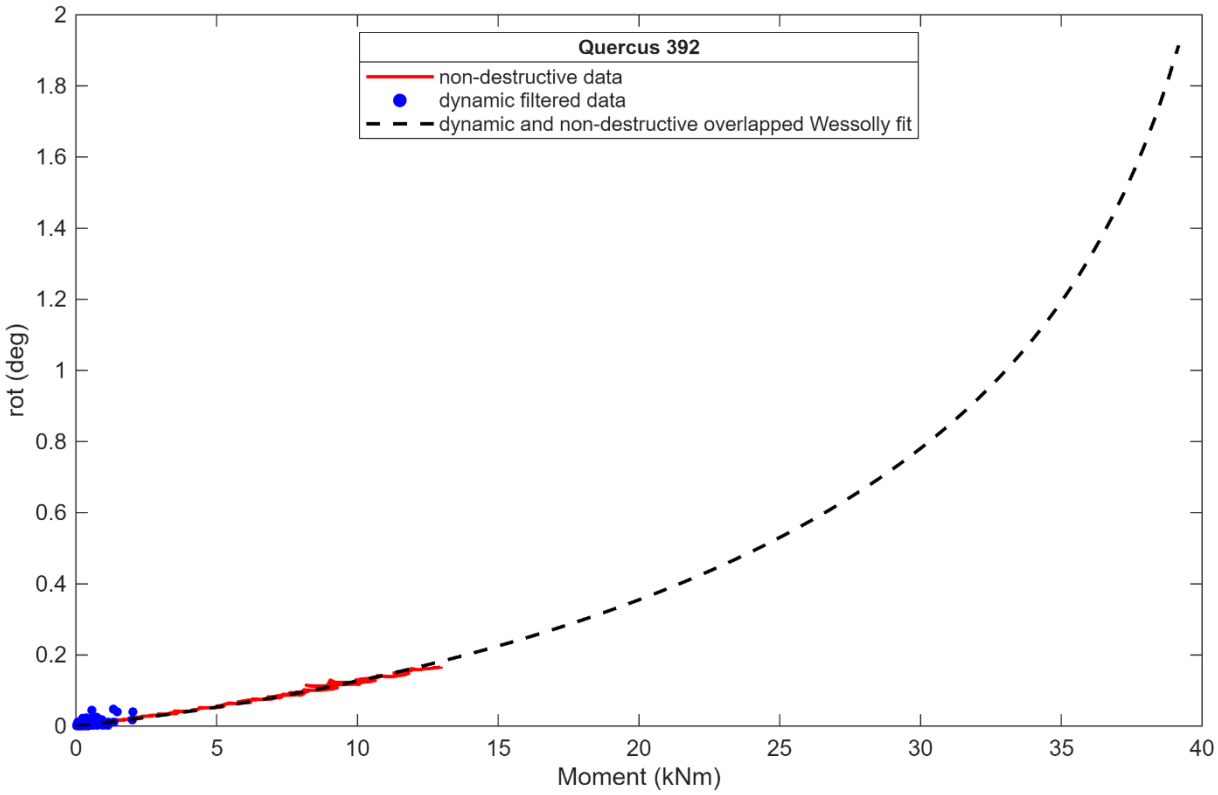

Figure A39: results of the iteration loop showing the overlayed Wessolly-fitted curves for both datasets.

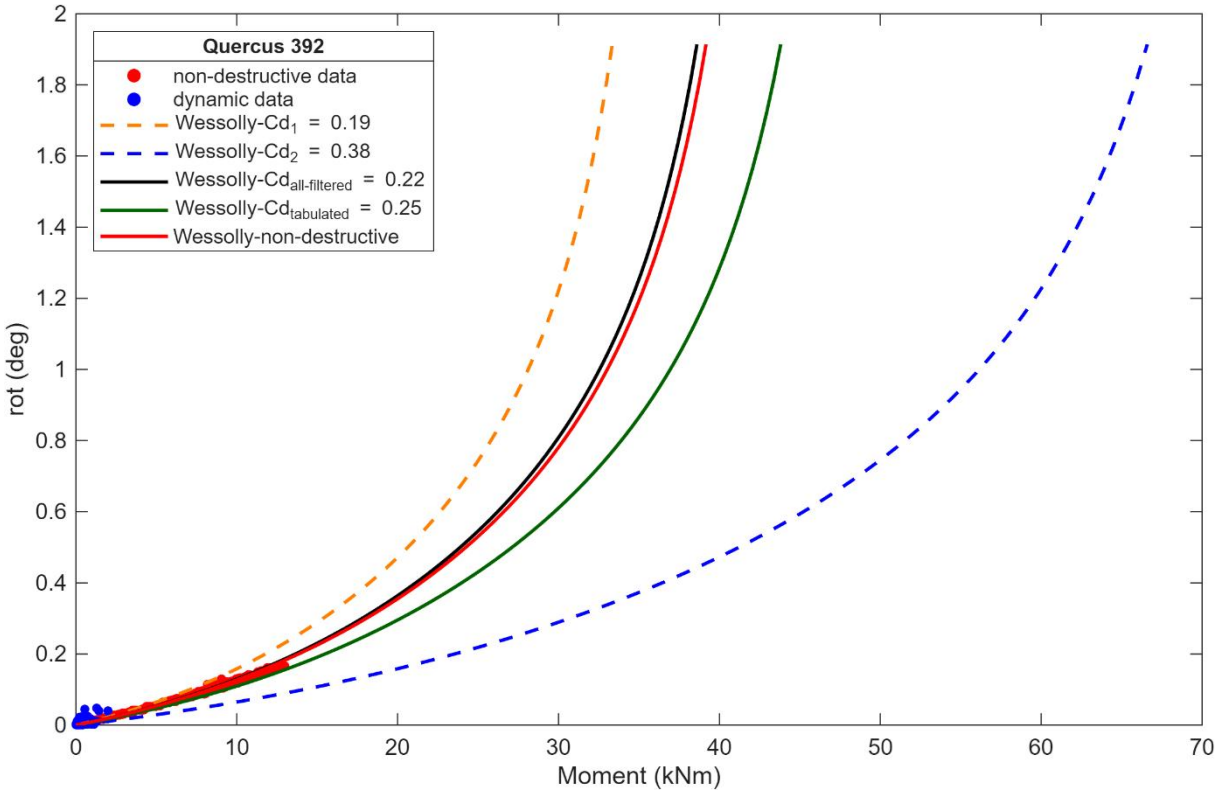

Figure A40: Wessolly's interpolation of the dynamic datasets (M-rot) obtained for each Cd values and comparison with non-destructive dataset.

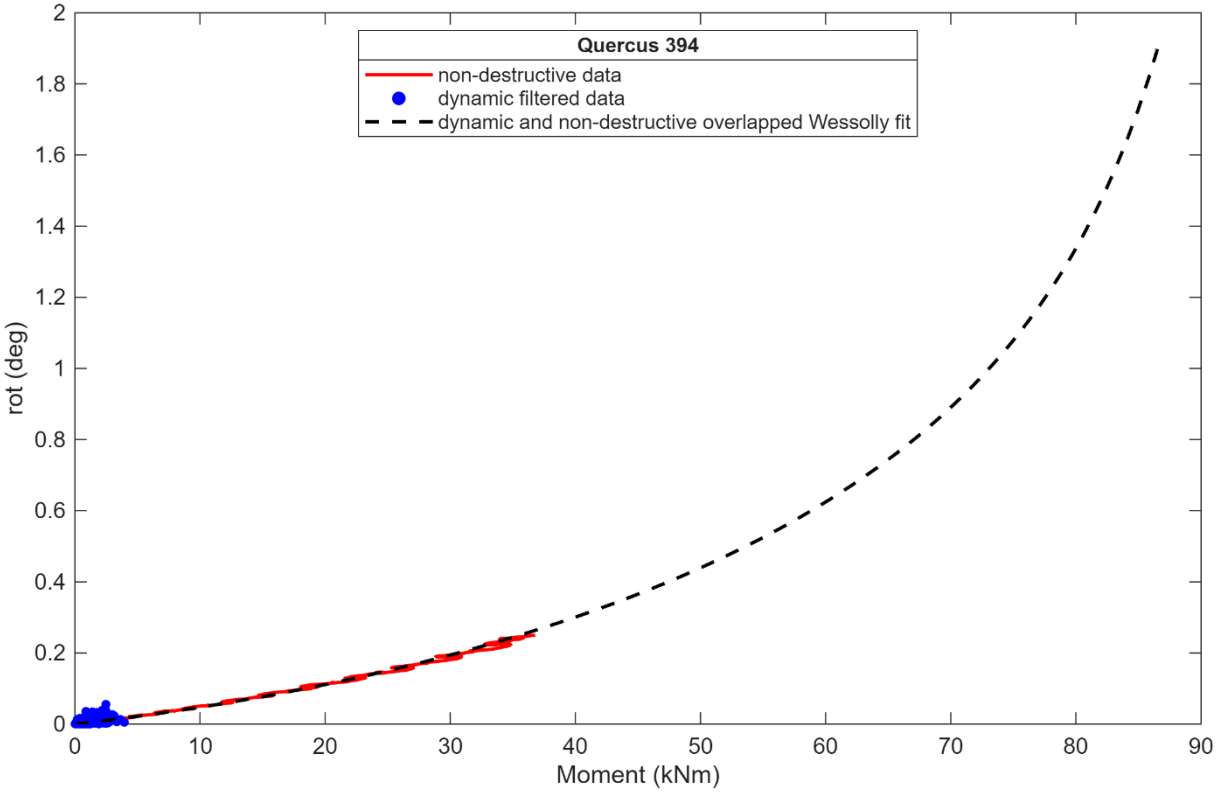

Figure A41: results of the iteration loop showing the overlayed Wessolly-fitted curves for both datasets.

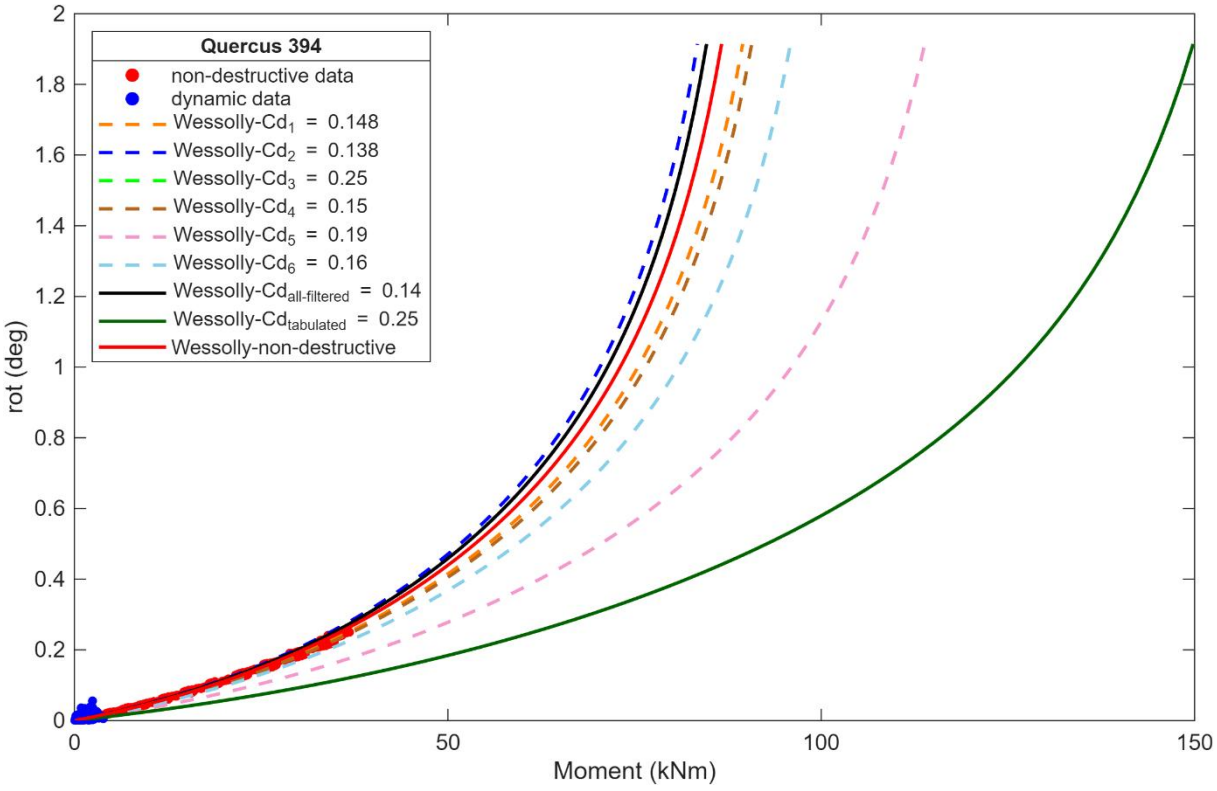

Figure A42: Wessolly's interpolation of the dynamic datasets (M-rot) obtained for each Cd values and comparison with non-destructive dataset.

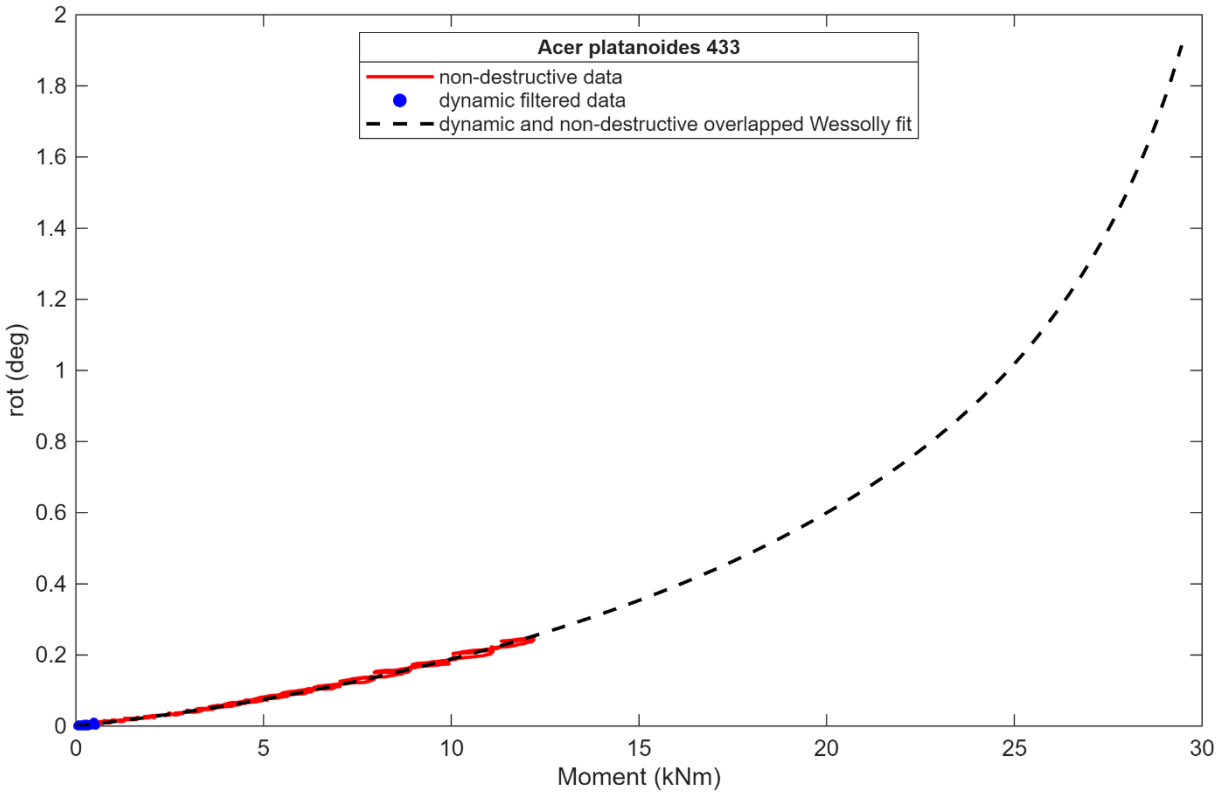

Figure A43: results of the iteration loop showing the overlayed Wessolly-fitted curves for both datasets.

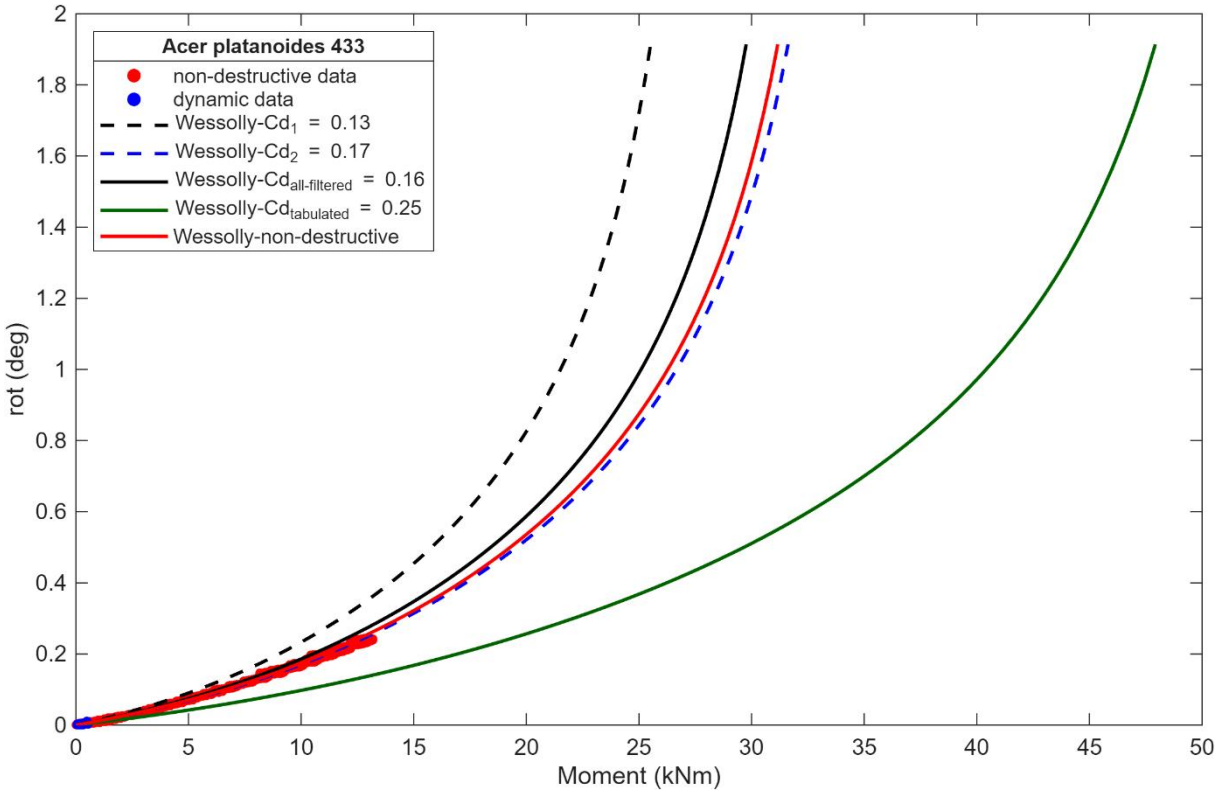

Figure A44: Wessolly's interpolation of the dynamic datasets (M-rot) obtained for each Cd values and comparison with non-destructive dataset.

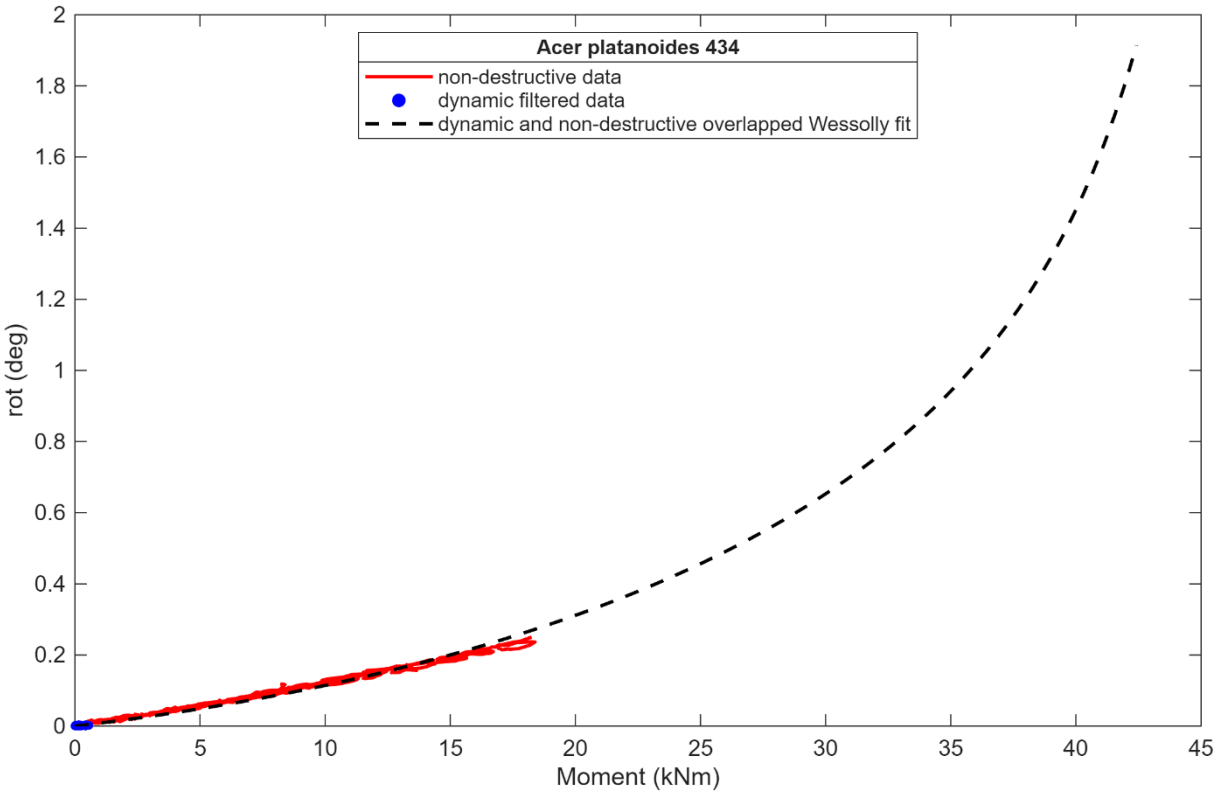

Figure A45: results of the iteration loop showing the overlayed Wessolly-fitted curves for both datasets.

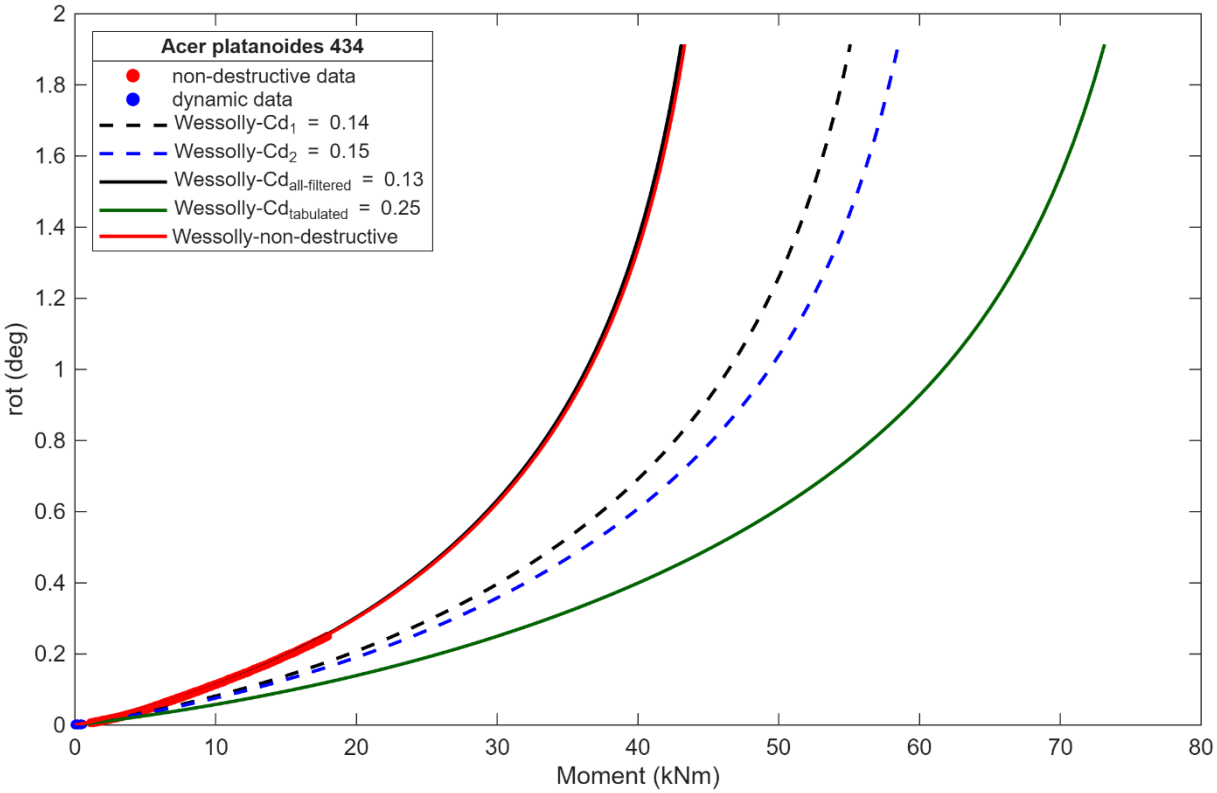

Figure A46: Wessolly's interpolation of the dynamic datasets (M-rot) obtained for each Cd values and comparison with non-destructive dataset.

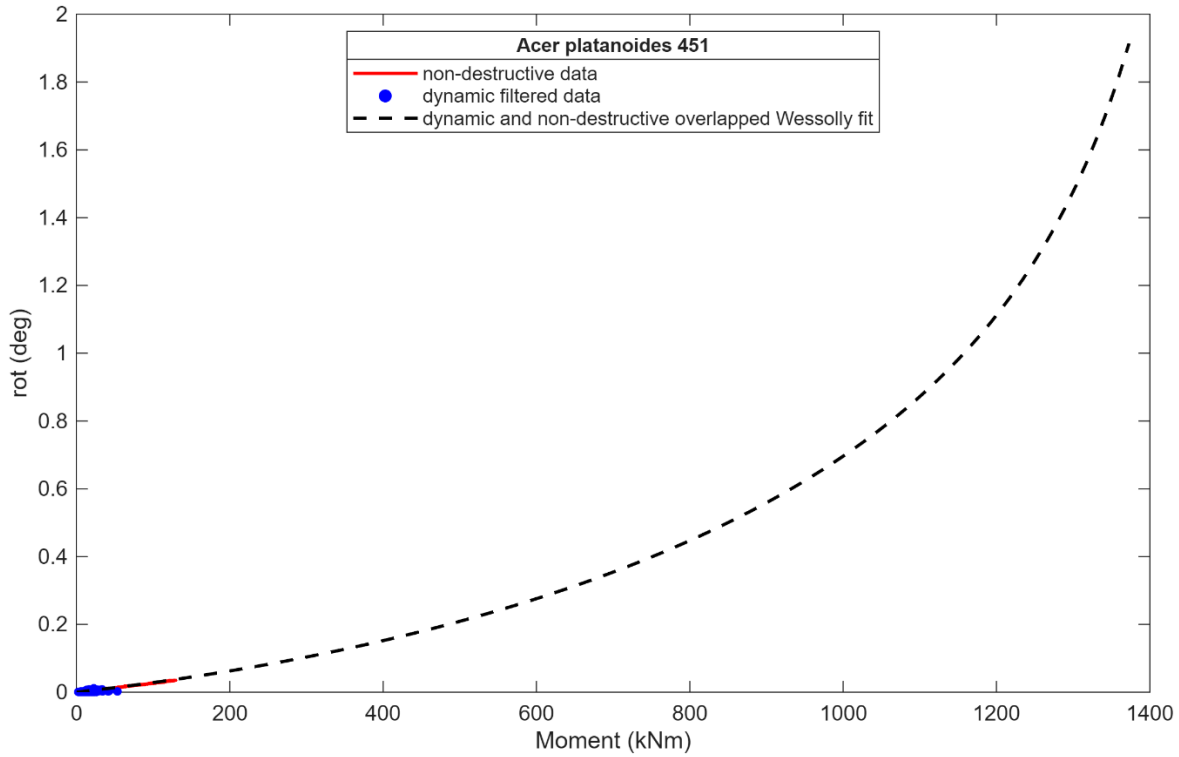

Figure A47: results of the iteration loop showing the overlayed Wessolly-fitted curves for both datasets.

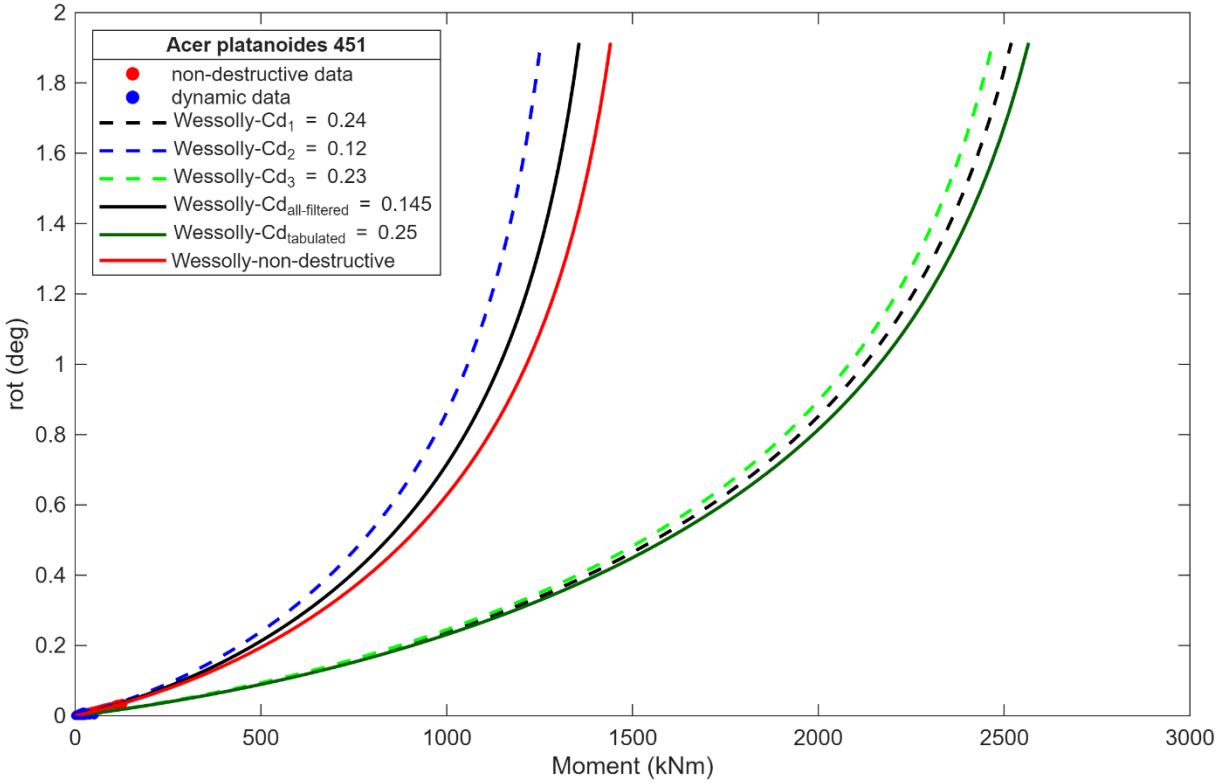

Figure A48: Wessolly's interpolation of the dynamic datasets (M-rot) obtained for each Cd values and comparison with non-destructive dataset.

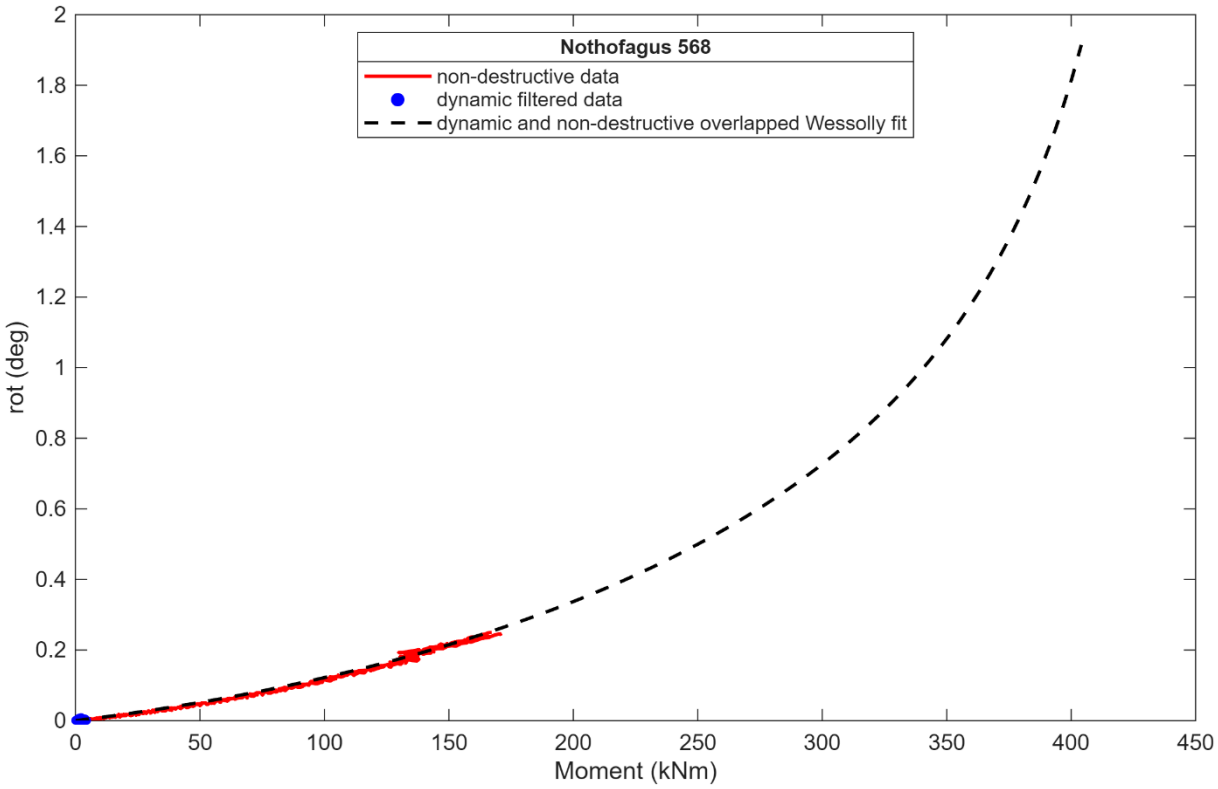

Figure A49: results of the iteration loop showing the overlayed Wessolly-fitted curves for both datasets.

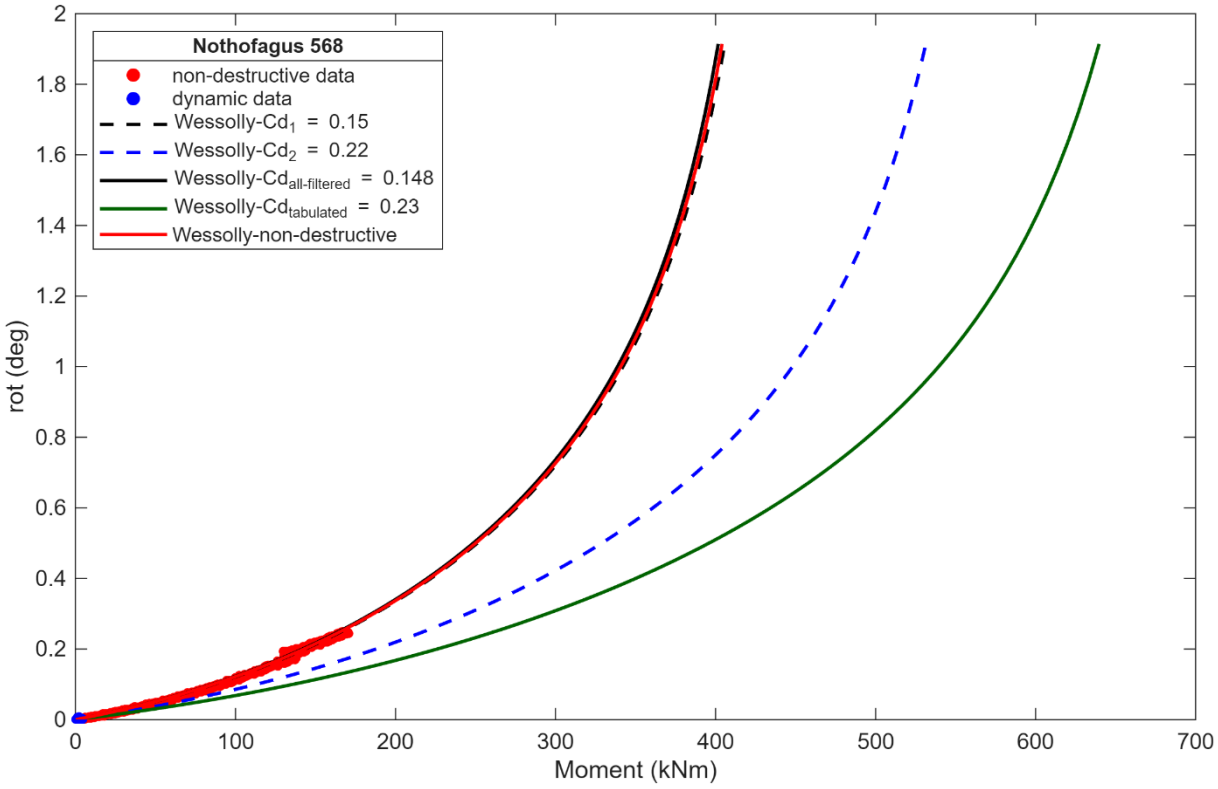

Figure A50: Wessolly's interpolation of the dynamic datasets (M-rot) obtained for each Cd values and comparison with non-destructive dataset.

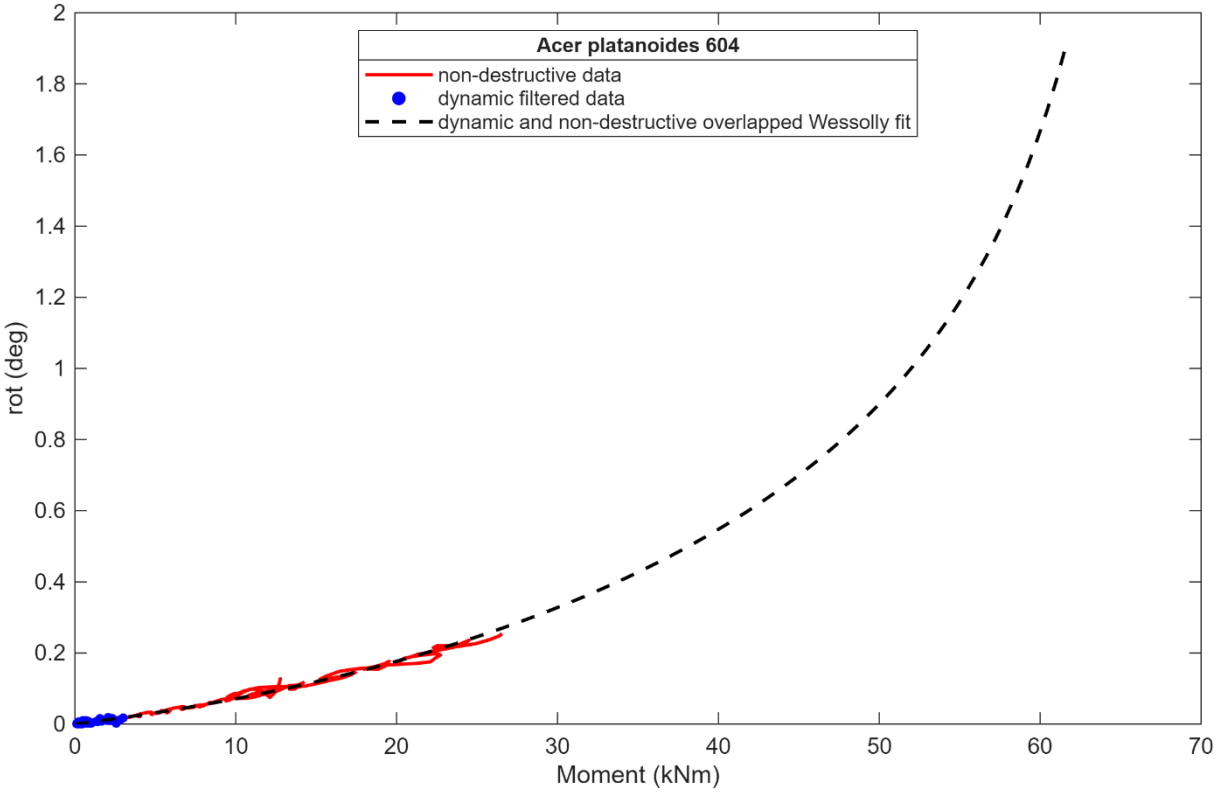

Figure A51: results of the iteration loop showing the overlayed Wessolly-fitted curves for both datasets.

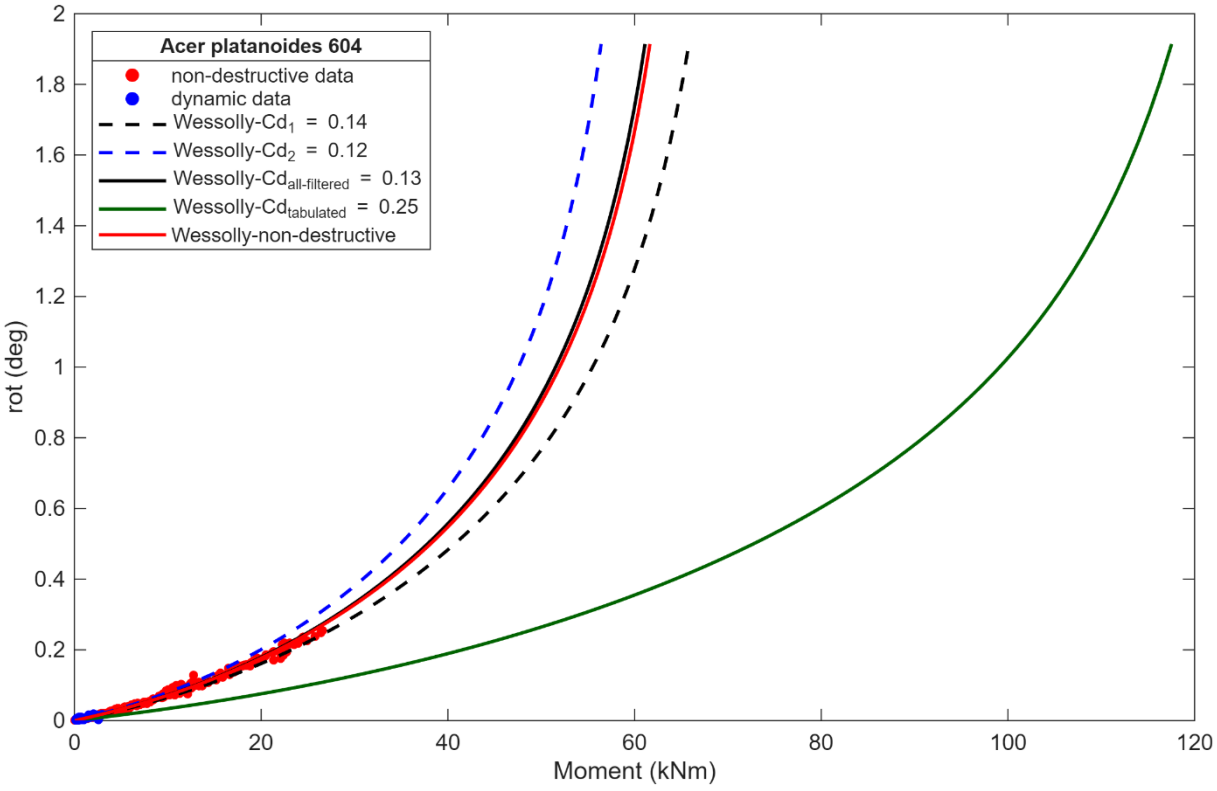

Figure A52: Wessolly's interpolation of the dynamic datasets (M-rot) obtained for each Cd values and comparison with non-destructive dataset.

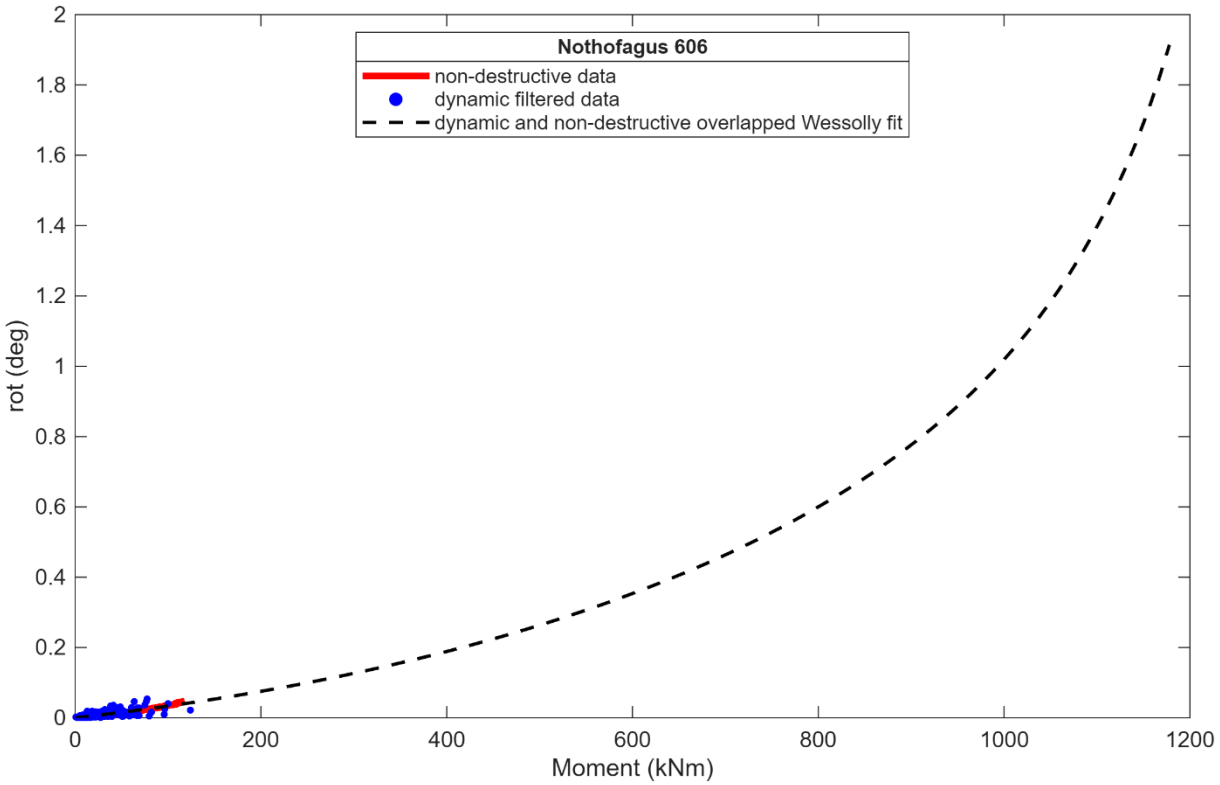

Figure A53: results of the iteration loop showing the overlayed Wessolly-fitted curves for both datasets.

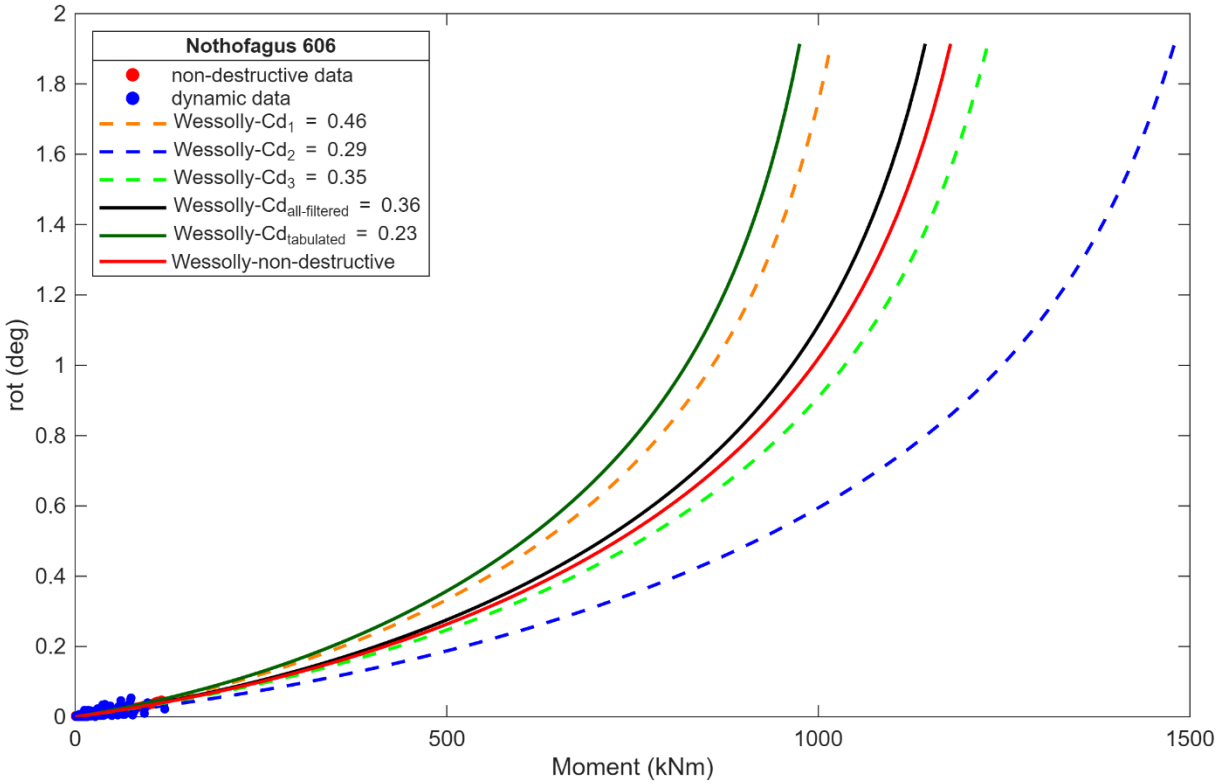

Figure A54: Wessolly's interpolation of the dynamic datasets (M-rot) obtained for each Cd values and comparison with non-destructive dataset.

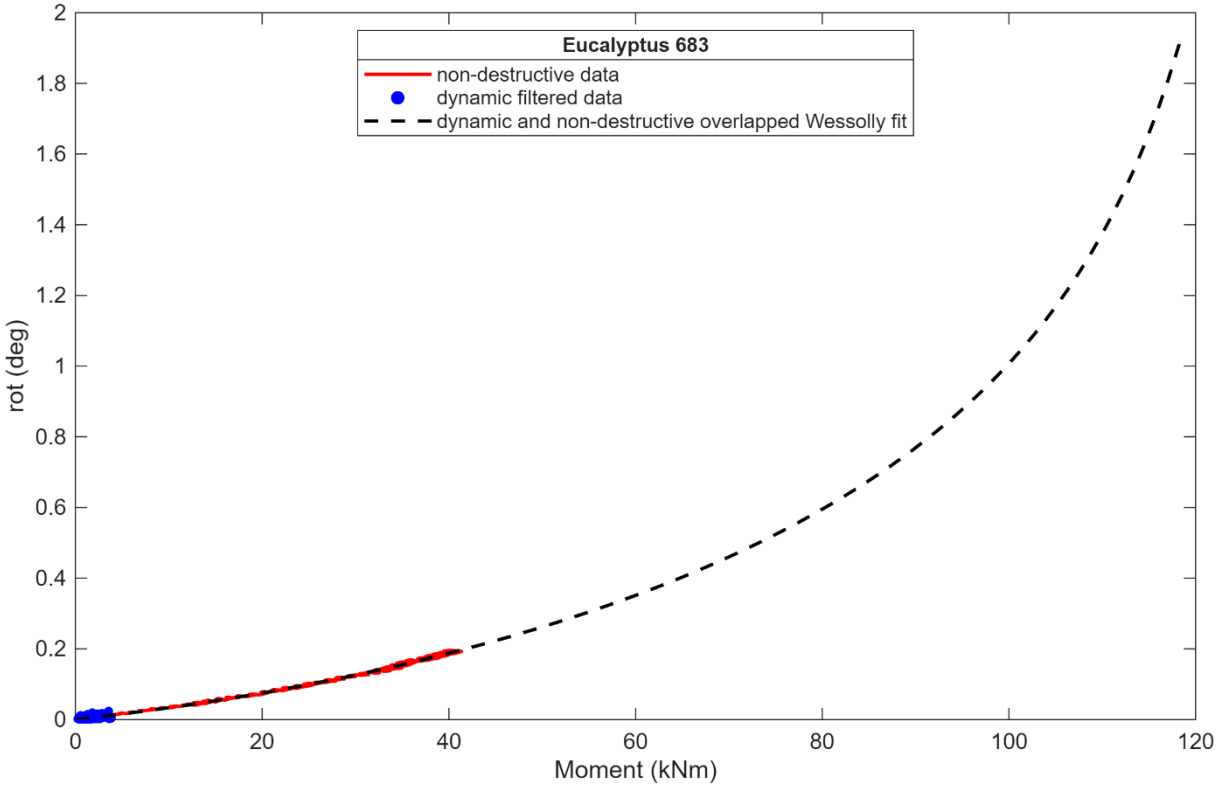

Figure A55: results of the iteration loop showing the overlayed Wessolly-fitted curves for both datasets.

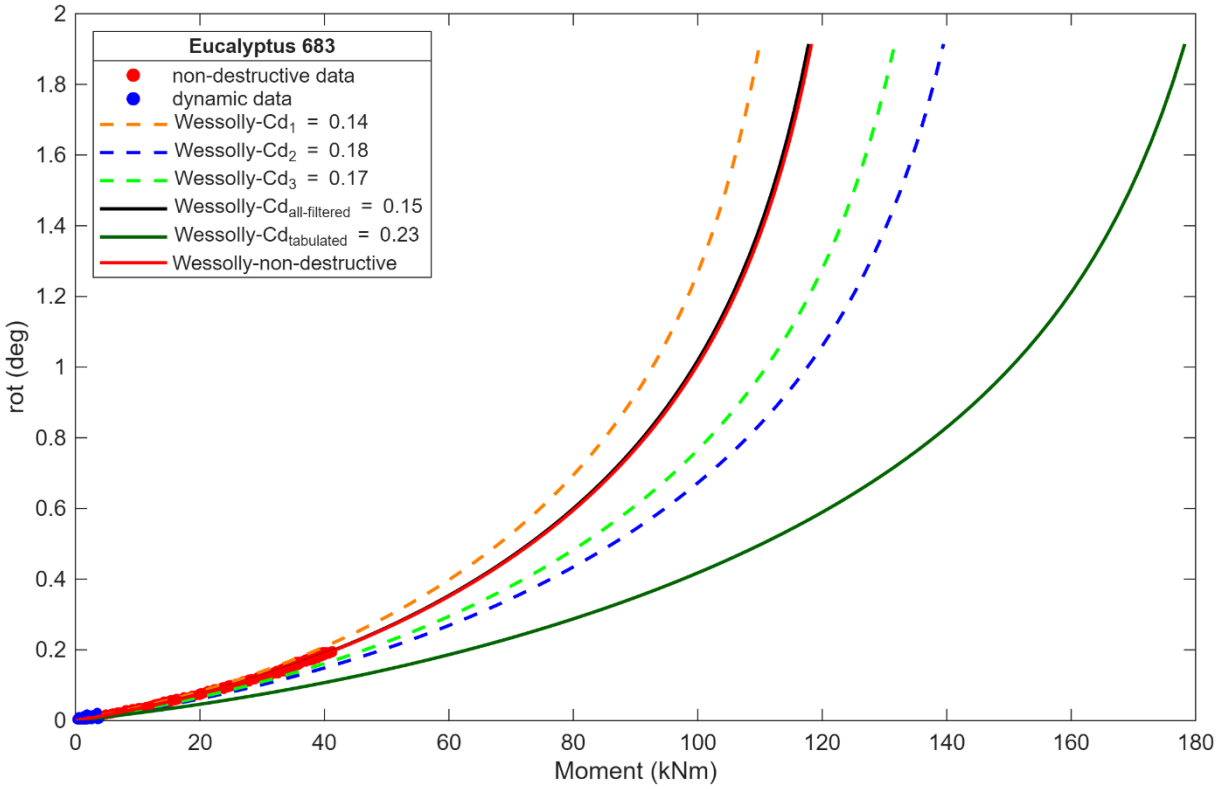

Figure A56: Wessolly's interpolation of the dynamic datasets (M-rot) obtained for each Cd values and comparison with non-destructive dataset.

Factors of Safety discussion

The F_S of a tree is typically determined by extrapolating the static pull test response and using the (Wessolly & Erb, 1998) curve to estimate the tree's maximum resisting moment. Static pull tests involve applying a force F at a height h and at an angle α to the horizontal ground surface, while recording the corresponding rotation φ of the root plate. The experimental data are then fit Wessolly & Erb (1998) equation.

The safety factor is then determined as:

$$F_s = \frac{M_L}{M_{wind}^{max}} \qquad \text{Eq. [20]}$$

where M_{wind}^{max} is calculated from the geometric parameters of the tree, the characteristic aerodynamic drag factor (C_D) of the given species and the expected maximum wind velocity value in the area:

$$M_{wind}^{max} = A_{cr} p_w^{max} C_d h_{cr} = A_{cr} \left(\frac{1}{2}\mu v_{max}^2\right) C_d h_{cr} \qquad \text{Eq. [21]}$$

where A_{cr} is the crown surface area, p_w^{max} is the maximum wind pressure (function of air density μ and maximum wind velocity v_{max}; p_w^{max} is e.g. equal to 667 Pa for v_{max} = 33m/s = 120km/h), C_D is the aerodynamic drag factor and h_{cr} is the crown centre point height as shown in Figure 61.

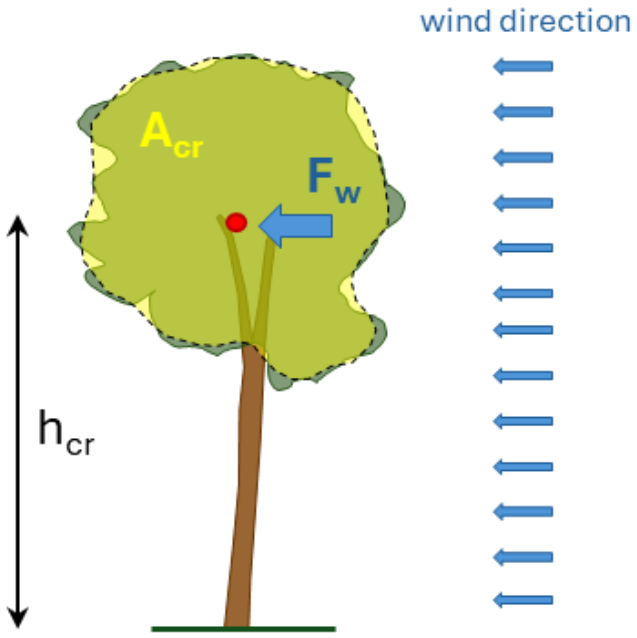

Figure 61: Schematic of geometries involved duirng wind loading force calcualtion.

This value is then compared with the overturning moment expected under a reference wind speed of 120 km/h. In the static determination of the safety factor, the pull-test curve is extrapolated until a rotation of 1.914° is reached; the moment at this extrapolated point is taken as ML. A complementary way to estimate ML is offered by the estimation of the response of the tree in dynamic conditions. As outlined in previous paragraph, the dynamic root evaluation replaces the controlled pulling test with simultaneous field measurements of wind loading and the associated root-plate response. The method relies on statistically pairing wind intensity (expressed as wind pressure) and inclination over moving time windows of a few minutes. Repeating the procedure across multiple intervals yields a set of mean pressure–inclination pairs that can be assembled into a pressure–inclination curve. This curve typically mirrors the functional relationship observed in the force–inclination response from static winching. As with the static approach, the curve can then be extrapolated to a limit pressure, which can be directly compared with the maximum wind pressure expected during severe wind events.
The Wessolly and Erb equation can be written as:

$$\varphi = \frac{1}{3}\tan\left(\frac{100}{73{,}85}\frac{p}{p_w^L}\right) + \frac{1}{2}\left(\frac{p}{p_w^L}\right)^2 - \frac{1}{10}\frac{p}{p_w^L} \qquad \text{Eq. [22]}$$

And from that M (from dynamic datasets) can be calculated with:

$$M = A_{cr} p_w C_D h_{cr} = A_{cr}\left(\frac{1}{2}\mu v^2\right) C_D h_{cr} \qquad \text{Eq. [23]}$$

So, now the Wessolly and Erb equation can be used even for the dynamic datasets to extrapolate the M_L. The reference overturning moments (Mwind,max) were computed using both Cd_{af} and Cd_{tab}, and are called *Mwind,max-*Cd_{af} (abbreviation = (1)) and *Mwind,max-*Cd_{tab} (abbreviation = (2)). These two values were then used to derive the following safety factors (using Eq. [20]):

- F_S from non-destructive M_L using (1);
- F_S from non-destructive M_L using (2);
- F_S from measured M_L using (1);
- F_S from measured M_L using (2);
- F_S from dynamic M_L (extrapolated with Cd_{af}) using (1);
- F_S from dynamic M_L (extrapolated with Cd_{af}) using (2);
- F_S from dynamic M_L (extrapolated with Cd_{tab}) using (1);

- F_S from dynamic M_L (extrapolated with Cd_{tab}) using (2);

All these values are grouped into Table 11

Table 11: resume of the safety factors calculated for each different type of Cd.

Tree ID	$M_{wind,max}$ Cd_{af}	$M_{wind,max}$ Cd_{tab}	F_S							
			non-destructive (1)	non-destructive (2)	Measured (1)	Measured (2)	Dynamic Cd-af (1)	Dynamic Cd-af (2)	Dynamic Cd-tab (1)	Dynamic Cd-tab (2)
433	13.61	21.26	2.30	1.47	3.34	2.14	2.19	1.40	3.52	2.25
434	20.86	38.35	2.08	1.13	2.56	1.39	2.08	1.13	3.51	1.91
260	51.23	38.42	1.36	1.82	2.05	2.74	1.38	1.83	1.17	1.57
268	25.92	21.21	4.84	5.91	4.76	5.81	4.76	5.81	4.32	5.28
568	66.63	103.55	21.62	13.92	-	-	6.03	3.88	9.60	6.18
258	-	30.54	-	2.12	-	2.53	-	-	-	-
270	-	32.69	-	0.77	-	1.59	-	-	-	-
158	-	43.55	-	6.65	-	-	-	-	-	-
604	23.98	46.11	2.58	1.34	-	-	2.55	1.33	4.90	2.55
451	155.23	267.63	9.28	5.38	-	-	8.74	5.07	16.53	9.59
606	363.06	309.27	3.26	3.82	-	-	3.15	3.70	2.69	3.15
142	89.32	44.66	2.08	4.16	-	-	2.04	4.09	1.02	2.04
383	-	10.72	-	7.58	-	8.30	-	-	-	-
682	107.15	136.92	1.76	1.38	1.71	1.33	1.73	1.35	2.34	1.83
683	41.32	63.36	2.87	1.87	4.74	3.09	2.85	1.86	4.31	1.87
143	182.49	57.63	1.71	5.40	2.30	7.29	1.70	5.37	0.54	1.72
234	20.41	21.61	3.68	3.48	5.59	5.28	3.71	3.51	3.87	3.65
243	-	18.16	-	3.24	-	3.91	-	-	-	-
392	19.02	21.61	2.07	1.82	1.91	1.38	2.03	1.79	2.30	2.04
394	28.01	50.03	3.10	1.74	3.31	1.74	3.02	1.69	5.35	2.99
971	38.42	42.69	6.11	5.50	5.96	5.36	6.03	5.42	6.53	5.88

The following considerations focus on the subset of trees for which the dataset is complete, i.e., those for which it was possible to obtain ML from uprooting tests, non-destructive tests, and dynamic monitoring. The trees involved are *Acer platanoides* (433, 434), *Pinus nigra* (260, 268, 143, 234), *Eucalyptus* (682, 683), *Quercus* (392, 394) and *Tsuga* 971 and their F_S values are plotted in Figure 62 where on the y-axes there's the F_S obtained from M_L measured from uprooting test with (1) and on the x-axes F_S obtained from M_L extrapolated from non-destructive test and dynamic datasets with both (1) and (2).

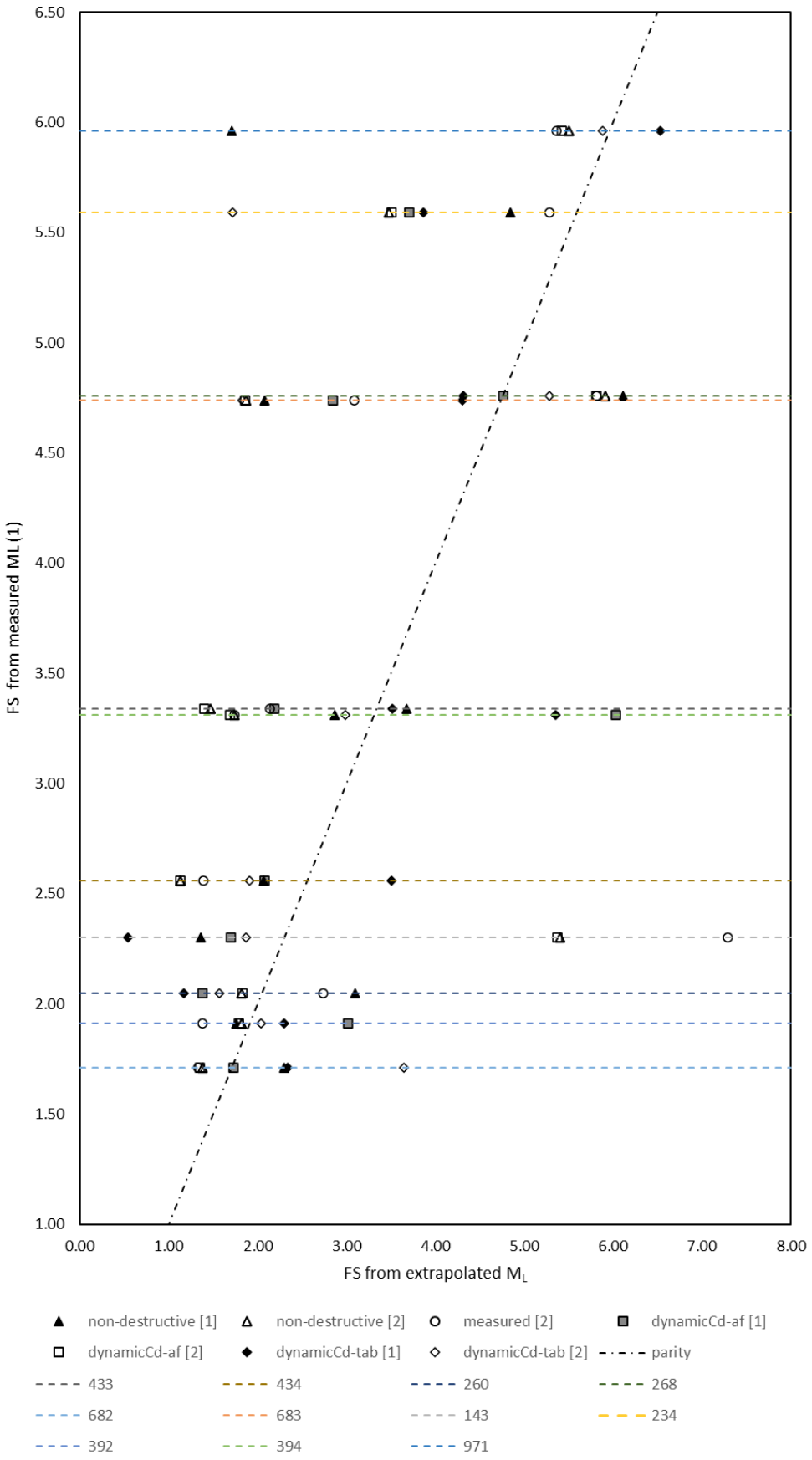

Figure 62: comparison among FS calculated form measured and extrapolated M_L

The ratio between the safety factors (FS) computed for each category (measured, non-destructive, and dynamic) using Mwind,max derived with Cdaf and with Cdtab is equal to:

- 1.56 for *Acer platanoides 433*;
- 1.84 for *Acer platanoides 434*;
- 0.75 for *Pinus nigra* 260;
- 0.82 for *Pinus nigra* 268;
- 1.29 for *Eucalyptus* 268;
- 1.53 for *Eucalyptus* 268;
- 0.32 for *Pinus nigra* 143;
- 1.06 for *Pinus nigra* 234;
- 1.38 for *Quercus* 392;
- 1.90 for *Quercus* 394;
- 1.11 for *Tsuga* 392;

Therefore, for eight out of the eleven trees, the safety factors computed with method (1) are higher than those obtained with (2). When the safety factor derived from measured data using (1) is compared against all the others (excluding the measured-data safety factor obtained with (2), which was already addressed above), the ratios computed with non-destructive data (1) and with dynamic Cd_{af} (1) are essentially the same, with the only notable exception being tree 433. Across the 66 ratios examined, equality was observed only in six cases (trees 268, 682, and 971). In fifteen comparisons, the safety factor from measured data using (1) was lower than the corresponding value, whereas in all remaining cases it was higher.

Technical data sheets

The summary of technical data sheets for each tree are shown.

433 Acer platanoides

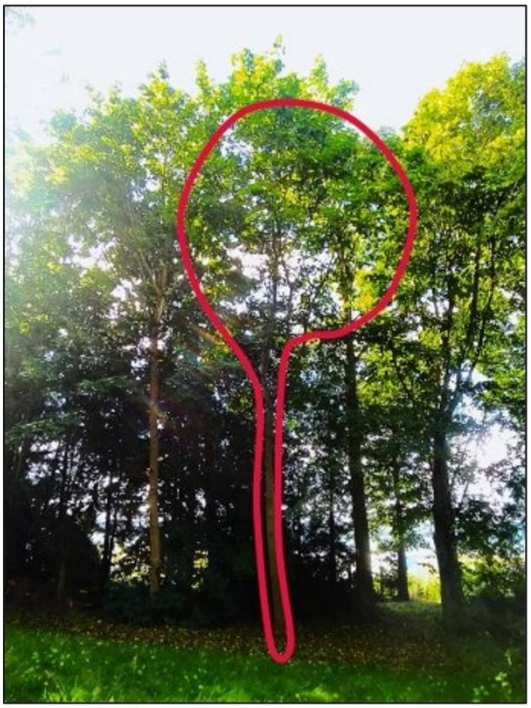

Biometric data	
DBH (cm)	23.24
H (m)	13.50
Acr (m^2)	15.00
hcr (m)	8.50
D1 (N-S) (m)	2.40
D2 (W-E) (m)	2.60
R2 (m)	-
Hrp (m)	0.50
Trp (m)	-
Zwetsoil (m)	0.15

Zone	Soil type	Test type			
		Standard	Uprooting	Multiple α	Dynamic
5	sandy loam	x	x	-	x

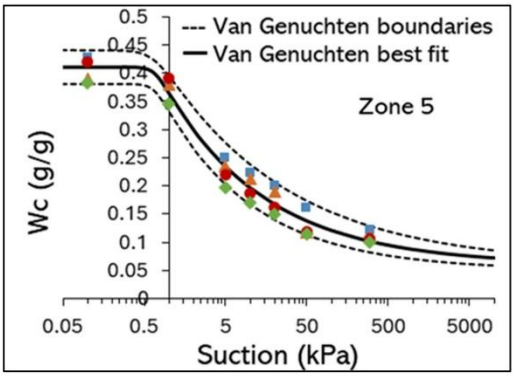

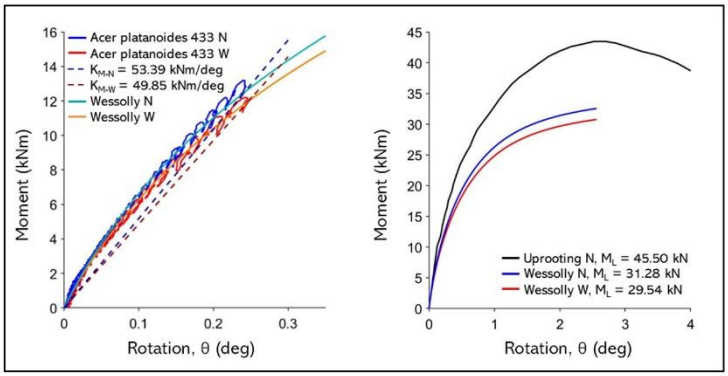

test direction	α (deg)	non-destructive pull test			uprooting			non-destructive dynamic				Mref	
		M_L (kNm)	θ_L (deg)	K_M (kNm/deg)	M_L (kNm)	θ_L (deg)	K_M (kNm/deg)	Cd_{af}	Cd_{tab}	$M_L\ Cd_{af}$ (kNm)	$M_L\ Cd_{tab}$ (kNm)	M_{ref} Cd_{af}	M_{ref} Cd_{tab}
N	17.6	31.3	1.914	53.4	45.5	2.61	62.4	0.16	0.25	29.76	47.92	13.6	21.3
W	21.9	29.5	1.914	49.8	-	-	-						

FS							
non-destructive [1]	non-destructive [2]	measured [1]	measured [2]	$dynamic_{Cd\text{-}af}$ [1]	$dynamic_{Cd\text{-}af}$ [2]	$dynamic_{Cd\text{-}tab}$ [1]	$dynamic_{Cd\text{-}tab}$ [2]
2.30	1.47	3.34	2.14	2.19	1.40	3.52	2.25

434 Acer platanoides

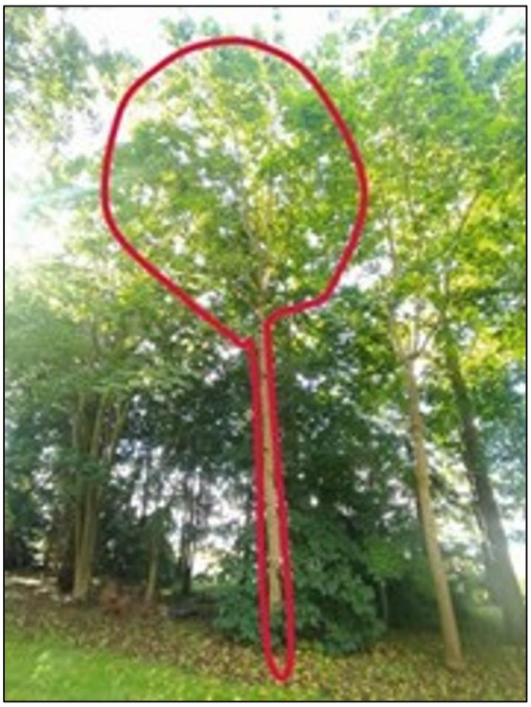

Biometric data	
DBH (cm)	27.06
H (m)	13.50
Acr (m^2)	23.00
hcr (m)	10.00
D1 (N-S) (m)	3.00
D2 (W-E) (m)	2.70
R2 (m)	-
Hrp (m)	0.50
Trp (m)	-
Zwetsoil (m)	-

Zone	Soil type	Test type			
		Standard	Uprooting	Multiple α	Dynamic
5	sandy loam	x	x	-	x

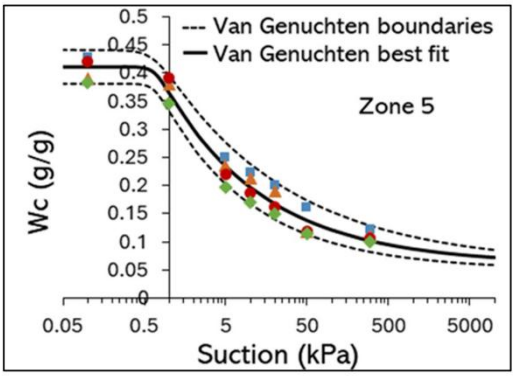

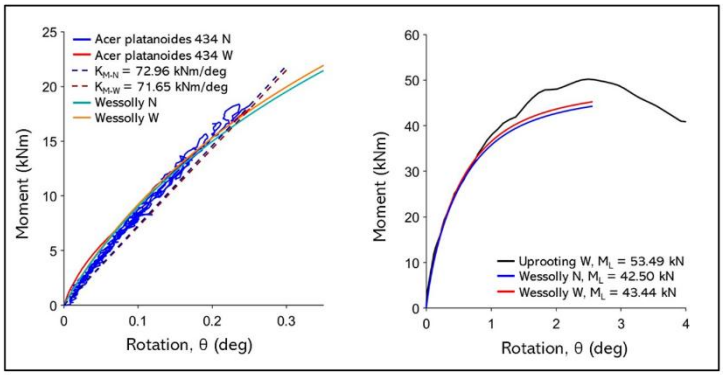

test direction	α (deg)	non-destructive pull test			uprooting			non-destructive dynamic				Mref	
		M_L (kNm)	θ_L (deg)	K_M (kNm/deg)	M_L (kNm)	θ_L (deg)	K_M (kNm/deg)	Cd_{af}	Cd_{tab}	$M_L\ Cd_{af}$ (kNm)	$M_L\ Cd_{tab}$ (kNm)	M_{ref} Cd_{af}	M_{ref} Cd_{tab}
N	23.4	23.4	1.914	73.0	-	-	-	0.14	0.25	43.3	73.1	20.9	38.4
W	21.3	12.3	1.914	71.7	53.5	2.93	72.6						

FS							
non-destructive [1]	non-destructive [2]	measured [1]	measured [2]	dynamic$_{Cd\text{-}af}$ [1]	dynamic$_{Cd\text{-}af}$ [2]	dynamic$_{Cd\text{-}tab}$ [1]	dynamic$_{Cd\text{-}tab}$ [2]
2.08	1.13	2.56	1.39	2.08	1.13	3.51	1.91

260 Pinus nigra

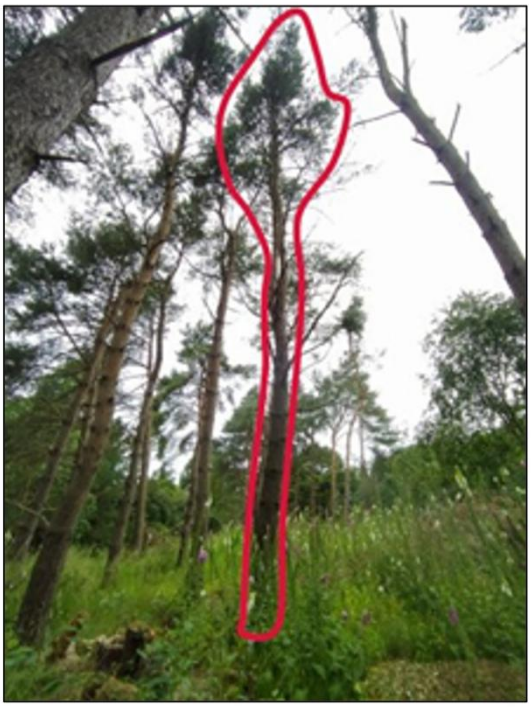

Biometric data	
DBH (cm)	37.56
H (m)	17.00
Acr (m^2)	20.00
hcr (m)	16.00
D1 (N-S) (m)	1.30
D2 (W-E) (m)	2.00
R2 (m)	-
Hrp (m)	0.70
Trp (m)	-
Zwetsoil (m)	-

Zone	Soil type	Test type			
		Standard	Uprooting	Multiple α	Dynamic
3	sandy loam	x	x	-	x

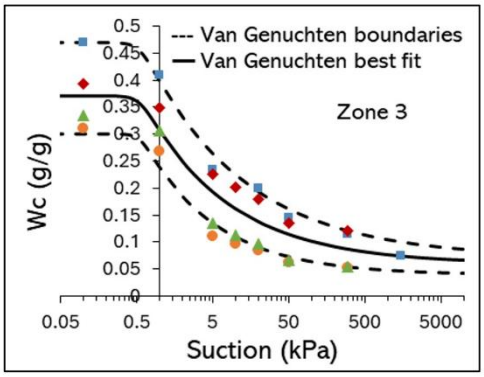

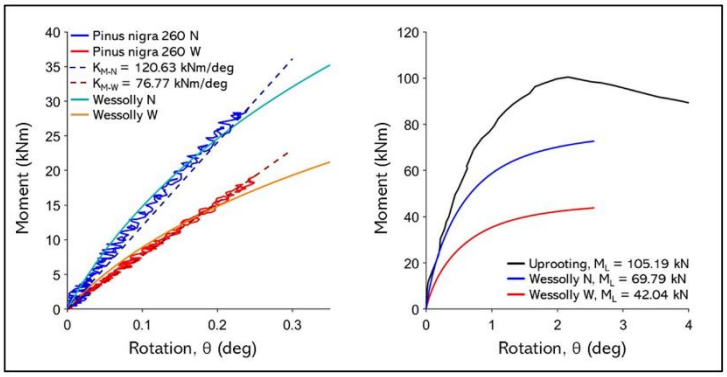

test direction	α (deg)	non-destructive pull test			uprooting			non-destructive dynamic				Mref	
		M_L (kNm)	θ_L (deg)	K_M (kNm/deg)	M_L (kNm)	θ_L (deg)	K_M (kNm/deg)	Cd_{af}	Cd_{tab}	$M_L\ Cd_{af}$ (kNm)	$M_L\ Cd_{tab}$ (kNm)	M_{ref} Cd_{af}	M_{ref} Cd_{tab}
N	16.6	69.8	1.914	120.6	105.2	2.15	130.0	0.24	0.18	70.4	60.2	51.2	38.4
W	17.8	42.0	1.914	76.8	-	-	-						

FS							
non-destructive [1]	non-destructive [2]	measured [1]	measured [2]	dynamic$_{Cd\text{-}af}$ [1]	dynamic$_{Cd\text{-}af}$ [2]	dynamic$_{Cd\text{-}tab}$ [1]	dynamic$_{Cd\text{-}tab}$ [2]
1.36	1.82	2.05	2.74	1.38	1.83	1.17	1.57

268 Pinus nigra

Biometric data	
DBH (cm)	44.56
H (m)	16.50
Acr (m^2)	13.80
hcr (m)	12.80
D1 (N-S) (m)	2.60
D2 (W-E) (m)	3.00
R2 (m)	-
Hrp (m)	0.60
Trp (m)	-
Zwetsoil (m)	0.45

Zone	Soil type	Test type			
		Standard	Uprooting	Multiple α	Dynamic
3	sandy loam	x	x	-	x

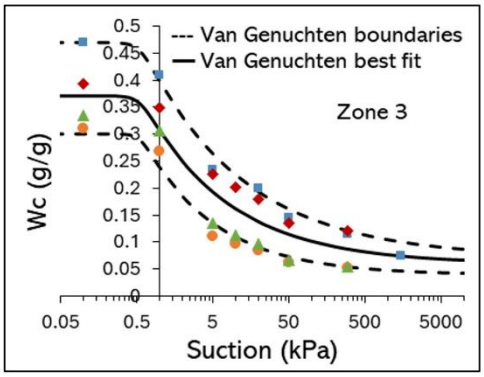

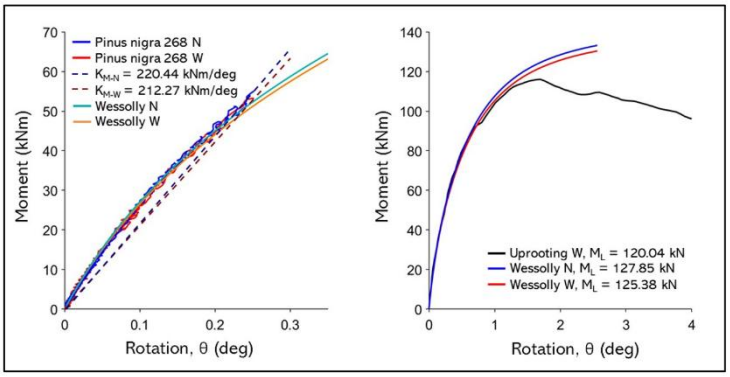

test direction	α (deg)	non-destructive pull test			uprooting			non-destructive dynamic				Mref	
		M_L (kNm)	θ_L (deg)	K_M (kNm/deg)	M_L (kNm)	θ_L (deg)	K_M (kNm/deg)	Cd_{af}	Cd_{tab}	$M_L\ Cd_{af}$ (kNm)	$M_L\ Cd_{tab}$ (kNm)	M_{ref} Cd_{af}	M_{ref} Cd_{tab}
N	11.8	127.9	1.914	220.4	-	-	-	0.22	0.18	123.3	111.9	25.9	21.2
W	16.3	125.4	1.914	212.3	120.0	2.6	206.6						

FS							
non-destructive [1]	non-destructive [2]	measured [1]	measured [2]	dynamic$_{Cd\text{-}af}$ [1]	dynamic$_{Cd\text{-}af}$ [2]	dynamic$_{Cd\text{-}tab}$ [1]	dynamic$_{Cd\text{-}tab}$ [2]
4.84	5.91	4.76	5.81	4.76	5.81	4.32	5.28

568 Nothofagus

Biometric data	
DBH (cm)	50.93
H (m)	15.60
Acr (m^2)	50.00
hcr (m)	13.50
D1 (N-S) (m)	-
D2 (W-E) (m)	-
R2 (m)	-
Hrp (m)	-
Trp (m)	-
Zwetsoil (m)	-

Zone	Soil type	Test type			
		Standard	Uprooting	Multiple α	Dynamic
5	sandy loam	x	-	-	x

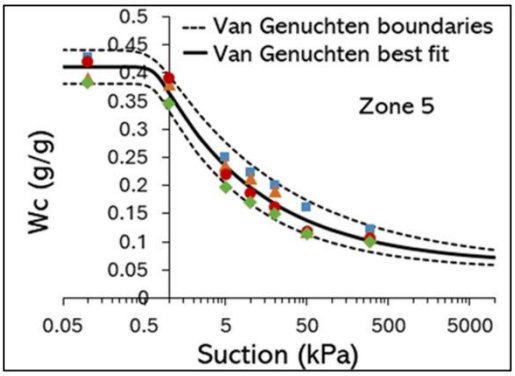

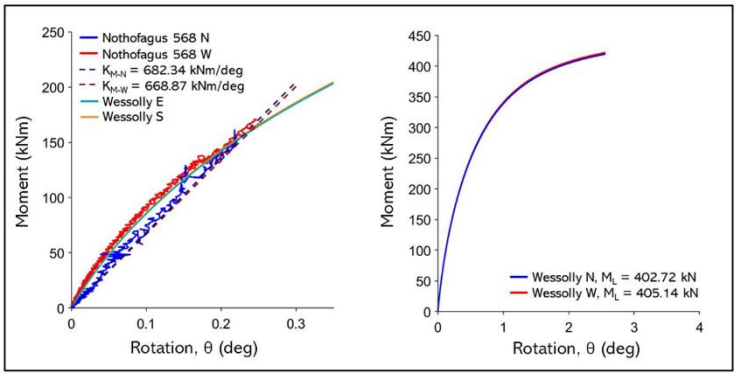

test direction	α (deg)	non-destructive pull test			uprooting			non-destructive dynamic				Mref	
		M_L (kNm)	θ_L (deg)	K_M (kNm/deg)	M_L (kNm)	θ_L (deg)	K_M (kNm/deg)	Cd_{af}	Cd_{tab}	$M_L\ Cd_{af}$ (kNm)	$M_L\ Cd_{tab}$ (kNm)	M_{ref} Cd_{af}	M_{ref} Cd_{tab}
N	20.9	402.7	1.914	682.3	-	-	-	0.15	0.22	401.7	639.7	66.6	103.6
W	20.2	405.1	1.914	668.9	-	-	-						

FS							
non-destructive [1]	non-destructive [2]	measured [1]	measured [2]	$dynamic_{Cd\text{-}cal}$ [1]	$dynamic_{Cd\text{-}af}$ [2]	$dynamic_{Cd\text{-}af}$ [1]	$dynamic_{Cd\text{-}tab}$ [2]
21.62	13.92	-	-	6.03	3.88	9.60	6.18

258 Pinus nigra

Biometric data	
DBH (cm)	35.65
H (m)	17.00
Acr (m^2)	15.70
hcr (m)	16.20
D1 (N-S) (m)	2.20
D2 (W-E) (m)	1.40
R2 (m)	-
Hrp (m)	0.90
Trp (m)	-
Zwetsoil (m)	0.65

Zone	Soil type	Test type			
		Standard	Uprooting	Multiple α	Dynamic
3	sandy loam	x	x	x	-

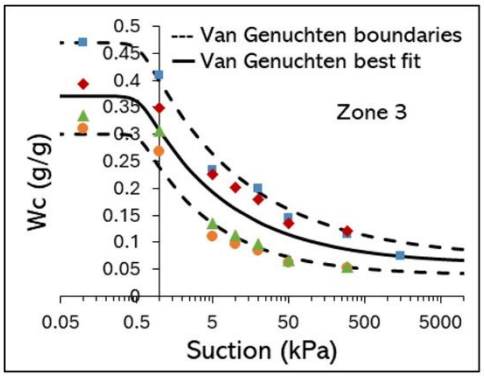

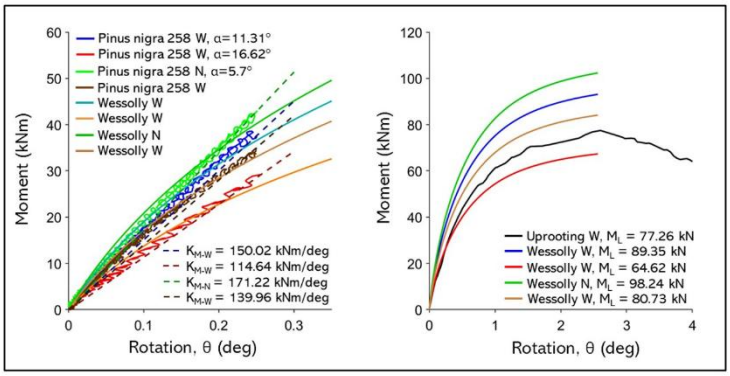

test direction	α (deg)	non-destructive pull test			uprooting			non-destructive dynamic				Mref	
		M_L (kNm)	θ_L (deg)	K_M (kNm/deg)	M_L (kNm)	θ_L (deg)	K_M (kNm/deg)	Cd_{af}	Cd_{tab}	$M_L\ Cd_{af}$ (kNm)	$M_L\ Cd_{tab}$ (kNm)	M_{ref} Cd_{af}	M_{ref} Cd_{tab}
N	5.7	98.2	1.914	171.2	-	-	-						
N	11.3	89.4	1.914	150.0	-	-	-						
N	16.7	80.7	1.914	134.0	-	-	-	-	0.18	-	-	-	30.5
W	16.6	64.6	1.914	114.6	77.3	2.61	107.2						

FS							
non-destructive [1]	non-destructive [2]	measured [1]	measured [2]	$dynamic_{Cd\text{-}af}$ [1]	$dynamic_{Cd\text{-}af}$ [2]	$dynamic_{Cd\text{-}tab}$ [1]	$dynamic_{Cd\text{-}tab}$ [2]
-	2.12	-	2.53	-	-	-	-

270 Pinus nigra

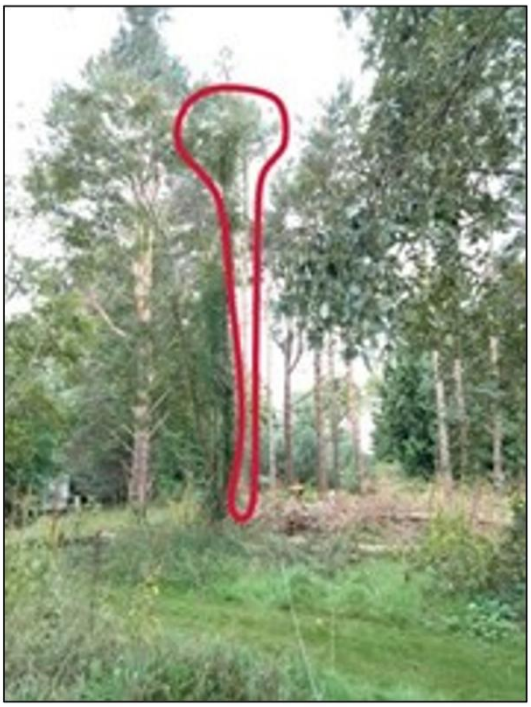

Biometric data	
DBH (cm)	28.65
H (m)	17.60
Acr (m^2)	11.70
hcr (m)	16.70
D1 (N-S) (m)	2.00
D2 (W-E) (m)	1.50
R2 (m)	-
Hrp (m)	0.80
Trp (m)	-
Zwetsoil (m)	0.60

Zone	Soil type	Test type			
		Standard	Uprooting	Multiple α	Dynamic
3	sandy loam	x	x	x	-

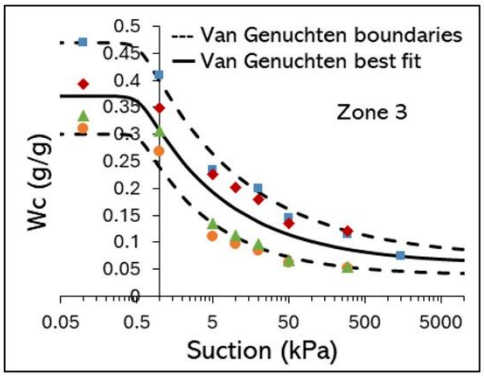

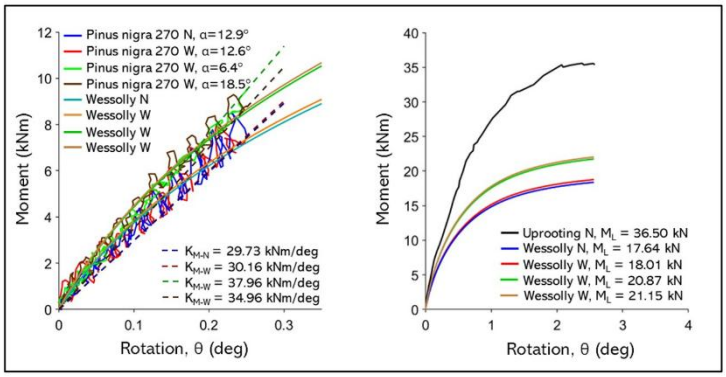

test direction	α (deg)	non-destructive pull test			uprooting			non-destructive dynamic				Mref	
		M_L (kNm)	θ_L (deg)	K_M (kNm/deg)	M_L (kNm)	θ_L (deg)	K_M (kNm/deg)	Cd_{af}	Cd_{tab}	$M_L\ Cd_{af}$ (kNm)	$M_L\ Cd_{tab}$ (kNm)	M_{ref} Cd_{af}	M_{ref} Cd_{tab}
N	12.9	17.6	1.914	29.7	36.5	2.4	43.7						
W	6.4	20.9	1.914	38.0	-	-	-						
W	12.6	18.0	1.914	30.2	-	-	-	-	0.18	-	-	-	32.7
W	18.5	21.2	1.914	35.0	-	-	-						

FS							
non-destructive [1]	non-destructive [2]	measured [1]	measured [2]	dynamic$_{Cd\text{-}af}$ [1]	dynamic$_{Cd\text{-}af}$ [2]	dynamic$_{Cd\text{-}tab}$ [1]	dynamic$_{Cd\text{-}tab}$ [2]
-	0.77	-	1.59	-	-	-	-

158 Picea abies

Biometric data	
DBH (cm)	54.11
H (m)	20.00
Acr (m^2)	17.00
hcr (m)	19.20
D1 (N-S) (m)	-
D2 (W-E) (m)	-
R2 (m)	-
Hrp (m)	-
Trp (m)	-
Zwetsoil (m)	-

Zone	Soil type	Test type			
		Standard	Uprooting	Multiple α	Dynamic
2	sandy loam	x	-	x	-

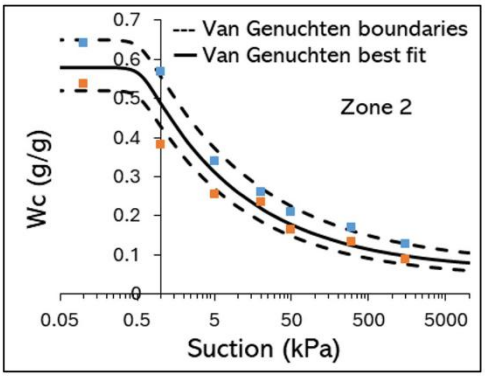

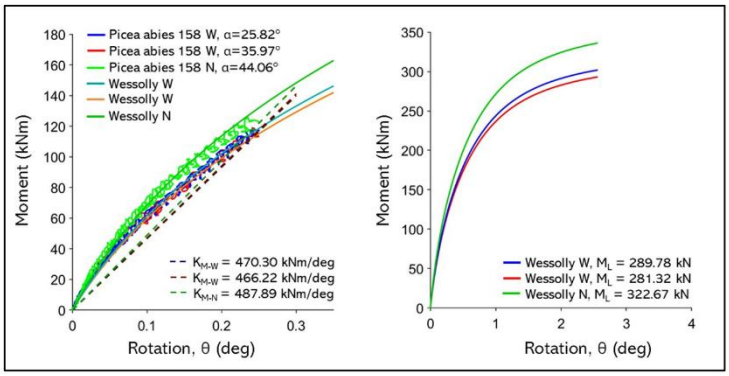

test direction	α (deg)	non-destructive pull test			uprooting			non-destructive dynamic				Mref	
		M_L (kNm)	θ_L (deg)	K_M (kNm/deg)	M_L (kNm)	θ_L (deg)	K_M (kNm/deg)	Cd_{af}	Cd_{tab}	$M_L\ Cd_{af}$ (kNm)	$M_L\ Cd_{tab}$ (kNm)	M_{ref} Cd_{af}	M_{ref} Cd_{tab}
W	25.8	289.8	1.914	470.3	-	-	-						
W	36.0	281.3	1.914	466.2	-	-	-	-	0.20	-	-	-	43.6
W	44.1	322.7	1.914	488.0	-	-	-						

FS							
non-destructive [1]	non-destructive [2]	measured [1]	measured [2]	$dynamic_{Cd\text{-}af}$ [1]	$dynamic_{Cd\text{-}af}$ [2]	$dynamic_{Cd\text{-}tab}$ [1]	$dynamic_{Cd\text{-}tab}$ [2]
-	6.65	-	-	-	-	-	-

604 Acer platanoides

Biometric data	
DBH (cm)	41.38
H (m)	9.30
Acr (m^2)	35.00
hcr (m)	7.90
D1 (N-S) (m)	-
D2 (W-E) (m)	-
R2 (m)	-
Hrp (m)	-
Trp (m)	-
Zwetsoil (m)	-

Zone	Soil type	Test type			
		Standard	Uprooting	Multiple α	Dynamic
5	sandy loam	x	-	-	x

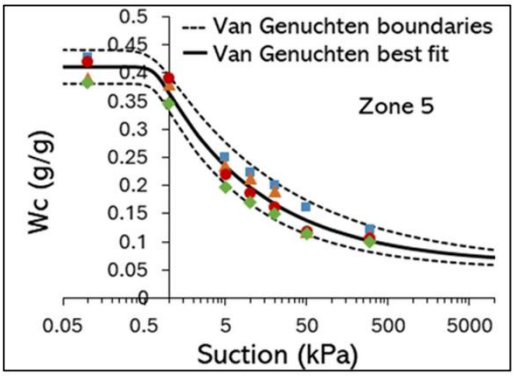

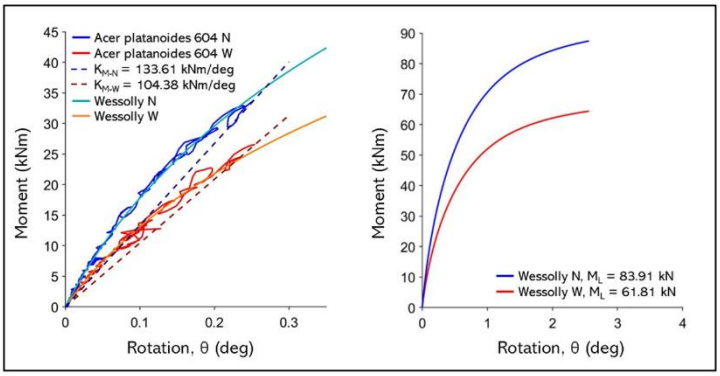

test direction	α (deg)	non-destructive pull test			uprooting			non-destructive dynamic				Mref	
		M_L (kNm)	θ_L (deg)	K_M (kNm/deg)	M_L (kNm)	θ_L (deg)	K_M (kNm/deg)	Cd_{af}	Cd_{tab}	$M_L\ Cd_{af}$ (kNm)	$M_L\ Cd_{tab}$ (kNm)	M_{ref} Cd_{af}	M_{ref} Cd_{tab}
N	17.7	133.6	1.914	83.9	-	-	-	0.13	0.25	61.1	117.5	23.9	46.1
W	15.2	104.4	1.914	61.8	-	-	-						

FS							
non-destructive [1]	non-destructive [2]	measured [1]	measured [2]	$dynamic_{Cd\text{-}cal}$ [1]	$dynamic_{Cd\text{-}af}$ [2]	$dynamic_{Cd\text{-}af}$ [1]	$dynamic_{Cd\text{-}tab}$ [2]
2.58	1.34	-	-	2.55	1.33	4.90	2.55

451 Acer platanoides

Biometric data	
DBH (cm)	120.00
H (m)	20.00
Acr (m^2)	107.00
hcr (m)	15.00
D1 (N-S) (m)	-
D2 (W-E) (m)	-
R2 (m)	-
Hrp (m)	-
Trp (m)	-
Zwetsoil (m)	-

Zone	Soil type	Test type			
		Standard	Uprooting	Multiple α	Dynamic
5	sandy loam	x	-	-	x

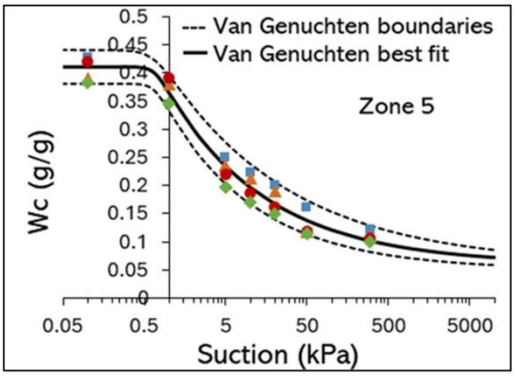

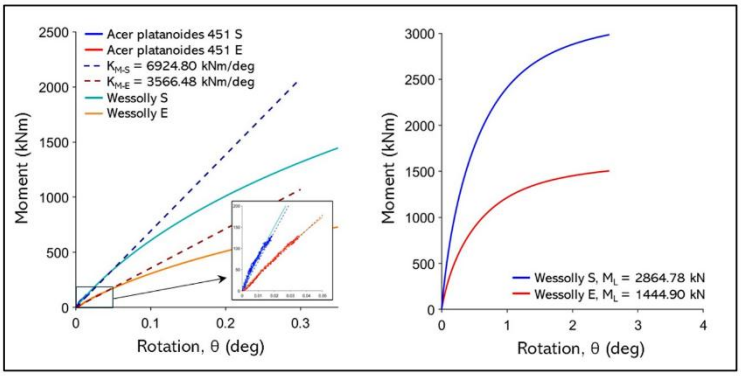

test direction	α (deg)	non-destructive pull test			uprooting			non-destructive dynamic				Mref	
		M_L (kNm)	θ_L (deg)	K_M (kNm/deg)	M_L (kNm)	θ_L (deg)	K_M (kNm/deg)	Cd_{af}	Cd_{tab}	$M_L\ Cd_{af}$ (kNm)	$M_L\ Cd_{tab}$ (kNm)	M_{ref} Cd_{af}	M_{ref} Cd_{tab}
E	16.0	1444.9	1.914	3566.5	-	-	-	0.15	0.25	1356.2	2566.2	155.2	267.6
S	26.3	2864.8	1.914	6924.8	-	-	-						

FS							
non-destructive [1]	non-destructive [2]	measured [1]	measured [2]	$dynamic_{Cd\text{-}cal}$ [1]	$dynamic_{Cd\text{-}af}$ [2]	$dynamic_{Cd\text{-}af}$ [1]	$dynamic_{Cd\text{-}tab}$ [2]
9.28	5.38	-	-	8.74	5.07	16.53	9.59

606 Nothofagus

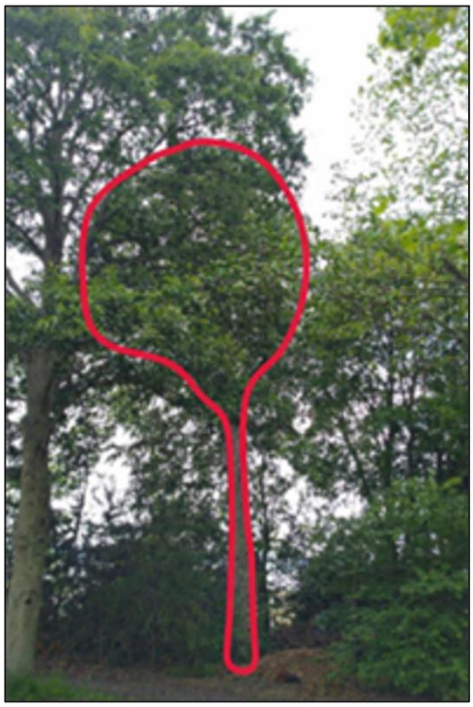

Biometric data	
DBH (cm)	85.00
H (m)	25.00
Acr (m^2)	112.00
hcr (m)	18.00
D1 (N-S) (m)	-
D2 (W-E) (m)	-
R2 (m)	-
Hrp (m)	-
Trp (m)	-
Zwetsoil (m)	-

Zone	Soil type	Test type			
		Standard	Uprooting	Multiple α	Dynamic
5	sandy loam	x	-	-	x

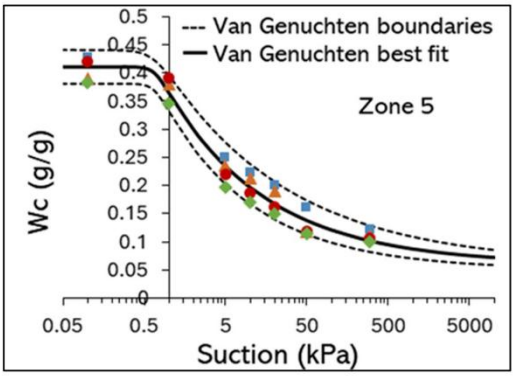

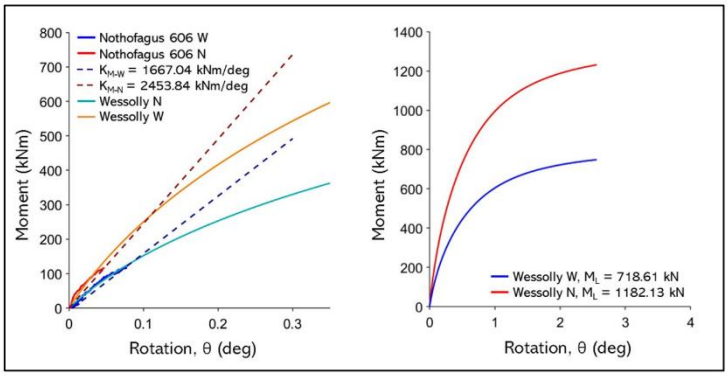

test direction	α (deg)	non-destructive pull test			uprooting			non-destructive dynamic				Mref	
		M_L (kNm)	θ_L (deg)	K_M (kNm/deg)	M_L (kNm)	θ_L (deg)	K_M (kNm/deg)	Cd_{af}	Cd_{tab}	$M_L\ Cd_{af}$ (kNm)	$M_L\ Cd_{tab}$ (kNm)	M_{ref} Cd_{af}	M_{ref} Cd_{tab}
N	24.8	1182.1	1.914	2453.8	-	-	-	0.27	0.22	1143.9	974.9	363.1	309.3
W	25.2	718.6	1.914	1667.0	-	-	-						

FS							
non-destructive [1]	non-destructive [2]	measured [1]	measured [2]	$dynamic_{Cd\text{-}cal}$ [1]	$dynamic_{Cd\text{-}af}$ [2]	$dynamic_{Cd\text{-}af}$ [1]	$dynamic_{Cd\text{-}tab}$ [2]
3.26	3.82	-	-	3.15	3.70	2.69	3.15

142 Pinus nigra

Biometric data	
DBH (cm)	53.00
H (m)	18.00
Acr (m^2)	31.00
hcr (m)	12.00
D1 (N-S) (m)	-
D2 (W-E) (m)	-
R2 (m)	-
Hrp (m)	-
Trp (m)	-
Zwetsoil (m)	-

Zone	Soil type	Test type			
		Standard	Uprooting	Multiple α	Dynamic
1	sandy loam	x	-	-	x

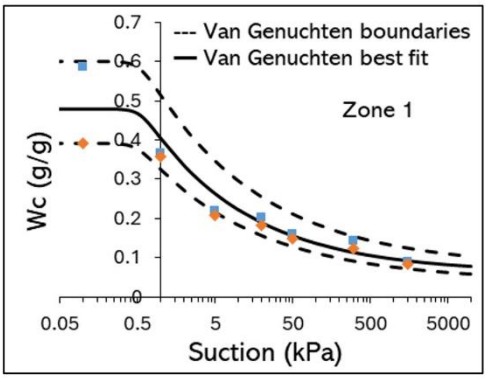

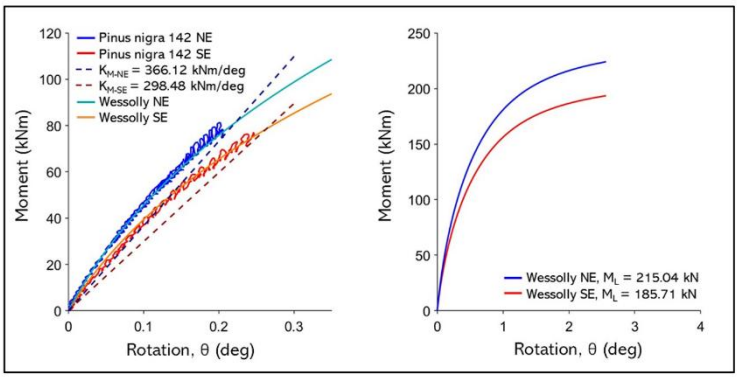

test direction	α (deg)	non-destructive pull test			uprooting			non-destructive dynamic				Mref	
		M_L (kNm)	θ_L (deg)	K_M (kNm/deg)	M_L (kNm)	θ_L (deg)	K_M (kNm/deg)	Cd_{af}	Cd_{tab}	$M_L\ Cd_{af}$ (kNm)	$M_L\ Cd_{tab}$ (kNm)	M_{ref} Cd_{af}	M_{ref} Cd_{tab}
SE	25.7	185.7	1.914	298.5	-	-	-	0.36	0.18	182.6	91.3	89.3	44.7
NE	20.2	215.0	1.914	366.1	-	-	-						

FS							
non-destructive [1]	non-destructive [2]	measured [1]	measured [2]	$dynamic_{Cd\text{-}af}$ [1]	$dynamic_{Cd\text{-}af}$ [2]	$dynamic_{Cd\text{-}tab}$ [1]	$dynamic_{Cd\text{-}tab}$ [2]
2.08	4.16	-	-	2.04	4.09	1.02	2.04

383 Betula

PICTURE
NOT AVAILABLE

Biometric data	
DBH (cm)	52.00
H (m)	13.00
Acr (m^2)	14.10
hcr (m)	9.50
D1 (N-S) (m)	3.00
D2 (W-E) (m)	2.30
R2 (m)	1.50
Hrp (m)	0.70
Trp (m)	-
Zwetsoil (m)	-

Zone	Soil type	Test type			
		Standard	Uprooting	Multiple α	Dynamic
3	sandy loam	x	x	-	-

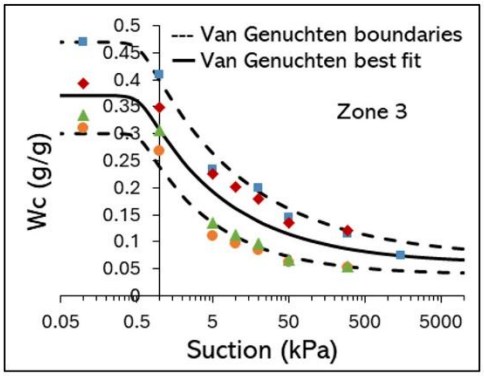

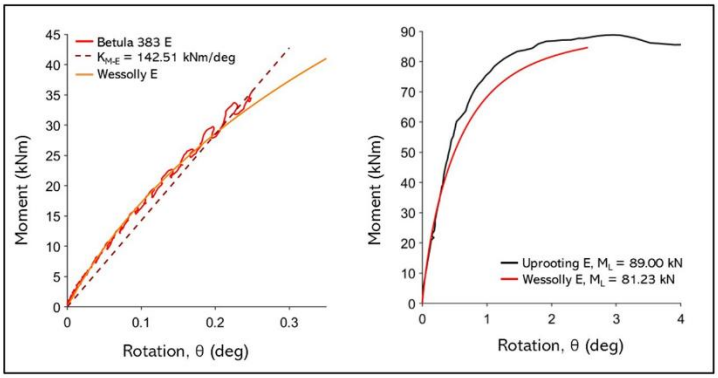

test direction	α (deg)	non-destructive pull test			uprooting			non-destructive dynamic				Mref	
		M_L (kNm)	θ_L (deg)	K_M (kNm/deg)	M_L (kNm)	θ_L (deg)	K_M (kNm/deg)	Cd_{af}	Cd_{tab}	$M_L\ Cd_{af}$ (kNm)	$M_L\ Cd_{tab}$ (kNm)	M_{ref} Cd_{af}	M_{ref} Cd_{tab}
E	20.8	81.2	1.914	142.5	89.0	2.90	130.8	-	0.12	-	-	-	10.7

FS							
non-destructive [1]	non-destructive [2]	measured [1]	measured [2]	$dynamic_{Cd\text{-}af}$ [1]	$dynamic_{Cd\text{-}af}$ [2]	$dynamic_{Cd\text{-}tab}$ [1]	$dynamic_{Cd\text{-}tab}$ [2]
-	7.58	-	8.30	-	-	-	-

682 Eucalyptus

Biometric data	
DBH (cm)	72.00
H (m)	16.00
Acr (m^2)	85.00
hcr (m)	10.50
D1 (N-S) (m)	-
D2 (W-E) (m)	-
R2 (m)	-
Hrp (m)	-
Trp (m)	-
Zwetsoil (m)	-

Zone	Soil type	Test type			
		Standard	Uprooting	Multiple α	Dynamic
6	sandy loam	x	x	-	x

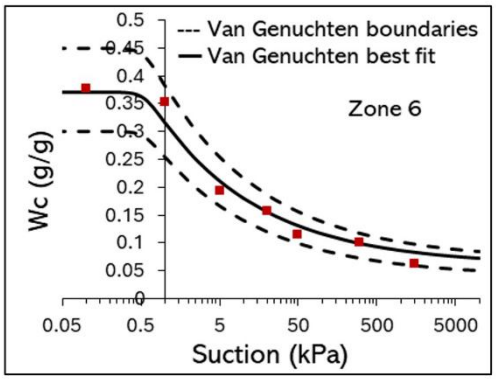

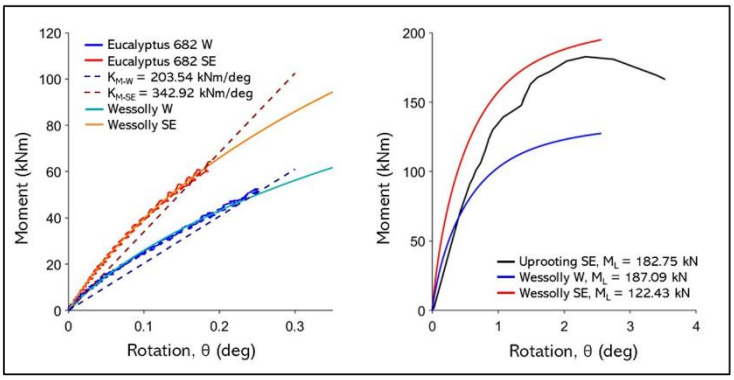

test direction	α (deg)	non-destructive pull test			uprooting			non-destructive dynamic				Mref	
		M_L (kNm)	θ_L (deg)	K_M (kNm/deg)	M_L (kNm)	θ_L (deg)	K_M (kNm/deg)	Cd_{af}	Cd_{tab}	$M_L\ Cd_{af}$ (kNm)	$M_L\ Cd_{tab}$ (kNm)	M_{ref} Cd_{af}	M_{ref} Cd_{tab}
SE	14.0	187.1	1.914	342.9	182.8	2.3	219.5	0.18	0.22	184.9	250.5	107.2	136.9
W	9.9	122.4	1.914	203.5	-	-	-						

FS							
non-destructive [1]	non-destructive [2]	measured [1]	measured [2]	$dynamic_{Cd\text{-}af}$ [1]	$dynamic_{Cd\text{-}af}$ [2]	$dynamic_{Cd\text{-}tab}$ [1]	$dynamic_{Cd\text{-}tab}$ [2]
1.76	1.38	1.71	1.33	1.73	1.35	2.34	1.83

683 Eucalyptus

Biometric data	
DBH (cm)	69.00
H (m)	15.00
Acr (m^2)	38.60
hcr (m)	10.70
D1 (N-S) (m)	1.60
D2 (W-E) (m)	1.10
R2 (m)	-
Hrp (m)	1.20
Trp (m)	1.00
Zwetsoil (m)	-

Zone	Soil type	Test type			
		Standard	Uprooting	Multiple α	Dynamic
6	sandy loam	x	x	-	x

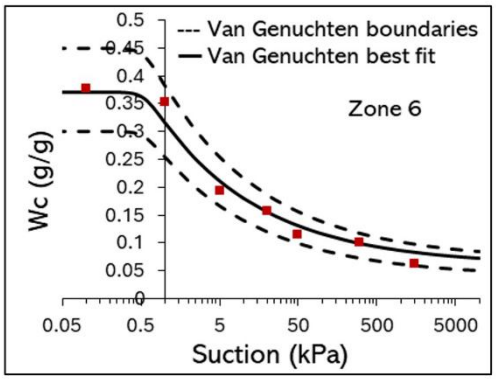

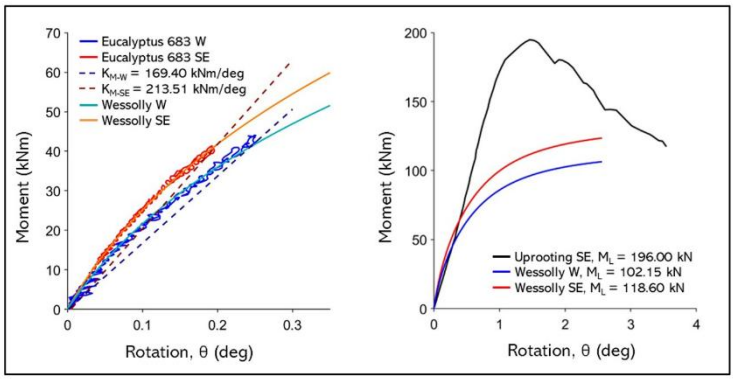

test direction	α (deg)	non-destructive pull test			uprooting			non-destructive dynamic				Mref	
		M_L (kNm)	θ_L (deg)	K_M (kNm/deg)	M_L (kNm)	θ_L (deg)	K_M (kNm/deg)	Cd_{af}	Cd_{tab}	$M_L\ Cd_{af}$ (kNm)	$M_L\ Cd_{tab}$ (kNm)	M_{ref} Cd_{af}	M_{ref} Cd_{tab}
SE	14.0	118.6	1.914	213.5	196.0	1.80	153.1	0.15	0.22	117.8	178.3	41.3	63.4
W	11.8	102.2	1.914	169.4	-	-	-						

FS							
non-destructive [1]	non-destructive [2]	measured [1]	measured [2]	dynamic$_{Cd\text{-}af}$ [1]	dynamic$_{Cd\text{-}af}$ [2]	dynamic$_{Cd\text{-}tab}$ [1]	dynamic$_{Cd\text{-}tab}$ [2]
2.87	1.87	4.74	3.09	2.85	1.86	4.31	1.87

143 Pinus nigra

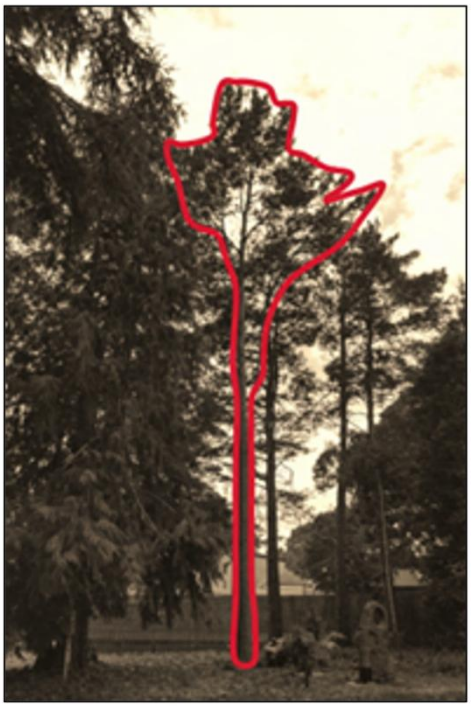

Biometric data	
DBH (cm)	51.00
H (m)	17.70
Acr (m^2)	30.00
hcr (m)	16.00
D1 (N-S) (m)	2.70
D2 (W-E) (m)	1.50
R2 (m)	0.51
Hrp (m)	0.80
Trp (m)	0.4
Zwetsoil (m)	-

Zone	Soil type	Test type			
		Standard	Uprooting	Multiple α	Dynamic
1	sandy loam	x	x	-	x

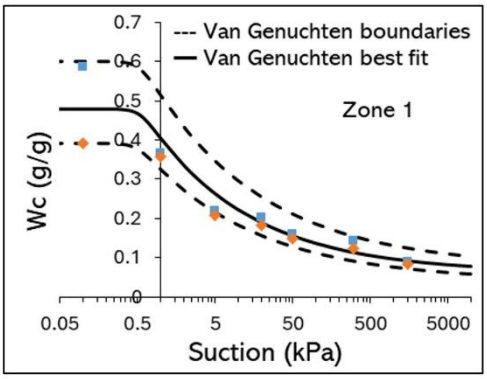

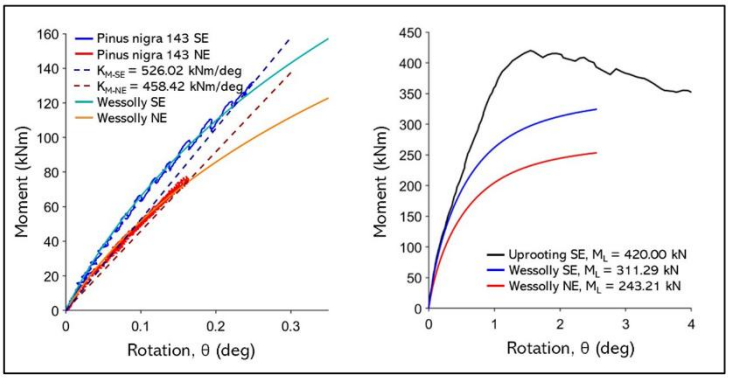

test direction	α (deg)	non-destructive pull test			uprooting			non-destructive dynamic				Mref	
		M_L (kNm)	θ_L (deg)	K_M (kNm/deg)	M_L (kNm)	θ_L (deg)	K_M (kNm/deg)	Cd_{af}	Cd_{tab}	$M_L\ Cd_{af}$ (kNm)	$M_L\ Cd_{tab}$ (kNm)	M_{ref} Cd_{af}	M_{ref} Cd_{tab}
SE	35.7	311.3	1.914	526.0	420.0	1.60	578.0	0.57	0.18	309.6	99.3	182.5	57.6
NE	24.1	243.2	1.914	458.4	-	-	-						

FS							
non-destructive [1]	non-destructive [2]	measured [1]	measured [2]	$dynamic_{Cd\text{-}af}$ [1]	$dynamic_{Cd\text{-}af}$ [2]	$dynamic_{Cd\text{-}tab}$ [1]	$dynamic_{Cd\text{-}tab}$ [2]
1.71	5.40	2.30	7.29	1.70	5.37	0.54	1.72

234 Pinus nigra

Biometric data	
DBH (cm)	48.00
H (m)	12.67
Acr (m^2)	20.00
hcr (m)	9.00
D1 (N-S) (m)	-
D2 (W-E) (m)	-
R2 (m)	-
Hrp (m)	-
Trp (m)	-
Zwetsoil (m)	-

Zone	Soil type	Test type			
		Standard	Uprooting	Multiple α	Dynamic
3	sandy loam	x	x	-	x

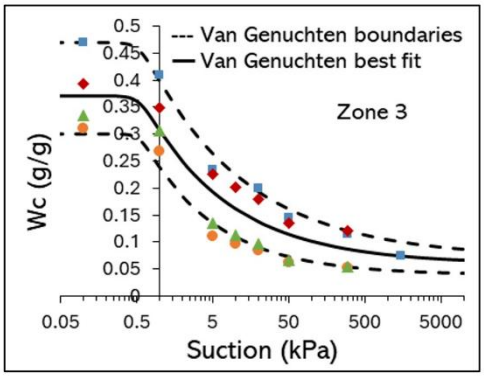

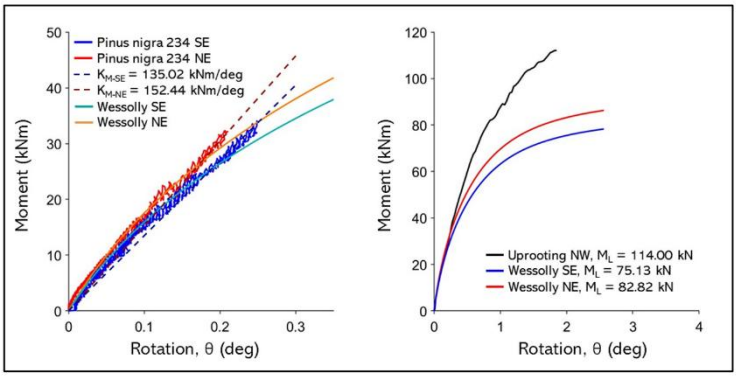

test direction	α (deg)	non-destructive pull test			uprooting			non-destructive dynamic				Mref	
		M_L (kNm)	θ_L (deg)	K_M (kNm/deg)	M_L (kNm)	θ_L (deg)	K_M (kNm/deg)	Cd_{af}	Cd_{tab}	$M_L\ Cd_{af}$ (kNm)	$M_L\ Cd_{tab}$ (kNm)	M_{ref} Cd_{af}	M_{ref} Cd_{tab}
NW	19.5	75.1	1.914	135.0	114.0	1.85	131.5	0.17	0.18	75.8	78.9	20.4	21.6
SE	33.2	82.8	1.914	152.4	-	-	-						

FS							
non-destructive [1]	non-destructive [2]	measured [1]	measured [2]	$dynamic_{Cd\text{-}af}$ [1]	$dynamic_{Cd\text{-}af}$ [2]	$dynamic_{Cd\text{-}tab}$ [1]	$dynamic_{Cd\text{-}tab}$ [2]
3.68	3.48	5.59	5.28	3.71	3.51	3.87	3.65

243 Pinus nigra

Biometric data	
DBH (cm)	53.00
H (m)	12.33
Acr (m^2)	12.60
hcr (m)	12.00
D1 (N-S) (m)	1.70
D2 (W-E) (m)	1.53
R2 (m)	1.03
Hrp (m)	0.63
Trp (m)	1.15
Zwetsoil (m)	-

Zone	Soil type	Test type			
		Standard	Uprooting	Multiple α	Dynamic
3	sandy loam	x	x	-	-

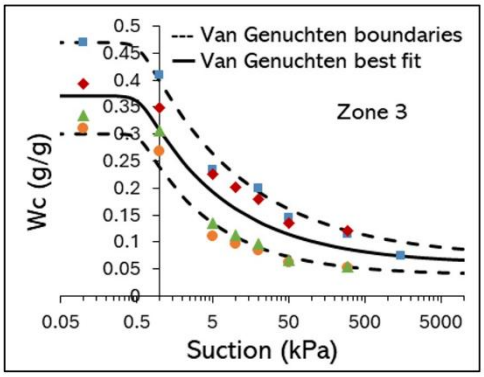

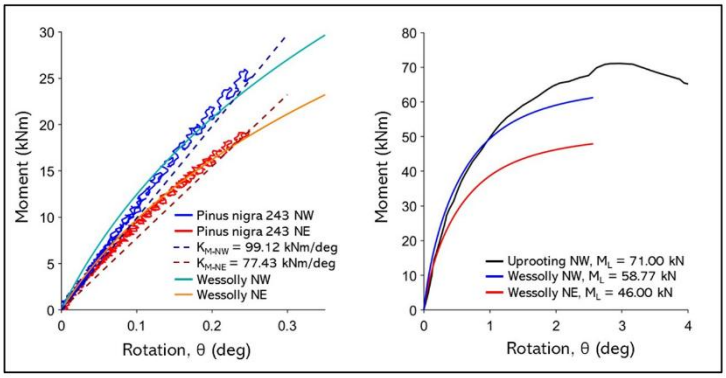

test direction	α (deg)	non-destructive pull test			uprooting			non-destructive dynamic				Mref	
		M_L (kNm)	θ_L (deg)	K_M (kNm/deg)	M_L (kNm)	θ_L (deg)	K_M (kNm/deg)	Cd_{af}	Cd_{tab}	M_L Cd_{af} (kNm)	M_L Cd_{tab} (kNm)	M_{ref} Cd_{af}	M_{ref} Cd_{tab}
NE	25.5	46.0	1.914	77.4	-	-	-	-	0.18	-	-	-	18.2
NW	33.2	58.8	1.914	99.1	71.0	2.96	86.0						

FS							
non-destructive [1]	non-destructive [2]	measured [1]	measured [2]	$dynamic_{Cd\text{-}af}$ [1]	$dynamic_{Cd\text{-}af}$ [2]	$dynamic_{Cd\text{-}tab}$ [1]	$dynamic_{Cd\text{-}tab}$ [2]
-	3.24	-	3.91	-	-	-	-

392 Quercus

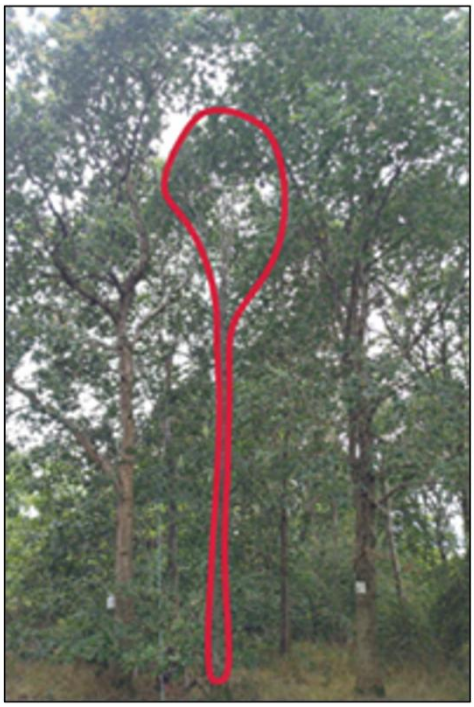

Biometric data	
DBH (cm)	22.60
H (m)	13.00
Acr (m^2)	10.80
hcr (m)	12.00
D1 (N-S) (m)	2.50
D2 (W-E) (m)	1.55
R2 (m)	0.93
Hrp (m)	1.65
Trp (m)	0.61
Zwetsoil (m)	-

Zone	Soil type	Test type			
		Standard	Uprooting	Multiple α	Dynamic
4	sandy loam	x	x	x	x

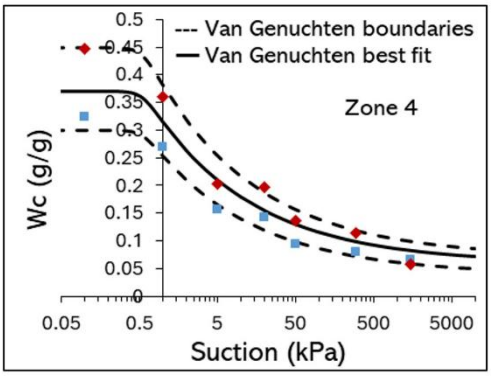

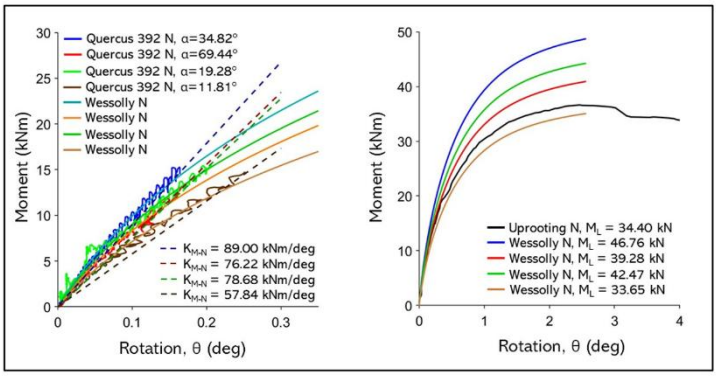

test direction	α (deg)	non-destructive pull test			uprooting			non-destructive dynamic				Mref	
		M_L (kNm)	θ_L (deg)	K_M (kNm/deg)	M_L (kNm)	θ_L (deg)	K_M (kNm/deg)	Cd_{af}	Cd_{tab}	$M_L\ Cd_{af}$ (kNm)	$M_L\ Cd_{tab}$ (kNm)	M_{ref} Cd_{af}	M_{ref} Cd_{tab}
N	20.0	42.5	1.914	78.7	-	-	-	0.22	0.25	38.6	43.8	19.0	21.6
N	34.8	46.7	1.914	89.0	-	-	-						
N	69.4	39.3	1.914	76.2	36.4	2.46	89.6						
N	11.8	33.7	1.914	57.8	-	-	-						

FS							
non-destructive [1]	non-destructive [2]	measured [1]	measured [2]	dynamic$_{Cd\text{-}af}$ [1]	dynamic$_{Cd\text{-}af}$ [2]	dynamic$_{Cd\text{-}tab}$ [1]	dynamic$_{Cd\text{-}tab}$ [2]
2.07	1.82	1.91	1.38	2.03	1.79	2.30	2.04

394 Quercus

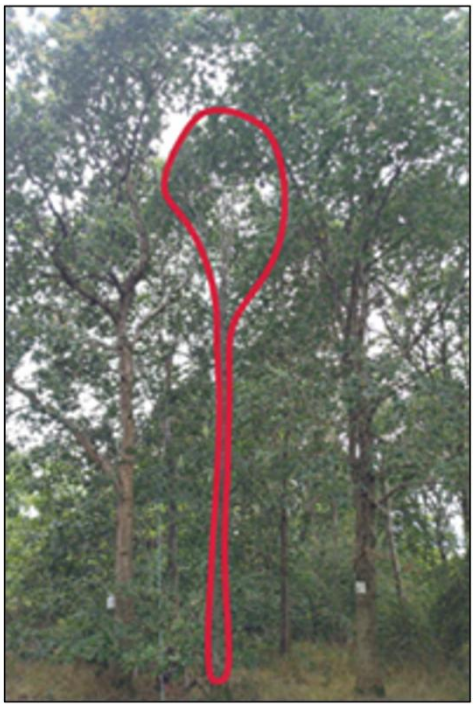

Biometric data	
DBH (cm)	37.00
H (m)	17.00
Acr (m^2)	30.00
hcr (m)	10.00
D1 (N-S) (m)	3.00
D2 (W-E) (m)	1.70
R2 (m)	0.89
Hrp (m)	0.50
Trp (m)	0.64
Zwetsoil (m)	-

Zone	Soil type	Test type			
		Standard	Uprooting	Multiple α	Dynamic
4	sandy loam	x	x	x	x

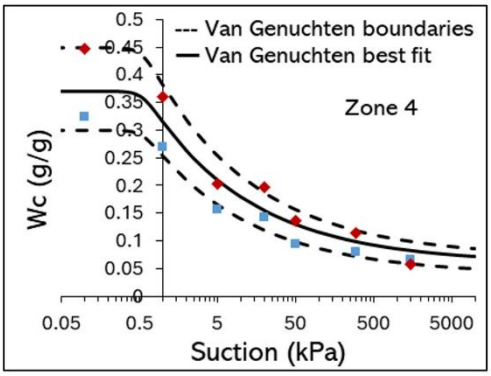

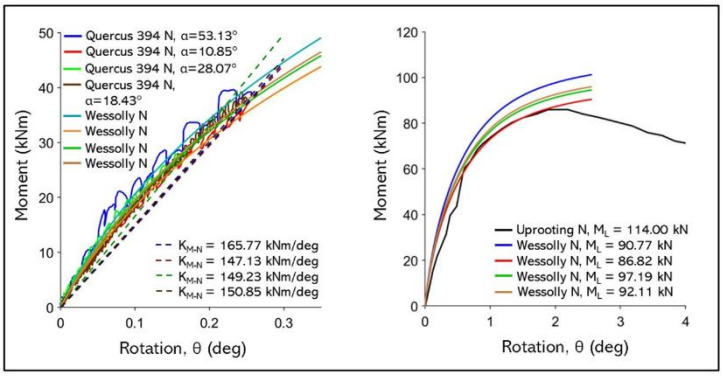

test direction	α (deg)	non-destructive pull test			uprooting			non-destructive dynamic				Mref	
		M_L (kNm)	θ_L (deg)	K_M (kNm/deg)	M_L (kNm)	θ_L (deg)	K_M (kNm/deg)	Cd_{af}	Cd_{tab}	$M_L\ Cd_{af}$ (kNm)	$M_L\ Cd_{tab}$ (kNm)	M_{ref} Cd_{af}	M_{ref} Cd_{tab}
N	10.9	86.8	1.914	147.1	86.9	1.95	92.3						
N	18.4	92.1	1.914	150.9	-	-	-						
N	28.1	97.2	1.914	149.2	-	-	-	0.14	0.25	84.6	149.8	28.0	50.0
N	53.1	90.8	1.914	165.8	-	-	-						

FS							
non-destructive [1]	non-destructive [2]	measured [1]	measured [2]	$dynamic_{Cd\text{-}af}$ [1]	$dynamic_{Cd\text{-}af}$ [2]	$dynamic_{Cd\text{-}tab}$ [1]	$dynamic_{Cd\text{-}tab}$ [2]
3.10	1.74	3.31	1.74	3.02	1.69	5.35	2.99

971 Tsuga

Biometric data	
DBH (cm)	78.00
H (m)	13.80
Acr (m^2)	47.20
hcr (m)	6.78
D1 (N-S) (m)	
D2 (W-E) (m)	
R2 (m)	
Hrp (m)	
Trp (m)	
Zwetsoil (m)	-

Zone	Soil type	Test type			
		Standard	Uprooting	Multiple α	Dynamic
2	sandy loam	x	x	-	x

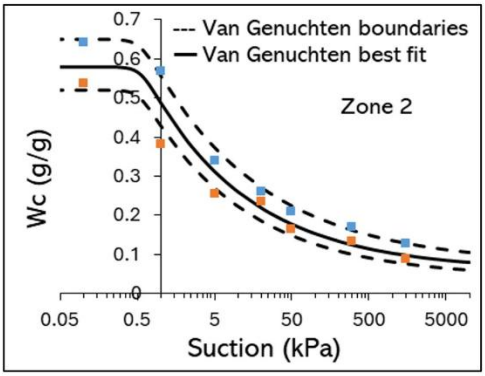

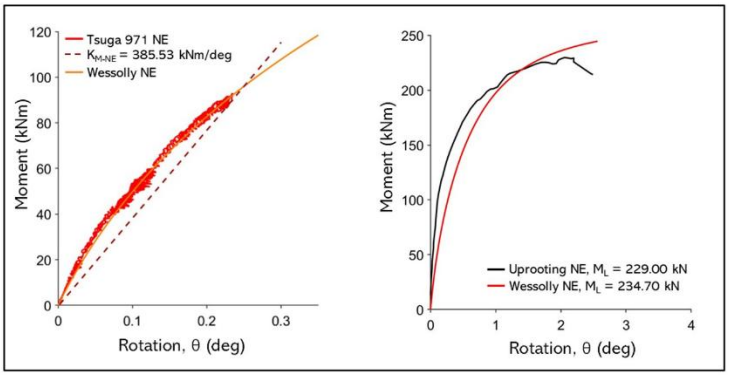

test direction	α (deg)	non-destructive pull test			uprooting			non-destructive dynamic				Mref	
		M_L (kNm)	θ_L (deg)	K_M (kNm/deg)	M_L (kNm)	θ_L (deg)	K_M (kNm/deg)	Cd_{af}	Cd_{tab}	$M_L\ Cd_{af}$ (kNm)	$M_L\ Cd_{tab}$ (kNm)	M_{ref} Cd_{af}	M_{ref} Cd_{tab}
NE	11.6	234.7	1.914	385.5	229.0	2.20	542.5	0.18	0.2	231.5	250.9	38.4	42.7

FS							
non-destructive [1]	non-destructive [2]	measured [1]	measured [2]	dynamic$_{Cd\text{-}af}$ [1]	dynamic$_{Cd\text{-}af}$ [2]	dynamic$_{Cd\text{-}tab}$ [1]	dynamic$_{Cd\text{-}tab}$ [2]
6.11	5.50	5.96	5.36	6.03	5.42	6.53	5.88

Generalized Wessolly Tipping curve: a bayesian approach

Non-destructive pulling tests have been found to provide a practical and widely adopted basis for assessing tree anchorage and overturning resistance. In the previous paragraphs, experimental moment-rotation responses were interpreted through the Wessolly tipping curve to extrapolate the ultimate overturning moment M_L, which was then used to derive stability indicators and safety factors. A recurrent outcome of these analyses is that the estimated M_L can vary when the calibration is performed on different portions of the same experimental dataset.

This sensitivity is not unexpected because the initial part of the response reflects an almost elastic response with limited mobilisation of soil-root resistance, while larger rotations progressively activate non-linear mechanisms (e.g., movement of the root-plate zone relative to the surrounding soil, soil collapse and geometric effects).

Consequently, utilizing a restricted, low-rotation segment may yield divergent extrapolations when compared to those derived from the fitting of more extensive portions of the curve. The practical implication of this is that the inferred stability limit can depend not only on the mechanical characteristics of the tree–soil system, but also on the data selection adopted for the calibration.

To address this issue in a systematic manner, this section revisits the applicability of the Wessolly relationship through a structured exploration of fitting ranges. Rather than restricting the analysis to the conventional small-rotation interval (e.g., rot $\leq 0.25°$), the model is calibrated repeatedly over progressively wider windows, namely rot $\leq 0.25°$, rot $\leq 0.5°$, rot $\leq 1.0°$, rot $\leq 1.5°$, and finally up to the last available rotation prior to the onset of collapse. This multi-window strategy allows for variable evaluation of M_L based on the amount of non-linear response included in the calibration and provides an explicit quantification of the sensitivity of the extrapolation to data selection.

In parallel, the analysis extends beyond the standard Wessolly formulation by introducing a generalized tipping-curve expression. In the classical approach, the curve shape is governed by fixed coefficients that implicitly encode assumptions about the characteristic evolution of rotation with increasing normalized load. While this fixed-parameter form is convenient and historically effective in operational practice, it may not fully capture the variability of real tree–soil systems across species, rooting architecture, soil conditions, and test configurations. The generalized formulation replaces the fixed coefficients with free parameters (a, b, c), enabling the curve shape to adapt to the observed response. Importantly, this parametrization is not pursued as an end in itself: its purpose is to couple the estimation of curve-shape parameters with the extrapolation of the stability limit M_L and,

consequently, to allow a consistent extraction of reference moments at prescribed rotation thresholds (e.g., M at rot = 1.914°).

$$rot(M; a, b, c, ML) = a \cdot \tan(K \cdot M/ML) + b \cdot (M/ML)^2 - c \cdot (M/ML) \quad \text{Eq. [24]}$$

where K = 100/73.85 is the constant used in the original Wessolly law.

From a conceptual point of view, Bayesian inference treats unknown model parameters as random variables and updates their probability distributions in light of observed data.

Let $\theta = \{a, b, c, M_L\}$ denote the parameter set, and let $D = \{(M_i, rot_i)\}$ denote the measured moment–rotation pairs within a selected fitting window. The calibration combines (i) a prior distribution $p(\theta)$, encoding plausible parameter values before seeing the data, and (ii) a likelihood $p(D \mid \theta)$, describing the probability of observing the data given a particular parameter set and an assumed error structure. The result is the posterior distribution $p(\theta \mid D)$, which quantifies parameter uncertainty after conditioning on the measurements.

The update from prior to posterior is formalised by Bayes' theorem:

$$p(\theta \mid D) = p(D \mid \theta) \cdot p(\theta) / p(D) \quad \text{Eq. [25]}$$

where p(D) is the marginal likelihood (a normalising constant ensuring that the posterior integrates to one). In practice, the posterior is typically evaluated up to proportionality:

$$p(\theta \mid D) \propto p(D \mid \theta) \cdot p(\theta) \quad \text{Eq. [26]}$$

In the present implementation, the likelihood links measurements to the tipping curve by assuming normally distributed residuals:

$$rot\_i \sim Normal(\, rot(M\_i; \theta), \sigma \,) \quad \text{Eq. [27]}$$

The priors are specified explicitly and should not be confused with "starting values": they define probability distributions, while the Markov chain Monte Carlo sampler selects its own initial points and then explores the parameter space according to the posterior density. The posterior distribution constitutes the central output of the analysis, providing a comprehensive distribution of plausible

values for each parameter given the data and the modelling assumptions. In order to facilitate the processes of reporting and plotting, it is possible to obtain a single representative tipping curve by evaluating the model at a point summary of the posterior. In this study, the posterior mean of each parameter has been employed as the point summary. Concurrently, the posterior facilitates uncertainty quantification through the propagation of posterior samples through the tipping-curve equation. This process yields a family of admissible curves, from which reliable bands can be derived when necessary. This probabilistic description is particularly relevant for stability assessment, because it allows uncertainty in curve shape and extrapolated capacity to be carried forward to derived indicators such as M at rot = 1.914° and the associated safety factors. Within the Bayesian framework, M_L is treated as a latent parameter of the tipping curve and is inferred jointly with the shape coefficients (a, b, c) from the observed data. As a result, the reported M_L is not the maximum measured during the test, but the asymptotic ultimate capacity implied by the model (i.e., the value the curve tends to as M/M_L approaches the $\tan(\cdot)$ singularity); for this reason, results also report M (1.914°) as an operational reference at a fixed rotation.

Three Bayesian calibration setups are considered, each designed to isolate a specific modelling question. (i) Bayesian case 1 with fixed M_L calibration: M_L is fixed to the maximum measured overturning moment within the pre-peak portion of the record, and only the generalized curve-shape parameters (a, b, c) are inferred. This setup tests whether adjusting the curve shape alone can reproduce the observed response without attributing unmeasured capacity beyond the available data. (ii) Bayesian case 2 with free M_L calibration on pre-peak data: the parameters (a, b, c) and M_L are inferred together using all data up to the first maximum of the measured moment. This represents the most direct probabilistic analogue of extrapolating the stability limit from the complete non-destructive loading branch while avoiding post-peak effects. (iii) Bayesian case 3 free M_L calibration on low-rotation data: (a, b, c) and M_L are inferred jointly using only the low-rotation segment (rot $\leq$ 0.25°) extracted from the same pre-peak data, i.e., using only the M values associated with rot $\leq 0.25°$ before the moment peak. This case reflects the operational practice of relying on small rotations while continuing to apply a consistent probabilistic extrapolation of M_L. The comparison among these three cases provides a structured basis to discuss identifiability, sensitivity to the fitting window, and the extent to which low-rotation measurements alone can constrain a reliable estimate of the stability limit. The following section presents the calibration results and compares the extrapolated M_L values across fitting windows and Bayesian setups, with the aim of clarifying both the strengths and the practical limitations of Wessolly-based extrapolation when applied to real non-destructive pulling-test records.

For illustrative purposes, only the calculations for some trees will be shown, particularly of the 434 *Acer platanoides*, 682 *Eucalyptus*, 143 *Pinus nigra* and 383 *Betula*.

434 *Acer platanoides*

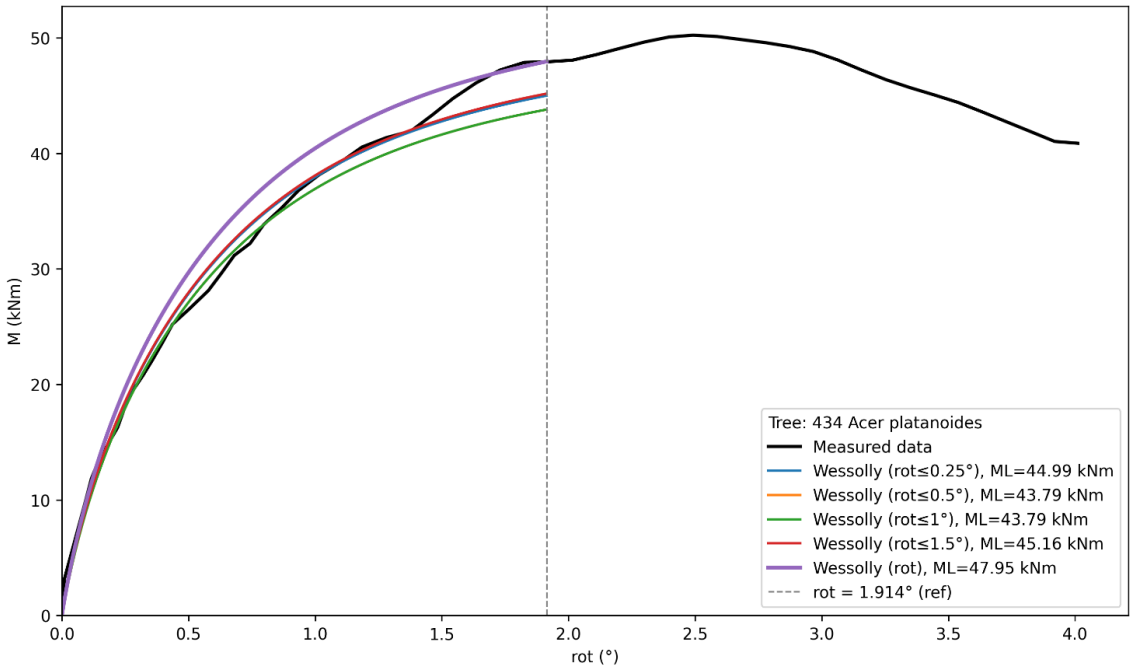

Figure 63: measured moment–rotation curve (black line) and Wessolly tipping-curve over rotation windows (rot ≤ 0.25°, 0.5°, 1.0°, 1.5°, and full pre-failure record; colored lines). The vertical dashed line marks the conventional reference rotation rot_L = 1.914°, used for stability-limit extrapolation.

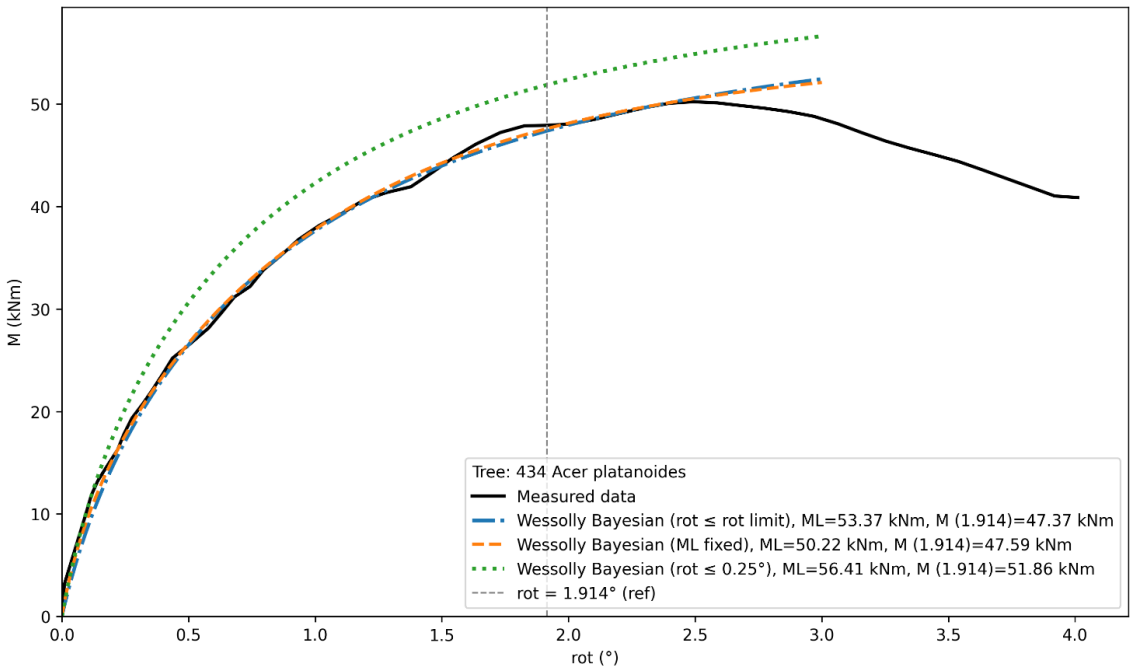

Figure 64: Bayesian calibration of the generalized Wessolly tipping curve. measured moment–rotation curve (black line) compared with three Bayesian setups (ML fixed to the maximum measured pre-peak moment - orange line; ML free on pre-peak data - blue line; ML free on rot ≤ 0.25° - green line).

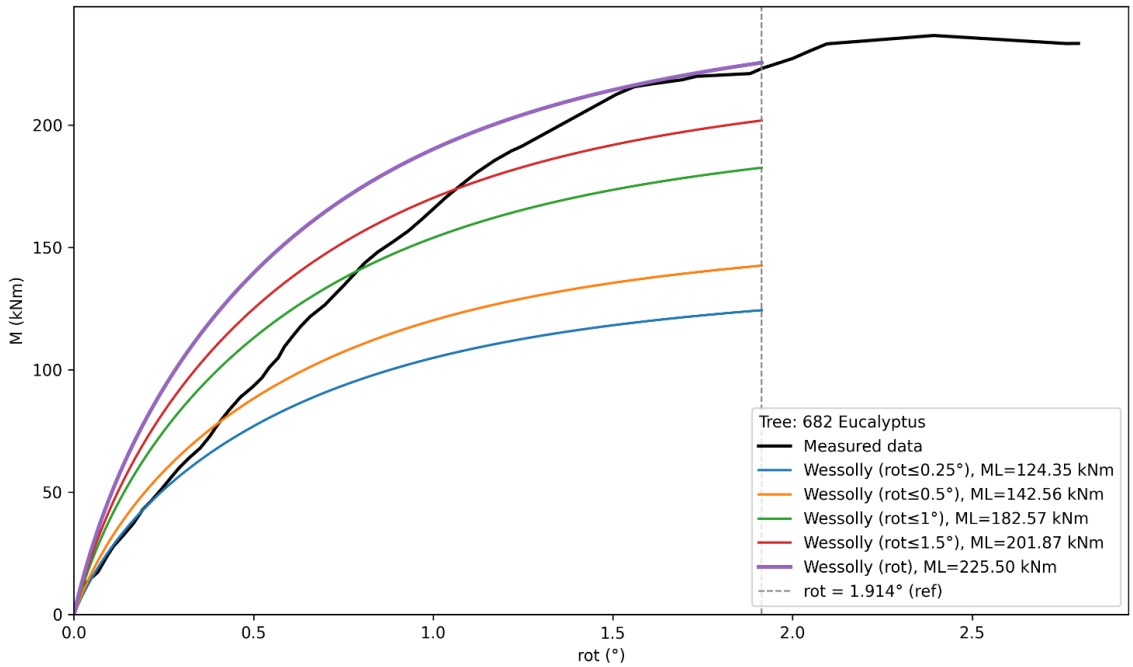

Figure 65: measured moment–rotation curve (black line) and Wessolly tipping-curve over rotation windows (rot ≤ 0.25°, 0.5°, 1.0°, 1.5°, and full pre-failure record; colored lines). The vertical dashed line marks the conventional reference rotation rot_L = 1.914°, used for stability-limit extrapolation.

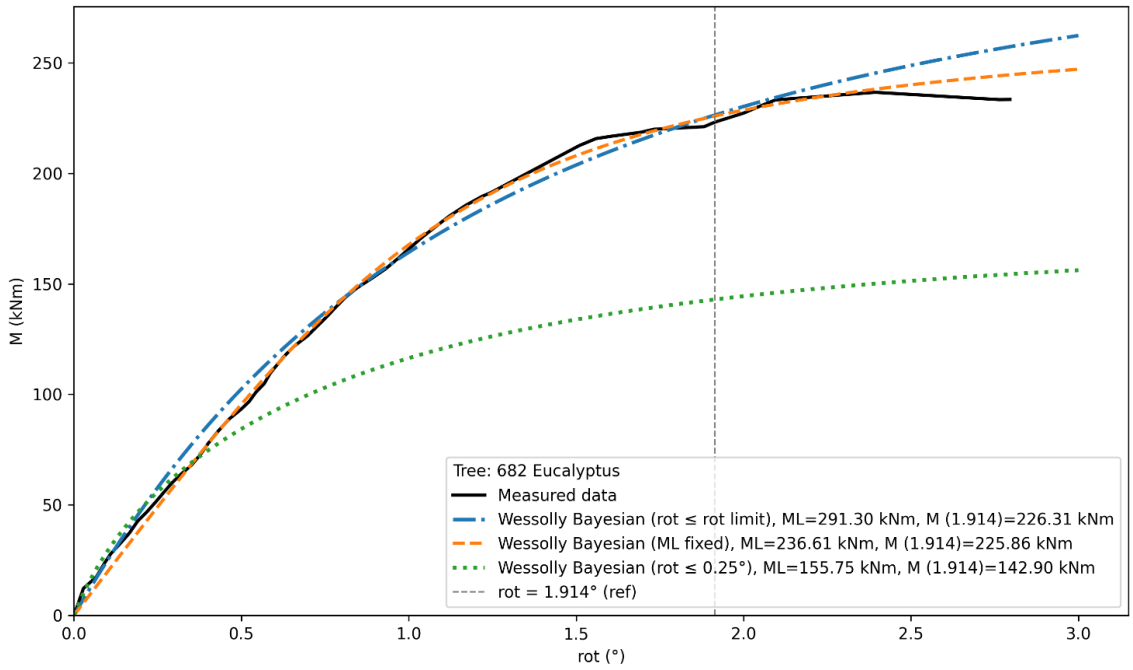

Figure 66: Bayesian calibration of the generalized Wessolly tipping curve. measured moment–rotation curve (black line) compared with three Bayesian setups (ML fixed to the maximum measured pre-peak moment - orange line; ML free on pre-peak data - blue line; ML free on rot ≤ 0.25° - green line).

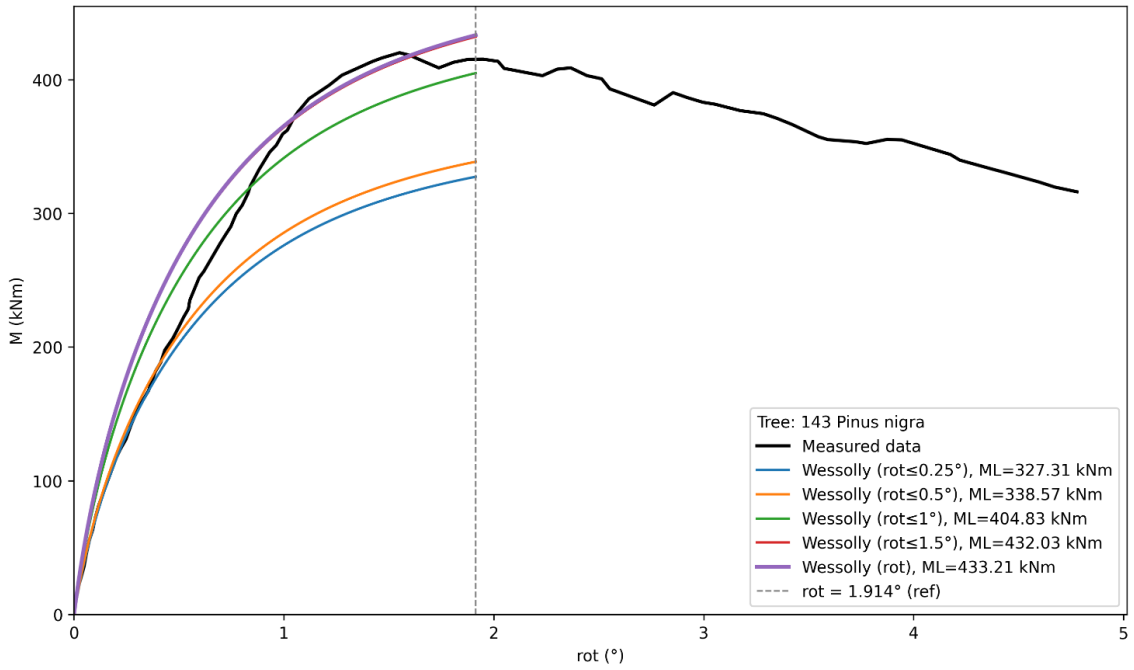

Figure 67: measured moment–rotation curve (black line) and Wessolly tipping-curve over rotation windows (rot ≤ 0.25°, 0.5°, 1.0°, 1.5°, and full pre-failure record; colored lines). The vertical dashed line marks the conventional reference rotation rot_L = 1.914°, used for stability-limit extrapolation.

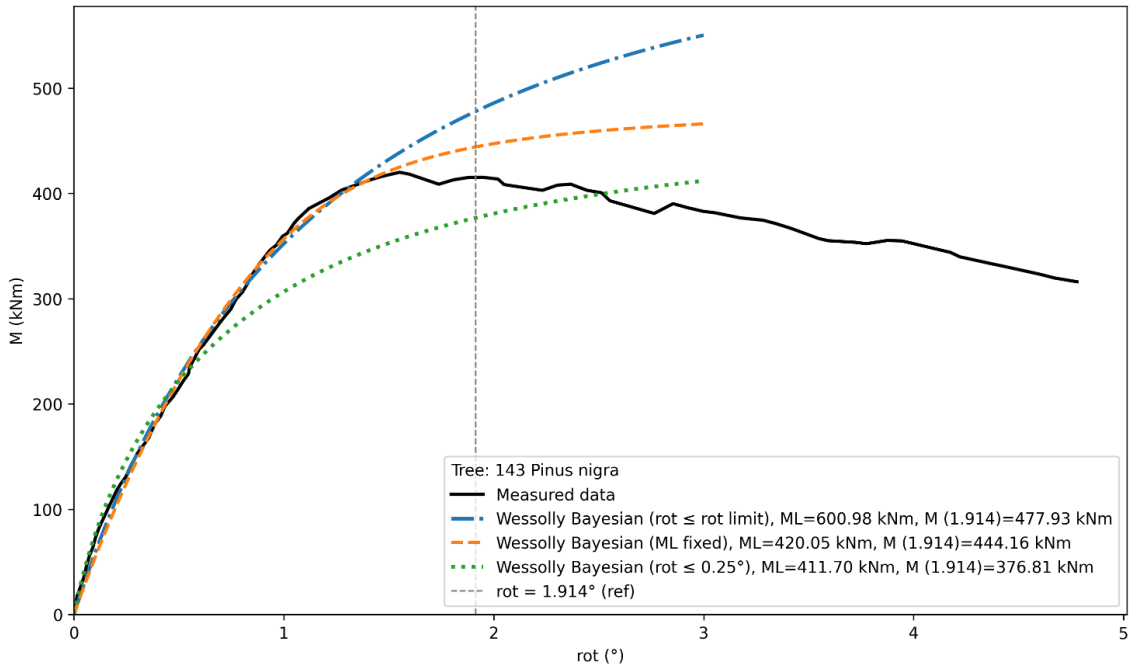

Figure 68: Bayesian calibration of the generalized Wessolly tipping curve. measured moment–rotation curve (black line) compared with three Bayesian setups (ML fixed to the maximum measured pre-peak moment - orange line; ML free on pre-peak data - blue line; ML free on rot ≤ 0.25° - green line).

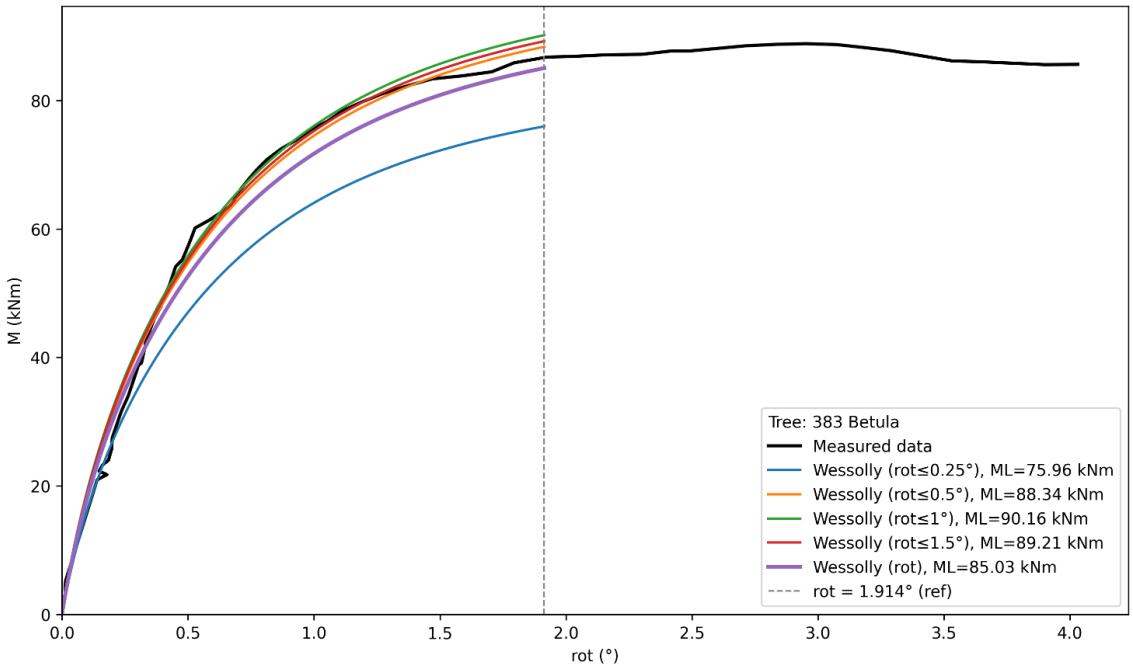

Figure 69: measured moment–rotation curve (black line) and Wessolly tipping-curve over rotation windows (rot ≤ 0.25°, 0.5°, 1.0°, 1.5°, and full pre-failure record; colored lines). The vertical dashed line marks the conventional reference rotation rot_L = 1.914°, used for stability-limit extrapolation.

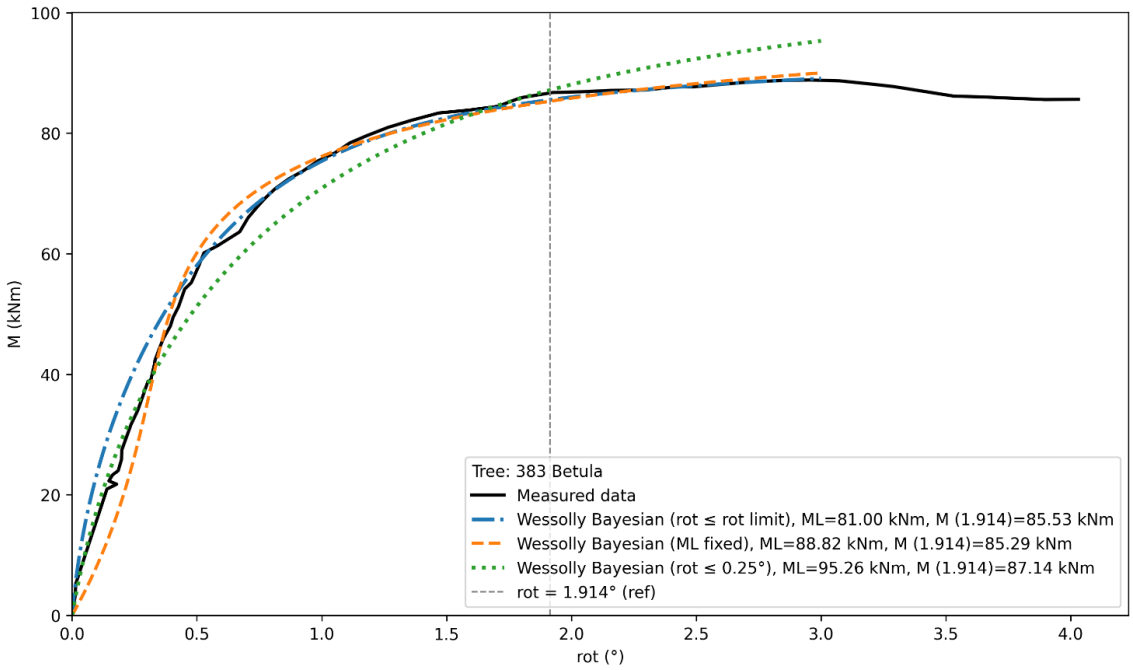

Figure 70: Bayesian calibration of the generalized Wessolly tipping curve. measured moment–rotation curve (black line) compared with three Bayesian setups (ML fixed to the maximum measured pre-peak moment - orange line; ML free on pre-peak data - blue line; ML free on rot ≤ 0.25° - green line).

Discussion and outlooks

The classic procedure, repeated on increasing windows (rot ≤ 0.25°, 0.5°, 1°, 1.5°, up to the last point before collapse), is useful because it makes the stability (or instability) of the estimate visible:

- For 434 *Acer platanoides* the estimate of M_L changes but remains within a relatively narrow range: the curves are consistent with each other, indicating that the shape of the experimental response is already well represented by the intermediate sections. In all five cases, there is an underestimation compared to the measured value of ML.
- For 682 *Eucalyptus* there is a very marked difference between the estimates obtained at low rotation and those obtained by including larger portions: this is a typical example where the initial section alone is not sufficient to describe the overall behavior. In practice, the more you widen the window, the more the estimate tends to "adapt" to the actual curvature of the test. In all five cases, there is an underestimation compared to the measured value of ML.
- For 383 *Betula* It falls somewhere between the two previous cases: the classic curves follow the trend well up to about rot_L, and the variability of M_L remains moderate. This suggests that the response is relatively regular and that the choice of window affects the outcome but does not distort it.
- For 143 *Pinus nigra,* although is the only one of these four in which the first maximum of the moment occurs before, shows results like 434 *Acer platanoides* and 383 *Betula*.

The Bayesian approach does not eliminate sensitivity to different calibration intervals; however, it explicitly and consistently quantifies it, making the results more transparent and comparable between windows and between trees, because allows to estimate the shape of the curve (a, b, c) and M_L and it clarify what part of the dataset leads the final results. The Case 1 is a check cause explains the data by adjusting only the shape of the curve. The Case 2 uses all the data till the collapse and shows that for some trees the estimate of M_L can grows a lot. The Case 3 is closest to the operational practice based on small rotations, but it is also the most "risky" from the point of view of robustness: in trees such as, it can lead to curves that describe the beginning well but then deviate when the rotation increases, with a clear effect on the final estimates. Regarding the trees:

- For 434 *Acer platanoides* the M_L values do not differ greatly from the measured value if the limit value is taken at 1,914°, in particular the value obtained in Case 2 underestimates the ML value, while Case 3 overestimates it.

- For 682 *Eucalyptus* the M_L value obtained from Case 2 is close (at 1.914°) to the measured but one from Case 3 is too underestimated (at 1.914°).
- For 383 *Betula* the three setups give very similar results and almost overlapping curves. This is a "well-conditioned" case. The differences between fixed ML and free ML remain limited. Case 3 is slightly higher, but without any obvious irregularities.
- For 143 *Pinus nigra* Cases 2 and 3 overestimate and underestimate ML respectively compared to the measured value. Case 1 also overestimates ML, due to the fact that the measured peak arrived before 1,914°.

The key point of this first attempt at a Bayesian approach to the Wessolly curve is to obtain a range of values for a, b, and c that can be used to estimate the ultimate resistance to windthrow for any tree. Case 1 serves precisely to try to obtain fixed values (or ranges) for the single interpolated tree, as does Case 2, because it at least uses all values up to the peak. These two cases, applied to a much larger dataset than the one used in this doctoral thesis, would serve to calibrate Case 3 and thus be able to interpolate the data (< 0.25°) and obtain estimates that are as close and reliable as possible to the real ML value (which is normally unknown).

Therefore, from an application point of view, the aim is to create a hierarchical model on multiple trees where parameters a, b, and c are described using population distributions. To complete the process, the inclusion and integration of certain covariates such as DBH, height, canopy area, weight, and geotechnical parameters would allow calibration from a descriptive model to a predictive model, increasing transferability to different operational contexts.

Chapter II

Physical model

(a lab test experience)

Introduction

In the assessment of tree stability, a key quantity has almost never been measured directly: the force transmitted into the root–plate system. During non-destructive static pulling tests, the load cell records the tensile force in the winching cable, but this is only the externally applied action; it is not the load that ultimately reaches the root plate and its anchoring zone. The internal force paths—how much of that applied action is redistributed through the stem, damped by crown aerodynamics, or filtered by the soil–root stiffness—remain inferred rather than observed.

The situation is even more pronounced in dynamic tests. Under natural wind excitation, instrumentation typically captures kinematics (inclinations, accelerations) and sometimes reaction trends at supports, but there is no direct, continuous measurement of the forces acting at the root–soil interface. As a result, current interpretations rely on models and assumptions to convert measured motion or external loads into estimates of root loads and overturning moments.

This evidence gap has motivated the development of a controlled small-scale physical model capable of monitoring the forces transmitted to the base while reproducing the main aero-mechanical features of the tree system.

Another important reason for building the apparatus was to test a monitoring system that transmits data in real time because, to date, commercial instruments cannot transmit filtered (and therefore useful) data in those conditions. With a view to managing and mitigating the risk of falling trees in urban areas, it is becoming increasingly important to try to design an early-warning measurement systems.

Structural components

The physical model comprises three structural components and a dedicated sensing/DAQ chain:

Ground support frame: (shown in Figure 71)

- Three parallel linear guides (each 2 m long) form the ground support.
- The frame rests on adjustable feet to level the entire setup and avoid bias in force readings.
- Axes are defined as: x (transverse), y (longitudinal), z (vertical).

Square base (50 × 50 cm): (shown in Figure 71)

- A rigid 50 × 50 cm plate interfaces mechanically with the force-measurement system and carries the pot/plant assembly.

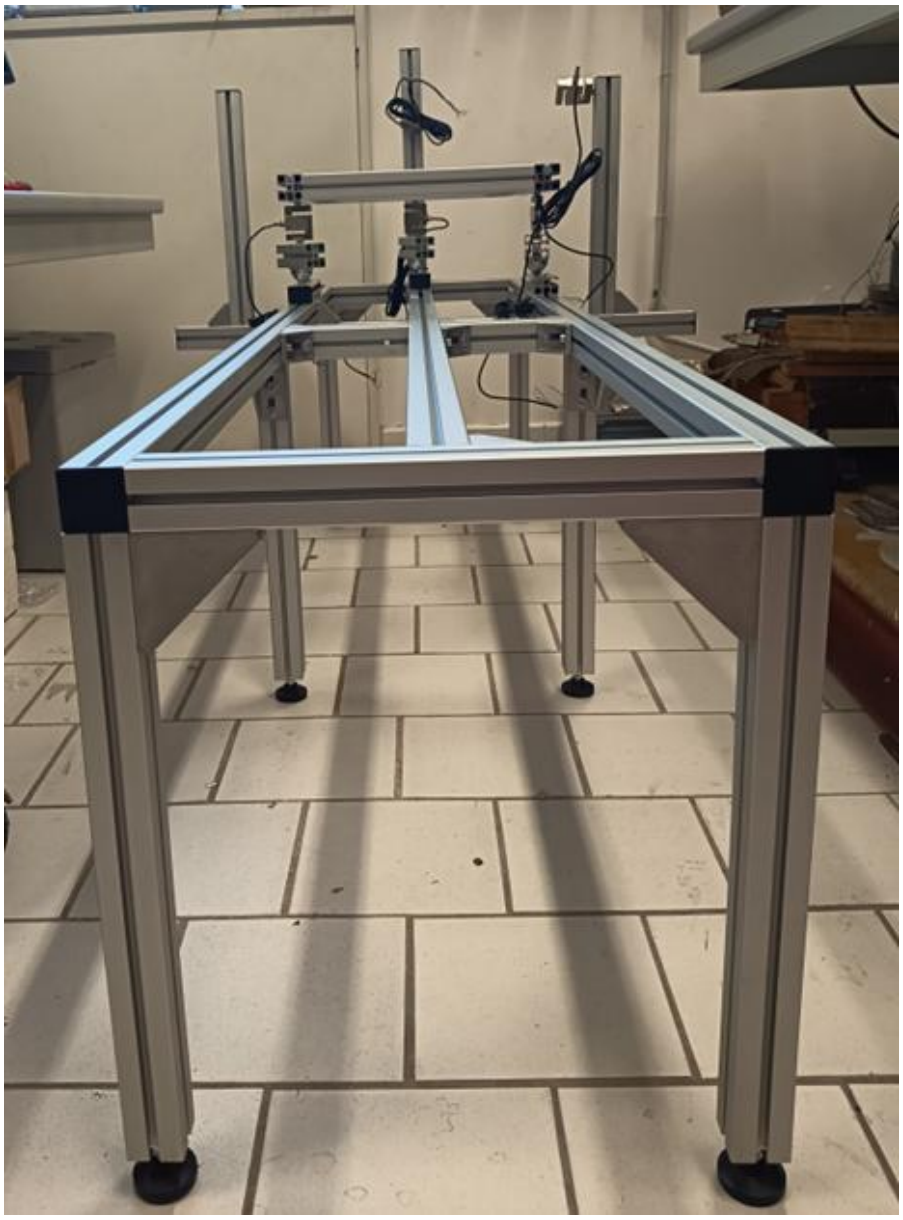

Figure 71: ground support frame and square base.

Pot–soil–plant assembly:

- Figure 72 shows the pot filled with selected soil hosts the plant and is rigidly fixed to the 50 × 50 cm base. The plant chosen for the test is a *Citrus* × *sinensis*.

Figure 72: pot soil plant assembly.

Force-measurement architecture and calibration

Vertical force (z-component): (shown in *Figure 73*)

- Three vertical load cells are installed between the ground frame and the 50 × 50 cm base in an isostatic 120° layout (triangular footprint).
- Each vertical cell bears on a small wheel that rolls along one of the three linear guides. This rolling contact removes parasitic shear/constraint, allowing vertical reactions to be measured without spurious horizontal coupling.

Horizontal forces (x–y components): (shown in Figure *73*)

- The 50 × 50 cm base is laterally constrained on three sides by independent side blocks, each instrumented with a horizontal load cell.
- These lateral cells read the longitudinal (along y) and transverse (along x) components of the wind-induced base reactions over the 2 m span of the support frame. These load cells are also attached to a spherical node, as described above for the cells mounted to read the vertical component of the load.

With the vertical cells decoupled by wheels and the lateral cells taking in-plane reactions, the system resolves the full reaction vector (N_x, N_γ, N_z).

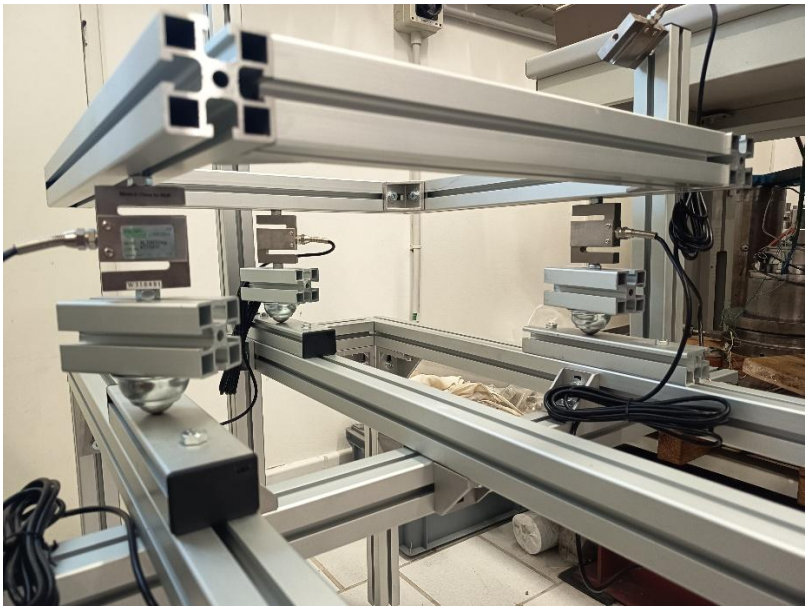

Figure 73: force-measurement architecture.

The load cells (shown in Figure *74*) used are Tedea-Huntleigh Model 614 units, which are rated at 50 kg and are suitable for both compression and tension.

Figure 74: load cells type used.

Each cell is a six-wire strain-gauge bridge with dedicated sense leads, wired as follows: +Excitation (green), −Excitation (black), +Output (red), −Output (white), +Sense (blue) and −Sense (brown) as shown in Figure *75*. The rated output is approximately 1.9525 mV/V, with a zero balance of around 0.0053 mV/V. The bridge is typically excited with 10 V DC in operation (compatible with 5–10 V). The input impedance is 415 ± 20 Ω and the output impedance is 350 ± 3 Ω, with an insulation resistance exceeding 2 GΩ.

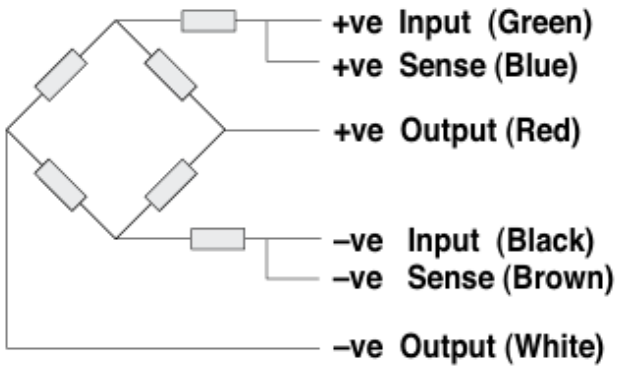

Figure 75: wiring schematic diagram (balanced bridge configuration).

A calibration test was performed on each load cell to verify its reliability before any experiments were conducted. First, three known masses were selected and weighed on a laboratory balance. The known weights are as follows: 764.55 g, 543.54 g, 199.88g. The plots below show the incremental readings from the load cells (with one weight added at a time) alongside the corresponding comparison charts between the known reference weights and the values measured by the cells.

Load cell n.1: measured weights are 761.9 g, 543.0 g, 200 g (Figure *76*). The $R^2 = 0.99$ as shown in Figure *76*.

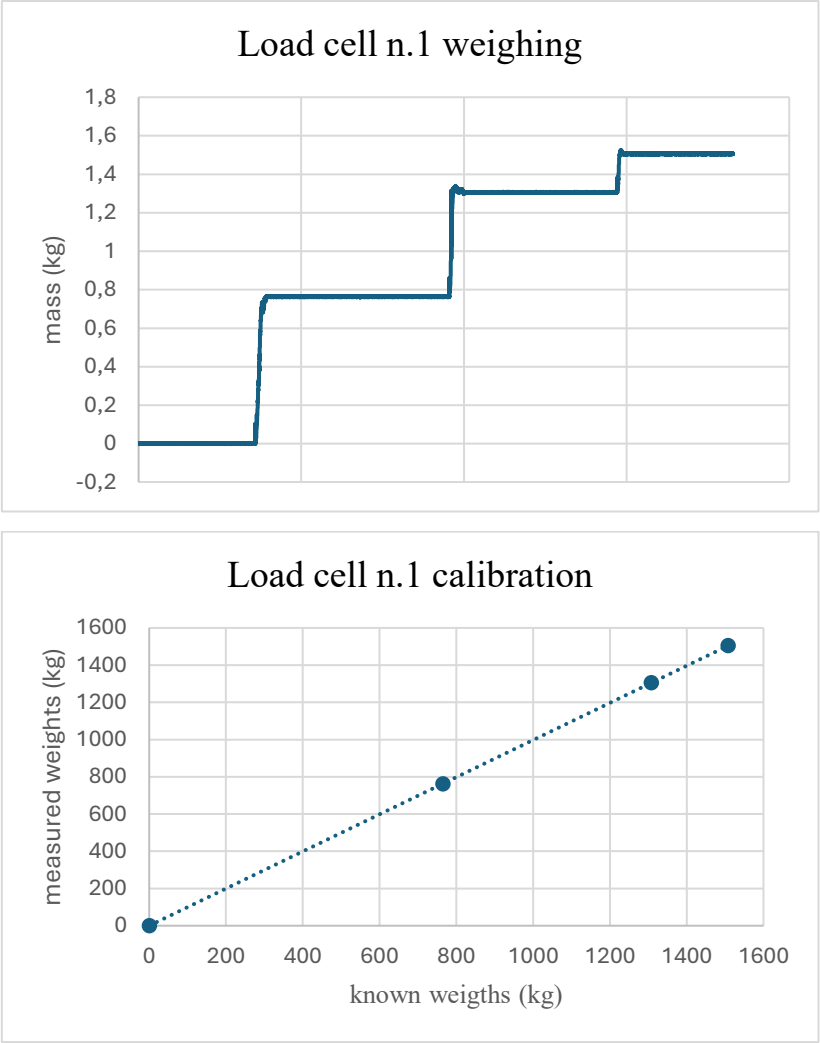

Figure 76: load cell n.1 weighing and calibration result.

Load cell n.2: measured weights are 759.5 g, 543.0 g, 199.5 g (Figure *77*). The $R^2 = 0.99$ as shown in Figure *77*.

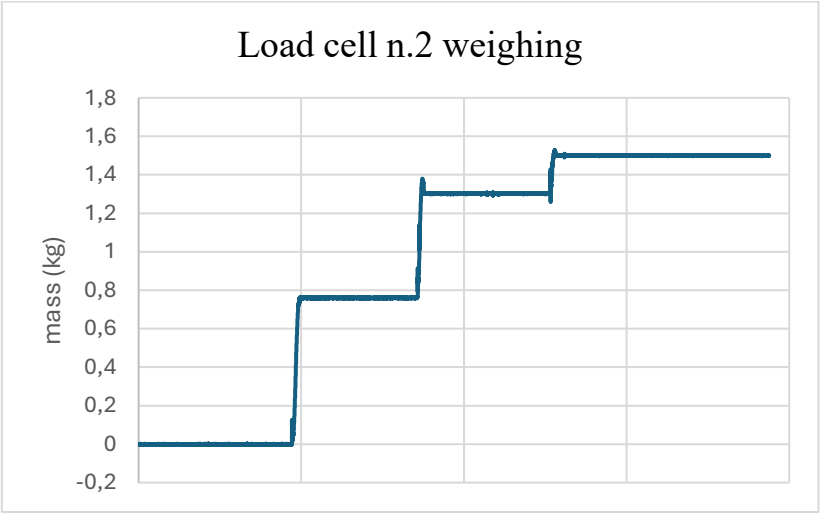

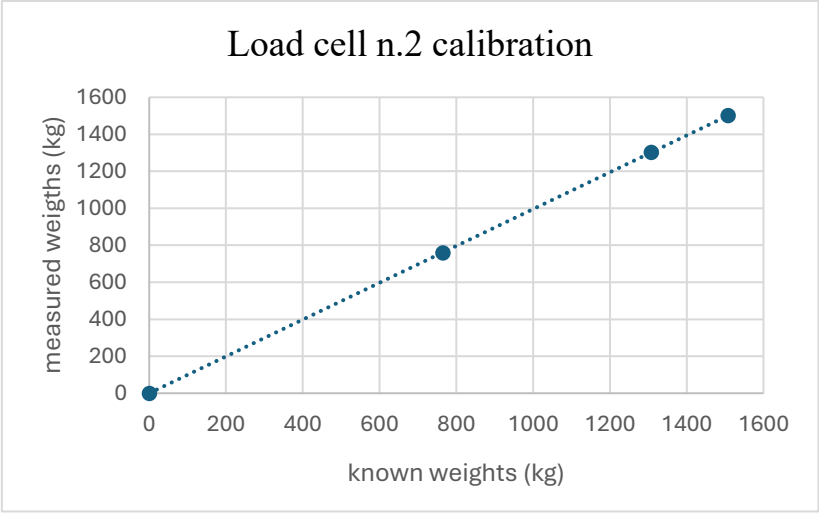

Figure 77: load cell n.2 weighing and calibration result.

Load cell n.3: measured weights are 758.5 g, 540.5 g, 198.9 g (Figure *78*). The $R^2 = 0.99$ as shown in Figure *78*.

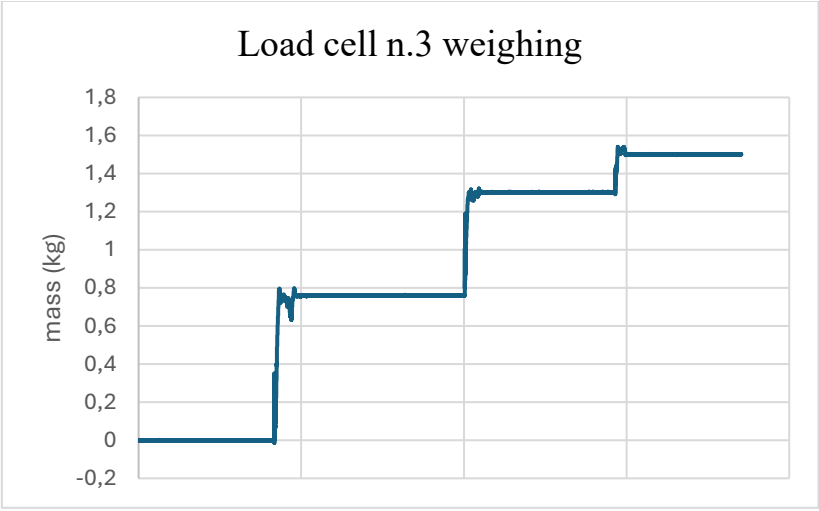

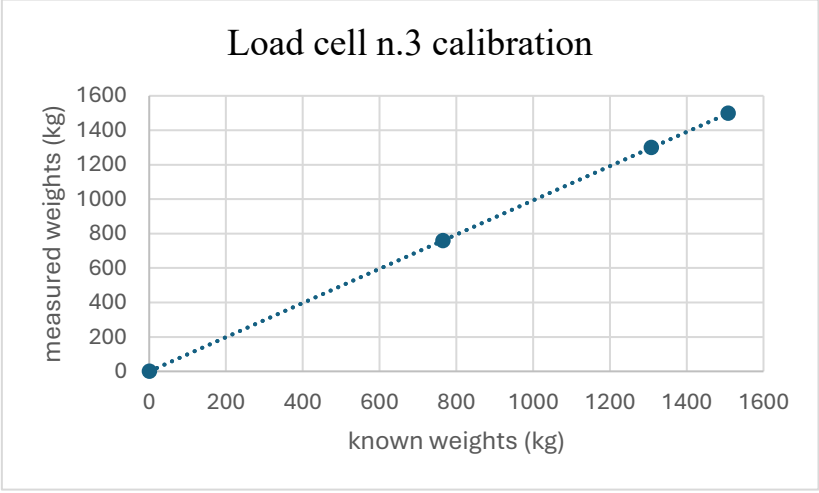

Figure 78: load cell n.3 weighing and calibration result.

Load cell n.4: measured weights are 764.55 g, 540.5 g, 198.9 g (Figure 79). The $R^2 = 0.99$ as shown in Figure 79.

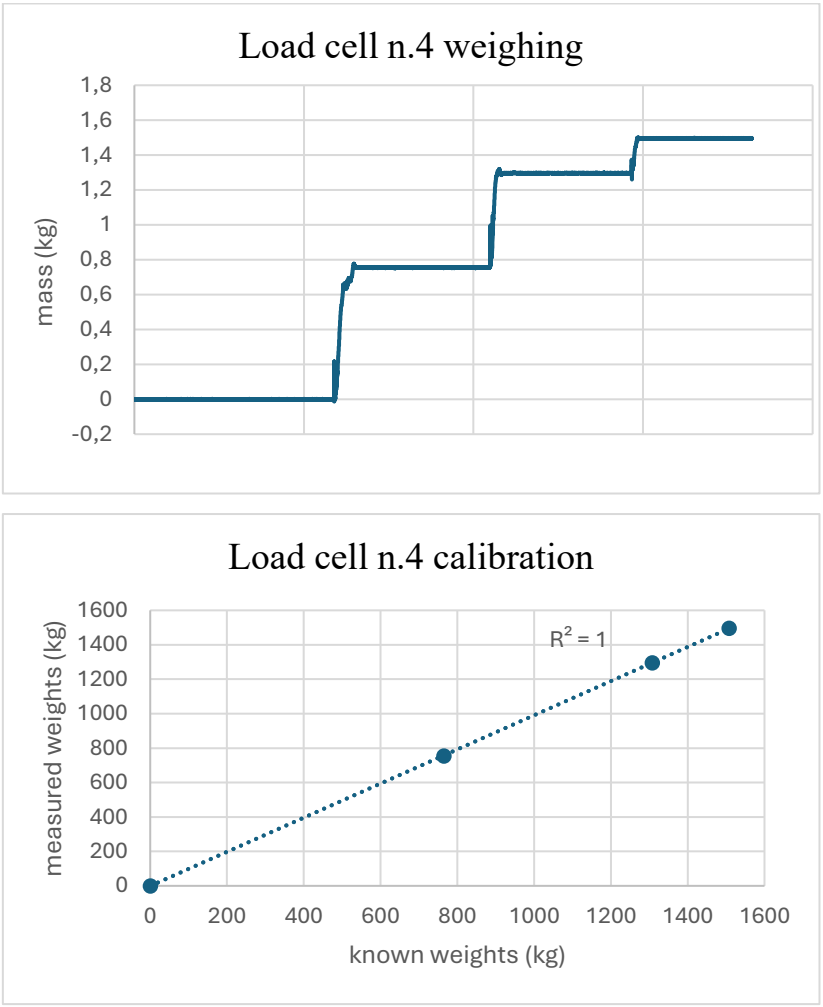

Figure 79: load cell n.4 weighing and calibration result.

Load cell n.5: measured weights are 758.06 g, 544.0 g, 197.0 g (Figure *80*). The $R^2 = 0.99$ as shown in Figure *80*.

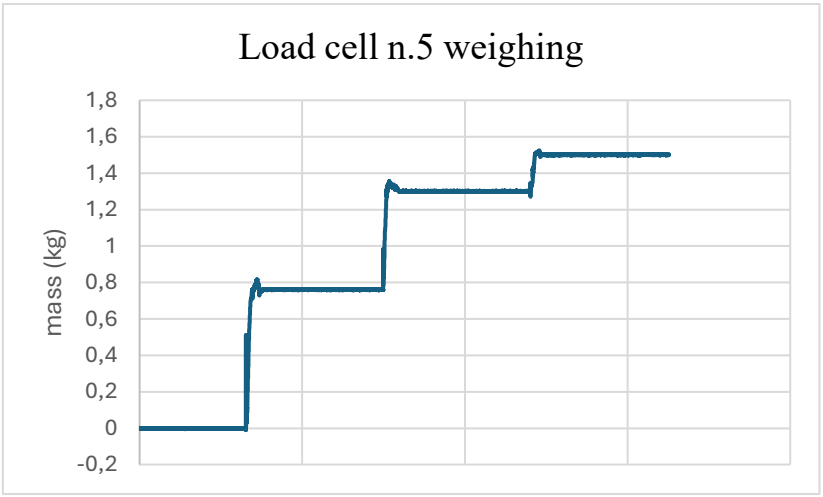

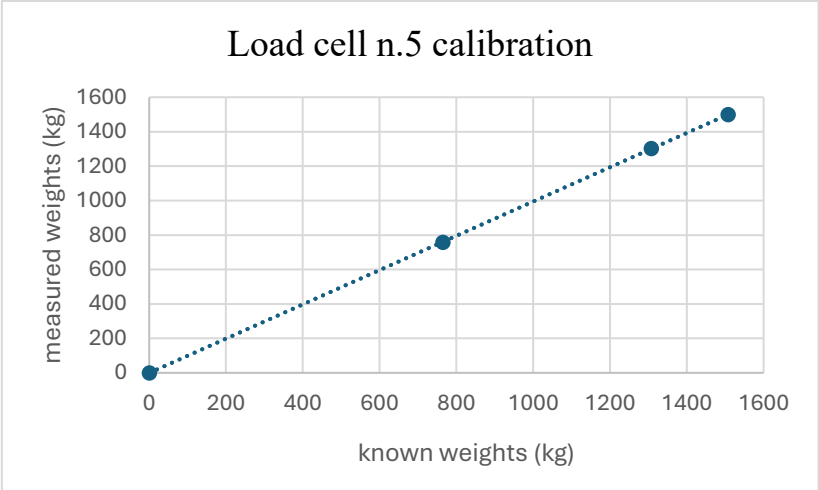

Figure 80: load cell n.5 weighing and calibration result.

Load cell n.6: measured weights are 764.9 g, 541.7 g, 200.3 g (Figure 81). The $R^2 = 0.99$ as shown in Figure *81*.

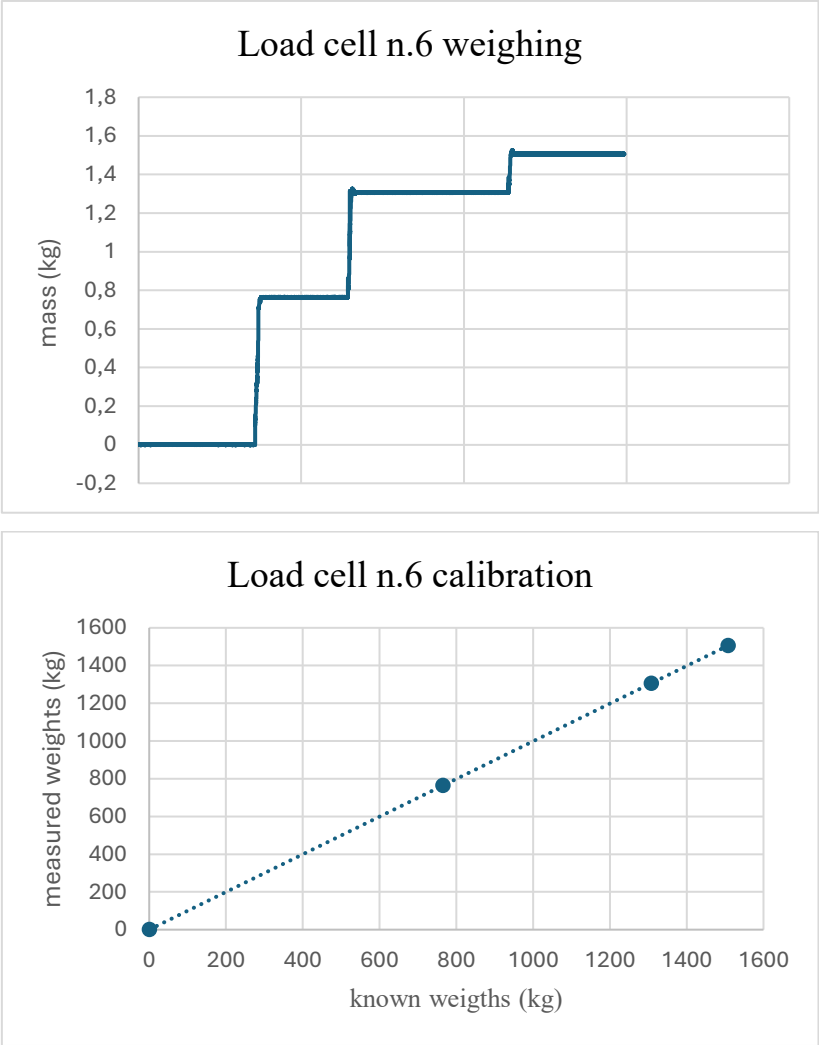

Figure 81: load cell n.6 weighing and calibration result.

Kinematic measurement

The Figure *82* illustrates the biaxial inclinometer/accelerometer, which is mounted at the plant collar. This Inertial Measurement Unit (IMU) is used to record rotations along x and y axes of the tree root-plate tilt. The device acquires measurements and publishes them to an MQTT broker, enabling real-time visualization via a dedicated software interface. Unlike the other sensors used in this PhD research (see Chapter II and Chapter IV for the Fakopp and IML instruments, respectively), this platform could support a rapid alert system based on configurable alarm thresholds. This feature is particularly relevant for future developments aimed at improving early warning systems, operational management and the mitigation of tree failure risk

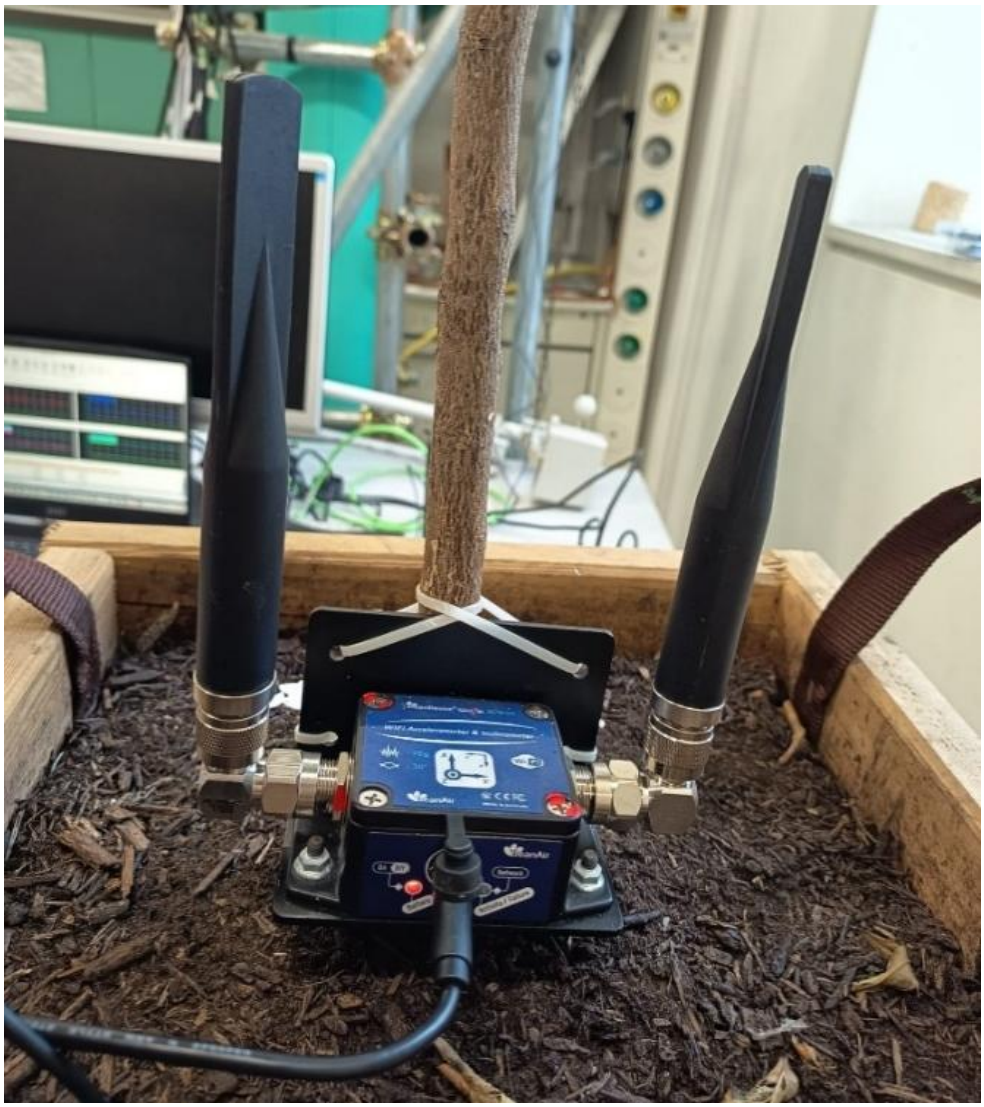

Figure 82: inclinometer/accelerometer with high gain antennas mounted on the collar of the tree.

Actuation

The canopy is excited aerodynamically by a high-power fan that directs an air jet along +y toward the crown. Tests include steady, pulsed, and gust-like profiles to probe quasi-static and dynamic behavior. Figure 83 illustrates the way used to excite the tree crown, using a portable air blower emitting up to a maximum of 100 km/h.

Figure 83: methods of blowing the tree canopy. A portable blower can be directed according to the type of test to be performed.

In Figure 84 is illustrated the schematic view of the apparatus used for the test on the selected tree.

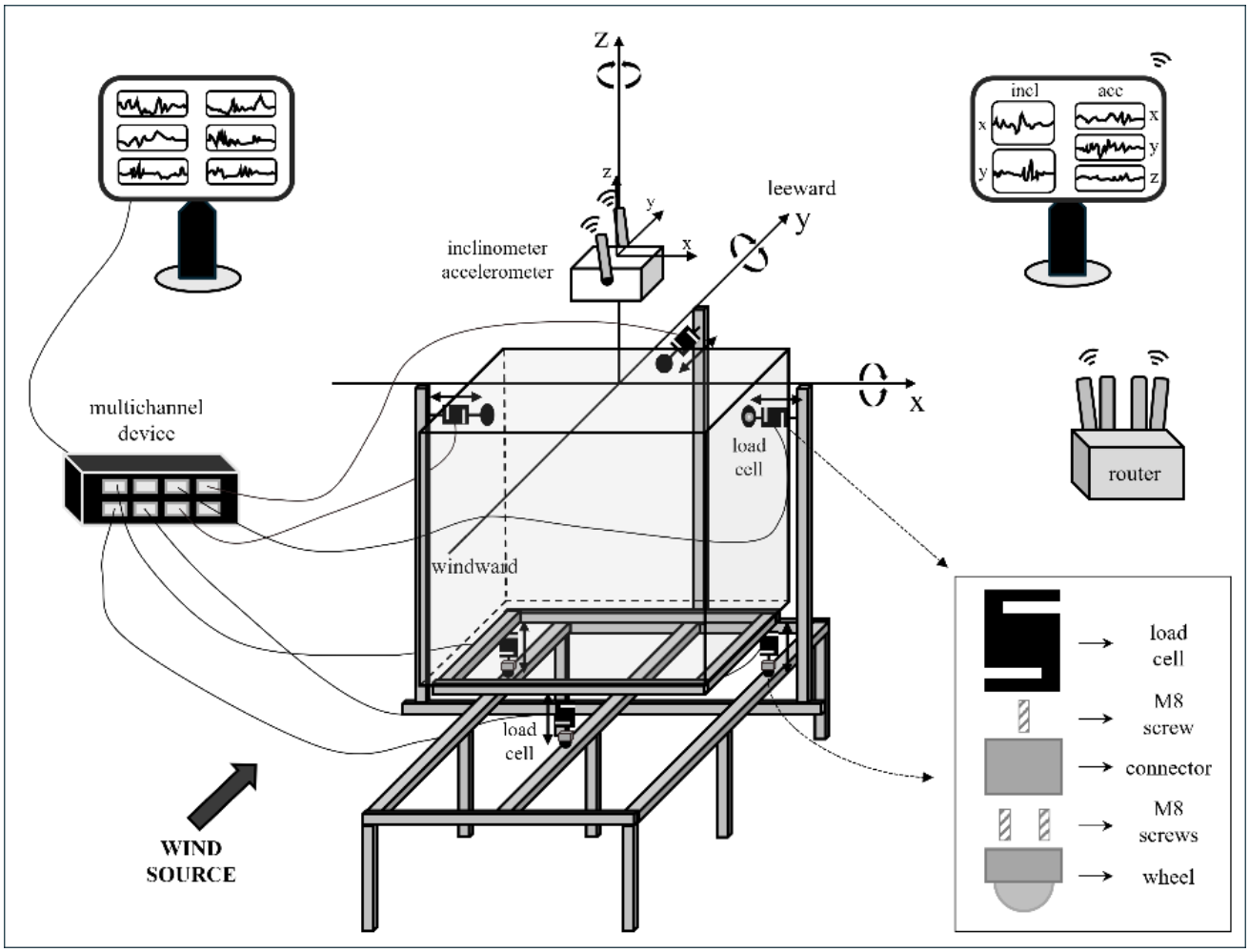

Figure 84: schematic view of the model testing apparatus.

Data acquisition

All load cells are wired to a multichannel data-acquisition system capable of true differential inputs, enabling nanovolt-level resolution. The resulting sensitivity is on the order of micrograms (effective mass resolution at the cells), which is crucial for capturing small dynamic fluctuations in force and rotation.

The QuantumX MX840, show in Figure 85 is a universal eight-channel acquisition module, each channel being isolated from the others and the power supply. It has D-Sub HD-15 connections. Each channel uses a dedicated 24-bit analogue-to-digital converter (ADC) with synchronous and parallel acquisition, a feature that enables consistent multi-sensor measurements in the time and frequency domains. Depending on the version, the MX840B achieves a sampling rate of up to 40 kS/s per channel (typical bandwidth of ~6–7 kHz), making the system ideal for medium- to high-bandwidth

dynamic analysis. In metrological terms, the module offers accuracy classes of up to 0.05%, depending on the sensor technology and range selected.

Figure 85: DAQ Quantum MX 840.

The system natively supports multiple transducer types: strain-gauge bridges (full and half-bridge), piezoresistive sensors, voltage inputs (from millivolts to tens of volts), current inputs (e.g. 4–20 mA), RTDs (such as PT100/1000), thermocouples (with cold-junction compensation in dedicated connectors) and frequency, pulse and encoder signals on designated channels. It also includes TEDS for automatic sensor identification and an internal shunt for quick verification and calibration. Sensor excitation is programmable (typically 5–24 V DC) and external synchronisation is possible via IRIG-B or the system clock. Ethernet connectivity is available for configuration, streaming and logging, depending on the variant. These features enable a rapid, traceable and stable setup with a high signal-to-noise ratio, providing the flexibility required for multi-physics experiments such as the present small-scale physical model.

To ensure the correct electrical connections of the load cells and the universal data acquisition unit (HBM QuantumX MX840B), I first conducted a study of the wiring and deployment scheme. I used HBM's catman® Easy/AP software for sensor configuration, data acquisition, visualization and logging during the laboratory tests. In Figure 86 it's shown the configuration on the connections of the load cells to the Quantum MX840b and in Table 12 a resume of the scheme followed for correct

configuration. To connect the wires (the colored ones) of the load cells to the DAQ it has been used a DB15 D-sub–Connector Breakout Board with Enclosure 15 Pin 3 Row Male.

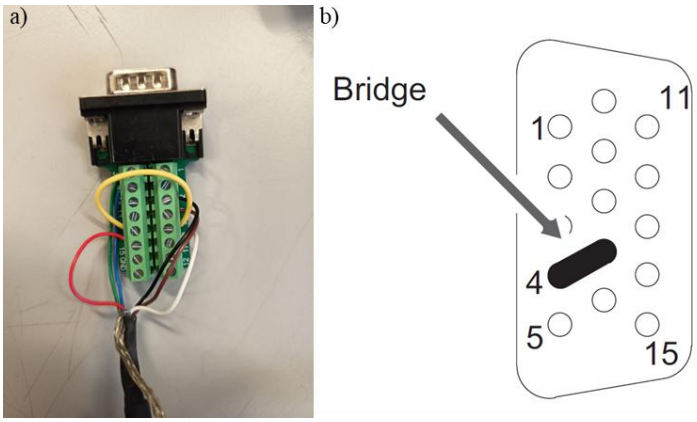

Figure 86: a) electrical connections of the load cell wires to the 15-pin connector; b) Pin arrangement of Quantum MX840b connector plug, view from the solder side.

Table 12: scheme for electrical connections between DAQ Quantum MX840b and the load cells by the 15-pin connector.

Pin Connector Quantum MX840b	**Load cell**
2 Bridge excitation voltage (-), 0°-reference pulse (zeroing pulse) (-)	**BLACK** WIRE
3 Bridge excitation voltage (+), 0°-reference pulse (zeroing pulse) (+)	**GREEN** WIRE
4 Always connect with Pin 9! (Plug-in detection)	**YELLOW** WIRE
5 Measurement signal (+), potentiometer measurement signal (+), voltage input 100 mV (+), f1(-) signal differential, SSI data (-)	**RED** WIRE
7 Sense lead (-), f2(-) signal differential, CAN-High, SSI clock (-)	**BROWN** WIRE
8 Sense lead (+), f2(+) signal differential, CAN-Low, SSI clock (+)	**BLUE** WIRE
9 Signal ground	**YELLOW** WIRE
10 Measurement signal (-), f1(+) signal differential, SSI data (+)	**WHITE** WIRE

Figure 87 shows the live visualisation screen of the DAQ device during the test. Active channels are displayed and processing or calculation tools can be applied directly to each one. Real-time visualisation enables verification that the sensors are acquiring data correctly and without interference, zero-balancing has been performed properly, the selected sampling rate is appropriate, and the signal-to-noise ratio is adequate.

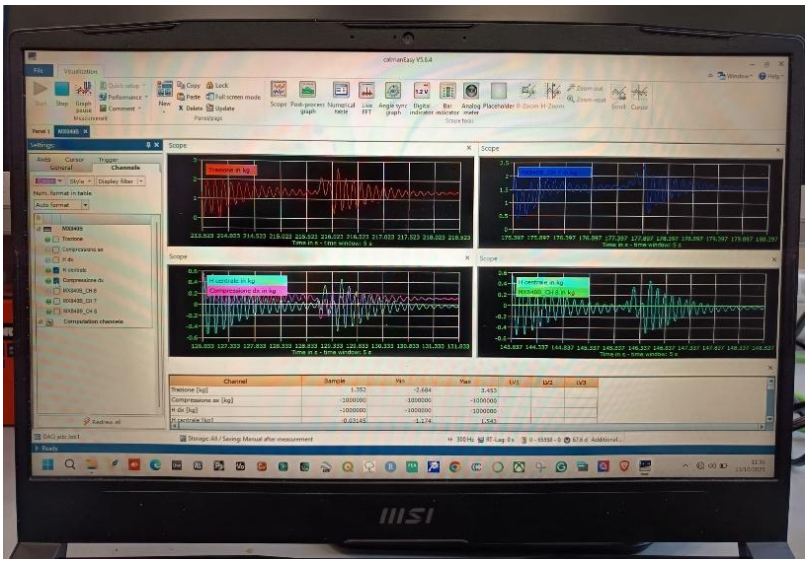

Figure 87: exemple of DAQ visualization during a laboratory test.

The acquisition system for inclinometric and accelerometric data was managed differently from the configuration of the load cells described earlier. The system uses the BeanDevice® Willow® X-INC, which is manufactured by BeanAir GmbH in Berlin, Germany. This sensor combines a biaxial inclinometer and a triaxial accelerometer within a single node and transmits data via low-power Wi-Fi (IEEE 802.11 b/g/n). The inclinometer is available with ±15° or ±30° ranges and offers a resolution of ~0.001° (with a 10 Hz bandwidth). The accelerometer is available in versions with a range of ±2 g (with a sensitivity of approximately 660 mV/g and a noise density of approximately 45 µg/√Hz) or ±10 g (with a sensitivity of approximately 200 mV/g and a noise density of approximately 100 µg/√Hz), with a 24-bit ADC and sampling rates of up to 2 kS/s per axis. Both sensors use 24-bit conversion with thermal compensation and synchronous channels. The electronics incorporate an onboard data logger with capacity for up to 460,000 records per channel, Store-and-Forward+ for lossless transmission, MQTT for Internet of Things (IoT) integration and over-the-air (OTA) firmware updates. With a high-gain antenna, the typical range is 100–200 metres line of sight (40–80 metres non-line of sight). There are flexible power options: a 900 mAh internal Li-ion battery, 5 V USB or an 8–24 V DC input that is compatible with energy harvesting.

For the experiment, we used MQTT (Message Queuing Telemetry Transport), a lightweight publish/subscribe messaging protocol that is ideal for the Internet of Things (IoT) and devices with limited resources. It facilitates the efficient exchange of information between devices (e.g. sensors and actuators) and the cloud via a central broker. In this setup, clients publish data to specific topics, and other clients can then subscribe to these topics. This architecture minimises overhead and provides a reliable, low-latency exchange of data, even over low-bandwidth or unstable networks. The MQTT broker was installed on a Wi-Fi router and ran locally, and the wireless link operated in

the 2.4 GHz band. The software was developed by an external company I commissioned—LISALAB by Ellegi s.r.l. (that produces systems and provides services for remote sensing measurement of displacements and deformations on natural hazards and manmade buildings)—and it was built in LabVIEW.

The data-acquisition system is configured as follows: switch on the 2.4 GHz router/access point (shown in Figure 88) and select its Wi-Fi network on the PC. The unit is a Teltonika Networks RUTM54 industrial router, manufactured by Teltonika Networks UAB (Kaunas, Lithuania). For the configuration test it provided the 2.4 GHz WLAN used by the IMU node and the acquisition PC (the MQTT broker/service ran on the PC; the router supplied connectivity). Then, power up the inclinometer/accelerometer sensor by placing a magnet directly on the device.

Figure 88: Teltonika Networks RUTM54 industrial router used for the 2.4 GHz WLAN connection in laboratory tests.

When the MQTT software is opened, a window appears as shown in Figure 89:

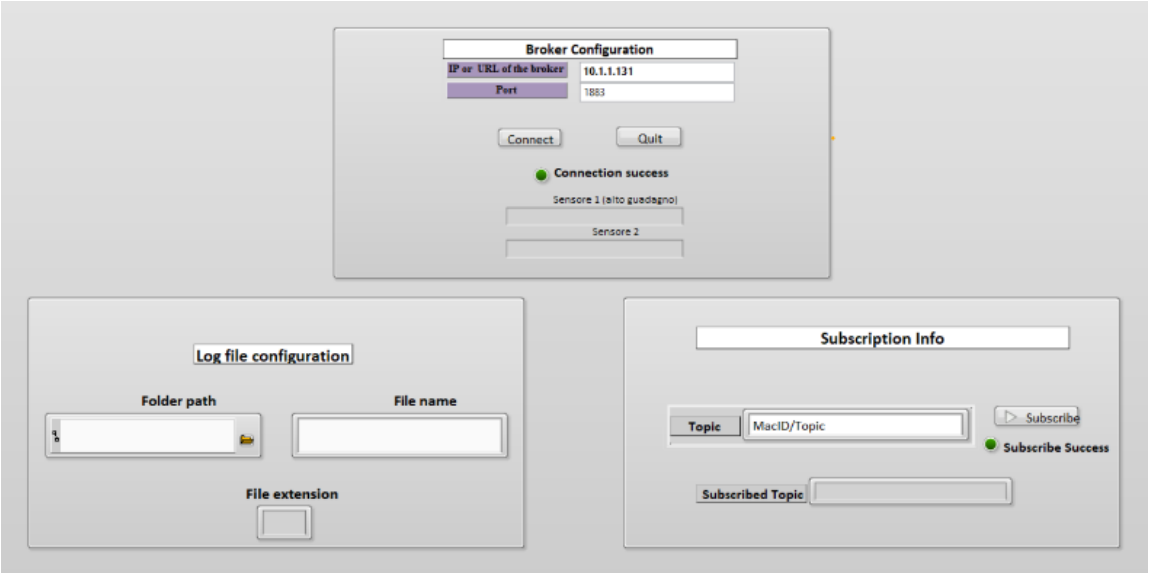

Figure 89: preliminary configuration required to connect IMU device to the broker for correct data streaming.

- Broker configuration: In the upper panel you configure the MQTT broker. Enter the broker address in “IP or URL of the broker”, then set the Port: use 1883 for an unencrypted connection. Click Connect. If the session is established successfully, the Connection success indicator turns green. The Quit button closes the session. Beneath the broker settings, two slots—Sensor 1 (high gain) and Sensor 2—display the status of the publishing nodes when they are available.
- Log file configuration: In the lower-left panel, select where and how to save the incoming stream. Specify the folder path (the destination directory), the file name (without the extension) and the file extension (e.g. .csv or .txt). Once these three fields have been set, the program will create or append to log files while you are subscribed to the topic.
- Subscription info: you configure the subscription in the right-hand panel. In the 'Topic' field and enter the sensor’s MQTT topic. Click Subscribe. If the subscription is successful, the 'Subscribe Success' indicator will turn on, and the 'Subscribed Topic' field will show the actual sensor in use. From that moment onwards, the PC will receive the payloads that the sensor publishes on that topic. These will appear live in the *StreamingModeData* tab and will also be available for Signal Analysis.

Once the subscription is complete, Streaming Mode will start automatically. Figure 90 shows the StreamingModeData panel, which includes three plots for viewing the X, Y and Z components of acceleration in the time domain, as well as a JFTA panel that maps frequency as a function of time; Joint time-frequency analysis is a technique that allows you to visualize how the frequencies of a

signal change over time. It overcomes the limitations of analysing the signal in either the time domain (x(t)) or the frequency domain (X(f)) using the Fourier transform (FFT). In practice, it displays the spectrum of a signal (i.e. its frequency components) as a function of time, which is crucial for non-stationary signals. There are also two plots showing the X and Y components of inclination, alongside their respective JFTA displays. A control panel on the right lets you adjust acquisition settings, such as the sampling rate and filtering (low-pass, high-pass or band-pass), as well as the configuration parameters for JFTA mode.

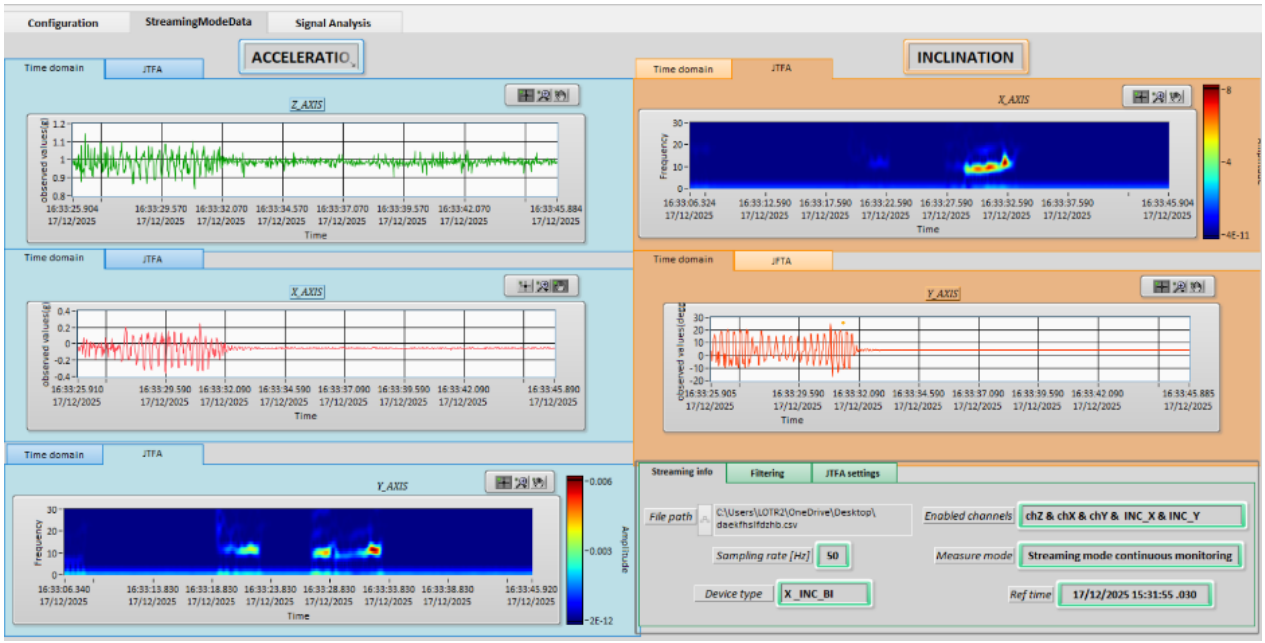

Figure 90: streaming visualization window.

Sensitivity test

Preliminary trials were carried out before running the actual tests to select an appropriate sampling rate for both the load cells and the IMU sensor. Data were acquired at 20 Hz, 50 Hz and 300 Hz. To enable fair comparison, a two-second segment was extracted from each trial to ensure the signals covered the same time span. This enabled us to determine which sampling rate was better suited to capturing the rapid variations, i.e. the short impulses generated by the 'gusts' produced with the blower. Figure 91 shows the three graphs for each of the three trials conducted at the chosen sampling frequencies, to evaluate which was adequate.

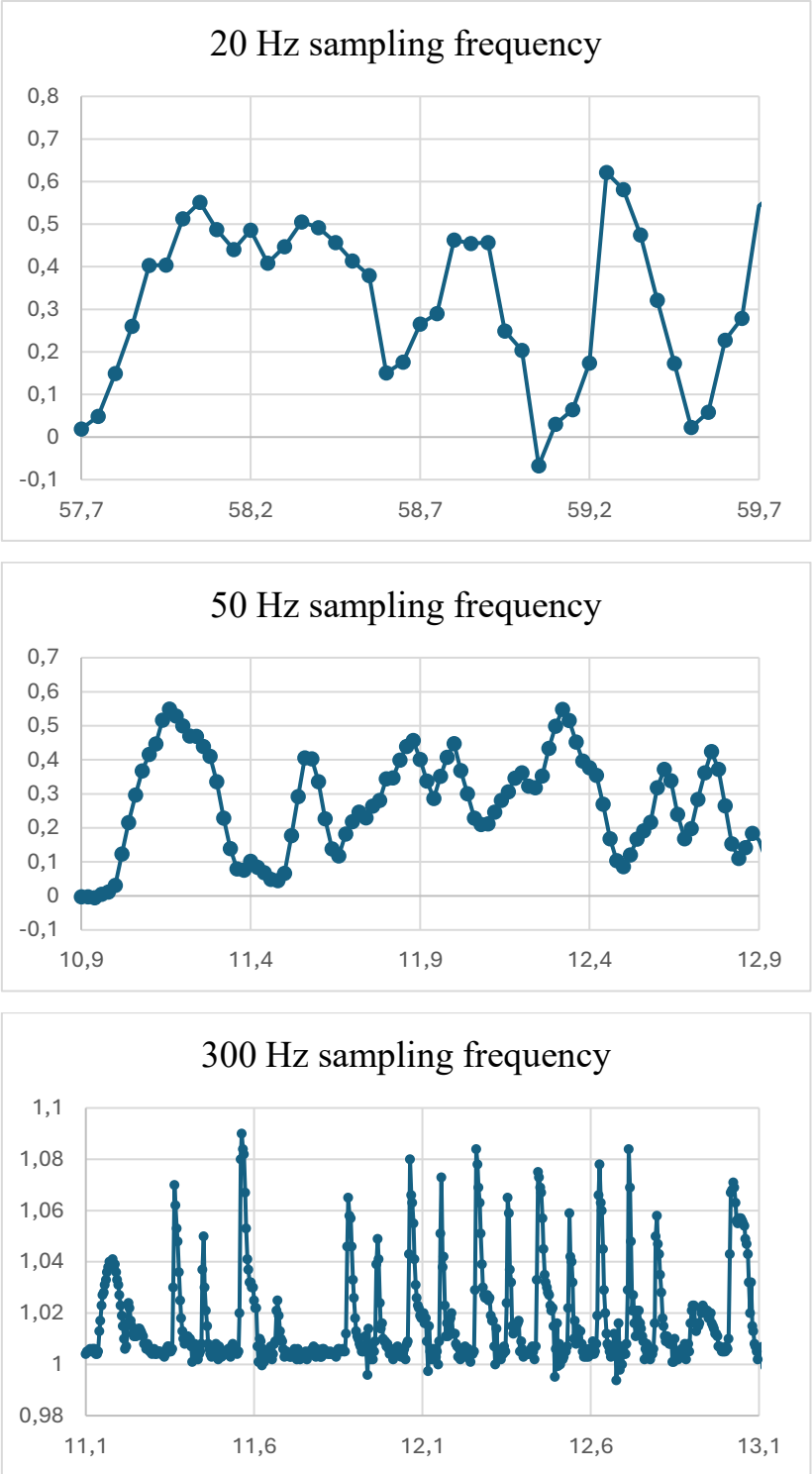

Figure 91: 20 Hz, 50 Hz and 300 Hz signal acquisition for the choice of the adequate sampling frequency.

The sampling rate was set to 50 Hz because this provides enough points to reconstruct the signal, especially the peaks, without losing information. At 20 Hz, the reconstructed signal appears more averaged and filtered than at 50 Hz. At the other extreme, very high sampling rates, such as 300 Hz, tend to overspecify the measurement and introduce substantial noise. Peak counts increase (many of

which are likely to be artefacts caused by the motion of the entire setup) and the nominal 'zero' baseline becomes unstable and noisy. Therefore, sampling-rate selection is critical for zero-balanced signals: lower rates (e.g. 20 Hz) produce a cleaner baseline in calm conditions, but miss fast peaks; whereas higher rates (e.g. 300 Hz) result in a noisy zero, which would require post-processing filters. For these reasons, 50 Hz was chosen as a practical compromise between 20 Hz and 300 Hz. For the moment, tests are being conducted in the laboratory and therefore the data transmission and storage capacity is virtually unlimited. If we want to apply this reasoning to a real-time rapid alert system, the choice of sampling frequency becomes crucial, also in terms of the weight (MB) of the acquired data to be transmitted and stored.

Results

The raw data acquired by the system are as follows: from the IMU, the X and Y inclination components (XY) and the X, Y, and Z acceleration components; from the load cells, the compression and tension measurements—i.e., the load components along the Z axis, along the X axis, and along the Y axis. As previously mentioned, both signals recorded by the two IMU and Quantum MX840b systems were acquired at a sampling frequency of 50 Hz. It is essential to choose the same sampling frequency because it then becomes easier to correlate the inclination and acceleration data (the tree's response to the wind) with the force and mechanical moment data (the action of the forcing agent - wind). Figure 92 shows the three subplots of the three acceleration components:

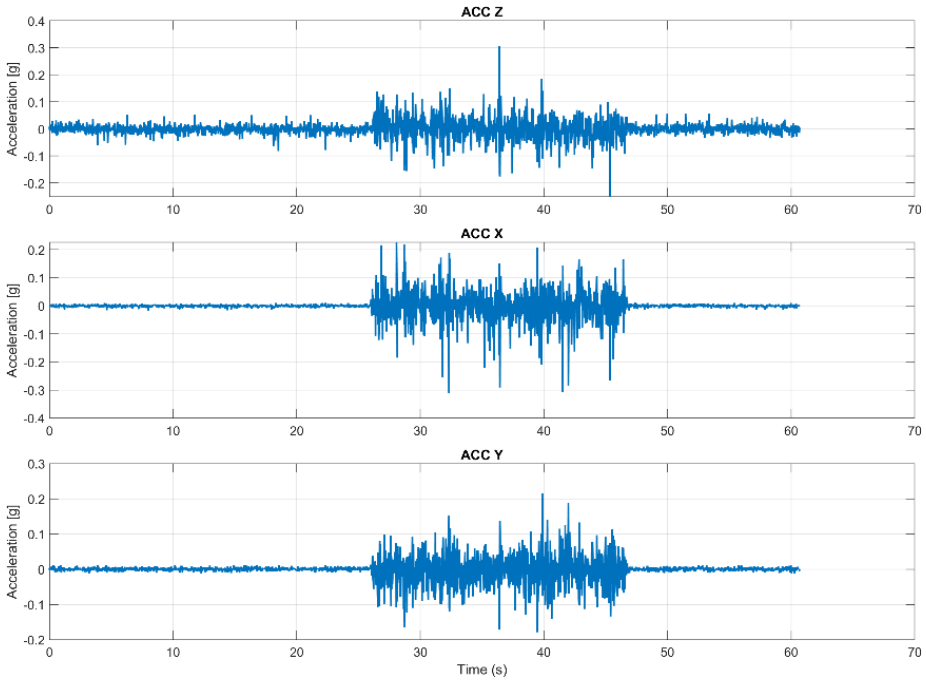

Figure 92: raw data of the three acceleration components (Z, X, Y).

Figure 93 shows the two components X and Y of the inclination recorded by IMU sensor:

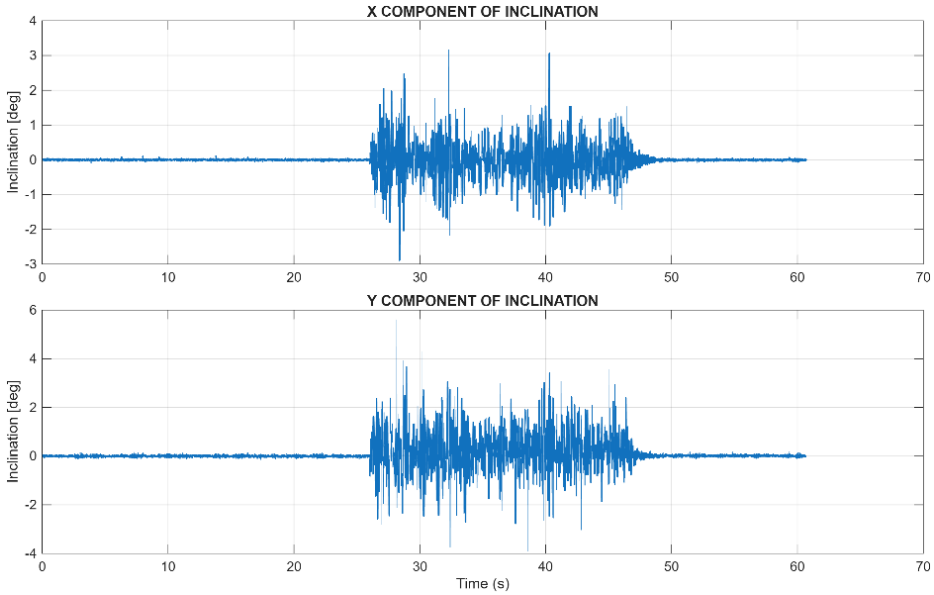

Figure 93: raw data of the two inclination components (X, Y).

After acquiring the inclinometric measurements along the X and Y axes, the complete inclination signal, or resultant inclination, was reconstructed. This was computed using the Pythagorean theorem, i.e. the magnitude of the inclination vector is the square root of the sum of the squared axial components:

$$R = \sqrt{X^2 + Y^2}$$

Figure 94 reports the time history of the resultant inclination:

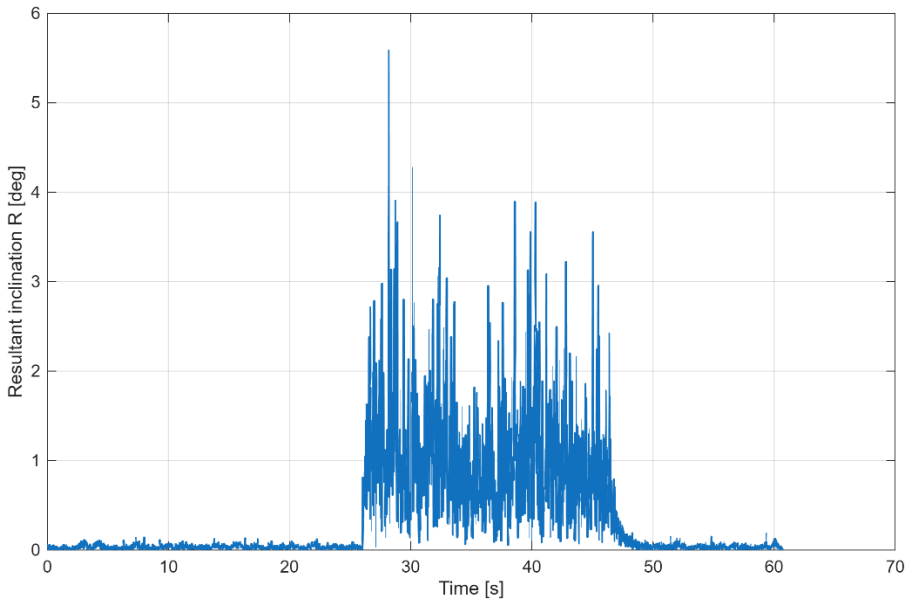

Figure 94: signal of the resultant of the inclination over time.

The remaining raw measurements were acquired from the load cells. These sensors natively record mass in kilograms; during post-processing, the readings are converted to force in newtons by multiplying by the value of gravitational acceleration (g = 9.81 m/s^2).

For vertical reactions, the devices were labelled as follows: C1-v-dx (leeward), C2-v-sx (leeward) and C3-v (windward), where *v* denotes the vertical direction and *dx* and *sx* indicate the right and left sides, respectively. The reference frame is oriented with the observer facing the tree and looking in the same direction as the wind. For in-plane horizontal reactions, the labels are: C4-h (leeward), C5-h-dx and C6-h-sx, where *h* denotes the horizontal plane.

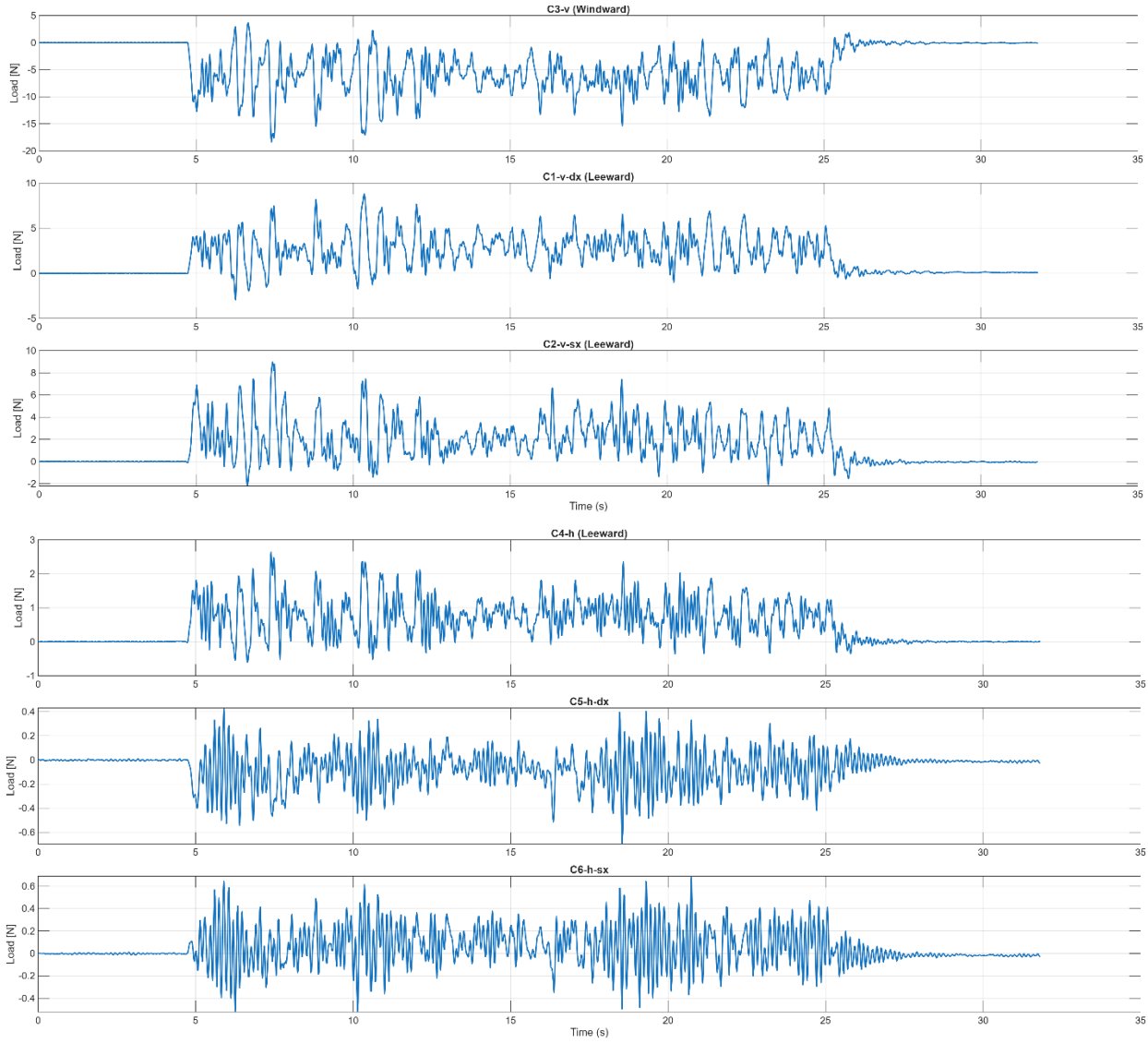

Figure 95: time series of wind load recorded by load cells.

Next, the bending moments about the three axes (X, Y, Z) are computed. Moments are obtained using the classical relation $M = F \cdot b$, where F is the measured force (N) and b is the lever arm (m). For the moments about the X and Y axes, the forces from the load cells mounted in the vertical plane (C1,

C2 and C3) are used. For the torsional moment about the Z-axis, forces from the load cells in the horizontal plane—C4, C5 and C6—are employed.
The data for calculating the moments are now listed. Next to each load cell is the abbreviation of the arm “b” used for the calculation.

MOMENT ALONG X AXIS: (C1, b1_X), (C2, b2_X), (C3, b3_X)

b1_X = 0.15 m

b2_X = 0.15 m

b3_X = -0.21 m

Mx_cd = C1 * b1_X

Mx_cs = C2 * b2_X

Mx_t = C3 * b3_X

Mx_tot = Mx_C1 + Mx_C2 + Mx_C3

MOMENT ALONG Y AXIS: (C1, b1_Y), (C2, b2_Y), (C3, b3_Y)

b1_Y = 0.255 m

b2_Y = -0.195 m

b3_Y = 0.025 m

My_cd = C1 * b1_Y

My_cs = C2 * b2_Y

My_t = C3 * b3_Y

My_tot = My_C1 + My_C2 + My_C3

MOMENT ALONG Z AXIS: (C4, b4_Z), (C5, b5_Z), (C5, b6_Z)

b4_Z = 0.018 m

b5_Z = 0.045 m

b6_Z = 0.045 m

Mz_HL = C4 * b4_Z

Mz_HT_dx = C5 * b5_Z

Mz_HT_sx = C6 * b6_Z

Mz_tot = Mz_C4 - Mz_C5 + Mz_HT_C6

The bending moments about the X, Y, and Z axes were computed at every time step of the acquired signals, thereby reconstructing the corresponding moment time series. As demonstrated in Figure 96, the following data is presented.

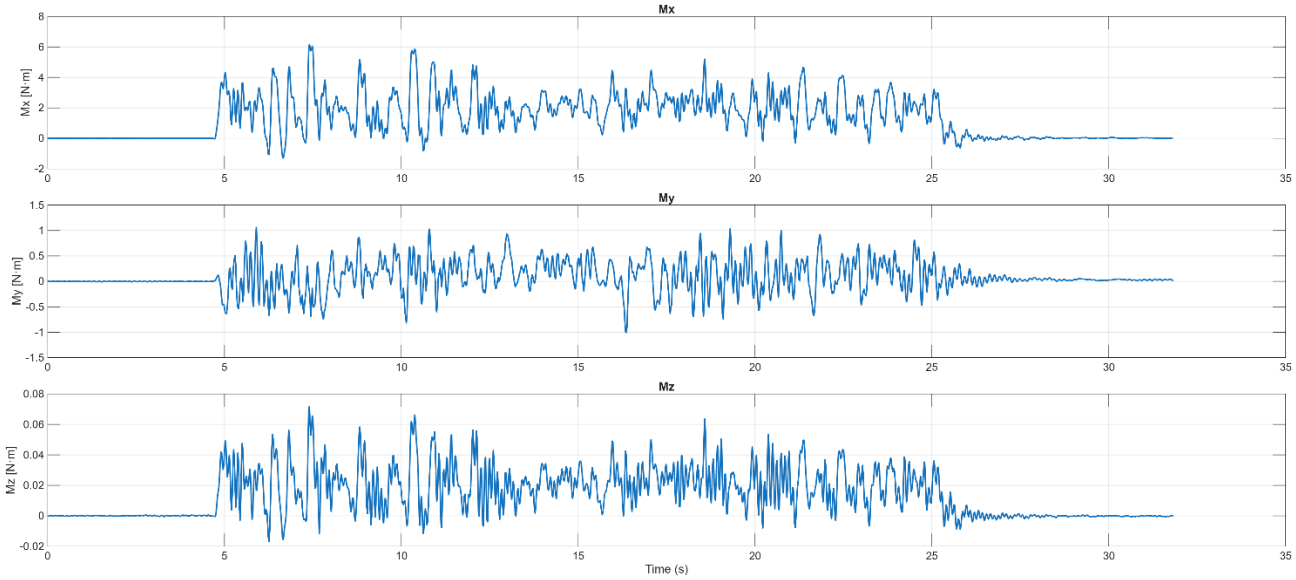

Figure 96: corresponding moment time series.

From this juncture onwards, the objective is to establish a correlation between the forcing data (wind) and the response (rotation of the tree root plate). The total moment was thus calculated initially using the Pythagorean theorem, with the components denoting the moments relative to the X-axis and relative to the Y-axis, respectively. The time series of the total moment is shown in Figure 97.

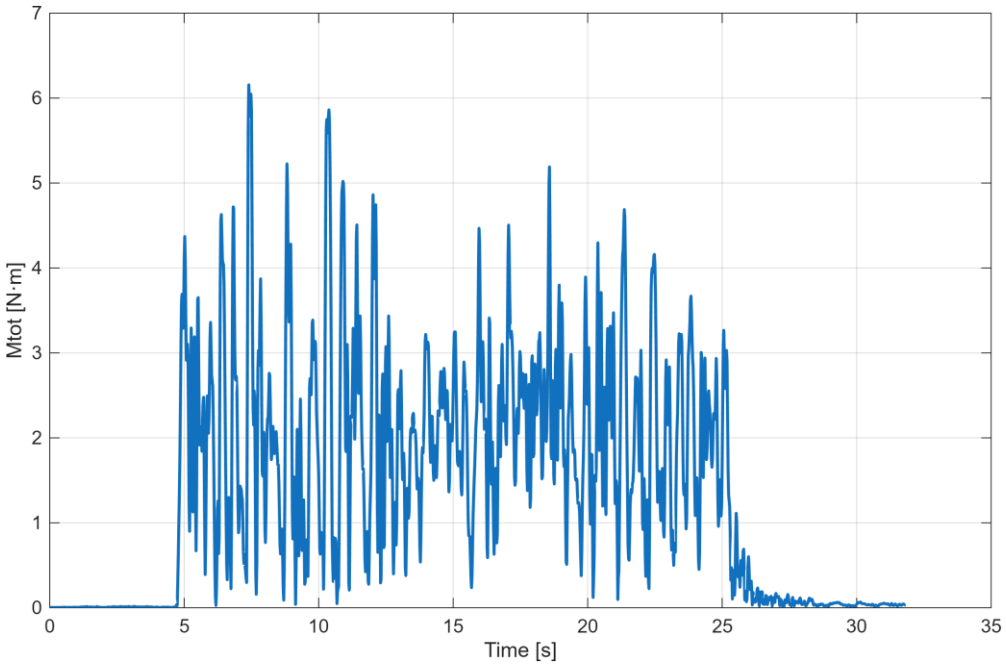

Figure 97: time series of the Moment total.

It is important to note that both signals, the resultant and the total moment, were acquired at the same sampling frequency. This allows for the plotting of both signals on the same graph. As illustrated in Figure 98, the total moment time series is displayed in blue, while the resultant inclination time series is shown in orange (for the sake of simplicity, merely a single example is presented, with the inclination series being truncated). At this point, it was possible to translate the resulting inclination signal with respect to the moment signal (precisely because both signals were acquired with the same sampling frequency). Coupling the two signals allows the action of the wind to be coupled with the response of the tree, thus obtaining couples (moment, rotation). Figure 99 shows the coupled moment and rotation signals.

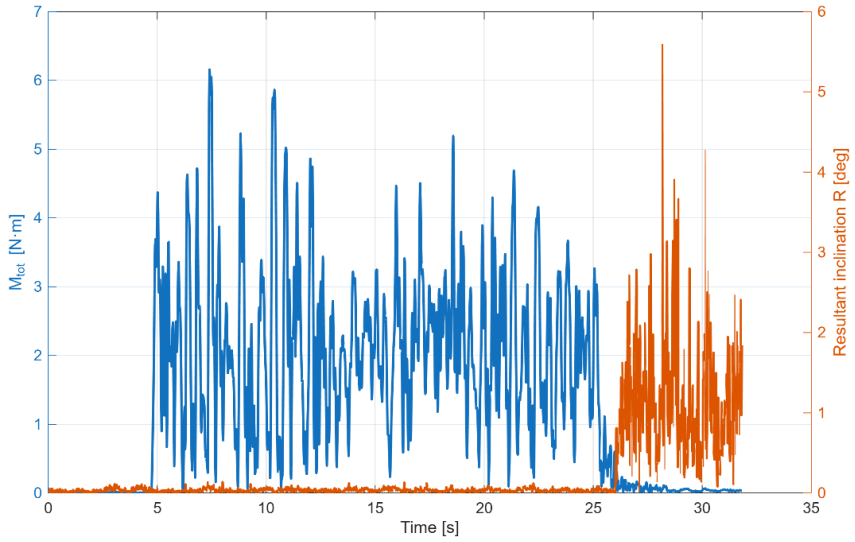

Figure 98: not aligned Moment and Inclination time series.

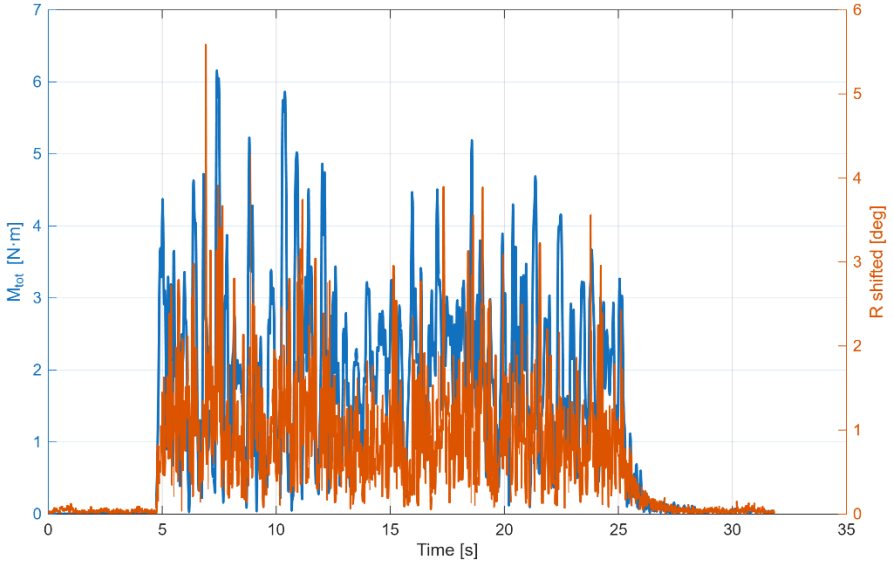

Figure 99: aligned Moment and Inclination time series.

In order to facilitate enhanced visualisation of the pairs (moment, rotation), a scatter plot was created, as illustrated in Figure 100. It is evident that there are some pairs that exhibit low rotation values for high applied moment values, and vice versa. It can be hypothesised that these two ranges of values may not accurately represent the instantaneous response of the tree to wind action. In this regard, a methodology has been formulated (elucidated in Chapter I) that facilitates enhanced congruence between the signal and the response, as well as the selection of the pairs that most accurately represent the rotation of the tree's root plate in relation to the imposed wind load.

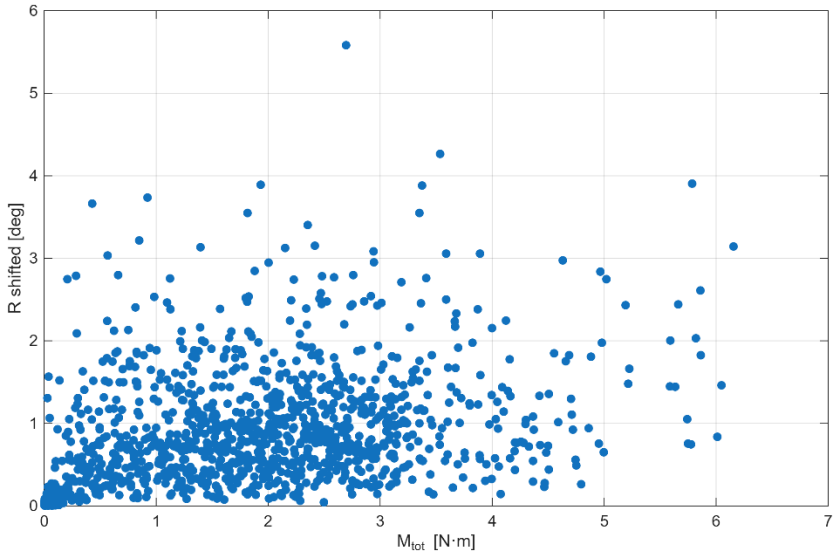

Figure 100:plot of the total moment – inclination resultant couples.

This results in a filtered data set that has been interpolated with the Wessolly curve, as shown in Figure 101.

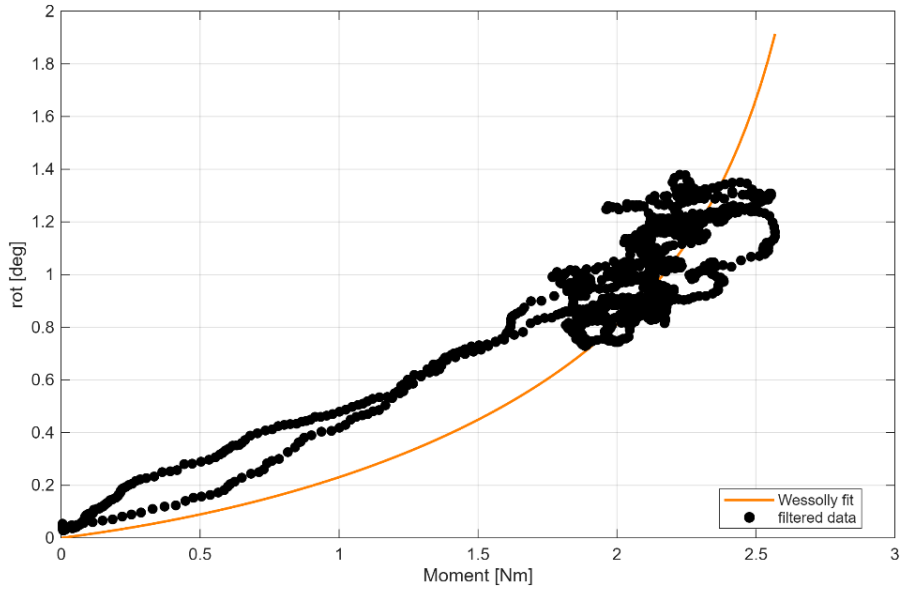

Figure 101: Wessolly's interpolation of the filtered data.

Trasmissibility and energy dissipation estimation

Loads at the base and transmissibility

From the load-cell array, has been extracted the three reaction components at the pot–base interface: the horizontal reaction along the wind direction, N_y(taken as $+Y$); the transverse horizontal reaction, N_x($+X$); and the vertical reaction, N_z(the sum of the three vertical cells, reported in modulus). Each component is non-dimensionalized by the imposed wind load F_{wind} to obtain transmissibilities:

$$T_x = F_{wind} / Nx \qquad T_y = F_{wind} / Ny \qquad T_z = F_{wind} / |Nz|$$

Figure 102 shows the time history of T_x, T_y, T_z and the Figure 103 illustrates a 100% stacked area chart showing, at each instant, the percentage share of $|T_x|$, $|T_y|$, $|T_z|$, relative to their instantaneous sum, thereby quantifying how the applied wind load partitions into transverse, longitudinal, and vertical reactions over time.

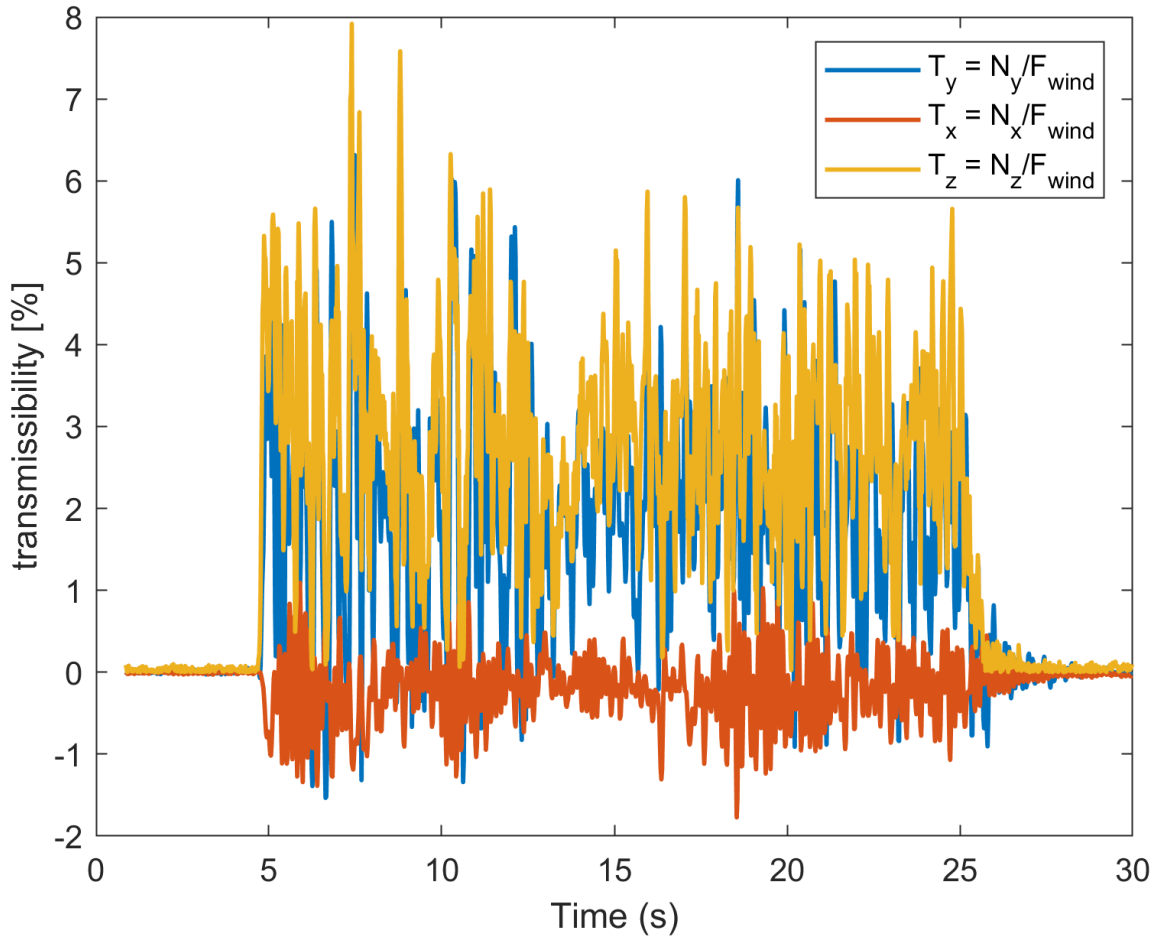

Figure 102: time series of T_x, T_y, T_z.

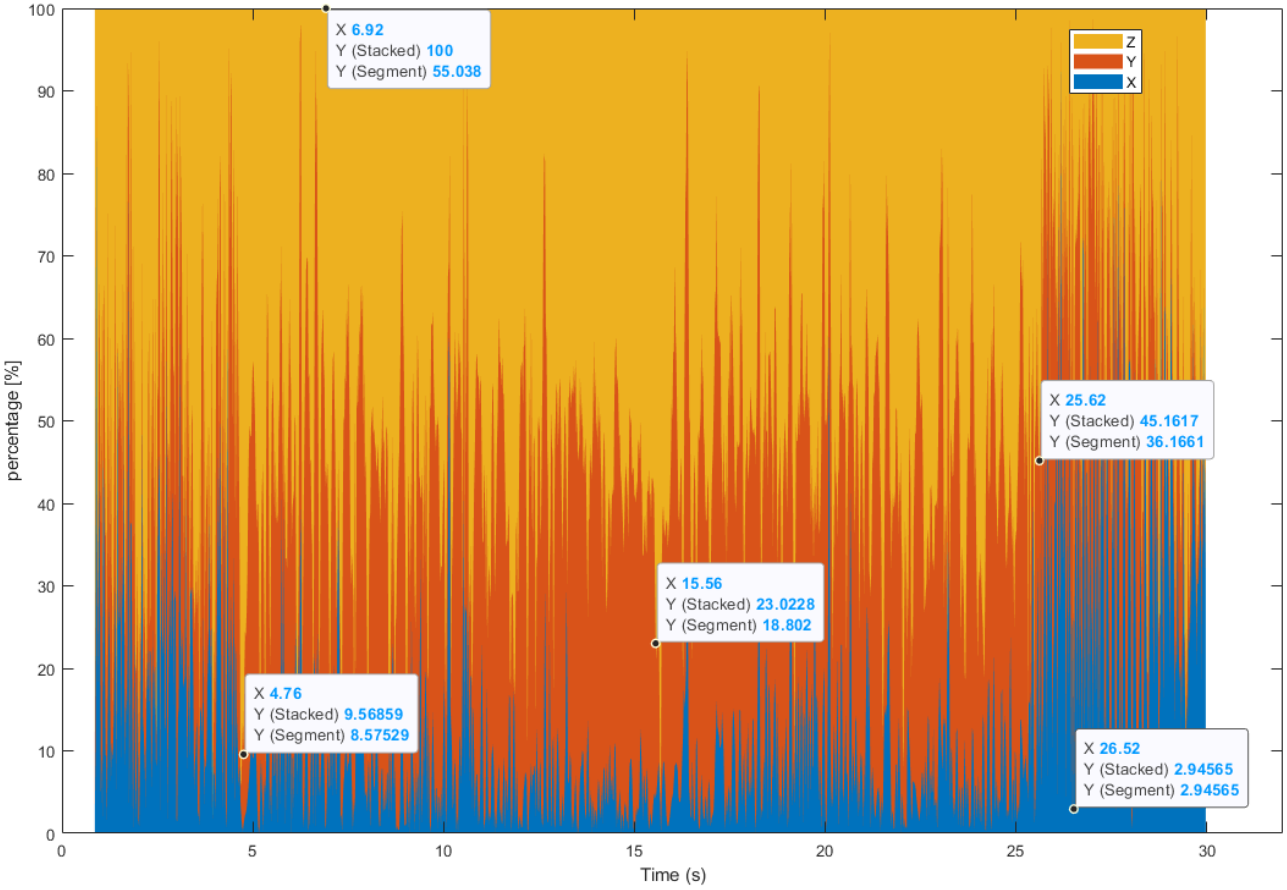

Figure 103: 100% stacked area chart of the percentage share of |Tx|, |Ty|, |Tz|.

Here's how to read those tooltips in a stacked area of Figure 103:

- Y (Segment) is the contribution of the Y series alone at time t. Denote the instantaneous percentages by $p_X(t), p_Y(t), p_Z(t)$ with $p_X + p_Y + p_Z = 100\%$. Then Y (Segment) = $p_Y(t)$.
- Y (Stacked) is the cumulative value up to and including Y, i.e., the sum of all layers beneath Y plus Y itself. For the ordering X(bottom), Y(middle), Z(top): Y (Stacked) = $p_X(t) + p_Y(t)$.

So, for exemple a tooltip showing "Y (Stacked) 45.16" and "Y (Segment) 36.17" means that at that instant $P_Y = 36.17\%$, and the cumulative share of $X + Y$ reaches 45.16% of the total height (which is normalized to 100%).

Energy and positive work at the base

Base work is computed incrementally as $\mathrm{d}E = M\,\mathrm{d}\theta$, using a trapezoidal average of the base moments and signed incremental rotations. Axis pairing is physically consistent: M_x is paired with rotation about X (obtained from the Y-inclination), and M_y with rotation about Y (from the X-

inclination). Only positive contributions are accumulated (i.e., energy is not recovered from negative work), yielding the cumulative base energy

$$E_{base}(t) = \sum[\max\ (M_x\, d\theta_X, 0) + \max\ (M_y\, d\theta_y, 0)] \qquad \text{Eq. [14]}$$

Instantaneous power at the base is the per-sample positive work divided by the sampling period Δt and its trend is shown in Figure 104.

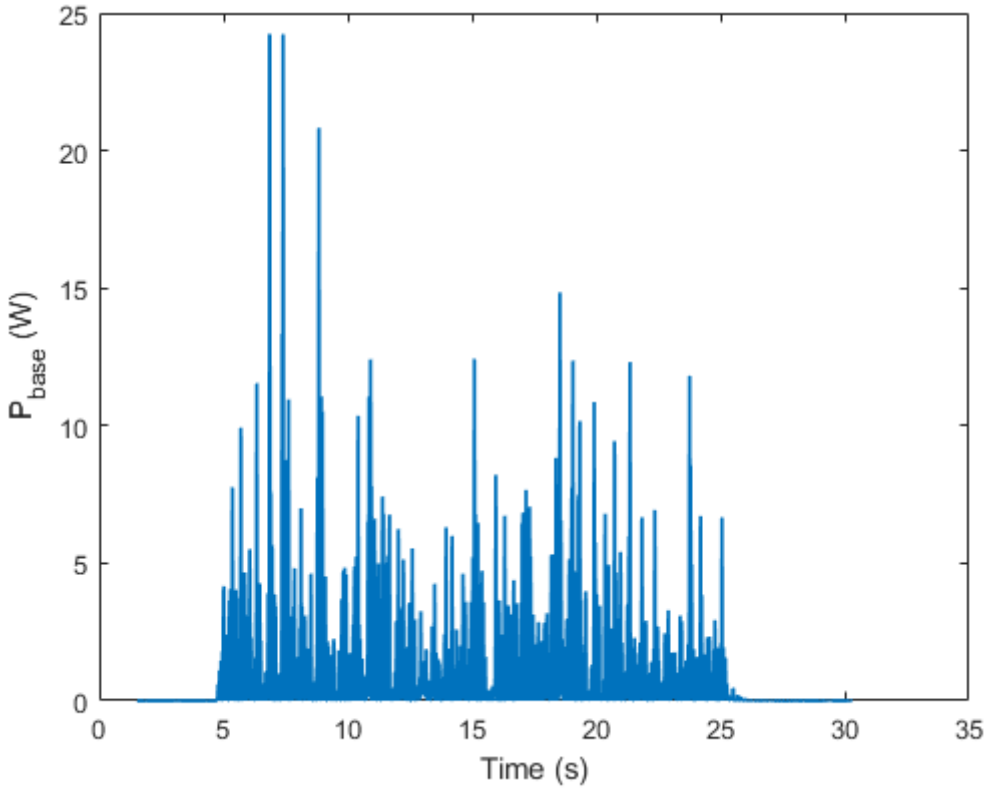

Figure 104: instantaneous power time series.

Input energy from the canopy and dissipation

Assuming wind along $+Y$, a constant input moment about the Xaxis is prescribed as

$$M_{in} = F_{vento} \cdot H_{ref} \cdot 0.66 \qquad \text{Eq. [15]}$$

where H_{ref} is an effective lever arm and the factor 0.66 accounts for empirical reduction (e.g., projected area and lever-arm effectiveness). Input energy accumulates only when rotation about X increases (positive work):

$$E_{in}(t) = \sum max\ (M_{in}\, d\theta_x, 0) \qquad \text{Eq. [16]}$$

The dissipated energy is then

$$E_{diss}(t) = max\ (E_{in}(t) - E_{base}(t), 0) \qquad \text{Eq. [17]}$$

and the final dissipation ratio $E_{\text{diss}}(t_{\text{end}})/E_{\text{in}}(t_{\text{end}})$ is reported as a percentage. Figure 105 summarizes cumulative energies E_{in}, E_{base}, E_{diss}, allowing a direct comparison between the driving input, the energy transmitted to the base, and the portion dissipated by the system.

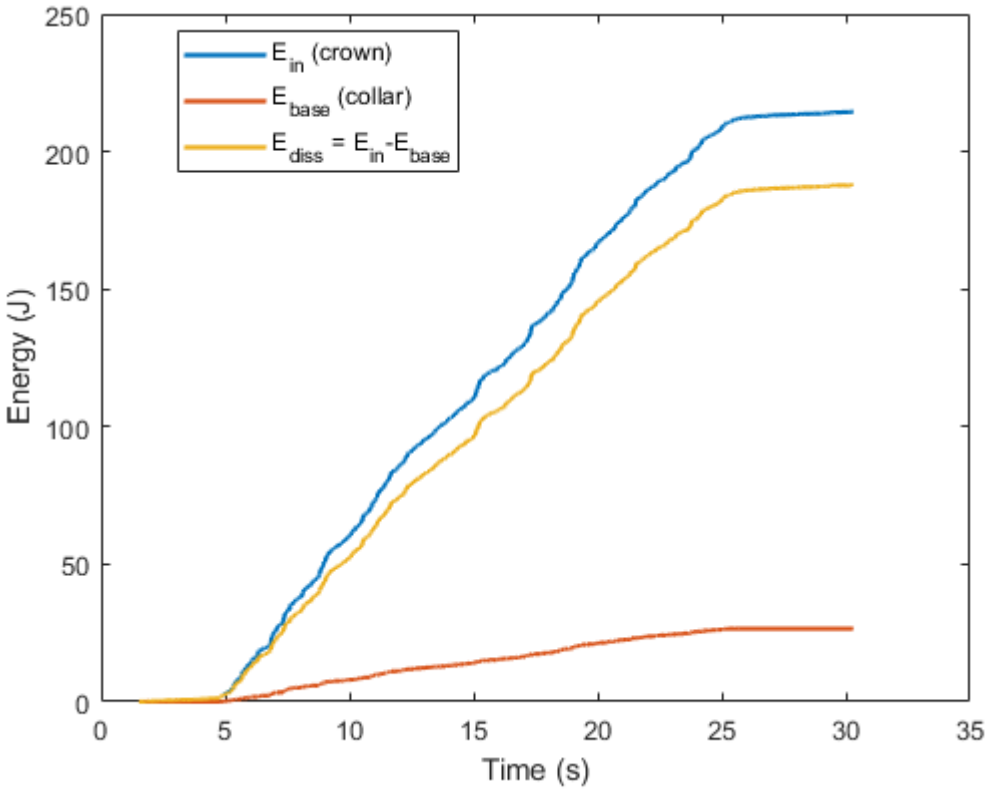

Figure 105: cumulative energies E_{in}, E_{base}, E_{diss}.

Discussion

The small-scale model made it possible to continuously acquire foot reactions in three directions, combining them with inclinations and accelerations of the sole. This fills a gap typical of both static tests (where only the applied traction is measured) and dynamic tests (where there are no direct measurements of the forces transmitted to the root-soil area). The architecture with three vertical isostatic cells (120°) on wheels and three horizontal side cells reduced constraints and made the contributions along X, Y and Z readable, allowing for transmissibility and energy balance analyses that are not available in the test setups that are normally carried out.

The calibration of the six cells with known masses confirmed repeatability, legitimising the use of signals for moment and power estimates. The sampling frequency of 50 Hz proved to be an effective compromise: at 20 Hz, peaks and micro-transients are lost; at 300 Hz, noise increases (unstable baseline and possible mechanical artefacts from the bench). The frequency alignment between DAQ and IMU made it possible to couple moment and rotation and subsequently interpolate with a Wessolly curve on the filtered data.

By normalizing the reactions $T_x=N_x/F_{wind}$, $T_y=N\_y/ F_{wind}$, $T_z=|N_z|/ F_{wind}$, the graphs show how the load imposed by the flow is distributed over time between the wind direction, transverse and vertical directions. The 100% area diagram shows that, during gusts, the longitudinal component T_y increases as expected, while T_x and T_z modulate the balance between transverse instability and vertical unloading, suggesting dissipative behaviour involving both canopy aerodynamics and stem-vessel-constraint flexibility. The distinction between the *segment* value (percentage of the single channel) and *stacked* value (cumulative up to the layer considered) helps to quickly read the relative contribution peaks.

The incremental calculation of the work at the foot (E_{base}) constructed with trapezoidal averages of the moments M_x, M_y and angular increments $d\theta_x$, $d\theta_y$ provides a reliable estimate of the energy transferred to the base.

The limitations and uncertainties involved are as follows. About the scale factor: blower jets and canopy in a tank do not perfectly replicate the dimensionless numbers of atmospheric wind. About the structure: although the presence of the wheels, micro-frictions and mechanical movements can introduce bias in the horizontal components. About the sensor alignment: small rotations of the IMU relative to the reference (+X,+Y) can project energy onto “non-ideal” axes, modifying apparent principal angles.

When relating the base moment (M) to rotation (rot), an almost static and linear response is assumed: a higher M should produce a higher rot. In practice, the data deviates from this ideal due to dynamics and non-linearity. Rapid wind transients introduce inertia and damping, so rotation lags loading one may observe a high M with a still low rot (phase lag) or a low M while rot remains high (energy release). Micro-slips at contact points can absorb moment without immediate angular change. Geometric constraints and nonlinearities further distort the apparent M-rot slope in the X-Y plane. Finally, the response is velocity-dependent: for the same peak M, an impulsive force produces less rotation than a slowly varying load, as part of the work accelerates the masses and is dissipated.

Although the moment equilibrium may be satisfied instantaneously (quasi-static condition), this does not imply zero energy exchange. Mechanical energy depends on the work $dE=Md\theta$, therefore any non-zero rotation produces a non-zero energy transfer. In real systems, damping, friction and hysteresis (e.g., at constraints and soil–root interface) convert part of the input mechanical work into irreversible losses. Consequently, even under moment balance, a positive dissipated energy can be observed over time.

The implications and outlooks are the calibration of root-plate and aerodynamic models and designing early warning strategies based on thresholds exploiting an infrastructure as the ones tested in the laboratory.

Part II

Supporting tools for tree risk management

Chapter III

Long-term monitoring (*a monitoring campaign at Vivaio Bicocca*)

Introduction

Vivaio Bicocca, located in Milan (Italy) (Figure 106) is a tangible commitment to protecting and enhancing biodiversity within the Milano-Bicocca campus while improving the environmental quality and liveability of the surrounding Bicocca district. From an operational perspective, the nursery, granted to the University of Milano-Bicocca by the Municipality of Milan, functions as an urban oasis and a direct interface between academia and citizens. Its spaces are dedicated to participatory science activities that focus on understanding and safeguarding the biodiversity that underpins key ecosystem services, including pollination, seed dispersal and ecological connectivity across the urban landscape. In this sense, Vivaio Bicocca acts as both a green space and a living socio-ecological laboratory, approaching biodiversity as a functional asset for the city.

Figure 106: location of the Vivaio Bicocca in the city of Milan and its area in planimetric view.

At the Vivaio Bicocca, tree species originating from the Americas, Europe, the Mediterranean region, and Asia are represented, and the nursery covers an area of approximately 7,000 m². The American taxa include California incense cedar (*Calocedrus decurrens*), American sweetgum (Liquidambar styraciflua), southern magnolia (*Magnolia grandiflora*), and red oak (*Quercus rubra*). European species comprise European beech (*Fagus sylvatica*), pedunculate oak (*Quercus robur*), and small-leaved lime (Tilia cordata). The Mediterranean group includes Atlas cedar (*Cedrus atlantica f. glauca*), hornbeam (*Carpinus betulus*), Turkey oak (*Quercus cerris*), Mediterranean cypress (Cupressus sempervirens), holm oak (Quercus ilex), and European nettle tree (*Celtis australis*). Finally, the Asian species include Himalayan cedar (*Cedrus deodara*), ginkgo (*Ginkgo biloba*), crape myrtle (*Lagerstroemia indica*), and Japanese maple (*Acer palmatum*).

To complement static and dynamic tests, a 62-day dynamic monitoring campaign was carried out on nine trees, including seven in a row, at the Vivaio Bicocca (University of Milano-Bicocca, Milan, Italy). The main objectives were to:

- continuously record wind forcing and tree inclination under natural loading conditions.
- characterise the response of different species within the same row.

Figure 107 shows the monitoring layout consisted of an anemometer (weather station) and a Tree Monitoring System based on inclinometer sensors and a central data collection unit (Main Unit). The campaign focused on a small but diverse group of coniferous and deciduous species: *Cupressus serpenvierens* (Cs), *Cedrus deodara* (Cd), *Magnolia grandiflora* (Mg), *Pinus pinea* (Pp).

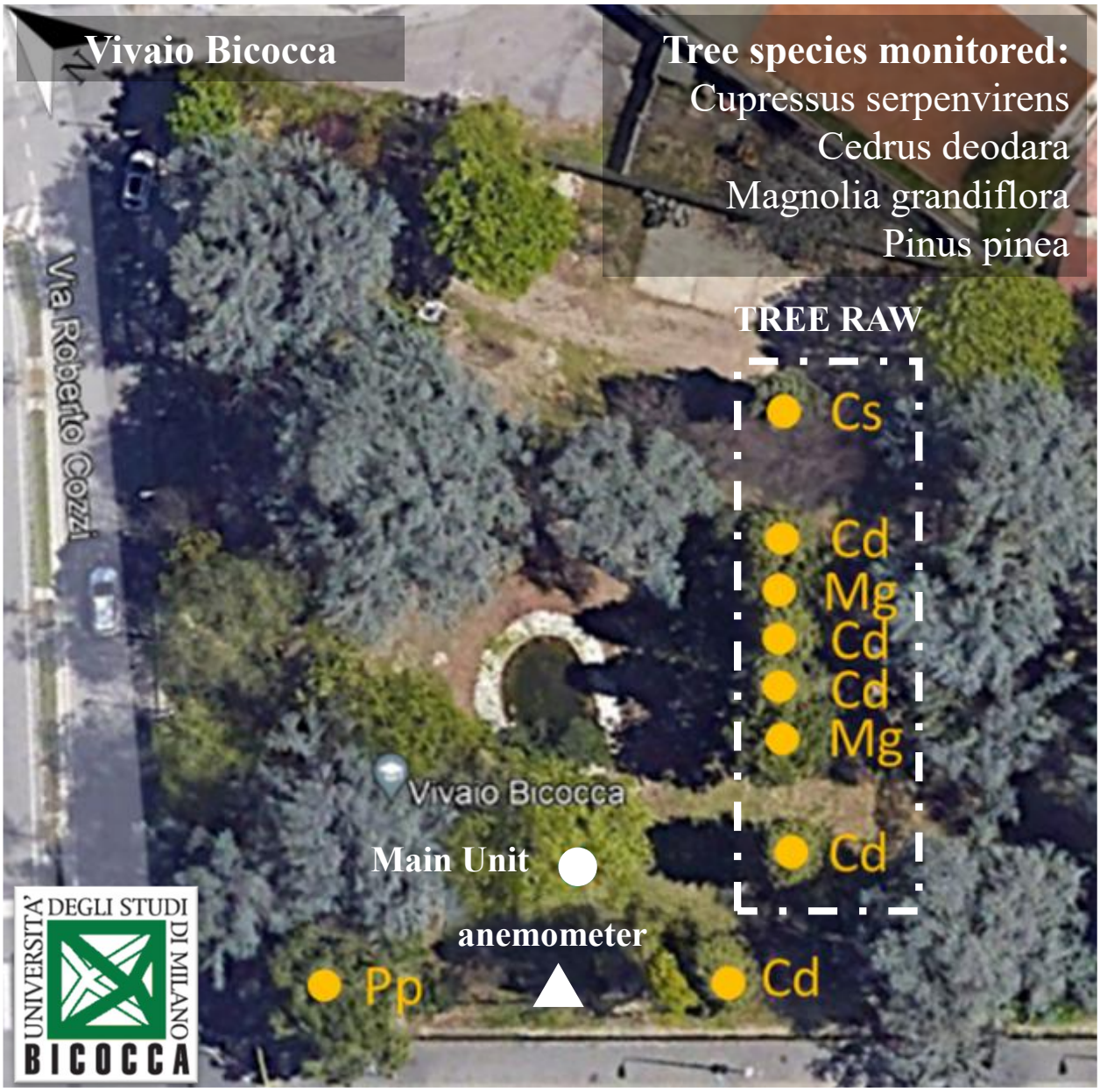

Figure 107: monitoring layout at the Vivaio Bicocca (Milan, Italy).

Method and results

The monitoring system used in this field campaign is the Tree Monitoring System (PiCUS TMSO, IML Electronic GmbH, Wiesloch, Germany) which is composed of:

- Anemometer station: wind data were recorded using an anemometer mounted on a metallic tripod as shown in Figure 108. The tripod supported an extendable metal pole reaching an overall height of approximately 10 m, with the anemometer installed at the top. This configuration ensured that wind speed and direction were measured above the immediate influence of the surrounding vegetation, providing a common reference forcing for all monitored trees. The sampling frequency used to acquire wind data was 20 Hz. The anemometer is equipped with an internal memory with a maximum capacity of 256 MB, but its real power lies in the fact that the instrument communicates via radio with the control unit to which it sends the acquired data. On one side of the anemometer there is a small solar panel that allows the instrument to continuously acquire data for an ideally infinite amount of time.

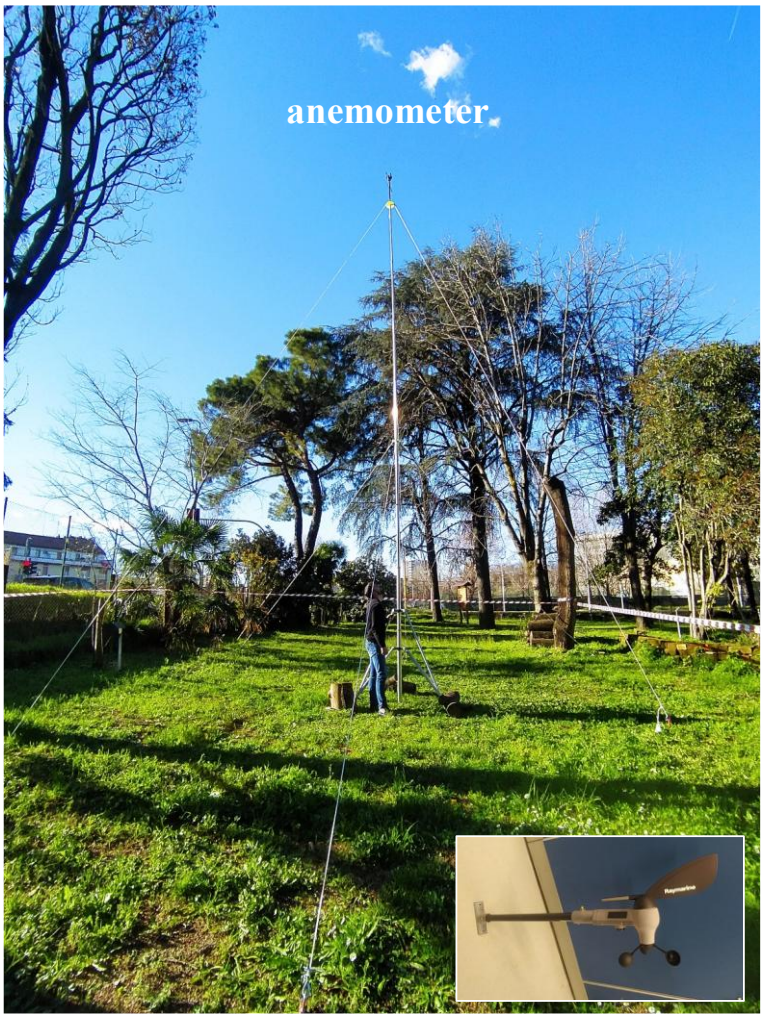

Figure 108: anemometer installed at the Vivavio Bicocca.

- Inclinometers to be screwed at the base of the trunk of selected trees, equipped with a small solar panel with a sampling frequency of 20 Hz. The data acquired by the inclinometers is sent via radio to the control unit. The internal battery of the inclinometers lasts for about two weeks, but thanks to the integrated solar panel, they, like the anemometer, can ideally acquire data indefinitely. When there is not enough solar energy, the battery takes over and provides power. Figure 109 shows the inclinometers on trees:

Figure 109: zoom on inclinometer installed on the base of the trunk and the tree row equipped with all the sensors.

- Main Unit with its solar panel were mounted on a separate tree chosen such that it was visible from all monitored trees. The unit and panel were strapped to the trunk with a synthetic strap and supported by a small metal base fixed with wood screws as shown in Figure 110. When planning the monitoring campaign, it is essential to choose the location of the control unit in relation to the trees to be monitored. There must be no structures or obstacles that could prevent proper radio communication between the sensors (inclinometers and anemometer) and the Main Unit. The data collected by the Main Unit is transmitted to the cloud, where it can be accessed for downloading, viewing and processing them.

Figure 110: Main Unit with solar panel integrated.

To obtain the biometric data of the trees, the point cloud was acquired using GeoSLAM technology. The following figure shows the entire Vivaio Bicocca and a zoom on the tree-lined row.

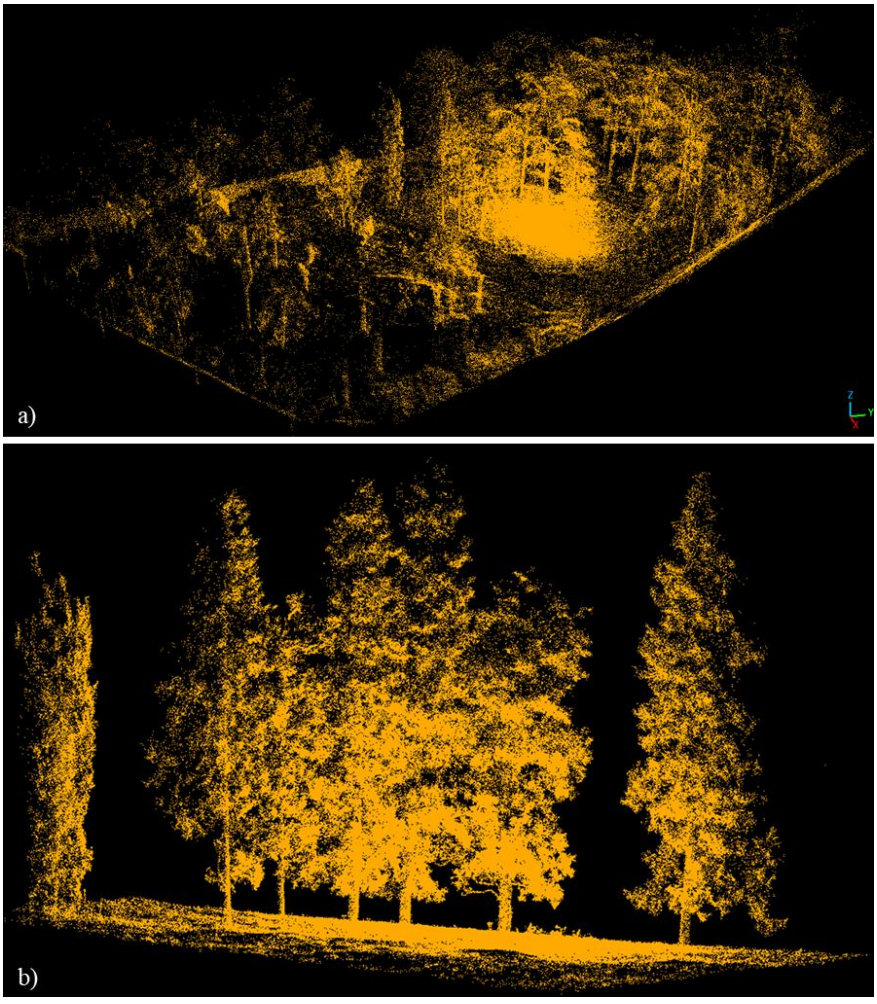

Figure 111: a) point cloud of Vivaio Bicocca from GeoSLAM technology, b) zoom on the tree row monitored.

Area of the crown of the trees has been estimated with the procedure described in Chapter II and are shown in Figure 112. Then the maximum experienced wind load on the canopy has been calculated. Table 13 shows the biometric data, the tabulated coefficient drag resistance, the wind load on tree (F_w) and ethe maximum moment applied on root-plate (M_{rp}) of the monitored trees.

Table 13: biometric and biomechanics data of monitored trees.

Tree	H (m)	DBH (m)	A (m^2)	Cd	ρ_{green} (kg/m^3)	F_w (kn)	$h_{barycentre}$ (m)	M_{rp} (kNm)
Cs	16	1.3	51	0.2	858	1070.2	10.7	11421.3
Cd_1	18	1.35	54.9	0.5	896	1203.1	12.0	14444.1
Mg_1	14	0.9	28.5	0.25	861	750.2	9.3	7005.3
Cd_2	18	1.26	44.5	0.2	896	975.2	12.0	11707.9
Cd_3	19	1.3	64.8	0.2	896	1420.0	12.7	17995.9
Mg_2	15	0.92	56.6	0.25	861	1489.8	10.0	14905.9
Cd_4	17	1.16	57.2	0.2	896	1253.5	11.3	14213.2
Cd_5	18	1.3	52.4	0.2	896	1148.3	12.0	13786.4
Pp	13	2	40.3	0.18	925	820.5	8.7	7114.9

Figure 112: crown area calculated with Arbosonic software by Fakopp Kft.

Data raw of all trees and anemometer acquired during the monitoring field campaign are shown in Figure 113. Light blue line is the velocity of the wind while all the other lines represent the inclination data of the nine monitored trees; it's also shown the wind rose diagram in a way to have a comprehension about the wind direction in time experienced associated with the distribution of wind velocity.

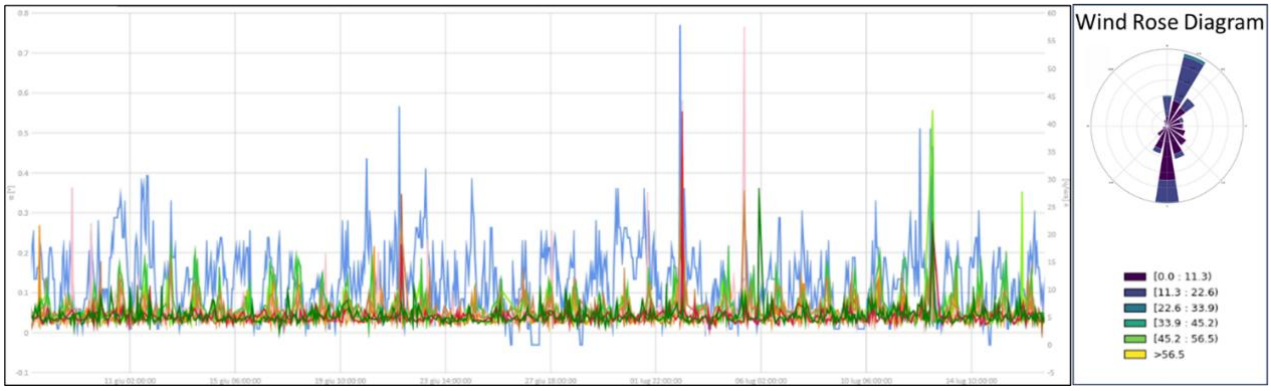

Figure 113: raw data acquired from field monitoring campaign at the Vivaio Bicocca.

Medium- and long-term monitoring shows the distribution of wind both in terms of direction and intensity. This makes it possible to obtain a clear picture of the acting forcing and therefore to define the initial and boundary conditions of the trees under observation. Depending on the season and on the meteorological state of the air at both large and local scale, trees are subjected to actions that influence their growth rate. As living organisms, trees continuously attempt to adapt to the new environmental conditions to which they are exposed. However, changes that are too abrupt in environmental conditions, and in this case in wind direction and intensity, do not leave sufficient time for a new adaptation. Long-term monitoring helps to identify the main loading directions, which may change over an extended period, and thus to understand which zones of the root system tend to be reinforced the most in order to better resist wind pressure.

From the monitoring data of the nine trees at the Vivaio Bicocca, a 10-minute time window (from 22:30 to 22:40) on 2 July 2024 was selected; Figure 114 reports the inclinations recorded by the inclinometers and the mean wind direction (red arrow). The selected time window is very short, but it was chosen because significant data were recorded for all trees. Depending on the configuration of the surrounding landscape (such as city roughness) and the presence of obstacles, even neighbouring trees within the same row can respond differently, despite being subjected to the same type of external forcing.

From the analyses it can be stated that:

- The *Cupressus sempervirens* (the first tree in the row, although slightly set back with respect to the *Cedrus deodara* CD_1) showed a uniform inclination pattern, with greater loading in the southern direction.
- In contrast, it is evident that the three *Cedrus deodara* (CD_1, CD_2 and CD_3), which together with the two magnolias more clearly belong to the identified row, exhibited a similar behaviour. All trees show a main and prevailing direction of inclination, namely towards the north-east. Considering that the mean wind direction was from the south-west, they responded consistently with the external forcing.
- The two *Magnolia grandiflora*, both belonging to the row in the strict sense and shorter than the adjacent *Cedrus deodara*, showed a different behaviour. *Magnolia grandiflora* Mg_1 exhibited a prevailing inclination direction towards the east/south-east, which does not differ greatly from that of the cedars next to it; however, unlike the two neighboring trees, its inclination distribution has a wider and less clearly defined spread than that of the cedars, most likely due to two factors: its lower centre of mass and its reduced height compared with the trees that have undoubtedly shielded it from the wind. *Magnolia grandiflora* Mg_2, being the terminal tree of the row (according to the nomenclature used in this context), was more exposed to the wind, with a larger portion of its crown not sheltered in the immediate surroundings by other trees. Its inclination pattern showed a tendency to move towards the north.
- *Cedrus deodara* CD_4 and CD_5, being more isolated, showed a very different – indeed almost opposite – behaviour compared with the trees described above. The first (CD_4) moved predominantly towards the north-west, whereas the second (CD_5) moved towards the west. CD_5 is located almost directly adjacent to the road and is therefore exposed in a different way from the preceding trees.
- The *Pinus pinea*, which does not belong to the row and has a crown architecture very different from all the other monitored trees, showed uniform behaviour, without marked or prevailing inclination directions. It is also located at the corner of the Vivaio Bicocca, facing towards a nearby road junction. Most likely, the large stem dimensions (DBH ≈ 2 m, and consequently a large root system) and the broad crown leaning towards the south-west caused the tree to respond in this way to wind coming from the south-west.
- The mean wind direction within the selected time window is south-west, but at any given moment the wind can change both direction and intensity (as previously discussed). The wind-

rose distribution shown in Figure 114j refers to 2 July 2024 and illustrates the pattern of wind direction, colored according to wind speed ranges. Consequently, the behaviour of the trees themselves can be highly variable even within a short time window.

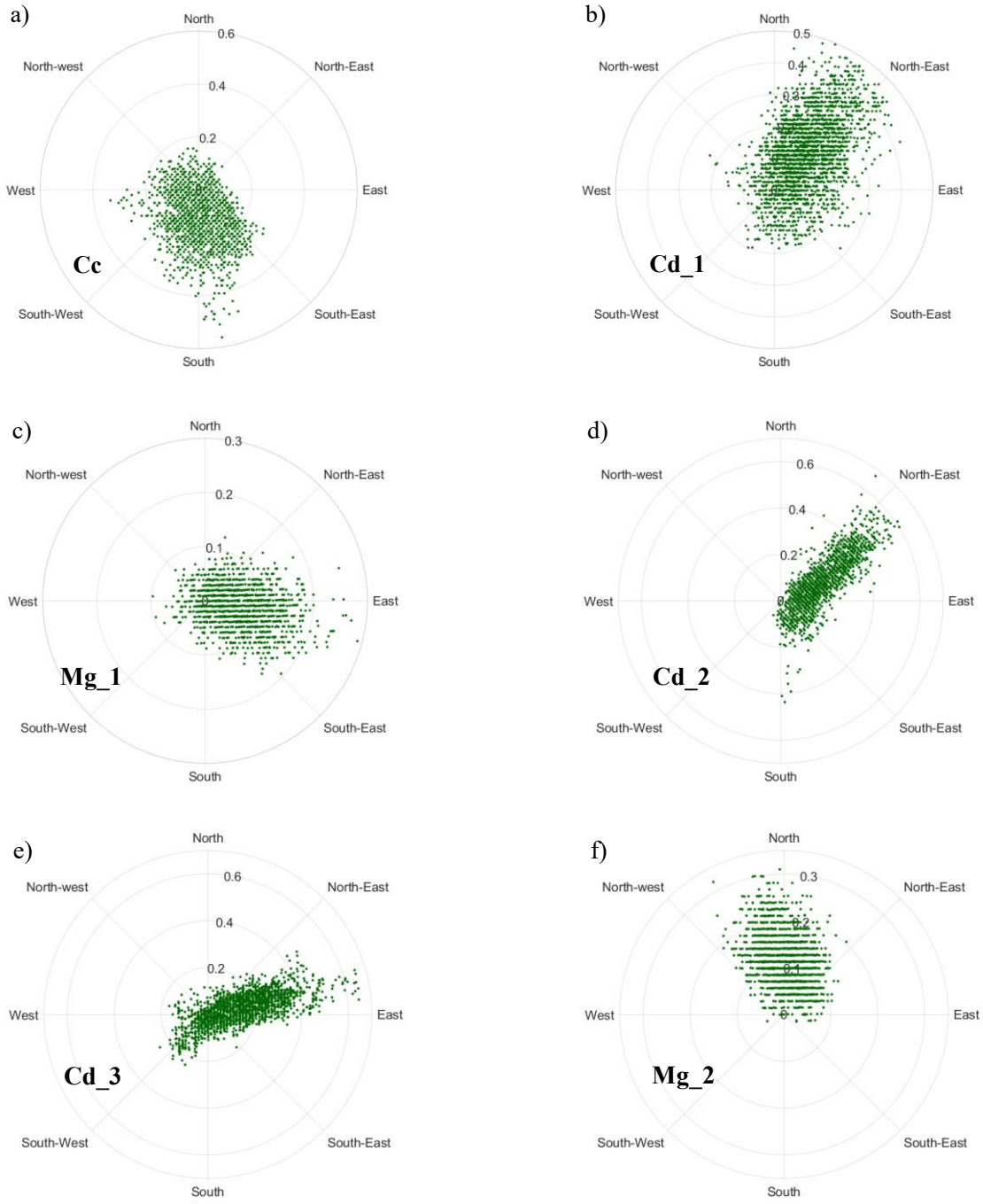

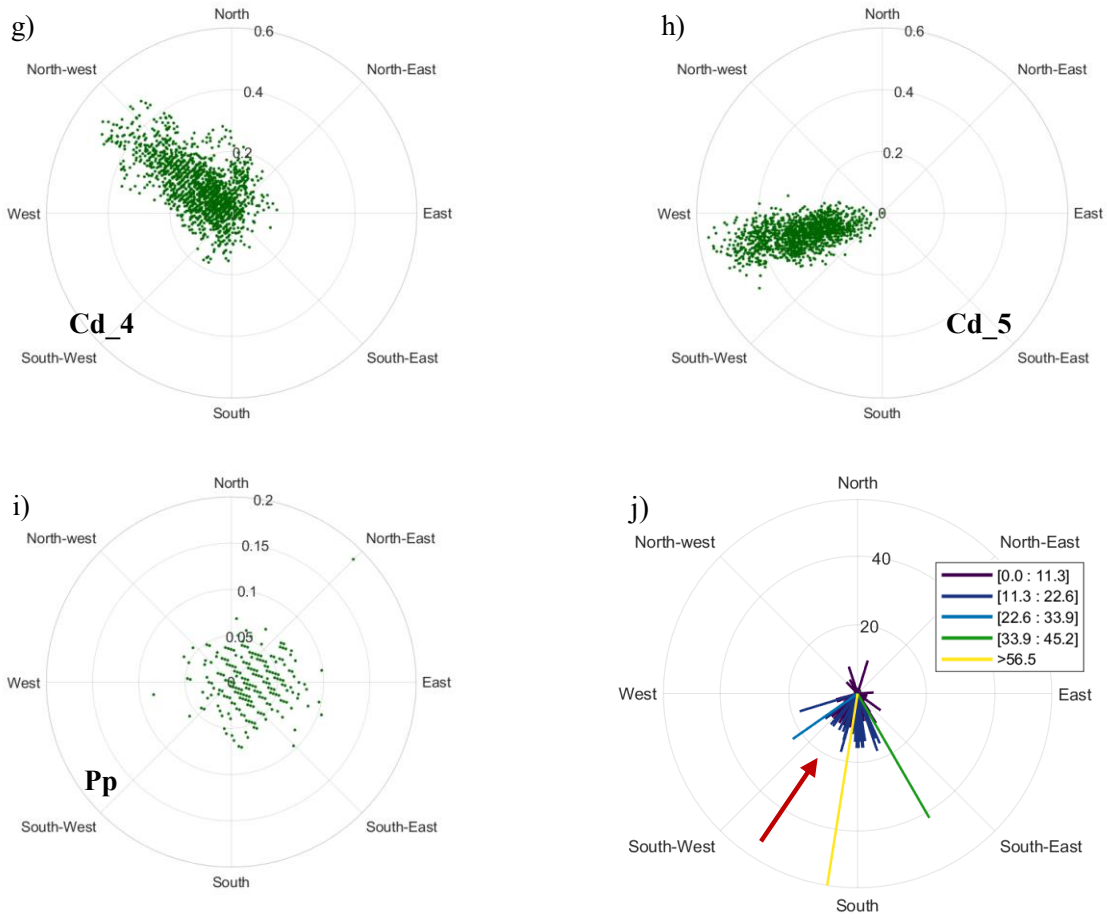

Figure 114: Distribution of inclinations of the trees monitored at the Vivaio Bicocca. Data refer to the selected 10-minute time window from 22:30 to 22:40 on 2 July 2024. a) inclinations of Cupressus sempervirens (Cs); b) inclinations of Cedrus deodara (Cd_1); c) inclinations of Magnolia grandiflora (Mg_1); d) inclinations of Cedrus deodara (Cd_2); e) inclinations of Cedrus deodara (Cd_3); f) inclinations of Magnolia grandiflora (Mg_2); g) inclinations of Cedrus deodara (Cd_4); h) inclinations of Cedrus deodara (Cd_5); i) inclinations of Pinus pinea (Pp); j) wind distribution with graduated wind-speed scale and mean wind direction for the selected time window (red arrow).

Chapter IV

Numerical modelling of wind at different scales

(a CFD approach on trees)

Introduction

Computational Fluid Dynamics (CFD), a branch of fluid mechanics that employs numerical analysis to solve problems related to fluid flow, is proving to be a valuable tool also for investigating tree stability (Zawawi et al., 2018). Although this may at first appear as an unusual connection, the integration of techniques originating from different fields, such as fluid dynamics and biomechanics, has become increasingly relevant to address the challenges posed by extreme climatic events. Kang et al. (2020) used a CFD code applied to a model that explicitly included trees to assess the effect of their presence on urban comfort.

The application of CFD models to trees also allows to analyse the impact of wind forces on these natural structures. The importance of this approach emerged clearly after the storm that struck Northern Italy on 24–25 July 2023, during which approximately 6,000 trees failed in the metropolitan area of Milan alone. This event highlighted how the urban layout of a city, shaped by the arrangement of buildings and streets, exerts a direct influence on wind behaviour. The so-called “canyoning effect”, which occurs when wind is accelerated between buildings, caused extensive damage, as observed along Viale Argonne in Milan, where many plane trees were uprooted.

The position of a tree with respect to the surrounding architecture, together with the limited space available for the expansion of its root system, has a significant influence on its stability. Trees planted along streets, often confined to narrow spaces and sharing the underground volume with utilities and other infrastructure, are particularly exposed to failure, especially in dense and heavily trafficked urban environments. Therefore, the exposure of a tree, that is, its spatial position within the city, is a crucial parameter in terms of hazard and, consequently, associated risk. A tree planted in an urban park and one planted along a boulevard have very different levels of associated risk, even for the same level of hazard: two trees may have the same likelihood of failure, but if they are located in different places and therefore in the vicinity of very different potential targets, the resulting level of risk will change accordingly. In the early development of assessment methods, arborists and urban forestry professionals commonly referred to their work as “hazard assessment,” focusing on evaluating the structural integrity of trees and identifying conditions that could pose safety concerns (Johnson, 1981; Smiley et al., 2011). Koeser et al. (2014) emphasised that the distinction between hazard and risk lies in how the likelihood of harm is interpreted. A hazard is anything that has the potential to cause harm, regardless of how great or small that harm may be. Risk, on the other hand, refers to the chance that this hazard will actually result in harm, and its magnitude is determined by the specific circumstances in which the hazard exists. Moreover, risk can be understood as the joint effect of how likely an event is to occur and how severe its potential consequences may be (Smiley

et al., 2012). Klein et al. (2019) described risk in terms of both the probability that an event will occur and the seriousness of the consequences that may result. Three key components must be considered when evaluating the risk posed by a tree: (1) its potential to cause damage or lead to a hazardous incident, (2) the probability that such an incident will occur, and (3) the nature and characteristics of the potential target.

Methodology and discussion

To better understand the influence of urban morphology on wind flow and tree stability, a three-dimensional model of the Bicocca district in Milan was developed as shown in Figure 115. This model has been obtained using polygonal data from the land registry of the Metropolitan City of Milan. To visualise the polygons and extract building height values, ArcMap (ESRI) was used. The polygons were then imported into AutoCAD, where the building volumes were modelled; within the same environment, the trees were also positioned. A simplified geometry was adopted for the trees: a cylindrical shape for the stem and a conical shape for the crown (the majority of the trees has this shape in the area considered). Several trees were placed that is approximately equal to the actual number present in the Bicocca district area.

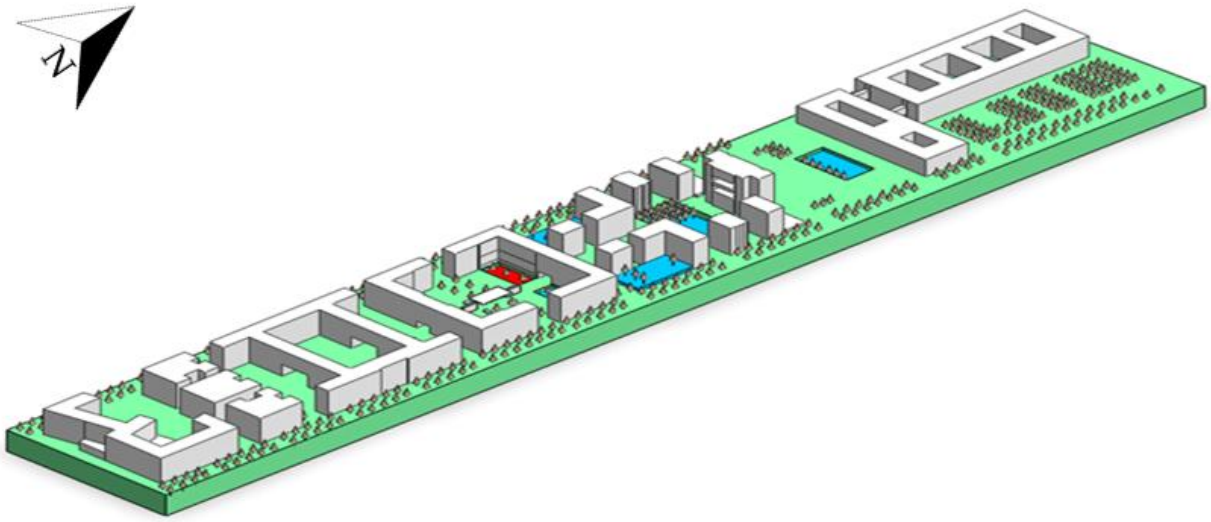

Figure 115: 3D model considering a part of Bicocca district in the city of Milan.

The model was subsequently imported into the software VENTO AEC, a computational fluid dynamics program. This software enables the simulation of wind conditions, including wind speed, direction, and physical characteristics such as pressure and temperature, as well as the interactions

between wind, buildings, and trees. The simulations offer a valuable visualization of how wind flows through urban spaces and how this affects the surrounding structures. In Figure 116 are shown some of the useful results (numerical and visual) for exemple the impact pressure on building and trees and how the city roughness changes the streamlines trend inside the city itself.

The analyses can be carried out at a large scale, as in the previous example, but they can also be performed at the scale of the individual tree, as illustrated in Figure 117. Key parameters and data can be visualised and extracted with a view to assessing tree stability, by quantifying the pressure acting on the crown and the stem.

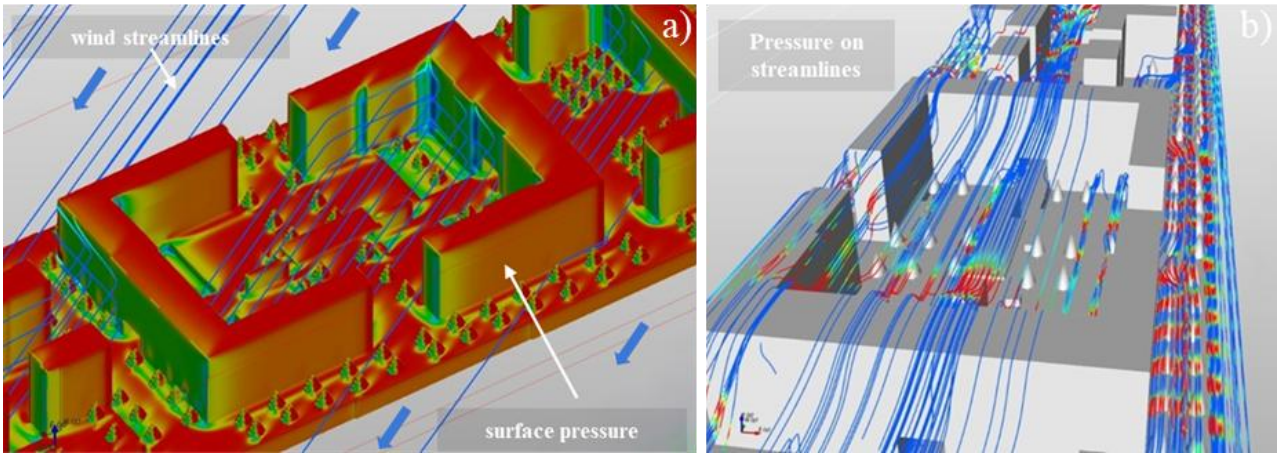

Figure 116: a) impact pressure on buildings and trees (graduated scale) with the flow direction highlighted by blue streamlines; b) streamlines showing how the impact pressure varies on structures and trees.

In Figure 117a, the following are shown: the wind velocity streamlines, which highlight the deceleration of the flow in the presence of the tree structure; the wind pressure mapped on the tree crown surface, indicating that pressure is higher where the streamlines impinge perpendicularly; and, finally, the volume of air "disturbed" by the presence of the tree structure. Figure 117b shows the impact pressure on the tree crown, the distribution of pressure in the XY plane represented by arrows, and the distribution of wind velocity in the XY plane. Figure 117c displays the impact pressure on the crown, the streamlines illustrating the velocity distribution, and the pressure distribution in the XY plane. In part d) of Figure 117, a graph is reported showing how wind speed varies as a function of the length of the two linear probes (the two dashed purple lines in Figure 117c).

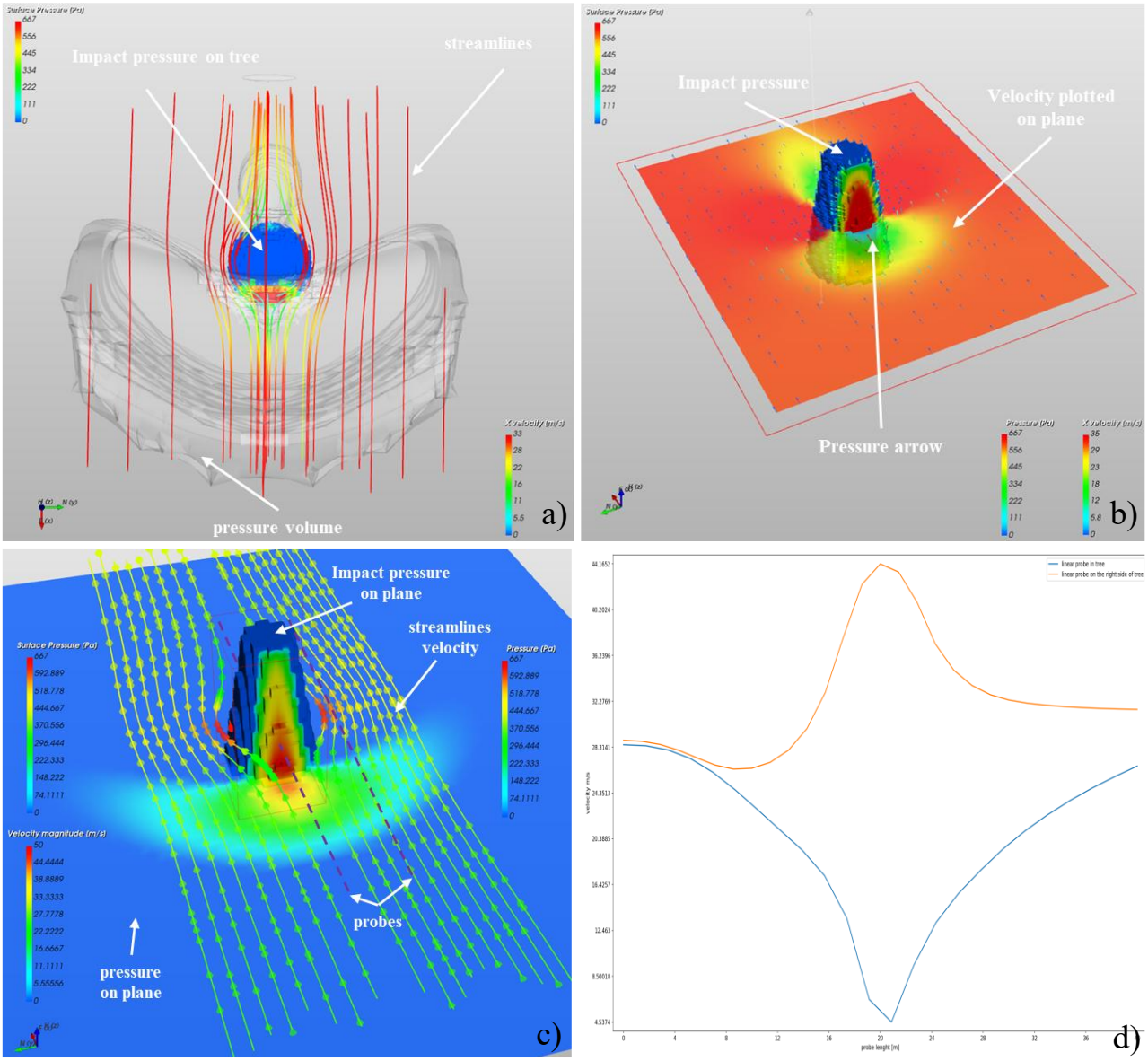

Figure 117: a) shows the wind velocity streamlines, the wind pressure mapped on the tree crown surface, volume of air "disturbed" by the presence of the tree structure; b) impact pressure on the tree crown, the distribution of pressure in the XY plane represented by arrows, and the distribution of wind velocity in the XY plane; c) impact pressure on the crown, the streamlines illustrating the velocity distribution, and the pressure distribution in the XY plane; d) variation of wind speed along the linear probe (violet dashed lines in c)).

The results of these analyses help to identify the portions of the tree that are most loaded by the wind and to understand which sectors of the root system experience the greatest mechanical stress. This information is crucial for determining the optimal direction for pulling tests, thereby allowing a more accurate estimation of the maximum overturning resistance and the corresponding safety factor. Andreozzi et al. (2025) shows that the choice of the loading direction in non-destructive tests is crucial,

since the maximum uprooting resistance values obtained by pulling the same tree in two different directions (one aligned with the prevailing wind direction and one orthogonal to it) can differ significantly. In addition, these data may support the planning of new plantings, making it possible to select tree species that are better suited to withstand wind exposure in critical urban environments.

In summary, the integration of computational fluid dynamics into urban green management would not only provide a useful tool for improving tree safety and stability but also represent a step forward in understanding and managing failure risk, thus contributing to the development of safer and more resilient cities throughout the realization of predictive models based on CFD.

Chapter V

Advanced multiple application in tree consolidation activities

(three case studies)

Introduction

Targeted interventions aimed at securing a tree through structural consolidation (both in the crown and at ground level) represent one of the key pillars of tree-failure risk mitigation. In this context, a handheld GeoSLAM laser scanner was employed to reconstruct the three-dimensional geometry of the tree. It's a portable laser scanner equipped with a LiDAR sensor for the acquisition of 3D point clouds and the generation of georeferenced three-dimensional models of the environment via a SLAM algorithm, for multidisciplinary applications (e.g. slope stability assessment, 3D analysis of geomorphic processes, forest measurements, estimation of vegetation biomass, urban planning, mapping of underground environments).

The handheld laser scanner implements a Simultaneous Localization and Mapping (SLAM) algorithm. SLAM refers to a class of probabilistic methods that enable a mobile sensor platform to estimate its own trajectory while concurrently building a map of the surrounding environment, without requiring a prior map or external positioning such as GPS. In practice, the algorithm fuses measurements from LiDAR and inertial sensors to infer the sensor "pose" (position and orientation) at each time step and uses these poses to project all LiDAR measurements into a common reference frame, thereby generating a globally consistent 3D point cloud (Bailey & Durrant-Whyte, 2006; Durrant-Whyte & Bailey, 2006). From an application perspective, SLAM algorithms have matured to the point of being routinely deployed in real-world surveying tasks, where they provide robust, centimeter-level 3D reconstructions in complex and GPS-denied environments such as forests. Their ability to deliver dense, georeferenced point clouds along arbitrary trajectories makes SLAM-based handheld LiDAR systems particularly suited to advanced geometric surveys for tree biomechanics, slope stability assessment and more general environmental and urban mapping applications (Cadena et al., 2016). 3D data were acquired using a GeoSLAM ZEB Horizon handheld LiDAR scanner (GeoSLAM Ltd., UK), optionally equipped with the ZEB-CAM / ZEB Horizon Pano system and a Ricoh Theta Z1 360° camera (Ricoh Imaging Co., Japan) for colorized point cloud generation. The resulting 3D model allows precise and accurate estimation of the tree's biometric parameters, which are required to quantify the acting loads and to design and size structural reinforcement measures, such as ground-anchored guiding cables, aimed at increasing the load-bearing capacity of the tree structure. Laser scanning technology therefore becomes a powerful decision-support tool in the design phase of structural reinforcement works. The output of a laser-based survey of the tree and its surroundings is a georeferenced point cloud. The main advantage of working with a point cloud is the possibility of three-dimensional exploration, which provides an effective means to define the initial conditions and to perform targeted measurements.

The following sections present three applications in which GeoSLAM technology was used with the objective of structurally consolidating trees of different species in different scenarios.

Figure 118: Handheld GeoSLAM ZEB Horizon LiDAR scanner used for mobile 3D point-cloud acquisition and SLAM-based reconstruction of the tree and its surroundings.

Villa Springwater case study

The work focused on the designing and installing a guying system (with ground-anchored cables) to control and restrain the potential collapse mechanism of 17 mature trees located on the grounds of Villa Springwater (Como), preventing their failure towards areas containing exposed elements, such as the villa itself. The property, shown in Figure 119, is located just north of Como, on the inner left bank of the Como branch of Lake Como, and faces north–northwest. The prevailing wind direction is northeast–southwest, and this data has been used to estimate the wind pressure acting on the crowns of the trees under consideration.

The design of the ground-based consolidation system, i.e. the selection of the appropriate type of anchor cables, was proceeded by the assessment of the actions (acting forces) in the cables. In order to compute the maximum design forces in the cables, several preliminary activities were required, specifically: (i) a 3D geometric survey of the entire area where the trees to be stabilized are located, carried out in situ; (ii) post-processing of the acquired data; and (iii) derivation of the geometric characteristics needed to calculate both the self-weight of the trees to be consolidated and the wind

action acting on them. The geometric survey was conducted using the GeoSLAM ZEB, the result of the acquisition is shown in the next Figure 120.

Figure 119: Location of Villa Springwater property (green square) and main wind direction in red arrow.

Figure 120: point cloud of property of Villa Springwater acquired by GeoSLAM ZEB.

In Figure 121, plan view of the property is shown, where the trees subjected to consolidation are plotted and grouped into five distinct groups. Each tree was assigned an ID code, where G is the group number, T denotes the progressive number within the same group, and the final part indicates the species. The species considered are: Picea abies (Pa), Cedrus deodara (Cd), Pinus nigra (Pn), Pseudotsuga menziesii (Pm) and Tilia (T).

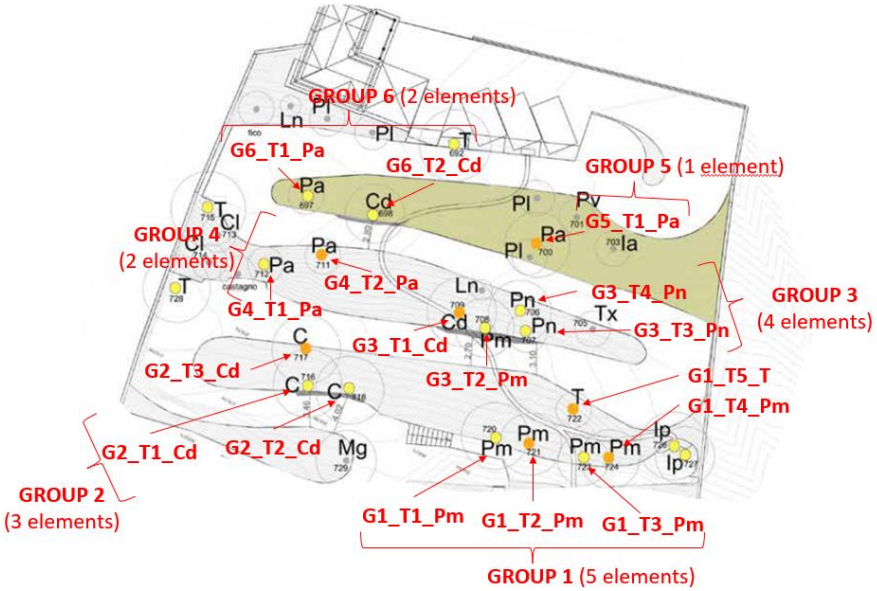

Figure 121: Planimetric view of the property, tree groups.

After selecting the grouping of trees to be restrained with guy cables, the anchorage points were identified in the field and subsequently mapped onto the point cloud. Figure 122 shows the trees together with their corresponding anchor cables.

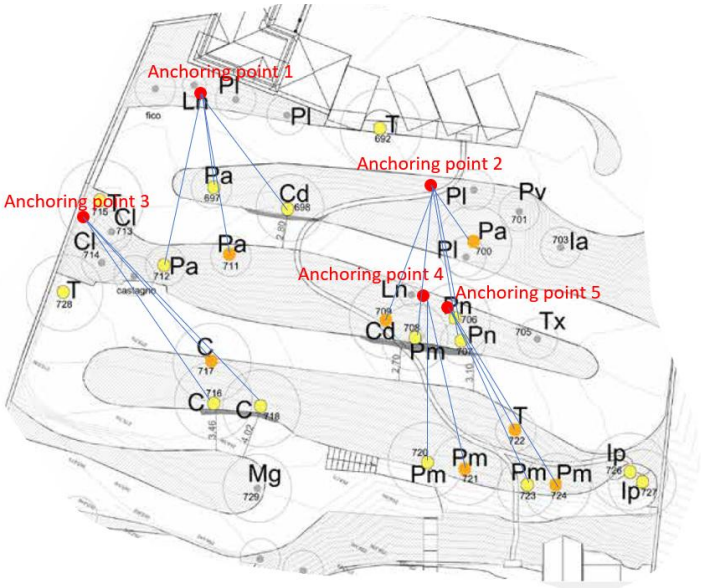

Figure 122:planimetric view shows anchoring points on the ground (red dots) and guide-rope (blue lines); main wind direction comes from SW in the local system coordinate of the map shown here.

At this stage, the point cloud comes into play. It was first cleaned and then segmented to retain only the relevant objects, namely: the slope without vegetation, the tree collars, the stems and the crowns as shown in Figure 123.

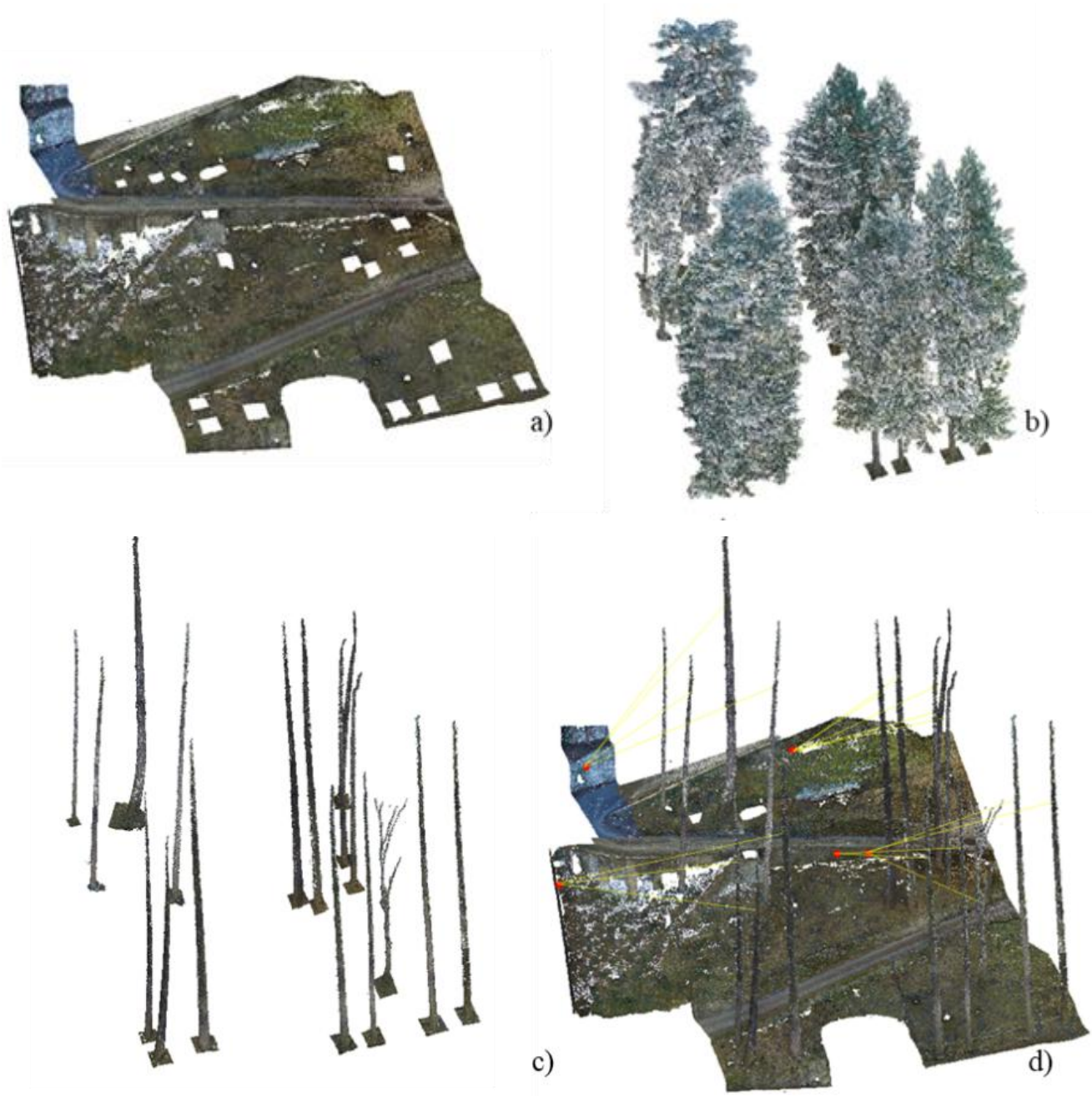

Figure 123: a) cleaned slope, b) trees (collars, trunks and crowns, c) collars and trunks, d) slope and trees without crown with anchoring points on the ground (red dots) and guiding rope (yellow lines).

Thanks to the point cloud, the coordinates of the ground-level and elevated anchorage points for each tree were determined with sub - millimetric precision, and the inclinations and exact lengths of the anchor cables were consequently computed. For each tree, the following parameters were extracted: DBH, coordinates of the tree peaks, coordinates of base of the trunks, wind load application point

coordinates, coordinates of the centre of gravity. Knowing the average green-wood density of each species, together with tree height and DBH, it was possible to estimate the mass and, consequently, the weight of each tree.

For each tree canopy area has been computed. Before performing the calculations, the tree crowns were oriented (by rotating the point cloud) so that they were perpendicular to the prevailing wind direction. A screenshot of the oriented view was then taken, as illustrated in Figure 124. The image was imported into the ArborSonic 3D software (ArborSonic 3D, Fakopp Enterprise Bt., Agfalva, Hungary), which allows the crown area to be estimated by providing a known reference length (yellow line), obtained from point cloud, and the angle with respect to the horizontal (orange angle), so the area is estimated after manually drawing the crown outline.

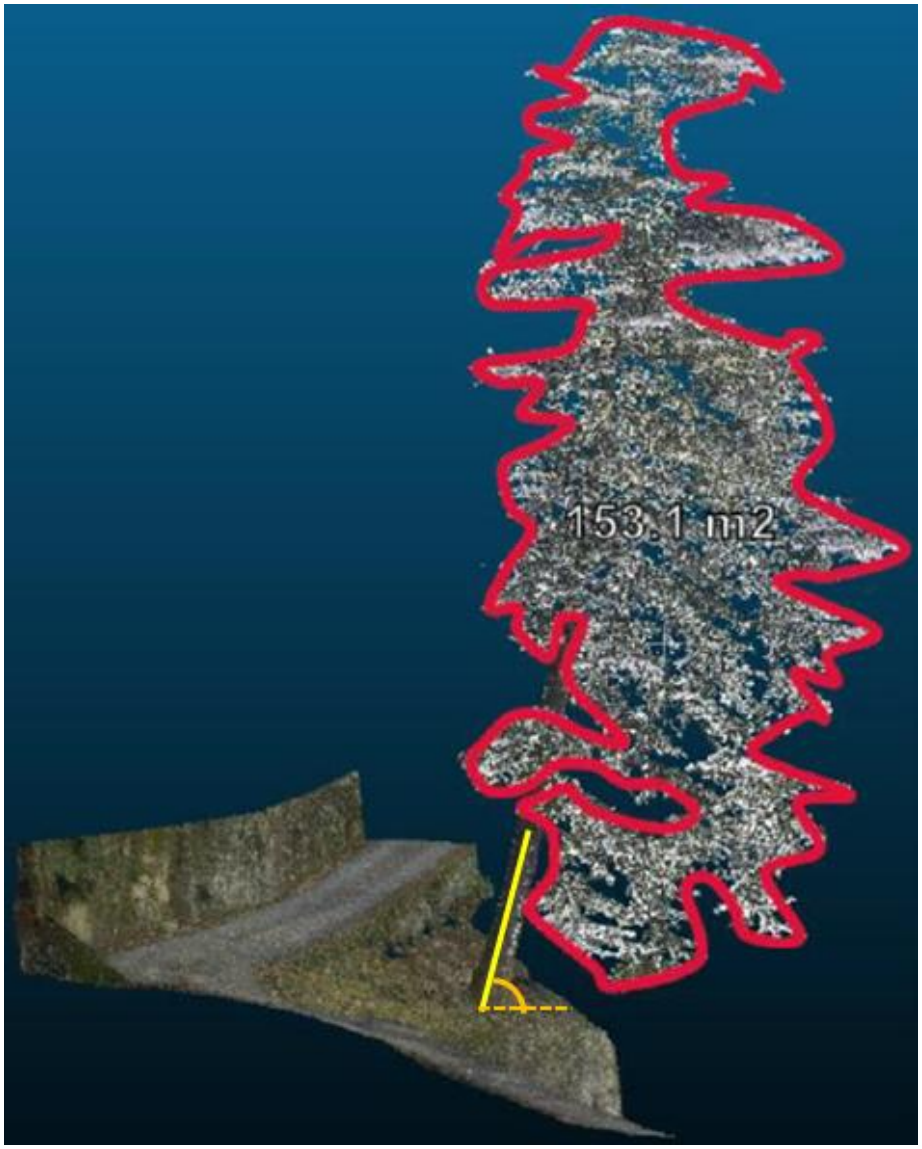

Figure 124: estimations of the crown area delineated in red line, in yellow line the reference lenght and the angle with respect to the horizontal (orange round line).

At this point the maximum wind load for each tree has been calculated using the following formula:

$$Fw = ½ \rho v\text{^}2 Cd A$$

Where ρ is the air density (1.2252 kg/m^3), v is the velocity of the wind with a value of 33 m/s (worst case scenario – hurricanes), Cd is the drag coefficient of the tree and A is the area of the crown. In Figure 125 the data for the calculation of the actions in cables for each trees involved.

The maximum forces in the cables were evaluated under the following conditions: incipient collapse, i.e. loss of load-bearing capacity of the root system (condition referred to as "at root failure"), and full overturning, with the tree falling into the positions constrained by the cable (ground projection). The two conditions described above were assessed for both wind parallel to the cable and wind perpendicular to it. Under incipient collapse, the tension in the cable is due to the self-weight of the tree (if the stem is not perfectly vertical) and to the wind action acting parallel to the cable itself. Under full collapse, the tension in the anchorage is mainly governed by the centripetal effects that develop as the tree falls along a predefined trajectory and into the positions constrained by the cable. The calculation of the forces in the cables, for the different conditions described above, was performed using a dedicated tool developed by Prof. Andrea Galli (Politecnico di Milano). For each tree and for the two wind configurations (wind parallel to the cable / wind perpendicular to the cable), the tool provides a graphical representation of the collapse mechanism, the constrained fall positions on the ground, and the acting forces. The tree stem is represented in orange, its weight is applied at the elevation of the centre of mass, and the wind action is represented by the blue vector in the Figure 126. The tool also reports the position of free fall in the absence of the cable and the two constrained collapse positions (pt. 1 and pt. 2).

N° achoring point	Species	ID	Canopy area [m2]	Weight [N]	Barycentre [m]	Wind load [kN]	Rope Lenght [m]	Rope inclination [°]
3	Cd-Cedrus deodara	G2_T1_Cd	153.29	78480.00	13.50	21.94	21.94	14.14
	Cd-Cedrus deodara	G2_T2_Cd	138.86	98100.00	17.80	24.01	24.01	26.32
	Cd-Cedrus deodara	G2_T3_Cd	37.66	78480.00	13.90	19.16	19.16	27.93
1	Pa-Picea abies	G4_T1_Pa	64.80	56113.20	18.00	28.10	28.10	17.44
	Pa-Picea abies	G4_T2_Pa	57.19	65334.60	19.60	34.23	34.23	13.64
	Pa-Picea abies	G6_T1_Pa	75.12	40711.50	10.84	24.27	24.27	23.49
	Cd-Cedrus deodara	G6_T2_Cd	159.61	93195.00	18.30	30.24	30.24	29.71
2	Pa-Picea abies	G5_T1_Pa	84.13	51796.80	16.38	20.61	20.61	58.29
	Cd-Cedrus deodara	G3_T1_Cd	297.92	73575.00	14.25	17.41	17.41	29.42
	Pm-Pseudotsuga mensiesii	G3_T2_Pm	184.92	83875.50	16.75	15.81	15.81	34.12
	Pn-Pinus nigra	G3_T3_Pn	40.36	51600.60	20.20	18.26	18.26	24.70
	Pn-Pinus nigra	G3_T4_Pn	46.70	50423.40	19.40	15.72	15.72	33.95
4	Pm-Pseudotsuga mensiesii	Gl_T1_Pm	170.30	66119.40	14.85	17.74	17.74	26.42
	Pm-Pseudotsuga mensiesii	Gl_T2_Pm	158.71	46597.50	15.05	18.88	18.88	27.93
5	Pm-Pseudotsuga mensiesii	Gl_T3_Pm	184.22	71122.50	16.75	19.96	19.96	30.42
	Pm-Pseudotsuga mensiesii	Gl_T4_Pm	210.10	71220.60	16.85	20.64	20.64	31.57
	T-Tiglio	Gl_T5_T	62.98	54053.10	13.60	13.25	13.25	3.93

Figure 125: tree data for the calculation of the actions in cables.

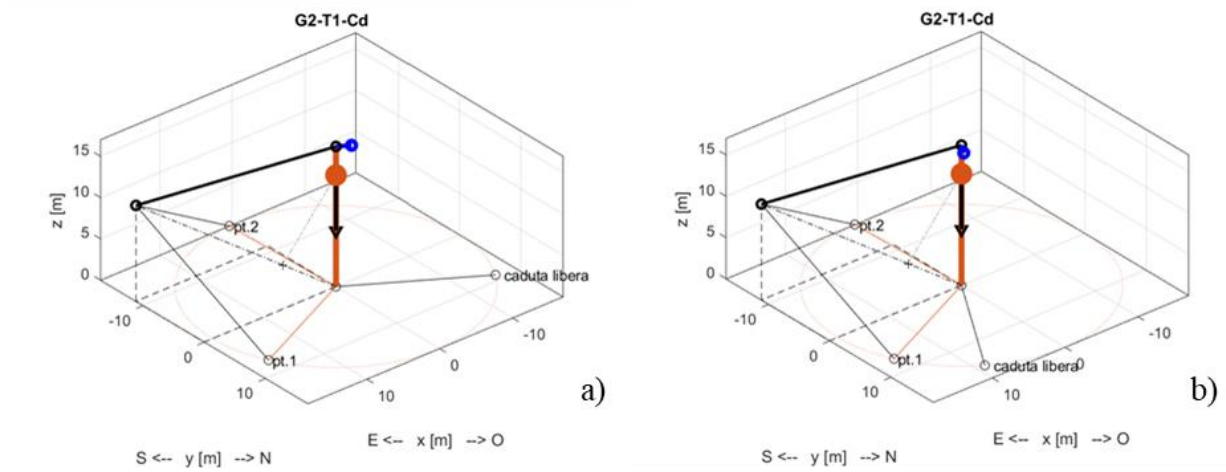

Figure 126: a) wind direction parallel with the cable, b) wind direction perpendicular with the cable.

The maximum tensile forces in each cable, required for the design of the anchorage system (cable + ground fixing at each position identified as an "anchorage point"), are summarized in the following Figure 127:

N° achoraging point	Species	Cod	Maximum pulling action [kN]
3	Cd-Cedrus deodara	G2_T1_Cd	127.00
	Cd-Cedrus deodara	G2_T2_Cd	150.00
	Cd-Cedrus deodara	G2_T3_Cd	129.00
1	Pa-Picea abies	G4_T1_Pa	73.00
	Pa-Picea abies	G4_T2_Pa	78.00
	Pa-Picea abies	G6_T1_Pa	35.00
	Cd-Cedrus deodara	G6_T2_Cd	91.00
2	Pa-Picea abies	G5_T1_Pa	120.00
	Cd-Cedrus deodara	G3_T1_Cd	150.00
	Pm-Pseudotsuga mensiesii	G3_T2_Pm	226.00
	Pn-Pinus nigra	G3_T3_Pn	125.00
	Pn-Pinus nigra	G3_T4_Pn	140.00
4	Pm-Pseudotsuga mensiesii	G1_T1_Pm	141.00
	Pm-Pseudotsuga mensiesii	G1_T2_Pm	94.00
5	Pm-Pseudotsuga mensiesii	G1_T3_Pm	145.00
	Pm-Pseudotsuga mensiesii	G1_T4_Pm	142.00
	T-Tiglio	G1_T5_T	158.00

Figure 127: maximum pulling action calculated for each tree.

Figure 128 shows the installation of the anchoring guiding system.

Figure 128: guiding system - anchoring, a) on tree, b) on the ground.

Wisteria's growth case study

During the exceptionally intense weather event that occurred in July 2023, the protected wisteria was partially damaged by the failure of the adjacent tree, which required an extraordinary summer pruning intervention to remove the portion of the crown damaged by the impact. To preserve the wisteria, a temporary wooden pergola was constructed to support the original metal structure, thereby allowing the plant to maintain photosynthetic activity and normal vegetative functions during late summer and early autumn. Following the construction of the temporary wooden support in addition to the original metal structure, a point cloud was acquired using GeoSLAM technology. The objective was to estimate both the current weight of the branches and their weight in ten years' time.

Thanks to the cleaned point cloud, it was possible to identify the branches and "map" them onto the image. In the Figure 129 below, the mapped branches are shown (numbered), with the thicker ones in red and the thinner ones in yellow. To simplify branch identification and the mapping process, the wisteria was partitioned into sections (left, central and right part).

To estimate the current weight of the branches and their weight in ten years' time, the following assumptions were made:

- From the literature, and confirmed empirically, the green-wood density of wisteria ranges between 400 and 700 kg/m³. From a safety and prevention perspective, the maximum value of 700 kg/m³ was adopted for each individual branch.
- The annual diameter growth was estimated to be 1 cm per year.
- The longitudinal (lengthwise) growth was estimated to be approximately 1 m per year.
- The cross-sections perpendicular to the branch elongation direction are assumed to be circular.
- During peak flowering, the wisteria can increase its mass per unit length by a factor of approximately 1.5.
- The final ten-year weight estimate was rounded up in order to remain on the safe side (i.e. to include a safety factor).

Thanks to the point cloud, it was possible to measure the diameter and length of each mapped branch. The volume of each individual branch was calculated using the following formula:

$V = \pi r^2 L$

where V is the volume, π is pi, and L is the length of the individual branch. Subsequently, the mass (in kg) and weight (in N) were calculated using the following equations:

$m = \rho * V$

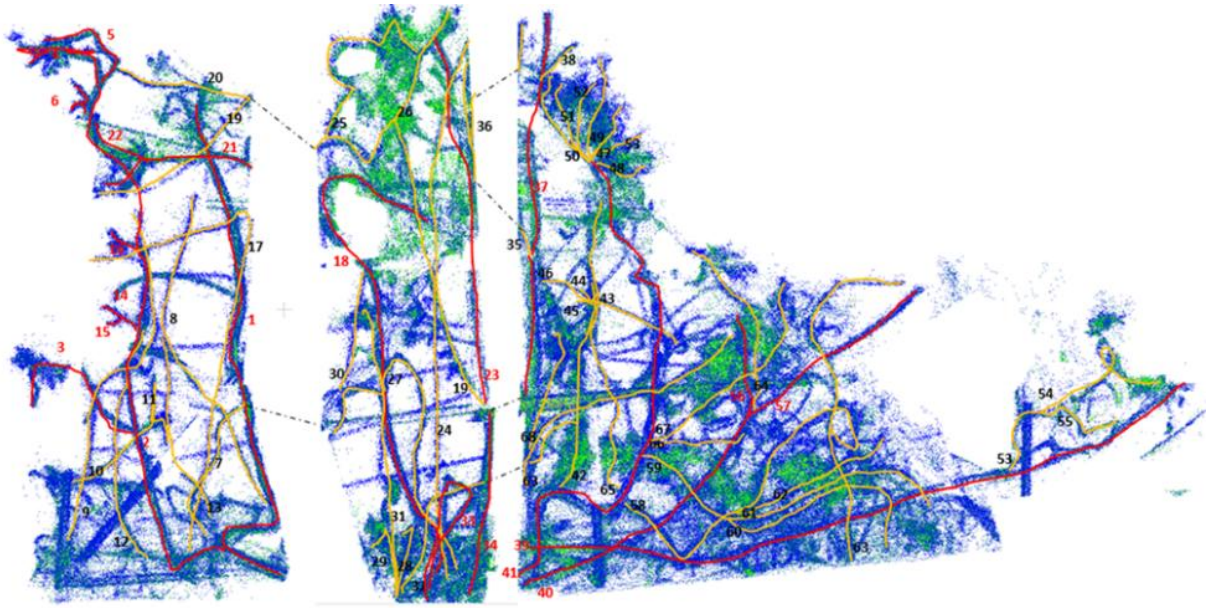

Figure 129: mapping and numbering of the branches of the wisteria. Thicker branches are shown in red, thinner ones in yellow.

where m is the mass, ρ is the density, and V is the volume.

$P = m * g$

where P is the weight, m is the mass, and g is the acceleration due to gravity.

In Table 14, the parameter values for each identified branch are reported, both for the current condition and for the 120-year forecast scenario.

Table 14: measured and calculated values of the parameters (diameter, length, volume, mass and weight) for each branch.

n° branch	NOW					10-year forecast				
	D [m]	L-tot [m]	V [m^3]	m [kg]	P [N]	D [m]	L-tot [m]	V [m^3]	m [kg]	P [N]
Branch 1	0.15	7.98	0.1410	**98.71**	**968.37**	0.25	17.98	0.8826	**617.81**	**6060.75**
Branch 2	0.11	6.42	0.0610	**42.71**	**418.96**	0.21	16.42	0.5687	**398.11**	**3905.43**
Branch 3	0.1	2.15	0.0169	**11.82**	**115.96**	0.2	12.15	0.3817	**267.19**	**2621.16**
Branch 4	0.1	2.12	0.0167	**11.66**	**114.34**	0.2	12.12	0.3808	**266.53**	**2614.69**
Branch 5	0.1	1.74	0.0137	**9.57**	**93.84**	0.2	11.74	0.3688	**258.18**	**2532.71**
Branch 6	0.1	0.54	0.0042	**2.97**	**29.12**	0.2	10.54	0.3311	**231.79**	**2273.83**
Branch 7	0.08	2.7	0.0136	**9.50**	**93.20**	0.18	12.7	0.3232	**226.22**	**2219.25**
Branch 8	0.06	4.43	0.0125	**8.77**	**86.01**	0.16	14.43	0.2901	**203.09**	**1992.34**
Branch 9	0.07	3.46	0.0133	**9.32**	**91.44**	0.17	13.46	0.3055	**213.86**	**2097.97**
Branch 10	0.07	2.64	0.0102	**7.11**	**69.77**	0.17	12.64	0.2869	**200.83**	**1970.16**
Branch 11	0.07	0.76	0.0029	**2.05**	**20.08**	0.17	10.76	0.2442	**170.96**	**1677.13**
Branch 12	0.09	2.54	0.0162	**11.31**	**110.96**	0.19	12.54	0.3555	**248.88**	**2441.53**
Branch 13	0.06	2.32	0.0066	**4.59**	**45.05**	0.16	12.32	0.2477	**173.40**	**1701.01**
Branch 14	0.1	0.68	0.0053	**3.74**	**36.67**	0.2	10.68	0.3355	**234.87**	**2304.03**
Branch 15	0.1	0.20	0.0016	**1.10**	**10.79**	0.2	10.20	0.3204	**224.31**	**2200.48**
Branch 16	0.11	0.6	0.0057	**3.99**	**39.16**	0.21	10.6	0.3671	**257.00**	**2521.17**
Branch 17	0.06	5.77	0.0163	**11.42**	**112.03**	0.16	15.77	0.3171	**221.95**	**2177.35**
Branch 18	0.13	7.33	0.0973	**68.10**	**668.11**	0.23	17.33	0.7200	**504.01**	**4944.37**
Branch 19	0.08	9.3	0.0467	**32.72**	**321.01**	0.18	19.3	0.4911	**343.79**	**3372.56**
Branch 20	0.07	2.49	0.0096	**6.71**	**65.80**	0.17	12.49	0.2835	**198.45**	**1946.78**
Branch 21	0.11	1.7	0.0162	**11.31**	**110.94**	0.21	11.7	0.4052	**283.67**	**2782.80**
Branch 22	0.11	0.7	0.0067	**4.66**	**45.68**	0.21	10.7	0.3706	**259.42**	**2544.95**
Branch 23	0.12	4.5	0.0509	**35.63**	**349.49**	0.22	14.5	0.5512	**385.83**	**3785.04**
Branch 24	0.07	4.68	0.0180	**12.61**	**123.68**	0.17	14.68	0.3332	**233.24**	**2288.13**
Branch 25	0.04	1.81	0.0023	**1.59**	**15.62**	0.14	11.81	0.1818	**127.26**	**1248.43**
Branch 26	0.04	1.3	0.0016	**1.14**	**11.22**	0.14	11.3	0.1739	**121.76**	**1194.51**
Branch 27	0.06	2.93	0.0083	**5.80**	**56.89**	0.16	12.93	0.2600	**181.98**	**1785.24**
Branch 28	0.08	3.96	0.0199	**13.93**	**136.69**	0.18	13.96	0.3552	**248.67**	**2439.42**
Branch 29	0.07	1.5	0.0058	**4.04**	**39.64**	0.17	11.5	0.2610	**182.72**	**1792.47**

Branch 30	0.07	1.6	0.0062	**4.31**	**42.28**	0.17	11.6	0.2633	**184.31**	**1808.06**
Branch 31	0.08	3.45	0.0173	**12.14**	**119.08**	0.18	13.45	0.3423	**239.58**	**2350.30**
Branch 32	0.06	3.51	0.0099	**6.95**	**68.15**	0.16	13.51	0.2716	**190.14**	**1865.32**
Branch 33	0.1	2.8	0.0220	**15.39**	**151.01**	0.2	12.8	0.4021	**281.49**	**2761.38**
Branch 34	0.15	3.7	0.0654	**45.77**	**448.99**	0.25	13.7	0.6725	**470.75**	**4618.04**
Branch 35	0.09	2.5	0.0159	**11.13**	**109.21**	0.19	12.5	0.3544	**248.09**	**2433.74**
Branch 36	0.09	1.19	0.0076	**5.30**	**51.99**	0.19	11.19	0.3173	**222.09**	**2178.68**
Branch 37	0.1	2.86	0.0225	**15.72**	**154.25**	0.2	12.86	0.4040	**282.81**	**2774.33**
Branch 38	0.07	0.6	0.0023	**1.62**	**15.86**	0.17	10.6	0.2406	**168.42**	**1652.19**
Branch 39	0.11	8.07	0.0767	**53.68**	**526.64**	0.21	18.07	0.6259	**438.11**	**4297.87**
Branch 40	0.11	4.9	0.0466	**32.60**	**319.77**	0.21	14.9	0.5161	**361.25**	**3543.90**
Branch 41	0.11	4.9	0.0466	**32.60**	**319.77**	0.21	14.9	0.5161	**361.25**	**3543.90**
Branch 42	0.07	3.38	0.0130	**9.11**	**89.32**	0.17	13.38	0.3037	**212.59**	**2085.50**
Branch 43	0.06	2.34	0.0066	**4.63**	**45.43**	0.16	12.34	0.2481	**173.68**	**1703.77**
Branch 44	0.06	1.8	0.0051	**3.56**	**34.95**	0.16	11.8	0.2373	**166.08**	**1629.22**
Branch 45	0.06	1.7	0.0048	**3.36**	**33.01**	0.16	11.7	0.2352	**164.67**	**1615.41**
Branch 46	0.08	5.17	0.0260	**18.19**	**178.45**	0.18	15.17	0.3860	**270.22**	**2650.86**
Branch 47	0.07	1	0.0038	**2.69**	**26.43**	0.17	11	0.2497	**174.77**	**1714.54**
Branch 48	0.06	0.5	0.0014	**0.99**	**9.71**	0.16	10.5	0.2111	**147.78**	**1449.73**
Branch 49	0.08	1.22	0.0061	**4.29**	**42.11**	0.18	11.22	0.2855	**199.86**	**1960.63**
Branch 50	0.08	2.1	0.0106	**7.39**	**72.49**	0.18	12.1	0.3079	**215.54**	**2114.40**
Branch 51	0.07	1.5	0.0058	**4.04**	**39.64**	0.17	11.5	0.2610	**182.72**	**1792.47**
Branch 52	0.07	1.4	0.0054	**3.77**	**37.00**	0.17	11.4	0.2588	**181.13**	**1776.89**
Branch 53	0.06	1.25	0.0035	**2.47**	**24.27**	0.16	11.25	0.2262	**158.34**	**1553.28**
Branch 54	0.07	2.4	0.0092	**6.47**	**63.43**	0.17	12.4	0.2815	**197.02**	**1932.75**
Branch 55	0.06	0.8	0.0023	**1.58**	**15.53**	0.16	10.8	0.2171	**152.00**	**1491.15**
Branch 56	0.11	1.2	0.0114	**7.98**	**78.31**	0.21	11.2	0.3879	**271.55**	**2663.87**
Branch 57	0.11	2.2	0.0209	**14.64**	**143.57**	0.21	12.2	0.4226	**295.79**	**2901.72**
Branch 58	0.09	3.5	0.0223	**15.59**	**152.90**	0.19	13.5	0.3828	**267.93**	**2628.44**
Branch 59	0.11	1.2	0.0114	**7.98**	**78.31**	0.21	11.2	0.3879	**271.55**	**2663.87**
Branch 60	0.08	2.2	0.0111	**7.74**	**75.94**	0.18	12.2	0.3105	**217.32**	**2131.88**
Branch 61	0.09	2.3	0.0146	**10.24**	**100.48**	0.19	12.3	0.3487	**244.12**	**2394.80**
Branch 62	0.09	1.8	0.0115	**8.02**	**78.63**	0.19	11.8	0.3346	**234.19**	**2297.45**
Branch 63	0.08	3.5	0.0176	**12.32**	**120.81**	0.18	13.5	0.3435	**240.47**	**2359.04**
Branch 64	0.07	3	0.0115	**8.08**	**79.28**	0.17	13	0.2951	**206.55**	**2026.27**
Branch 65	0.08	3.2	0.0161	**11.26**	**110.46**	0.18	13.20	0.3359	**235.13**	**2306.62**

Branch 66	0.07	2.5	0.0096	**6.73**	**66.07**	0.17	12.5	0.2837	**198.61**	**1948.34**
Branch 67	0.07	2.9	0.0112	**7.81**	**76.64**	0.17	12.9	0.2928	**204.96**	**2010.69**
Branch 68	0.08	2.5	0.0126	**8.80**	**86.29**	0.18	12.5	0.3181	**222.66**	**2184.30**

The acquisition of the point cloud by means of georadar made it possible to reconstruct the geometry of the *Wisteria* and to estimate its mass effectively. It was therefore possible to measure the length of the branches and to calculate their weight, with a view to subsequently designing the supporting framework that will provide structural support for the plant itself. The total weight of the wisteria, obtained from the table, corresponds to the sum of the weights of all branches, excluding leaves and flowers, and therefore represents the weight of the plant during the dormant winter period. To account for the wet vegetative biomass during late spring, when flowering is at its peak, the total weight is empirically increased by 50%. Below, the current weight and the ten-year weight estimate are reported, considering the empirical increase in weight during the peak flowering period.

Total weight from table (woody biomass only, winter condition):

- Now: 886 kg (0,9 tons)
- 10 years growth: around 17000 kg (17 tons)

Increased weight during peak flowering (+50%):

- Now: 1.350 kg (1,35 tons)
- 10 years growth: around 25.000 kg (25 tons)

According to the latest available design drawings, the trellis structure to be built and colonized by the wisteria is expected to cover a total area of approximately 300 m². Assuming that, over a 10-year period, the wisteria will be able to cover the entire trellis area, by dividing the above weights by this surface it is possible to estimate the long-term (10-year) load distribution per square meter exerted by the wisteria, obtaining the following values. Estimated 10-year load distribution:

- Woody biomass only (winter condition): 50-60 Kg/m2
- During peak flowering (+50%): 80-85 Kg/m2

Cedrus deodara case study

Following the extreme weather events (storms and strong winds) that affected northern Italy on 24–25 July 2023, with gusts reaching 70 km/h and cumulative rainfall of approximately 50 cm in 48 hours, extensive damage to trees, structures and people was recorded. In particular, the *Cedrus deodara* located in the car park area of the San Fruttuoso Garden Centre (Monza, MB) experienced a rotation of about 20° of the entire system (above-ground part: stem–crown; sub-surface part: root

system–soil) in the north–south direction. The Figure 130 shows the biomentric data of the tree, its position in the property and in red the area at risk.

The aim of this work is to design a supporting structure that minimizes the risk of tree failure. The ground-based consolidation of the tree involves the installation of a pair of anchor cables. Calculations were carried out to dimension the entire anchorage system (cables and ground anchors with foundations), considering the pulling direction, the weight of the cedar and the weight of the cables themselves. A survey was carried out using GeoSLAM from which the tree's biometric data, as well as the length and inclination of the anchor cables, were derived. The results of the survey is shown in Figure 131.

Figure 130: a) biometric parameters of the Credus deodara, b) position of the tree within the property with the area at risk in red.

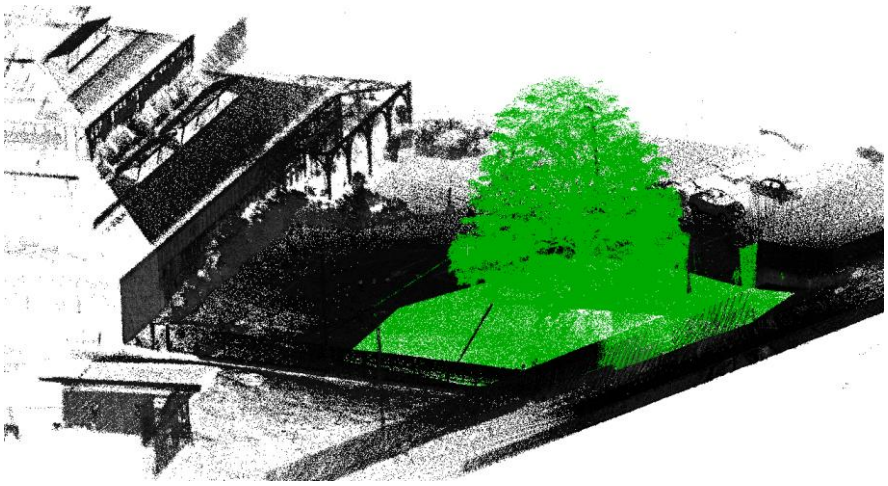

Figure 131: point cloud acquired with GeoSLAM.

To estimate the wind action on the crown, the crown area was calculated; its dimensions are shown in the previous figure. Biometric parameters:

- Tree height = 15 m
- DBH = 0.95 m
- Gravity centre of height = 7,07 m
- Density = 800 kg/m^3
- Mass = 90 q
- Cd = 0.2

The crown of the cedar is approximately uniform for each section considered. The wind action is calculated using the following equation:

$$Fw = ½ \rho v\text{^}2 \, Cd \, A$$

The calculated wind force is 19 kN. The scheme of the force involved in the computation and in the physics, analysis is shown in the Figure 132.

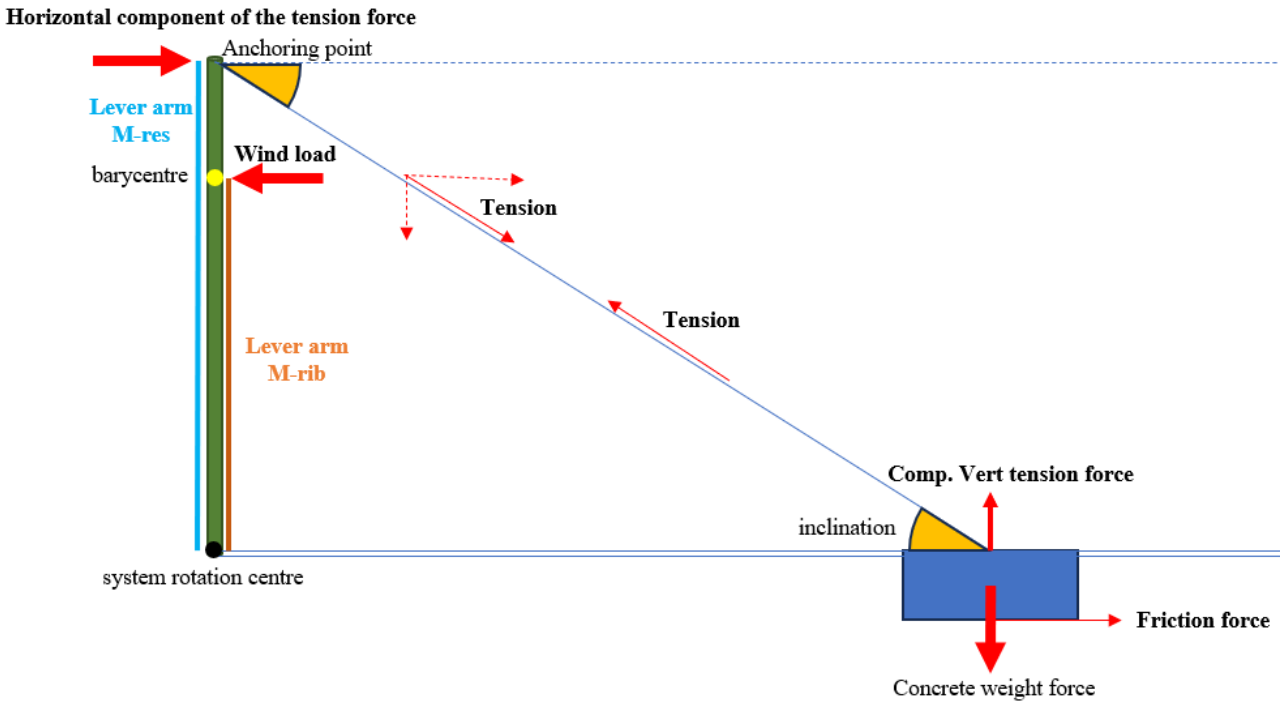

Figure 132: force scheme for the computation.

The safety factor is calculated using the following formula:

$$FS = Mres / Mrib$$

That is, the ratio between the resisting moment and the overturning moment. The overturning moment is calculated by multiplying the wind action (force) acting on the crown area of the tree by the lever arm (height from the tree base to the crown centroid, equal to 7.7 m). The resulting overturning moment is 138.7 kNm (assuming a maximum wind speed of 33 m/s). The resisting moment is calculated by multiplying the maximum tension in the cable by the lever arm (height from the tree base to the attachment point of the cables on the stem, equal to 9.25 m). The maximum cable tension had to satisfy three criteria: (1) the minimum breaking load of the cable, (2) the minimum force required to cause sliding of the concrete block, and (3) the minimum force required to break the steel ring connecting the cable to the concrete block. The corresponding values are:

- minimum force required to break the cable = 209 kN
- minimum force required to cause sliding of the concrete block = 77.3 kN
- shear resistance of the steel ring = 40.9 kN

The resistance considered is the minimum of the three values listed above, of which only the horizontal component (i.e. the component opposing the wind force) was considered; the resulting minimum value is approximately 38 kN. The safety factor was calculated by considering wind directions in 10° increments starting from north, as well as the two directions of the anchor cables. The red area corresponds to all safety factor values lower than the minimum threshold of 1.25, whereas the green area corresponds to safety factor values greater than or equal to 1.25, for which the anchorage system ensures stability.
It was possible to superimpose on the map the projected fall footprint of the tree as shown in Figure 134, also accounting for the crown dimensions. In fact, for the limiting positions between the green area (FS sufficient for stability) and the red area (FS insufficient for stability), the area that would be occupied by the cedar crown in a fallen position was projected (in orange).

wind direction	M-res	FS
0	0.00	0.00
10	0.00	0.00
20	0.00	0.00
30	0.00	0.00
40	0.00	0.00
50	0.00	0.00
60	0.00	0.00
70	0.00	0.00
80	24.64	0.18
90	85.45	0.62
100	143.66	1.04
110	197.51	1.42
120	294.51	2.12
130	394.89	2.85
140	483.27	3.48
150	556.96	4.02
160	613.74	4.42
166	638.94	4.61
170	651.86	4.70
180	670.18	4.83
190	668.14	4.82
200	645.80	4.66
202	638.94	4.61
210	603.83	4.35
220	543.51	3.92
230	466.69	3.36
240	375.68	2.71
250	273.25	1.97
260	187.17	1.35
270	132.31	0.95
280	73.43	0.53
290	12.33	0.09
300	0.00	0.00
310	0.00	0.00
320	0.00	0.00
330	0.00	0.00
340	0.00	0.00
350	0.00	0.00
360	0.00	0.00

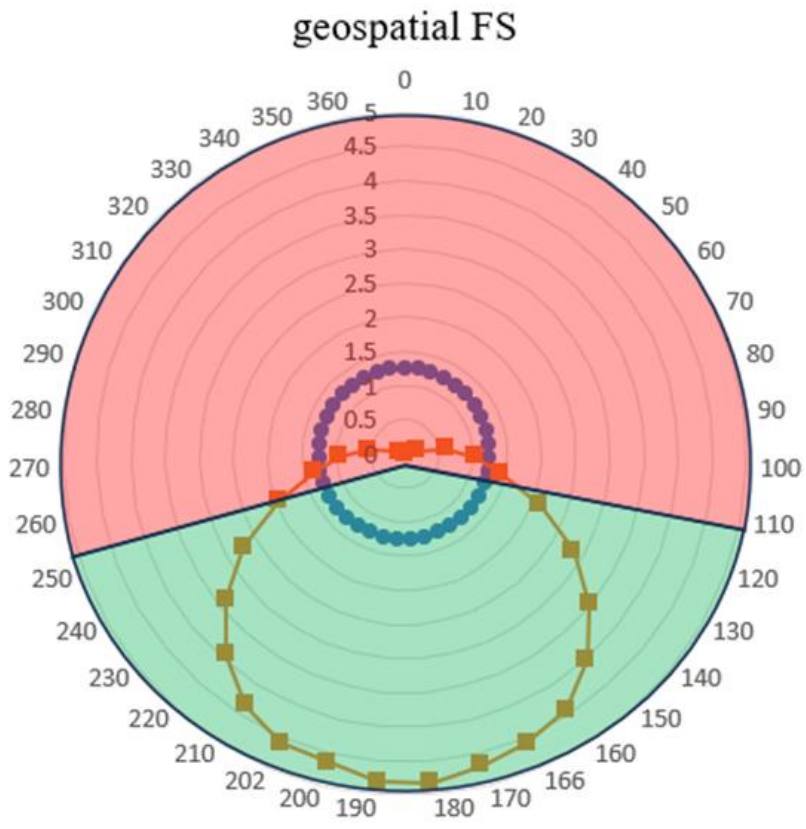

Figure 133: on the left, table with wind direction, resisting moment and safety factor values; on the right, geospatial representation of the safety factor, with the FS values obtained shown in orange and the minimum FS value of 1.25 shown in blue.

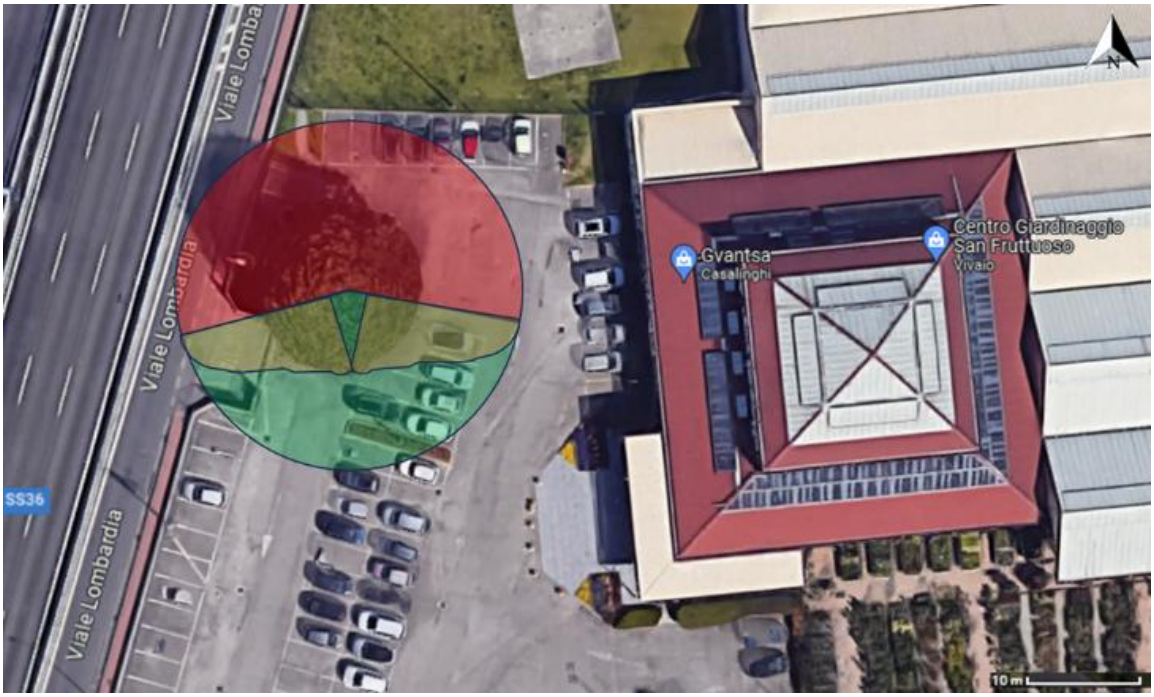

Figure 134: identification of safe areas and areas requiring attention.

Figure 135 shows the results of the structure at the end of the works.

Figure 135: top left: connection of the cables to the tree; top right: wide-angle view of the anchor cables; bottom: connection of the cables to the metal ring.

Conclusions

This PhD thesis presents a quantitative, multi-scale framework for assessing the wind-induced overturning stability of urban trees. This framework integrates controlled laboratory experimentation (1-g physical modelling), full-scale testing (including non-destructive and destructive pulling tests), dynamic wind–inclination monitoring with a method for estimating of aerodynamic drag coefficient, exemple of the use of computational fluid dynamics wind modelling and operational workflows for designing and verifying structural mitigation measures, supported by 3D surveys.

Main findings and scientific contributions:

- About the physical model. A dedicated 1-g physical model was developed to reproduce the coupled wind–tree-structure response under controlled boundary conditions. This setup enabled repeatable trials and high-resolution measurements of base reactions and the kinematic response. This provided a controlled benchmark to: (i) validating the measurement chain and signal-processing, (ii) quantifying power and energy exchanges along the system (input, transfer and dissipation) and (iii) interpreting how the observed dynamic response can be mapped onto moment–rotation behaviour. It put a strong base for the future construction of an early-warning system based on thresholds for the management and mitigation of urban tree fall risk.

- Full-scale testing and geotechnical interpretation of anchorage. The experimental campaign at the Botanic Garden of Dundee enabled a direct link between the moment–rotation response and soil parameters and local site conditions. Destructive tests showed that peak resistance occurs at rotations on the order of a few degrees (1.59° - 2.93°), highlighting the value of failure tests for verifying ultimate limit states.

- Directional bias and test geometry: what matters in pulling tests. By varying pulling direction and pulling angle, the results indicate that the plan-direction can strongly affect inferred anchorage capacity: when comparing north (assumed aligned with the predominant wind axis) versus west directions, differences reached up to 66%, and on average capacity was 23% higher along the north direction, consistent with wind-driven acclimation effects. In contrast, the moment capacity appeared comparatively insensitive to even large changes in pulling angle, in line with the analytical interpretation adopted.

- Reliability of capacity estimates and the role of site-specific conditions. In the Dundee dataset, capacity estimates obtained using commonly employed approaches (moment-based and stiffness-based) were, in most instances, conservative in relation to the measured values. Only a small proportion of trees exhibited overestimation, whereas underestimation was more prevalent, offering a safety margin. At the same time, the lack of a clear correlation between maximum moment and 'similar' trees in terms of species and biometrics confirms that overturning stability is strongly influenced by local conditions and cannot be reduced to biometric descriptors alone.

- New method for estimating the aerodynamic drag coefficient. A contribution of the thesis is a workflow to estimate the aerodynamic drag coefficient (Cd) from wind–inclination time series by reconstructing wind-induced moments and comparing moment–rotation curves through Wessolly-type fitting using as constraints the curves from the non-destructive datasets (based on the stiffness of the tree). The results show that using filtered data is an efficient way of producing ML values from dynamic data that are very close to those derived from non-destructive pulling tests: for 9 trees out of 11, the difference remains within ~2% (maximum 5%). Conversely, adopting a tabulated Cd coefficient can introduce substantially larger discrepancies (in extreme cases >200%), with the potential to over- or under-estimate ML and, consequently, the safety factor. When compared to destructive ML values, estimates based on extrapolated Cd remain generally conservative, preserving a prudent stance in safety assessment.

- Safety factors. This thesis compares the safety factors derived from the measured M_L, the M_L extrapolated from non-destructive tests and the M_L reconstructed from dynamic monitoring using the different values of Cd. Overall, assessments based on extrapolated Cd and non-destructive tests are largely consistent, with few exceptions. However, tabulated Cd tends to produce pronounced variability in FS ratios, which can bias the interpretation of available safety margins.

- Bayesian approach to Wessolly Tipping curve. From an applied perspective, a natural next step is to formulate a hierarchical multi-tree model in which the Wessolly shape parameters a, b, c are drawn from population-level distributions. Incorporating relevant covariates (such as DBH, tree height, canopy area, mass, and key geotechnical descriptors) would then shift

the calibration from a purely descriptive fit to a genuinely predictive framework, improving robustness and transferability across operational settings.

Operational outcomes and practical implications:

- Medium–long-term monitoring. The monitoring campaign at the Vivaio Bicocca demonstrated that combining an anemometer with inclinometers allows the direction and intensity of wind to be tracked over time and, crucially, reveals markedly different responses even among nearby trees due to local shielding and urban roughness effects. Monitoring is also effective in assessing the effectiveness of a safety measure by evaluating how the stability of the tree changes before, during and after the consolidation system is put in place.

- CFD to quantify exposure of trees in urban environment. The simulations—ranging from district scale to single-tree scale—provide a physically grounded description of how urban morphology modifies wind speed and pressure fields, enabling identification of the crown sectors most heavily loaded and, by implication, the root-system sectors most stressed. This information is directly useful to select optimal pulling directions and to support planting and management decisions in critical urban contexts.

- 3D surveys as a bridge between measurements and mitigation design. Across three case studies, georeferenced point clouds were used to derive biometric and geometric parameters required for intervention design: (i) at Villa Springwater, 3D data supported the design of a cable reinforcement system for 17 trees by estimating geometry, cable lengths/angles, and design actions; (ii) in the wisteria case, the 3D reconstruction enabled estimation of current and 10-year biomass, translated into expected distributed loads (order of magnitude: tens of kg/m^2), providing a quantitative basis to verify the supporting structure; (iii) for the cedar in Monza, following the 24–25 July 2023 events, the survey supported cable-system sizing and the evaluation of the safety factor in a real risk scenario. Overall, these cases demonstrate how the measurement–model–design chain can be made traceable and replicable, with immediate benefits for practitioners and public administrations.

The results are robust in demonstrating directional sensitivity, the reliability for the Cd estimating method, and the value of integrating tests, monitoring, and modelling; however, broader generalization requires larger and more diverse datasets (species, architectures, soils, and urban morphologies), explicitly including seasonal effects (soil moisture/suction, canopy state, growth) that

alter both aerodynamic demand and anchorage response. All this information and data would enable predictive models to be constructed and reinforced for forecasting the maximum uprooting resistance of trees in urban environments.

Moreover, full integration of monitoring-derived response indicators, CFD exposure maps, and mechanically consistent models is a natural next step towards uncertainty-aware workflows implementable as site-specific digital twins for high-value areas. From an applied perspective, the priority is to translate these tools into operational guidance (minimum monitoring requirements, post-event validation protocols, criteria for test direction selection, and low-impact mitigation choices) capable of reconciling public safety with biodiversity goals.

Bibliography

Achim, A., & Nicoll, B. C. (2009). Modelling the anchorage of shallow-rooted trees. *Forestry: An International Journal of Forest Research*, *82*(3), 273–284. https://doi.org/10.1093/FORESTRY/CPP004

Allotey, N., & Foschi, R. (2005). Coupled P-y T-z analysis of single piles in cohesionless soil under vertical and/or horizontal ground motion. *Journal of Earthquake Engineering*, *9*(6), 755–775. https://doi.org/10.1142/S1363246905002316

Andreozzi, M., Marrazzo, G., Marsiglia, A., Boldrin, D., Castellanza, R. Pietro, Knappett, J., & Ciantia, M. O. (2025). On the Uprooting Stability of Trees: Combined Loading Effect on Tree Stability Assessment. *Forests 2025, Vol. 16, Page 1780*, *16*(12), 1780. https://doi.org/10.3390/F16121780

Armstrong, M., & Paterson, I. B. (1970). *The Lower Old Red Sandstone of the Strathmore Region*.

Bailey, T., & Durrant-Whyte, H. (2006). *Simultaneous Localization and Mapping (SLAM): Part II*. https://ieeexplore.ieee.org/stamp/stamp.jsp?tp=&arnumber=1678144

Bejo, L., Divos, F., & Fathi, S. (2017). Dynamic Root Stability Assessment—Basics and Practical Examples. *In International NDTE of Wood Symposium* , 262–269. https://www.fpl.fs.fed.us/documnts/fplgtr/fpl_gtr249.pdf

Bejo L., Sumegi I., & Divos F. (2022). Dynamic tree stability: improved testing method-ology and indications of reliability. *Proc. 22nd NDTE Symposium*, 175–183.

Bekkers, C. C. A., Angelou, N., & Dellwik, E. (2022). Drag coefficient and frontal area of a solitary mature tree. *Journal of Wind Engineering and Industrial Aerodynamics*, *220*, 104854. https://doi.org/10.1016/J.JWEIA.2021.104854

Blackwell, P. G., Rennolls, K., & Coutts, M. P. (1990). A Root Anchorage Model for Shallowly Rooted Sitka spruce. *Forestry: An International Journal of Forest Research*, *63*(1), 73–91. https://doi.org/10.1093/FORESTRY/63.1.73

Cadena, C., Carlone, L., Carrillo, H., Latif, Y., Scaramuzza, D., Neira, J., Reid, I., & Leonard, J. J. (2016). Past, present, and future of simultaneous localization and mapping: Toward the robust-perception age. *IEEE Transactions on Robotics*, *32*(6), 1309–1332. https://doi.org/10.1109/TRO.2016.2624754

Cao, J., Tamura, Y., & Yoshida, A. (2012). Wind tunnel study on aerodynamic characteristics of shrubby specimens of three tree species. *Urban Forestry & Urban Greening*, *11*(4), 465–476. https://doi.org/10.1016/J.UFUG.2012.05.003

Carinanos, P., & Calaza, P. (2018). *The role of urban and peri-urban forests in reducing risks and managing disasters*. https://geotour2016.com/Viewproject

Cavender-Bares, J. M., Nelson, E., Meireles, J. E., Lasky, J. R., Miteva, D. A., Nowak, D. J., Pearse, W. D., Helmus, M. R., Zanne, A. E., Fagan, W. F., Mihiar, C., Muller, N. Z., Kraft, N. J. B., & Polasky, S. (2022). The hidden value of trees: Quantifying the ecosystem services of tree lineages and their major threats across the contiguous US. *PLOS Sustainability and Transformation*, *1*(4 April). https://doi.org/10.1371/journal.pstr.0000010

Chandler, R. J. (1988). *The in-situ measurement of the undrained shear strength of clays using the field vane. Vane shear strength testing in soils: field and laboratory studies.*

Ciftci, C., Arwade, S. R., Kane, B., & Brena, S. F. (2014). Analysis of the probability of failure for open-grown trees during wind storms. *Probabilistic Engineering Mechanics*, *37*, 41–50. https://doi.org/10.1016/j.probengmech.2014.04.002

Coutts, M. P. (1983). Root architecture and tree stability. *Plant and Soil*, *71*(1–3), 171–188. https://doi.org/10.1007/BF02182653/METRICS

Coutts, M. P. (1986). Components of tree stability in sitka spruce on peaty gley soil. *Forestry*, *59*(2), 173–197. https://doi.org/10.1093/FORESTRY/59.2.173

Crook, M. J., & Ennos, A. R. (1996). The anchorage mechanics of deep rooted larch, Larix europea × L. japonica. *Journal of Experimental Botany*, *47*(10), 1509–1517. https://doi.org/10.1093/JXB/47.10.1509

Crook, M. J., & Ennos, A. R. (1998). The increase in anchorage with tree size of the tropical tap rooted tree Mallotus wrayi, King (Euphorbiaceae). *Annals of Botany*, *82*(3), 291–296. https://doi.org/10.1006/ANBO.1998.0678

Danjon, F., Barker, D. H., Drexhage, M., & Stokes, A. (2008). Using three-dimensional plant root architecture in models of shallow-slope stability. *Annals of Botany*, *101*(8), 1281–1293. https://doi.org/10.1093/AOB/MCM199

Danjon, F., Fourcaud, T., & Bert, D. (2005). Root architecture and wind-firmness of mature Pinus pinaster. *New Phytologist*, *168*(2), 387–400. https://doi.org/10.1111/J.1469-8137.2005.01497.X

Dattola, G., Ciantia, M. O., Galli, A., Blyth, L., Zhang, X., Knappet, J. A., Castellanza, R., Sala, C., & Leung, A. K. (2020). A Macroelement Approach for the Stability Assessment of Trees. *Lecture Notes in Civil Engineering*, *40*, 417–426. https://doi.org/10.1007/978-3-030-21359-6_44

Défossez, P., Veylon, G., Yang, M., Bonnefond, J. M., Garrigou, D., Trichet, P., & Danjon, F. (2021). Impact of soil water content on the overturning resistance of young Pinus Pinaster in sandy soil. *Forest Ecology and Management*, *480*, 118614. https://doi.org/10.1016/J.FORECO.2020.118614

Detter, A., Rust, S., & Krišāns, O. (2023). Experimental Test of Non-Destructive Methods to Assess the Anchorage of Trees. *Forests 2023, Vol. 14, Page 533*, *14*(3), 533. https://doi.org/10.3390/F14030533

Duckett, N. R. (2014). *Development of improved predictive tools for mechanical soil root interaction*. PhD Thesis.

Dupont, S., & Brunet, Y. (2008). Impact of forest edge shape on tree stability: A large-eddy simulation study. *Forestry*, *81*(3), 299–315. https://doi.org/10.1093/FORESTRY/CPN006

Dupuy, L., Fourcaud, T., & Stokes, A. (2005a). A numerical investigation into factors affecting the anchorage of roots in tension. *European Journal of Soil Science*, *56*(3), 319–327. https://doi.org/10.1111/j.1365-2389.2004.00666.x

Dupuy, L., Fourcaud, T., & Stokes, A. (2005b). A numerical investigation into the influence of soil type and root architecture on tree anchorage. *Plant and Soil*, *278*(1–2), 119–134. https://doi.org/10.1007/s11104-005-7577-2

Dupuy, L. X., Fourcaud, T., Lac, P., & Stokes, A. (2007). A generic 3D finite element model of tree anchorage integrating soil mechanics and real root system architecture. *American Journal of Botany*, *94*(9), 1506–1514. https://doi.org/10.3732/ajb.94.9.1506

Durrant-Whyte, H., & Bailey, T. (2006). *Simultaneous Localisation and Mapping (SLAM): Part I The Essential Algorithms*. https://doi.org/10.1109/MRA.2006.1638022

Fourcaud, T., Ji, J. N., Zhang, Z. Q., & Stokes, A. (2008). Understanding the Impact of Root Morphology on Overturning Mechanisms: A Modelling Approach. *Annals of Botany*, *101*(8), 1267–1280. https://doi.org/10.1093/AOB/MCM245

Fraser, A. I., & Gardiner, J. B. H. (1967). *Rooting and stability in Sitka Spruce: Vol. Forestry Commission*. https://cdn.forestresearch.gov.uk/1967/03/fcbu040.pdf

Frediani K. (2021). *Botanic Garden and Grounds strategy*.

Galli, A., Sala, C., Castellanza, R., Marsiglia, A., & Ciantia, M. O. (2024). Lesson learnt from static pulling tests on trees: an experimental study on toppling behaviour of complex foundations. *Acta Geotechnica*, *19*(3), 1477–1494. https://doi.org/10.1007/s11440-023-02004-1

Gardiner, B. A., & Quine, C. P. (2000). Management of forests to reduce the risk of abiotic damage - A review with particular reference to the effects of strong winds. *Forest Ecology and Management*, *135*(1–3), 261–277. https://doi.org/10.1016/S0378-1127(00)00285-1

Ghani, M. A., Stokes, A., & Fourcaud, T. (2009). The effect of root architecture and root loss through trenching on the anchorage of tropical urban trees (Eugenia grandis Wight). *Trees - Structure and Function*, *23*(2), 197–209. https://doi.org/10.1007/S00468-008-0269-9/FIGURES/5

Giachetti, A., Ferrini, F., & Bartoli, G. (2021). A risk analysis procedure for urban trees subjected to wind- or rainstorm. *Urban Forestry and Urban Greening*, *58*. https://doi.org/10.1016/j.ufug.2020.126941

Grant, P. F., & Nickling, W. G. (1998). DIRECT FIELD MEASUREMENT OF WIND DRAG ON VEGETATION FOR APPLICATION TO WINDBREAK DESIGN AND MODELLING. *Land Degrad. Develop*, *9*, 57–66. https://doi.org/10.1002/(SICI)1099-145X(199801/02)9:1

Gromke, C., & Ruck, B. (2008). Aerodynamic modelling of trees for small-scale wind tunnel studies. *Forestry: An International Journal of Forest Research*, *81*(3), 243–258. https://doi.org/10.1093/FORESTRY/CPN027

Guitard, D. G. E., & Castera, P. . (1995). Experimental analysis and mechanical modelling of windinduced tree sways. *Wind and Trees*, 182–194. https://doi.org/10.1353/pcg.1941.0006

Hand, K. L., Doick, K. J., & Moss, J. L. (2019). *Modelling the delivery of regulating ecosystem services for large stature trees in the urban environment with i-Tree Eco*.

Harnas, F. R., Rahardjo, H., Leong, E. C., Tan, P. Y., & Ow, L. F. (2016). Stability of containerized urban street trees. *Landscape and Ecological Engineering*, *12*(1), 13–24. https://doi.org/10.1007/S11355-015-0272-4

Holbo, H. R., Corbett, T. C., & Horton, P. J. (1980). Aeromechanical behavior of selected Douglas-fir. *Agricultural Meteorology*, *21*(2), 81–91. https://doi.org/10.1016/0002-1571(80)90056-4

Jackson, T. D., Sethi, S., Dellwik, E., Angelou, N., Bunce, A., Van Emmerik, T., Duperat, M., Ruel, J.-C., Wellpott, A., Bloem, S. Van, Achim, A., Kane, B., Ciruzzi, D. M., Loheide, S. P., 11, I. I., James, K., Burcham, D., Moore, J., Schindler, D., … Gardiner, B. (2021). The motion of trees

in the wind: a data synthesis. *Biogeosciences*, *18*, 4059–4072. https://doi.org/10.5194/bg-18-4059-2021

Jakob, M., & Lambert, S. (2009). Climate change effects on landslides along the southwest coast of British Columbia. *Geomorphology*, *107*(3–4), 275–284. https://doi.org/10.1016/J.GEOMORPH.2008.12.009

James, K. R., Haritos, N., & Ades, P. K. (2006). Mechanical stability of trees under dynamic loads. *American Journal of Botany*, *93*(10), 1522–1530. https://doi.org/10.3732/ajb.93.10.1522

Johnson, D. W. (1981). *ree Hazards: Recognition and Reduction in Recreation Sites*. http://books.google.com

Jonsson, M. J., Foetzki, A., Kalberer, M., Lundström, T., Ammann, W., & Stöckli, V. (2007). Natural frequencies and damping ratios of Norway spruce (Picea abies (L.) Karst) growing on subalpine forested slopes. *Trees - Structure and Function*, *21*(5), 541–548. https://doi.org/10.1007/S00468-007-0147-X/FIGURES/4

Kamimura, K., Kitagawa, K., Saito, S., & Mizunaga, H. (2012). Root anchorage of hinoki (Chamaecyparis obtuse (Sieb. Et Zucc.) Endl.) under the combined loading of wind and rapidly supplied water on soil: Analyses based on tree-pulling experiments. *European Journal of Forest Research*, *131*(1), 219–227. https://doi.org/10.1007/S10342-011-0508-2/FIGURES/6

Kane, B., & Clouston, P. (2008). Tree pulling tests of large shade trees in the genus Acer. *Arboriculture and Urban Forestry*, *34*(2), 101–109. https://doi.org/10.48044/jauf.2008.013

Kane, B., & Smiley, E. T. (2011). Drag coefficients and crown area estimation of red maple. *Https://Doi.Org/10.1139/X06-086*, *36*(8), 1951–1958. https://doi.org/10.1139/X06-086

Kang, G., Kim, J. J., & Choi, W. (2020). Computational fluid dynamics simulation of tree effects on pedestrian wind comfort in an urban area. *Sustainable Cities and Society*, *56*. https://doi.org/10.1016/j.scs.2020.102086

Klein, R. W., Koeser, A. K., Hauer, R. J., Hansen, G., & Escobedo, F. J. (2019). Risk Assessment and Risk Perception of Trees: A Review of Literature Relating to Arboriculture and Urban Forestry. *Arboriculture & Urban Forestry (AUF)*, *45*(1), 26–38. https://doi.org/10.48044/JAUF.2019.003

Koeser, A. K., Hasing, G., Mclean, D., & Northrop, R. (2014). *Tree Risk Assessment Methods: A Comparison of Three Common Evaluation Forms*. https://edis.ifas.ufl.edu

Koizumi, A., Motoyama, J. ichi, Sawata, K., Sasaki, Y., & Hirai, T. (2010). Evaluation of drag coefficients of poplar-tree crowns by a field test method. *Journal of Wood Science 2010 56:3*, *56*(3), 189–193. https://doi.org/10.1007/S10086-009-1091-8

Liang, D., & Huang, G. (2023). Influence of Urban Tree Traits on Their Ecosystem Services: A Literature Review. In *Land* (Vol. 12, Issue 9). Multidisciplinary Digital Publishing Institute (MDPI). https://doi.org/10.3390/land12091699

Liang, T., Knappett, J. A., & Duckett, N. (2015). Modelling the seismic performance of rooted slopes from individual root-soil interaction to global slope behaviour. *Geotechnique*, *65*(12), 995–1009. https://doi.org/10.1680/JGEOT.14.P.207

Lonsdale, D. (2007). Current issues in arboricultural risk assessment and management. *Arboricultural Journal*, *30*(2), 163–174. https://doi.org/10.1080/03071375.2007.9747490;WGROUP:STRING:PUBLICATION

Manickathan, L., Defraeye, T., Allegrini, J., Derome, D., & Carmeliet, J. (2018). Comparative study of flow field and drag coefficient of model and small natural trees in a wind tunnel. *Urban Forestry & Urban Greening*, *35*, 230–239. https://doi.org/10.1016/J.UFUG.2018.09.011

Marsiglia, A., Ciantia, M. O., Galli, A., & Canepa, D. (2022). Vertical loading tests on a simplified tree root prototype. *In Physical Modelling in Geotechnics (ICPMG 2022 Proceedings)*, 832–835.

Mattheck, C., & Breloer, H. (1994). FIELD GUIDE FOR VISUAL TREE ASSESSMENT (VTA). *Arboricultural Journal*, *18*(1), 1–23. https://doi.org/10.1080/03071375.1994.9746995

Mayhead, G. J. (1973). SOME DRAG COEFFICIENTS FOR BRITISH FOREST TREES DERIVED FROM WIND TUNNEL STUDIES. *Agricultural Meteorology*, *12*, 123–130.

Meijer, G., Bengough, G., Knappett, J., Loades, K., & Nicoll, B. (2019). Measuring the strength of root-reinforced soil on steep natural slopes using the corkscrew extraction method. *Forests*, *10*(12). https://doi.org/10.3390/F10121135

Meijer, G. J., Bengough, A. G., Knappett, J. A., Loades, K. W., & Nicoll, B. C. (2018). In situ measurement of root reinforcement using corkscrew extraction method. *Canadian Geotechnical Journal*, *55*(10), 1372–1390. https://doi.org/10.1139/CGJ-2017-0344/ASSET/IMAGES/CGJ-2017-0344IEQ24.GIF

Meijer, G. J., Muir Wood, D., Knappett, J. A., Bengough, G. A., & Liang, T. (2019). Analysis of coupled axial and lateral deformation of roots in soil. *International Journal for Numerical and Analytical Methods in Geomechanics*, *43*(3), 684–707. https://doi.org/10.1002/NAG.2880

Mickovski, S. B., Bransby, M. F., Bengough, A. G., Davies, M. C. R., & Hallett, P. D. (2010). Resistance of simple plant root systems to uplift loads. *Canadian Geotechnical Journal*, *47*(1), 78–95. https://doi.org/10.1139/T09-076/ASSET/IMAGES/LARGE/T09-076F16.JPEG

Mickovski, S. B., & Ennos, A. R. (2003). Model and whole-plant studies on the anchorage capabilities of bulbs. *Plant and Soil*, *255*(2), 641–652. https://doi.org/10.1023/A:1026007229517

Mickovski, S. B., Stokes, A., & Van Beek, L. P. H. (2005). A decision support tool for windthrow hazard assessment and prevention. *Forest Ecology and Management*, *216*(1–3), 64–76. https://doi.org/10.1016/J.FORECO.2005.05.043

Moore, J. R., & Maguire, D. A. (2005). Natural sway frequencies and damping ratios of trees: Influence of crown structure. *Trees - Structure and Function*, *19*(4), 363–373. https://doi.org/10.1007/S00468-004-0387-Y/FIGURES/8

Moore, J. R., & Maguire, D. A. (2008). Simulating the dynamic behavior of Douglas-fir trees under applied loads by the finite element method. *Tree Physiology*, *28*(1), 75–83. https://doi.org/10.1093/TREEPHYS/28.1.75

Moore, J. R., Tombleson, J. D., Turner, J. A., & Van Der Colff, M. (2008). Wind effects on juvenile trees: a review with special reference to toppling of radiata pine growing in New Zealand. *Forestry: An International Journal of Forest Research*, *81*(3), 377–387. https://doi.org/10.1093/FORESTRY/CPN023

Nelson, O., Kassim, A., Yunusa, G. H., & Talib, Z. A. (2015). Modelling the effect of wind forces on landslide occurrence in Bududa district, Uganda. *Jurnal Teknologi*, *77*(11), 35–42. https://doi.org/10.11113/JT.V77.6392

Nicoll, B. C., Gardiner, B. A., & Peace, A. J. (2008). Improvements in anchorage provided by the acclimation of forest trees to wind stress. *Forestry*, *81*(3), 389–398. https://doi.org/10.1093/forestry/cpn021

Nicoll, B. C., Gardiner, B. A., Rayner, B., & Peace, A. J. (2006). Anchorage of coniferous trees in relation to species, soil type, and rooting depth. *Canadian Journal of Forest Research*, *36*(7), 1871–1883. https://doi.org/10.1139/X06-072

Nova, R., & Montrasio, L. (1991). Settlements of shallow foundations on sand. *Geotechnique*, *41*(2), 243–256. https://doi.org/10.1680/GEOT.1991.41.2.243

Ow, L. F., Harnas, F. R., Indrawan, I. G. B., Sahadewa, A., Sim, E. K., Rahardjo, H., Leong, E. C., Fong, Y. K., & Tan, P. Y. (2010). Tree-pulling experiment: An analysis into the mechanical stability of rain trees. *Trees - Structure and Function*, *24*(6), 1007–1015. https://doi.org/10.1007/S00468-010-0470-5/FIGURES/5

Peltola, H. (1996). Swaying of trees in response to wind and thinning in a stand of Scots pine. *Boundary-Layer Meteorology 1996 77:3*, *77*(3), 285–304. https://doi.org/10.1007/BF00123529

Peltola, H., Kellomäki, S., Hassinen, A., & Granander, M. (2000). Mechanical stability of Scots pine, Norway spruce and birch: an analysis of tree-pulling experiments in Finland. *Forest Ecology and Management*, *135*(1–3), 143–153. https://doi.org/10.1016/S0378-1127(00)00306-6

Pollen, N., & Simon, A. (2005). Estimating the mechanical effects of riparian vegetation on stream bank stability using a fiber bundle model. *Water Resources Research*, *41*(7), 1–11. https://doi.org/10.1029/2004WR003801;PAGE:STRING:ARTICLE/CHAPTER

Rudnicki, M., Mitchell, S. J., & Novak, M. D. (2011). Wind tunnel measurements of crown streamlining and drag relationships for three conifer species. *Https://Doi.Org/10.1139/X03-233*, *34*(3), 666–676. https://doi.org/10.1139/X03-233

Ruel, J. C. (2000). Factors influencing windthrow in balsam fir forests: from landscape studies to individual tree studies. *Forest Ecology and Management*, *135*(1–3), 169–178. https://doi.org/10.1016/S0378-1127(00)00308-X

Salmond, J. A., Tadaki, M., Vardoulakis, S., Arbuthnott, K., Coutts, A., Demuzere, M., Dirks, K. N., Heaviside, C., Lim, S., MacIntyre, H., McInnes, R. N., & Wheeler, B. W. (2016). Health and climate related ecosystem services provided by street trees in the urban environment. In *Environmental Health: A Global Access Science Source* (Vol. 15). BioMed Central Ltd. https://doi.org/10.1186/s12940-016-0103-6

Satterthwaite, D., Huq, S., Pelling, M., Reid, H., & Romer-Lankao, P. (2007). Adapting to climate change in urban areas: the possibilities and constraints in low and middle income nations. *Building for Climate Change Resilience*, *November*, 1–109. https://www.iied.org/10549iied

Schmidlin, T. W. (2009). Human fatalities from wind-related tree failures in the United States, 1995-2007. *Natural Hazards*, *50*(1), 13–25. https://doi.org/10.1007/S11069-008-9314-7

Schwarz, M., Cohen, D., & Or, D. (2010). Root-soil mechanical interactions during pullout and failure of root bundles. *Journal of Geophysical Research: Earth Surface*, *115*(4), 4035. https://doi.org/10.1029/2009JF001603;ISSUE:ISSUE:DOI

Schwarz, M., Cohen, D., & Or, D. (2011). Pullout tests of root analogs and natural root bundles in soil: Experiments and modeling. *Journal of Geophysical Research: Earth Surface*, *116*(2). https://doi.org/10.1029/2010JF001753

Sellier, D., & Fourcaud, T. (2005). A mechanical analysis of the relationship between free oscillations of Pinus pinaster Ait. saplings and their aerial architecture. *Journal of Experimental Botany*, *56*(416), 1563–1573. https://doi.org/10.1093/JXB/ERI151

Sellier, D., & Fourcaud, T. (2009). Crown structure and wood properties:Influence on tree sway and response to high winds. *American Journal of Botany*, *96*(5), 885–896. https://doi.org/10.3732/AJB.0800226;WEBSITE:WEBSITE:BSAPUBS;WGROUP:STRING:PUBLICATION

Smiley, E. T., Matheny, N., & Lilly, S. (2011). *Tree Risk Assessment: A Foundation*.

Smiley, E. T., Matheny, N., & Lilly, S. (2012). Qualitative Tree Risk Assessment. *Arborist News*, 12–18.

Speak, A. F., & Salbitano, F. (2021). Thermal comfort and perceptions of the ecosystem services and disservices of urban trees in florence. *Forests*, *12*(10). https://doi.org/10.3390/f12101387

Urata, T., Shibuya, M., Koizumi, A., Torita, H., & Cha, J. Y. (2012). Both stem and crown mass affect tree resistance to uprooting. *Journal of Forest Research*, *17*(1), 65–71. https://doi.org/10.1007/S10310-011-0249-6

van Genuchten, M. Th. (1980). A Closed-form Equation for Predicting the Hydraulic Conductivity of Unsaturated Soils. *Soil Science Society of America Journal*, *44*(5), 892–898. https://doi.org/10.2136/SSSAJ1980.03615995004400050002X

van Wassenaer, P., & Richardson, M. (2009). A review of tree risk assessment using minimally invasive technologies and two case studies. *Aboricultural Journral*, *32*(4), 275–292. https://doi.org/10.1080/03071375.2009.9747583

Vollsinger, S., Mitchell, S. J., Byrne, K. E., Novak, M. D., & Rudnicki, M. (2005). Wind tunnel measurements of crown streamlining and drag relationships for several hardwood species. *Canadian Journal of Forest Research*, *35*(5), 1238–1249. https://doi.org/10.1139/x05-051

Wessolly, L., & Erb, M. (1998). *Handbuch der Baumstatik und Baumkontrolle. Berlin: Patzer Verlag.*

Yang, M., Défossez, P., Danjon, F., Dupont, S., & Fourcaud, T. (2017). Which root architectural elements contribute the best to anchorage of Pinus species? Insights from in silico experiments. *Plant and Soil*, *411*(1–2), 275–291. https://doi.org/10.1007/s11104-016-2992-0

Yang, M., Défossez, P., Danjon, F., & Fourcaud, T. (2014). Tree stability under wind: Simulating uprooting with root breakage using a finite element method. *Annals of Botany*, *114*(4), 695–709. https://doi.org/10.1093/aob/mcu122

Yang, M., Défossez, P., Danjon, F., & Fourcaud, T. (2018). Analyzing key factors of roots and soil contributing to tree anchorage of Pinus species. *Trees - Structure and Function*, *32*(3), 703–712. https://doi.org/10.1007/s00468-018-1665-4

Yang, M., Défossez, P., & Dupont, S. (2020). A root-to-foliage tree dynamic model for gusty winds during windstorm conditions. *Agricultural and Forest Meteorology*, *287*. https://doi.org/10.1016/J.AGRFORMET.2020.107949

Zawawi, M. H., Saleha, A., Salwa, A., Hassan, N. H., Zahari, N. M., Ramli, M. Z., & Muda, Z. C. (2018). A review: Fundamentals of computational fluid dynamics (CFD). *AIP Conference Proceedings*, *2030*. https://doi.org/10.1063/1.5066893

Zhang, X., Knappett, J. A., Leung, A. K., Ciantia, M. O., Liang, T., & Danjon, F. (2020). Small-scale modelling of root-soil interaction of trees under lateral loads. *Plant and Soil*, *456*(1–2), 289–305. https://doi.org/10.1007/S11104-020-04636-8

Zhang, X., Knappett, J. A., Leung, A. K., Ciantia, M. O., Liang, T., & Nicoll, B. C. (2023). Centrifuge modelling of root-soil interaction of laterally loaded trees under different loading conditions. *Geotechnique*, *73*(9), 766–780. https://doi.org/10.1680/jgeot.21.00088

Zhang, X., Knappett, J. A., Leung, A. K., & Liang, T. (2018). Physical modelling of soil-structure interaction of tree root systems under lateral loads. *Physical Modelling in Geotechnics*, *1*, 481–486. https://doi.org/10.1201/9780429438660-70

Zhu, S., Huang, C., Su, Y., & Sato, M. (2014). 3D ground penetrating radar to detect tree roots and estimate root biomass in the field. *Remote Sensing*, *6*(6), 5754–5773. https://doi.org/10.3390/rs6065754

Tesi di dottorato realizzata nell'ambito del progetto NBFC finanziato dal PNRR Missione 4 Componente 2 Investimento 1.4, finanziato dall'Unione Europea - NextGenerationEU - Cup H43C22000530001